THESE DE DOCTORAT DE

L'UNIVERSITE DE NANTES

COMUE UNIVERSITE BRETAGNE LOIRE

ECOLE DOCTORALE N° 600
Ecole doctorale Ecologie, Géosciences, Agronomie et Alimentation
Spécialité : **Sciences de la Terre et des Planètes**

Par

Chloé LARRE

H2O and S behaviors in martian magmatic system: An experimental and spectroscopic approach

Thèse présentée et soutenue à **Nantes**, le **25 Novembre 2019**
Unité de recherche : UMR CNRS 6112 LPG

H2O and S behaviors in martian magmatic system: An experimental and spectroscopic approach.

Remerciements

Résumé étendu

Mars est la planète la plus étudiée de notre système solaire. De par sa position au sein du système solaire, plus particulièrement parmi les planètes telluriques, Mars est une planète attractive pour les missions spatiales. En effet, aujourd'hui, plus de 40 missions spatiales ont été menées sur Mars. Comprendre son évolution, caractériser sa structure interne et comprendre son passé permettra de mieux comprendre comment les planètes telluriques, plus particulièrement la Terre, se sont formées.

Mars possède une taille 2 fois plus petite que celle de la Terre avec un rayon moyen de 3389 km. Actuellement, l'atmosphère martienne est riche en CO_2 et la pression atmosphérique très basse, de l'ordre de 6 mbar. Cependant, plusieurs indices obtenus à la surface impliquent la présence d'une atmosphère passée plus épaisse et riche en éléments volatils.

De par l'absence apparente de plaques tectoniques, la surface de Mars a pu conserver les traces géologiques de son passé. Grâce aux missions spatiales orbitales telle que Mars Global Surveyor (en orbite depuis 2005), la minéralogie et géologie de surface ont pu être mieux contraintes. Ainsi, la surface de Mars est recouverte en majorité de roches volcaniques, de composition basaltique. Ces roches proviennent d'une activité volcanique accrue pendant les temps primitifs de Mars, soit pendant le Noachien et l'Hespérien principalement (< 3 Ga). Cette activité a permis l'édification du volcan le plus important de tout le système solaire, Olympus Mons, avec un diamètre basal atteignant les 500 km et 25 km de hauteur.

Suite à cette intense activité volcanique martienne, la présence de minéraux mafiques tels qu'olivine, pyroxènes, plagioclase ont été détectés à la surface. Ces minéraux se retrouvent liés à des roches sédimentaires, recouvrant aussi la surface de Mars. Parmi les minéraux secondaires formés par altération, des sulfates, carbonates, phyllosilicates et oxydes de fer prédominent sur Mars. Ces minéraux mafiques et sédimentaires ont aussi été observés dans les météorites martiennes obtenues sur Terre.

Ainsi, l'histoire géologique de Mars a pu être découpée en plusieurs ères : l'ère des phyllosilicates au Noachien (< 3.5 Ga), des sulfates fin Noachien et Hespérien (< 3 Ga), puis l'ère des oxydes de fer à l'Amazonien (3 Ga et aujourd'hui). Ces trois ères caractéristiques traduisent l'évolution climatique de la surface de Mars. La présence de phyllosicilates et sulfates est une preuve indéniable de la présence passée d'eau liquide sur Mars. De plus, différentes structures géologiques traduisant des traversées de fluides aqueux impliquent que de l'eau liquide était présente pendant les temps primitifs de la planète.

Cependant, pour maintenir de l'eau liquide, l'atmosphère martienne doit être épaisse, et donc riches en espèces volatiles tels que CO_2, H_2O, S, CH_4. La présence de sulfates, chlorures, carbonates, fluorures et apatites impliquent l'existence des éléments volatils S, C, O, Cl, F et P. Ces éléments volatils ont une origine volcanique et ont dû contribuer à l'élaboration d'une atmosphère primitive dense lors de leur dégazage.

En premier lieu, les objectifs principaux des missions martiennes étaient de déterminer si la surface de Mars contenait de la vie. Les échecs de ces missions ont permis de redéfinir les objectifs pour envisager des signes de vies microscopiques passés, lorsque de l'eau liquide était présente à la surface. La future mission spatiale Mars 2020 est un rover qui comportera à la fois d'anciens instruments similaires au rover Curiosity déjà présent sur Mars ; mais aussi de

nouveaux outils pour mieux caractériser la surface. Parmi ces nouveaux outils, l'instrument SuperCam comportera un spectromètre Raman.

Cette thèse est articulée autour de l'étude des matériaux analogues aux roches volcaniques martiennes par spectroscopie Raman pour définir une base de données pour la future mission spatiale Mars 2020. Couplée à l'élaboration de cette base de données spectrales, le comportement des éléments volatils H, O et S a été étudié dans des analogues aux basaltes martiens synthétisés à hautes pressions et températures. Comprendre le comportement de ces éléments dans un milieu atypique que sont les magmas basaltiques de Mars, contribue à établir le budget des élémenets volatils liés au transfert de ces magmas vers la surface. Ces budgets permettront de comprendre comment a pu se former une atmosphère dense ayant maintenue de l'eau liquide.

Cette thèse comporte trois sujets de recherche. Un premier chapitre permet l'introduction et description des différentes méthodes expérimentales et analytiques employées. Une étude expérimentale sur le comportement de H_2O et du S dans des verres basaltiques de compositions similaires aux basaltes martiens, a été réalisée et détaillée dans deux chapitres (Chapitre II et III). Le troisième sujet de recherche, et quatrième chapitre, développe la réalisation d'une quantification de S dans des mélanges de minéraux mafiques et sulfates, que nous pouvons retrouver à la surface de Mars via la spectroscopie Raman. Ces minéraux sont issus de l'altération de roches volcaniques.

Chapitre I

La pétrologie expérimentale est un outil de plus en plus utilisé par les géologues afin de modéliser le comportement des magmas en profondeur. En effet, les roches volcaniques récoltées aux pieds des volcans ont très souvent perdu de l'information, notamment sur la quantité d'éléments volatils présents dans les magmas. Ainsi, synthétiser des analogues aux roches volcaniques naturelles permet de comprendre quelles étaient les conditions de pression, température, d'oxydo-réduction et la teneur en éléments volatils du magma avant son ascension et dégazage.

Pour réaliser ces synthèses, plusieurs outils sont mis à disposition permettant d'échantillonner différentes gammes de pressions et températures. Pour des basses pressions, l'autoclave à chauffage interne permet de synthétiser des roches à moins de 15 - 20 km de profondeur sur Terre. Au contraire, l'enclume multi-diamant va permettre de réaliser des expériences correspondant au manteau voire jusqu'au noyau externe sur Terre. Enfin, se situant entre ces deux techniques, le piston-cylindre reproduit des conditions de pressions de la fin de la croûte jusqu'au manteau (~150 km).

Les expériences réalisées au piston-cylindre installé récemment au Laboratoire de Planétologie et Géodynamique de Nantes, n'ont pas permis d'obtenir des résultats probants dès ses premières utilisations. En effet, toute une série d'optimisation du matériel a été réalisée afin d'obtenir les résultats attendus. Parmi les changements majeurs, nous avons décidé de prendre des fours non-modelés, malgré le gradient de température, car ils présentaient plus de résistance lors des expériences sous pression. Aussi, un modelage particulier de la gaine de thermocouple est systématiquement réalisé avant chaque expérience pour contrer les effets de remontée qui engendrait sa casse. Enfin, un chiller a été acheté en complément du piston-cylindre pour

réaliser des trempes à bonnes températures et obtenir un verre. Malgré de nombreux mois d'optimisation du matériel, certaines expériences ne donnaient pas de verres. Ces résultats seront discutés dans le chapitre suivant (Chapitre II).

Une fois les synthèses contrôlées, leurs analyses ont été multiples. Elles se distinguent en trois grandes catégories.

La spectroscopie

La spectroscopie Raman, infra-rouge et l'XPS font parties de la même catégorie d'outil analytique permettant la caractérisation de nos échantillons de manière non-destructive.

La spectroscopie Raman est une méthode de caractérisation suite à l'excitation des molécules présentes dans le matériel avec un laser possédant une longueur d'onde spécifique. Chaque molécule vibre selon différents modes :

- v_1 : « symmetric stretch »
- v_2 : « bending »
- v_3 : « anti-symmetric stretch »

La représentation schématique des trois types de vibrations Raman est exposée dans la Fig.A.
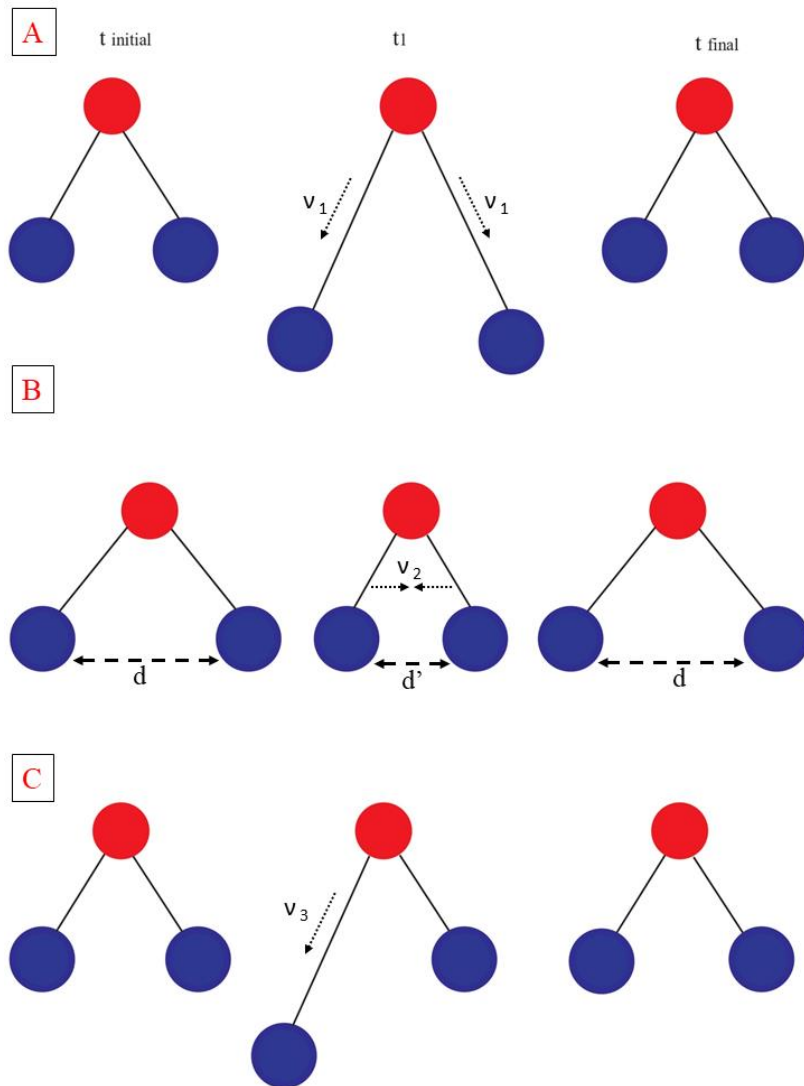
Fig.A: Modes de vibration utilisant la molécule d'H_2O (Hydrogène en rouge et Oxygènes en bleu) suivant différentes étapes : avant excitation "t", pendant l'action du laser "t1", après l'excitation "tfinal". A) symmetric stretch ν_1; B) symmetric bending ν_2; C) anti-symmetric stretch ν_3. Avec d indiquant la distance entre deux atomes d'oxygènes et d'la distance lors de la vibration de la molécule.

La spectroscopie Infra-Rouge a été utilisée dans cette étude pour la quantification d'H_2O dans nos verres. Cette méthode nous permet de coupler ces résultats avec la quantification en H_2O réalisée par Raman. L'infra-Rouge est une technique de vibration de molécules utilisant le domaine de l'infra-rouge.

La spectroscopie XPS (X-Photoelectron Spectroscopy) a été utilisée de différentes manières :

- spéciation du Fe
- spéciation du S
- détermination du degré de polymérisation du verre

<u>Caractérisation chimique</u>

Le couplage de la microscopie électronique à balayage (MEB) avec la microsonde électronique nous permet d'obtenir à la fois la structure de notre échantillon, la présence d'éventuels cristaux et la composition chimique. Le MEB nous permet d'obtenir à la fois la structure et la composition chimique grâce à une technique de quantification mis en place à l'Institut des Matériaux Jean Rouxel de Nantes (IMN). La microsonde électronique renseignant sur la composition chimique des échantillons était réalisée à l'institut d'IFREMER de Brest.

L'état redox du fer a aussi pu être déterminé chimiquement grâce à la technique de colorimétrie réalisée au sein du Laboratoire de Planétologie et Géodynamique de Nantes (LPG). Cette méthode permet d'obtenir le Fe_{2+} ainsi que le FeO_{tot} dans nos échantillons.

<u>XRD et XPS</u>

Les dernières techniques analytiques utilisées au cours de cette thèse était réalisée à l'IMN.

La Diffraction Rayons-X (XRD) nous a permis d'identifier les minéraux présents dans des échantillons présentant des cristaux de tailles nanométriques. En raison de leur trop petite taille, l'identification de ces cristaux ne pouvaient être réalisée par MEB ou Raman.

La spectroscopie photonique à rayon-X (XPS) permettait de déterminer le degré d'oxydation du Fe, du S, et de déterminer le degré de polymérisation du verre analysé. Cette technique nous a permis la confrontation entre les données obtenues par colorimétrie pour le degré d'oxydation du fer, et la comparaison du degré de polymérisation observé par Raman.

A l'aide de ces divers outils, j'ai pu réaliser les trois études présentées dans le manuscrit, qui constituent un article soumis et en cours de révision (Chapitre II), un en cours de soumission (Chapitre III) et un article accepté (Chapitre IV), respectivement.

Chapitre II

La présence d'eau sur Mars est indéniable. Les structures géologiques observées à la surface ainsi que les minéraux hydratés en sont la preuve. Cette espèce volatile a donc joué un rôle important pendant les temps primitifs de la planète et résulte probablement de l'intense activité volcanique de Mars.

Afin de déterminer quelle quantité d'eau peut être transportée par les magmas martiens jusqu'à la surface, il faut comprendre son comportement dans ce type de composition. En effet, la solubilité de H_2O est bien contrainte dans les différentes compositions de magmas terrestres. Cependant, les études de magmas martiens, caractérisés par leurs fortes teneurs en fer, en présence d'espèces volatiles sont peu abondantes, du aux difficultés de réaliser des synthèses riches en fer et en H_2O.

Dans ce chapitre, nous avons réalisé des expériences hautes pressions et températures sur des analogues aux basaltes martiens avec 15.5 et 23.5 %pds FeO_{ini}. Ces synthèses sont comparées à des verres analogues aux basaltes terrestres (~10 %pds FeO_{ini}). Les verres réalisés contenaient moins de 3 pds % H_2O dans les basaltes martiens, et jusqu'à 6 pds % H_2O dans les basaltes terrestres. Les produits expérimentaux ont été analysées par spectroscopie Raman principalement. Des synthèses contenant > 3 pds % H_2O dans les analogues martiens ont été réalisées mais n'ont pas donné de verre. Ces résultats constituent la deuxième partie de ce chapitre.

Comportement d'H_2O dans des verres riches en Fe

Les principaux résultats obtenus lors de cette étude ont été difficiles à interpréter en raison du manque d'étude expérimentale dans ce domaine. La première différence entre les basaltes terrestres et martiens réside dans la signature spectrale. En effet, sur les analogues martiens, les vibrations entre 800 et 1200 cm^{-1} dominent les basses fréquences se situant entre 200 et 600 cm^{-1}. A l'inverse, pour des compositions pauvres en fer, les basses fréquences dominent. Avec cette étude, nous pourrons comprendre davantage le signal d'un verre basaltique à la surface de Mars par spectroscopie Raman. Des exemples de signatures spectrales sur les analogues martiens et terrestres sont représentés dans la Fig.B.

D'autre part, la teneur en H_2O dissoute dans nos verres riches en fer (11 - 16 pds % FeO_{tot}) n'excède pas les 1.5 pds % et semble dépendante de la teneur en FeO_{tot} dans le verre. En effet, pour une même pression, les verres pauvres en Fer (< 8 pds % FeO_{tot}) peuvent dissoudre plus de 6 pds % H_2O. Un maximum de 1 pds % semble être atteint pour la composition la plus riche en Fer (16 pds %), bien que nous ne soyons pas à saturation.

A cette corrélation s'ajoutent de nouvelles espèces observées par spectroscopie Raman. En effet, dans nos verres riches en Fer contenant peu d'H_2O (< 2 pds %), des espèces OH libres ont été détectées dans la zone de vibration de H_2O, à 3660 cm^{-1}. Ce pic est représenté par une flèche sur la Fig.B. Cette espèce a déjà été observée par spectroscopie Raman, et traduit un verre très riche en H_2O (> 5 wt %). Nous avons observé les mêmes espèces dans nos verres terrestres qui contenaient plus de 6 pds % H_2O. La présence des OH libres semble être corrélée avec un pic observé à 670 cm^{-1} (voir Fig.B). La présence des OH libres dans des verres riches en Fer peut avoir un impact sur son degré de polymérisation. En effet, d'après les déconvolutions effectuées, les verres présentant des OH libres semblent montrer une structure plus polymérisée, même s'il est nécessaire de procéder à davantage de recherche sur ce point.
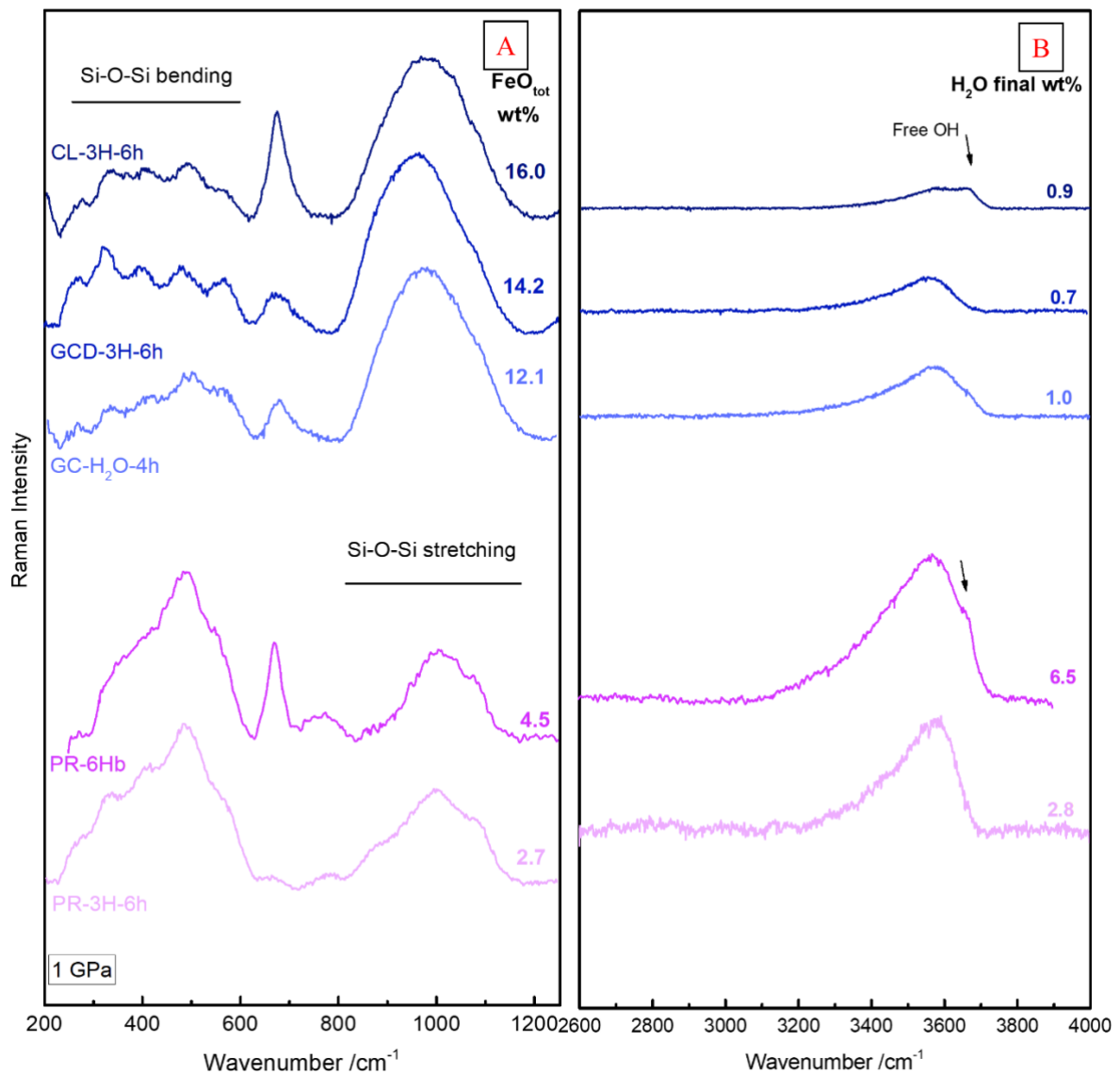
Fig.B: A) Signatures spectrales de la matrice silicatée des verres analogues aux basaltes martiens (en dégradé de bleu) et basaltes terrestres (dégradé de rose) avec la teneur en Fer totale après expérience ; B) Signatures spectrales des mêmes échantillons dans le domaine de H_2O, avec la teneur en H_2O finale quantifiée.

<u>Expériences à forte teneur en H_2O dans des compositions riches en Fer</u>

Des expériences contenant > 3 pds % initial en H_2O ont été réalisées dans les mêmes compositions GC et CL (15.5 et 23.5 pds % FeO_{ini}). Il en résulte une cristallisation avec la présence de cristaux très fins de taille nanométrique. Des exemples de cette texture dite dendritique, sont présentés dans la Fig.C.
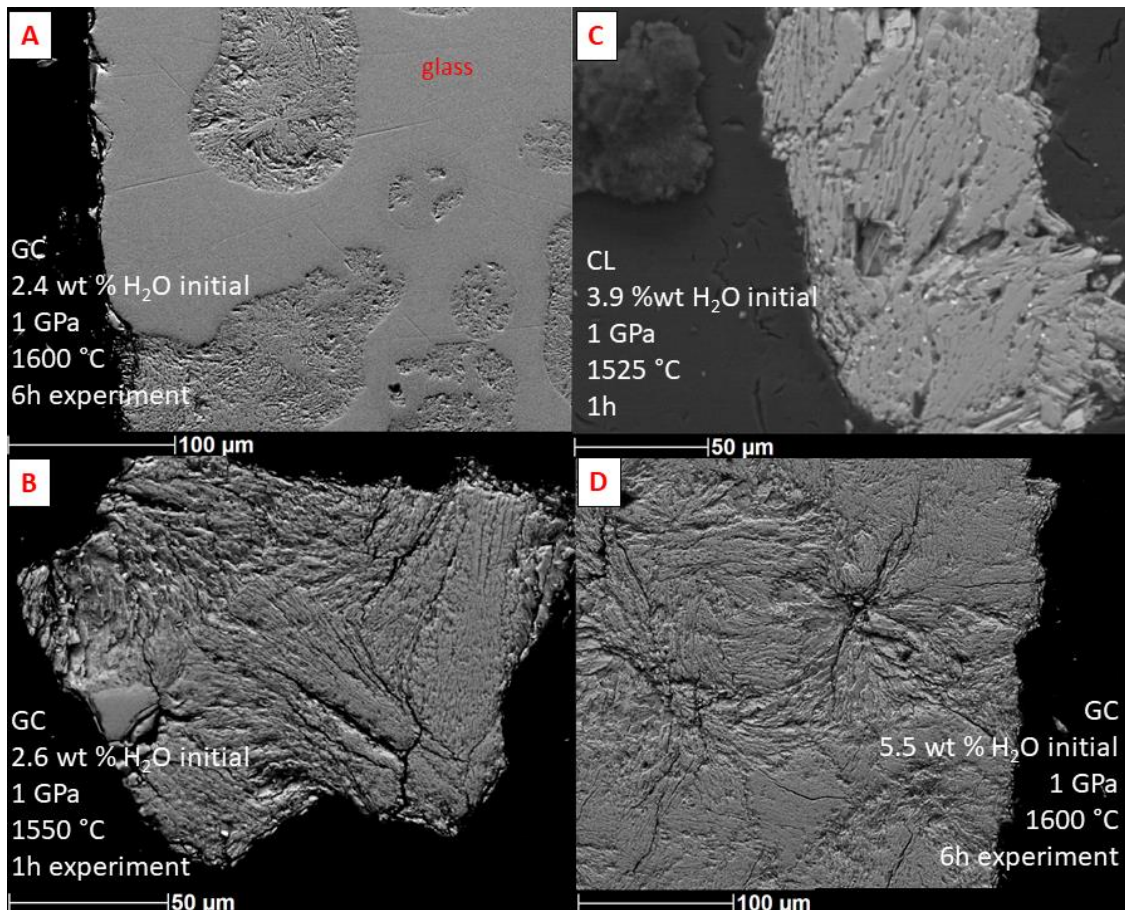
Fig.C: Images obtenues par MEB: A) composition GC (15.5 pds % FeO_{ini}) avec 2.4 H_2O_{ini}, 6h d'expérience; B) GC avec 1h d'expérience; C) composition CL (23.5 pds % FeO_{ini}) + 3.9 pds % H_2O_{ini} + 1h; D) GC + 5.5 pds % H_2O_{ini}

Après analyse par DRX, les cristaux seraient probablement un mélange de pyroxènes et d'amphiboles. Un liquide de composition trachy-dacitique (appauvri en Fe et Mg) a été analysé entre les cristaux.

Les verres pauvres en eau (1 pds % dissout) ont été trempés, nous n'avons pas observé une texture dendritique sur tout l'échantillon. Au contraire, les échantillons riches en eau (> 3 pds % H_2O_{ini}) sont caractérisés par d'abondants cristaux de trempe. Dans ce chapitre, nous avons remarqué que très peu d'H_2O (~1 pds %) peut se dissoudre dans des compositions riches en Fe et obtenir un verre. Les phénomènes de dissolution de H_2O dans un magmas riche en fer sont donc atypiques et sont différentes des conditions de dissolution dans des magmas basaltiques terrestres. Nous avons donc voulu regarder si d'autres espèces volatiles étaient impactées par cette composition, et notamment le S dans le chapitre suivant.

Chapitre III

Plus de 6 pds % SO_3 est détecté dans le régolithe martien, dont 5 – 10 % sont des sulfates. D'après des modélisations à partir des données de météorites et de calculs cosmochiques, le noyau et manteau martien seraient très enrichis en S, par rapport à la Terre. Ainsi, une moyenne

entre 14 – 18 pds % de S est estimée dans le noyau martien, contre ~2000 ppm dans le manteau. En comparaison, le manteau terrestre ne contiendrait entre 700 et 1000 ppm S.

Les études du comportement du S dans les magmas martiens sont plus fréquentes que celles considérant H_2O. Une étude expérimentale ainsi que des modèles géochimiques estiment un maximum de 4000 ppm de S dissout dans des basaltes martiens en conditions réductrices et à 0.8 GPa. Néanmoins, en conditions oxydantes, il n'existe pas d'étude utilisant des analogues aux basaltes martiens. En effet, les conditions d'oxydo-réductions présentent dans l'intérieur de Mars restent toujours débatues. Plusieurs études s'accordent pour suggérer un manteau primitif reduit, autour du tampon Iron-Wüstite. Pour la croûte primitive de Mars, les conditions redox sont moins claires, on propose un milieu réduit voire oxydé jusqu'au tampon Quart-Fayalite-Magnétite. Ainsi, selon les conditions d'oxydo-réduction, le comportement du S dans le magma sera différent.

Dans notre étude, nous avons synthétisé des verres en présence de S introduit sous deux formes : S^{6+} et S^0 ; conférant un état rédox différent au début de l'expérience.

Solubilité du S dans des verres riches en Fer

La composition synthétique, GC (15.5 pds % FeO_{ini}), expérimentée dans le chapitre précédent a été réutilisée pour étudier le comportement du S pour des pressions entre 0.5 et 2 GPa (~200 km dans le manteau martien).

Un maximum de solubilité du S est atteint à 1.7 pds % dans les échantillons présentant du S^{6+} au début de l'expérience. Les expériences contenant du S^0 vont dissoudre presque autant de S dans le liquide, ~1.3 pds %. L'état rédox après expérience a été déterminé par Raman. Les résultats obtenus par quantification du S^{6+} s'exprimant à 1000 cm^{-1}, sont en accord avec la quantification du S_{tot} réalisée au MEB. Ainsi, le S dans nos verres est entièrement oxydé après expérience. L'état redox du Fe a aussi été observé par colorimétrie. Les expériences avec S^0 au départ, sont fortement réduites avec une très forte proportion de Fe^{2+}, contrairement aux échantillons avec S^{6+} initial.

Les analyses par XPS nous ont permis d'observer l'état redox du S, Fe, et le degré de polymérisation de nos verres. Ces analyses confirment la présence unique de S^{6+}, et la dominance de Fe^{2+} dans nos échantillons avec S^0 au début de l'expérience. Un couple redox a donc été mis en place pendant les expériences, conduisant à l'oxydation du S aux dépends du Fe, initialement présent sous sa forme Fe^{3+}.

Le degré de polymérisation déterminé par XPS et Raman indique des compositions fortement polymérisées.

Nouveau modèle de solubilité du S

Les valeurs obtenues de dissolution du S peuvent traduire une solubilité dans les expériences où 2 pds % S ont été ajouté initialement. On suppose la saturation en S dans ces expériences puisque la quantité initialement ajoutée n'est pas retrouvée à la fin de l'expérience. Néanmoins, des expériences supplémentaires avec davantage de S_{ini}, sont envisagées pour définir plus précisément la saturation en S dans ce type de composition.

Avec les nouvelles données de solubilité du S dans nos verres riches en Fe, nous avons établi un modèle permettant de déterminer le maximum de S pouvant être dissout selon différents paramètres. Les paramètres utilisés sont : P, T, fO_2, H_2O, S_{ini}, IFS, NBO/T. Les deux derniers

paramètres représentent différents aspects chimiques du magma. Tandis que l'IFS (Ionic Field Strength) traduit les interactions entre les cations présents, le NBO/T (Non Bridging Oxygen per Tetrahedron) va représenter le degré de polymérisation. Un fort IFS (~12) correspondra à une composition riche en Si, telle qu'une composition rhyolitique. Au contraire, ce type de composition présentera un NBO/T à 0.

Le modèle utilise donc les données de solubilité obtenus dans la première partie du chapitre, couplés à 150 données de la littérature. Ces dernières représentent des compositions entre basalte et rhyolite, des conditions de P et T variées, ainsi qu'une fO_2 (fugacité d'oxygène traduisant l'état rédox du système) variant de NNO – 2.3 à 0.6 (NNO = Nickel Nickel Oxygen). Les résultats du modèle sont représentés dans la Fig.D.
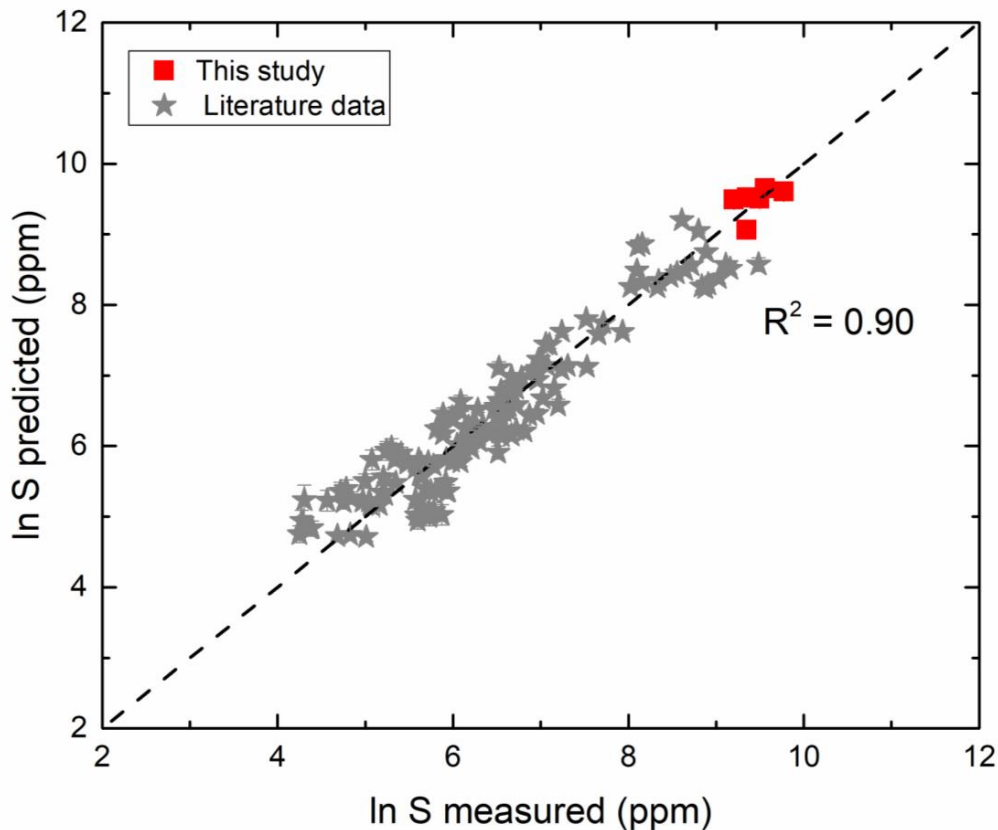
Fig.D : S mesuré dans les échantillons en fonction du S calculé via le modèle. En rouge les données saturées obtenues dans la première partie du chapitre, et en gris les données issues de la littérature. Le R_2 représente le coefficient de régression linéaire définissant la qualité du modèle.

Le modèle obtenu représente l'équation suivante :

$$\ln S \ (ppm) = -\frac{a}{T} + b \times \frac{P}{T} + c \times \ln fO_2 + d \times (\ln fO_2)^2 + e \times \ln S^{ini} + f \times IFS$$
$$+ g \times IFS^2 + h \times \ln(1 + \frac{NBO}{T}) + i \times H_2O$$

Avec, a,b,c,d,e,f,g,h,i des paramètres définis dans le Chapitre III.

Ce modèle permet alors de déterminer le maximum de S dissout dans diverses compositions terrestres mais aussi martiennes. Si le S dissout est connu, le modèle peut permettre d'obtenir la teneur en S présent dans la source (S_{ini}).

Dans ce chapitre, nous avons constaté que la solubilité du S dans les magmas martiens peut dépasser le pds %. Cela indique que les magmas basaltiques martiens peuvent transporter une grande quantité de S jusqu'à la surface. L'altération de ces roches peut ainsi amener à la formation de sulfates.

Chapitre IV

L'ère des sulfates sur Mars a dominé pendant l'Hespérien (3.7 – 3.2 Ga). Il en résulte une majorité de sulfates de Fe et Mg, ainsi que des sulfates de Ca.

Le S des sulfates peut avoir diverses origines : 1) altération de roches ignées riches en S ou 2) retombées d'aérosols émis par dégazage volcanique. L'altération des roches ignées par un liquide acide permet la précipitation de sulfates. Ils se retrouvent ainsi mélangés avec les roches sédimentaires recouvrant les roches ignées martiennes. Actuellement, le rover Curiosity possède un instrument permettant de quantifier le S : le Laser Induce Breakdown Spectroscopy (LIBS). Seulement, cette technique ne permet pas de quantifier le S en dessous de 10 pds % dans les matériaux. Ainsi, l'élaboration d'un budget de S ne peut être complète sans ajouter le S présents en-deçà de cette valeur.

La spectroscopie Raman est un instrument qualitatif qui peut être calibré pour devenir quantitatif. A la différence du LIBS, le Raman est non destructif. L'objectif de cette étude était donc de réaliser une calibration en utilisant la spectroscopie Raman, sur des mélanges contenant différentes proportions de sulfates. Cette calibration pourra servir d'outil de quantification du S à la surface de Mars grâce au Raman au sein de l'instrument SuperCam du futur rover Mars 2020.

Méthodes et calibrations

Plusieurs mélanges ont été réalisés utilisant des sulfates de Ca et Mg entre 1 et 10 pds %. Aux sulfates sont ajoutés des minéraux silicatés mafiques (olivine, clinopyroxène, orthopyroxène, plagioclase) selon un mélange binaire ou ternaire. Chaque mélange est préparé sous forme de pastille puis analysé par spectroscopie Raman en utilisant des conditions d'acquisition proches du futur Raman de Mars 2020.

La calibration présentée et publiée dans le journal Mineralogical Magazine, est spécifique. Chaque mélange comporte des critères de calibration. En fonction des minéraux présents, plusieurs signatures Raman sont choisies pour quantifier le S. Par exemple pour le mélange olivine-gypse (sulfate de Ca), un pic à 910 cm^{-1} pour l'olivine et 1006 cm^{-1} pour le gypse sont pris comme critères de calibration. En utilisant l'aire sous le pic à 910 cm^{-1} dans le mélange et en le comparant avec un spectre d'olivine pure, un coefficient R est obtenu. Ce ratio définit alors la proportion de chaque espèce dans le mélange. Par la suite, on utilise le rapport des aires du sulfate sur les espèces mélangées (considérant un mélange binaire ou ternaire). On obtient alors un coefficient qui peut être corrélé avec la teneur en S initialement ajoutée dans le mélange.

Résultats

Les résultats de calibration des mélanges binaires contenant du sulfate de Ca sont représentés dans la Fig.E.
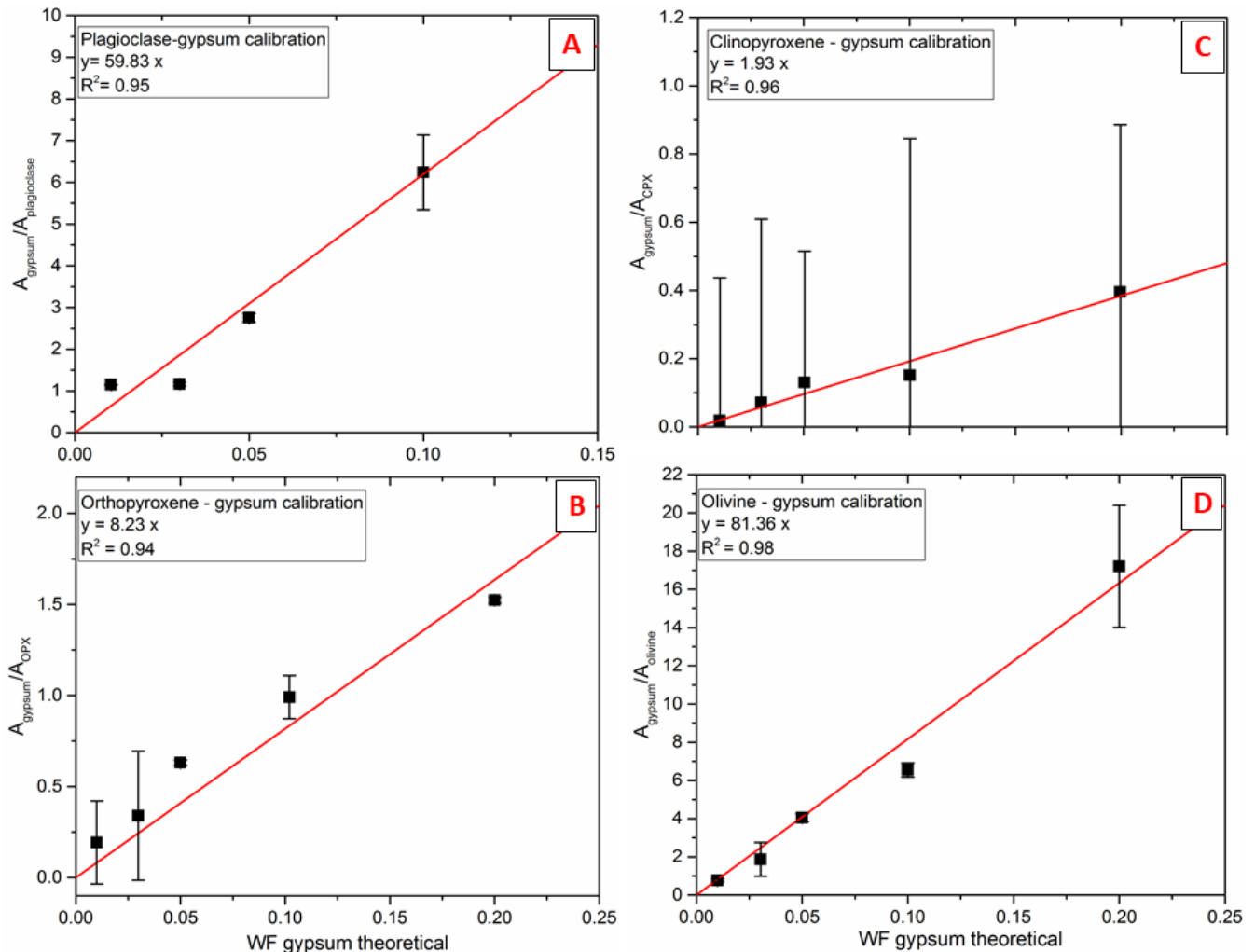
Fig.D: Coefficient de calibration en fonction de la fraction massique (WF = weight fraction) de gypse théorique. En noir, les échantillons avec leurs erreurs relatives. Les droites de calibrations sont représentées en rouge. Quatre mélanges avec sulfate de calcium (gypse) : A) plagioclase; B) orthopyroxène; C) clinopyroxène; D) olivine. Le gypse est mélangé suivant différentes proportions : = 0.20, 0.10, 0.05, 0.03, 0.01. Les équations et coefficients de régressions (R_2) sont reportés sur chaque graphes.

La méthode de calibration établie par spectroscopie Raman permet de quantifier du S dans des mélanges binaires et ternaires jusqu'à 1 pds %, ce qui est bien en-deçà de la limite de détection du LIBS.

Néanmoins, la méthode proposée nécessite encore quelques améliorations, notamment en augmentant la complexité des mélanges afin d'être plus représentatif des structures géologiques de la surface martienne.

Conclusion

Une partie de cette thèse était dédiée à l'expérimentation haute pression permettant de synthétiser des verres silicatés contenant du S et H_2O, analogues aux basaltes martiens enrichis en fer. La deuxième partie de cette étude était axée sur l'altération de ces basaltes riches en S contribuant à la formation de sulfates. La quantification des sulfates via une nouvelle méthode de calibration par spectroscopie Raman permet alors de quantifier le S à la surface et dans l'intérieur de Mars. En couplant cette étude ainsi que l'étude expérimentale de verres saturés en S, nous pouvons connaître la teneur maximale transportée à la surface dans les roches éruptées.

En couplant nos données expérimentales, nous avons établi un modèle de prédiction du S dissout dans un magma de composition martienne lors de sa remontée jusqu'à la surface, à partir du modèle établi dans le Chapitre III. Ainsi, en fonction de la composition chimique du magma, la teneur en S dissoute ne sera pas la même. L'option favorisant le maximum de S correspond à des conditions où le magma est fortement hydraté (0.9 pds % H_2O), oxydé (QFM = Quartz-Fayalite-Magnétite) et dans des compositions pauvres en silice (IFS ~9), tel que montre le Fig.F.
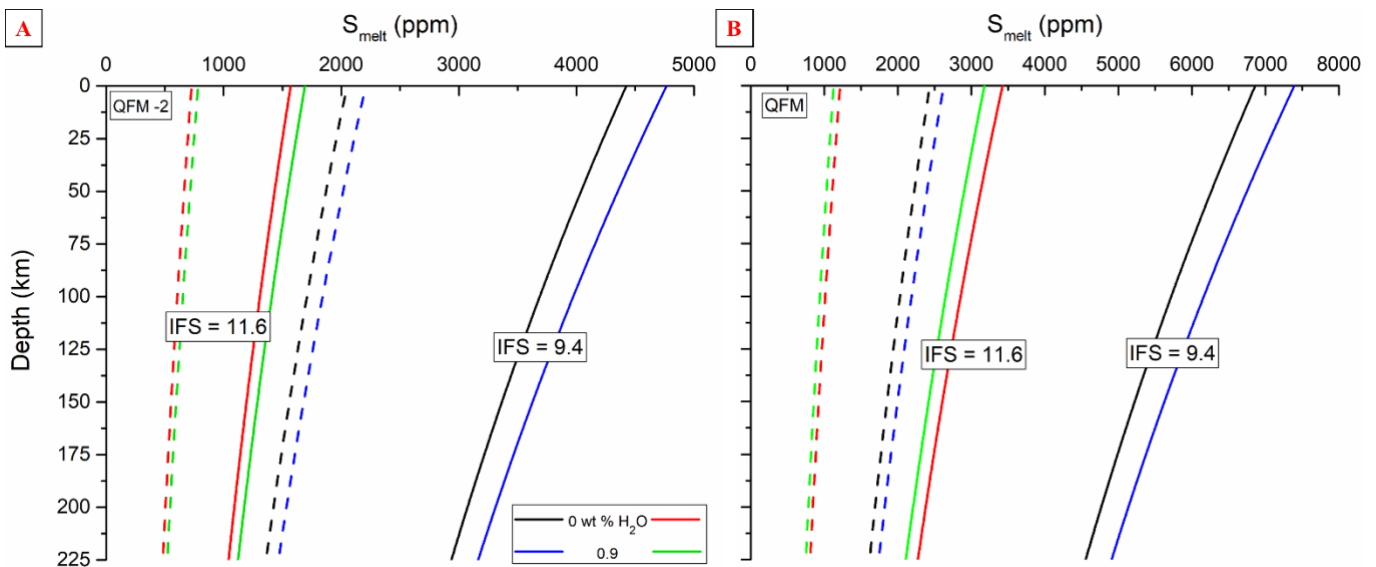
Fig.F: Modèle d'évolution du S dissout dans un magma martien remontant à la surface, considérant les données de solubilité établies dans le Chapitre III. A) Conditions réduites (QFM -2); B) Conditions oxydantes (QFM). Les lignes pointillées renseignent le modèle avec 0.7 pds % S_{ini}, tandis que les lignes pleines indiquent 1.8 pds % S_{ini}. Les courbes vertes et rouges sont pour des compositions riches en SiO_2 (IFS ~12) tandis que les courbes noires et bleues sont pour des compositions plus mafiques (IFS~9).

Néanmoins, ce modèle ne permet pas d'estimer la teneur en S dégazée dans l'atmosphère primitive de Mars. Ce type d'étude pourrait être réalisé à la suite de ce travail de thèse.

Par ailleurs, nous pourrons avoir une meilleure idée du budget du S sur Mars à travers les nouvelles données de solubilité couplées aux futures acquisitions du spectromètre Raman

permettant de quantifier les sulfates. Nous n'avons pas réussi à réaliser des expériences saturées en H_2O, ce qui ne nous permet pas de contraindre le budget de cet élément. Néanmoins, les expériences ayant permis l'obtention d'un verre hydraté similaire aux basaltes martiens, et ne dissolvent que 1 pds % H_2O. Nous avons observé que la formation d'OH libres pouvaient impacter la viscosité des magmas martiens.

Ce travail de 3 ans sur les éléments volatils H, O et S soulève de nouvelles questions et suscite de nouveaux axes de recherche. Un des points les plus critique est la meilleure compréhension des magmas martiens en présence d'H_2O, car les résultats obtenus lors de cette thèse ont été surprenants et impliquent de nouvelles expériences et des analyses plus poussées. Aussi, les espèces volatiles étudiées ne permettront pas de réaliser un budget global de la quantité de gaz émis lors des éruptions volcaniques de Mars. En effet, d'autres éléments ont été détectés à la surface de Mars tels que le Cl et F, qui doivent avoir joués un rôle dans l'élaboration d'une atmosphère dense. L'impact de ces espèces entre elles et sur les autres espèces telles que le S et H_2O est aussi un axe de recherche à développer dans le futur.

Table of content

List of Figures

List of Tables

General introduction

Mars

Mars is located farthest from the Sun relative to Earth and is smaller. Its radius has been calculated at 3 389 km, versus 6 371 km for Earth. Due to its distance to the Sun, the solar flux is 2.5 weaker than on Earth, with 1.5 AU (i.e., Astronomical Unit, 1 UA = 1.5 x 10_8 km). Days on Mars are slightly longer than on Earth, with 24h39min35s. Due to its similarity in landscapes with Earth, its proximity, and easier accessibility than Venus, it has been the most studied of the Solar System, after the Earth/Moon system. The internal structure of Mars is still misunderstood. Indeed, previous studies have demonstrated the presence of a past dynamo may have been present, creating a remnant magnetic field located in old terrains at the surface of Mars (Langlais et al. 2004). Also, the plate tectonics is a specific feature of Earth that enable material recycling and various geologic edifices at the surface or deep below water level. Studying Mars will help to understand if past plate tectonics ever started. However, it is admitted that the planet has evolved most of its time in a stagnant-lid regime, hence with a single plate (Grott et al. 2013). Finally, the planet shows strong potential for future human exploration. Hence, prior such missions, understanding the planetary evolution better is required.

From previous missions, we know that the current atmosphere of Mars is very thin, ~6 mbar (Tillman et al. 1993) against 1 bar for Earth. While most of the martian atmosphere is composed of CO_2 (95 mol%), other molecules have been detected in relatively high abundances (Owen et al. 1977) : N_2 at 2.7 mol% and $_{40}Ar$ at 1.6 mol%. These two molecules are followed by O_2 and CO, even though their proportion do not reach 1 mol%. Even though the current atmosphere of Mars is tenuous, many authors suggest the presence of a denser atmosphere in the primitive time of the planet (Elkins-Tanton 2008, Craddock and Greeley 2009). The current atmosphere is probably a combination of residual atmosphere after part of it escaped after the dynamo stopped, and more recent degassing of volatiles by volcanic activity (Pepin 1994; Chassefière and Leblanc 2004; Lundin et al. 2004; Lammer et al. 2018).

In interaction with the current atmosphere, the surface of Mars presents some interesting features, observed through various space missions. At global scale, the particularity of Mars' surface is its dichotomy that can be well represented with data from laser altimetry that informs on the surface topography. This dichotomy is still debated: it could represent a different crustal thickness or a variation in the mineralogical composition, caused either by giant impact(s) or internal dynamics (McGill and Dimitriou 1990; Marinova et al. 2008; Nimmo et al. 2008). The internal characteristics of Mars still requires further investigations. Recent studies favor a crustal thickness between 39 - 77 km, and a core radius from 1729 to 1859 km (Rivoldini et al. 2011). The wide range of density and thickness highlight the need for further investigation of the internal structure of Mars. The decomposition of the internal structure of Mars according to physical (density, pressure, temperature) and chemical properties (chemical composition and mineralogy) is reported in the Fig.GI.1. From surface analysis using near-infrared spectroscopy, mafic minerals (olivine, pyroxene) have been detected predominantly (Ehlmann and Edwards 2014). Although quartz and plagioclase are not easily detected by these techniques, the

occurrences of mafic minerals is specifically observed over large igneous rocks provinces, with an overall basaltic composition (Nimmo and Tanaka 2005, Sautter et al. 2015). While a basaltic crust is still a leading paradigm for Mars, recent studies have shown the presence of more felsic rocks locally in an old Mars meteorite (Humayun et al., 2011) and in rocks at Gale crater (Sautter et al., 2015) questioning their extent in Mars crust. The mineralogy of the deep interior of Mars has been proposed from the experimental work Bertka and Fei (1997), represented in the Fig. GI.1. Density and the pressure panels provided in the Fig.GI.1 are calculated according to the mineralogy assemblage of the martian interior. On the other hand, the chemical composition of each martian internal structure has been estimated by coupling cosmochemical models and from meteorite data (Morgan and Anders 1979; Halliday et al. 2001). New data to better constrain the structure of Mars will be provided thanks to the Insight mission that will be developed in the next section. The martian surface observations enable the observation of varying degree of crater density, which have permitted the datation of martian terrains. Hence, three geological epochs have been proposed to characterize the geologic evolution of the planet: the Noachian (> 3.7 Gy), the Hesperian (~3.7 – 3.2 Gy) and the Amazonian (< 3.2 Gy).

All the information that we currently possess on Mars have been available, mostly, thanks to the many space missions toward the planet. In the next subsection, we will present a review of some results from the martian missions.
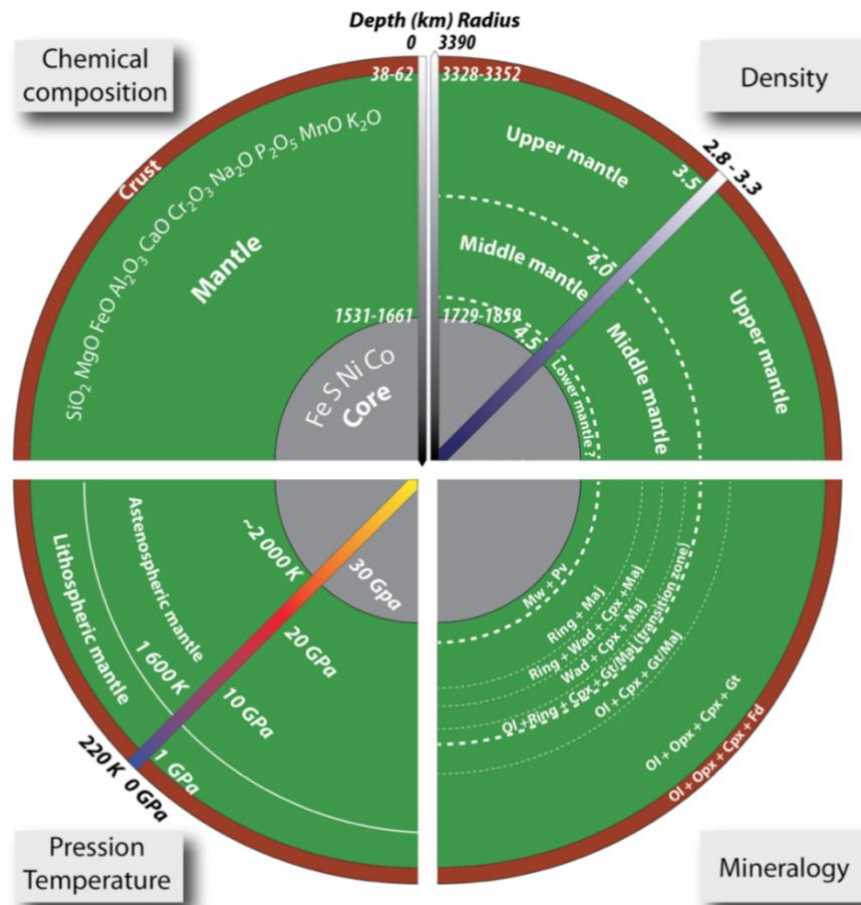
Fig.GI.1: Schematic representation of the internal structure of Mars according to different physical and chemical aspects, from Mangold et al. (2016). The mineralogical panel is adapted from Bertka and Fei (1997) study. Ol: olivine; Opx: orthopyroxene; Cpx: clinopyroxene; Fd: feldspath; Gt: grenat; Maj: majorite; Wad: Wadsleyite; Ring: ringwoodite; Mw: Magnetowüstite; Pv: perovskite.

Past and future spatial missions to Mars

The space missions toward Mars started in the 1970s by the possibility of present life on Mars. Nowadays, more than 40 landers and orbital missions have scrutinized the Mars planet. Most of them were American, with the National Aeronautics and Space Administration (NASA), coupled to the Russian (Roscosmos), European (ESA), Japanese (JAXA) and more recently Indian (ISRO) contributions.

The first mission dedicated to the investigation of the red planet began during the 1960's, starting the spatial era toward Mars. The first successful missions on Mars were the US orbiters Mariner 4 and 9, in 1965 and 1972, respectively, followed by Viking 1 and 2 in 1976, which enabled the imaging of the whole planet, while the URSS space agency experienced several failures. The 90's have permitted the detection of a past magnetic field, and the topography of Mars thanks to the Mars Global Surveyor mission arrived in Mars orbit in 1997. During the year 2000, the Mars Odyssey mission, and the first European mission, Mars Express, continued the acquisition of various type of data (especially near infrared, thermal infrared and neutron/gamma spectroscopy). The latter have permitted the production of a mineralogical surface maps, including the finding of abundant hydrated minerals such as phyllosilicates and

sulfates (Bibring et al., 2005). The Mars Reconnaissance Orbiter took place in the orbit of Mars in 2005, to explore further its atmospheric composition, surface geology and mineralogy.

Meanwhile, the first lander to reach the surface of Mars is, again, attributed to the NASA agency, with its two-in-one mission that includes both orbiter and lander spacecrafts, named Viking (1976 - 1980). The investigation of Mars surface with the Vikings instruments revealed that no life was present. Two other landers replaced Viking with the arrival of the Phoenix lander near the North Pole in 2007. The dedicated mission of Phoenix was to analyze the subsurface and the ice present in the pole. Then, the last lander to have reached the surface of Mars recently, is Insight at the beginning of 2019. Insights aims principally at determining the internal structure of Mars, detecting any seismic activity and studying the remnant magnetosphere.

Finally, the last kind of spacecraft launched to Mars are rovers that enable exploration of the geology at the surface. After a successful engineering-oriented mission Pathfinder in the 90s, the first rovers to have crossed kilometers in the martian surface were the Mars Exploration Rovers, named Spirit and Opportunity, both landed in 2004. After having lost communication with the Spirit rover in 2011, Opportunity kept on searching the martian surface until June 2018, after 43 km of traverse. The Curiosity rover landed in 2012 and is still in activity after >20 km of traverse. One of the main goals of this mission was to determine the presence and state of carbon in past sediments as well as understand the aqueous activity in the early Mars.

Determine whether life happened on Mars, characterize the climate and geology and prepare for possible human exploration are key goals that animate the scientists for preparation of new rovers to send on Mars. These objectives were those in mind of the NASA agency when they prepared the future rover that should be launched current 2020. Coupled to the Mars 2020 mission (NASA project), an ESA project, more centered onto the exobiological objective, is supposed to leave Earth in the same year and is currently called ExoMars 2020. For the following part, we will further discuss the American future rover, almost ready to be launched as this manuscript is written. As the ExoMars 2020 mission is not the main subject of this thesis we will not detail this mission.

NASA Mars 2020 mission

The NASA's next rover mission will be launched in July 2020, for a 7-month trip to Mars. The landing is scheduled in February 2021. This new martian mission has been proposed few months after the landing of the Curiosity rover. Since spatial missions to Mars are triggered by the possibility of past life and future human mission, the Mars 2020 mission has four main goals. These objectives are taken from the Program Level Requirements Appendix (Williford et al. 2018), and are the following:

1. Characterize the processes that formed and modified the geologic record within a field exploration area on Mars selected for evidence of an astrobiologically relevant ancient environment and geologic diversity
2. Perform astrobiologically relevant investigations on the geologic materials at the landing site
3. Assemble documented and returnable cached samples for possible future return to Earth
4. Contribute to the preparation for human exploration of Mars by making significant progress toward filling at least one major strategic knowledge gap

The followed results (in the next chapters) of this thesis will mostly contribute to the first objective of the Mars 2020 mission.

To realize such goals, the 2020 Mars rover be equipped of both improved instruments that can be found in the Curiosity rover, and new ones that will be located inside the rover. In Fig. GI.2,

the various instruments in the rover are represented. Hence, we will find sensing units located in the remote sensing mast, which includes MastCaman-Z and SuperCam instruments. At the end of the robot arm, the Planetary Instrument for X-ray Lithochemistry (PIXL) and Scanning Habitable Environments with Raman and Luminescence for Organics and Chemicals (SHERLOC). Below the rover, we can find a Radar Imager for Mars' Subsurface Experiment (RIMFAX). Different sensors are located around the rover attributed to the MEDA instrument (Mars Environmental Dynamics Analyzer). The new instrument MOXIE (Mars Oxygen In-Situ Resource Utilization Experiment) will be, on the contrary, located inside the rover. The ACA refered in the Fig.GI.1, is the Adaptative Caching Assembly instrument whereas the MultiMission Radioisotope Thermoelectric Generator (MMRTG) finalize the rover.
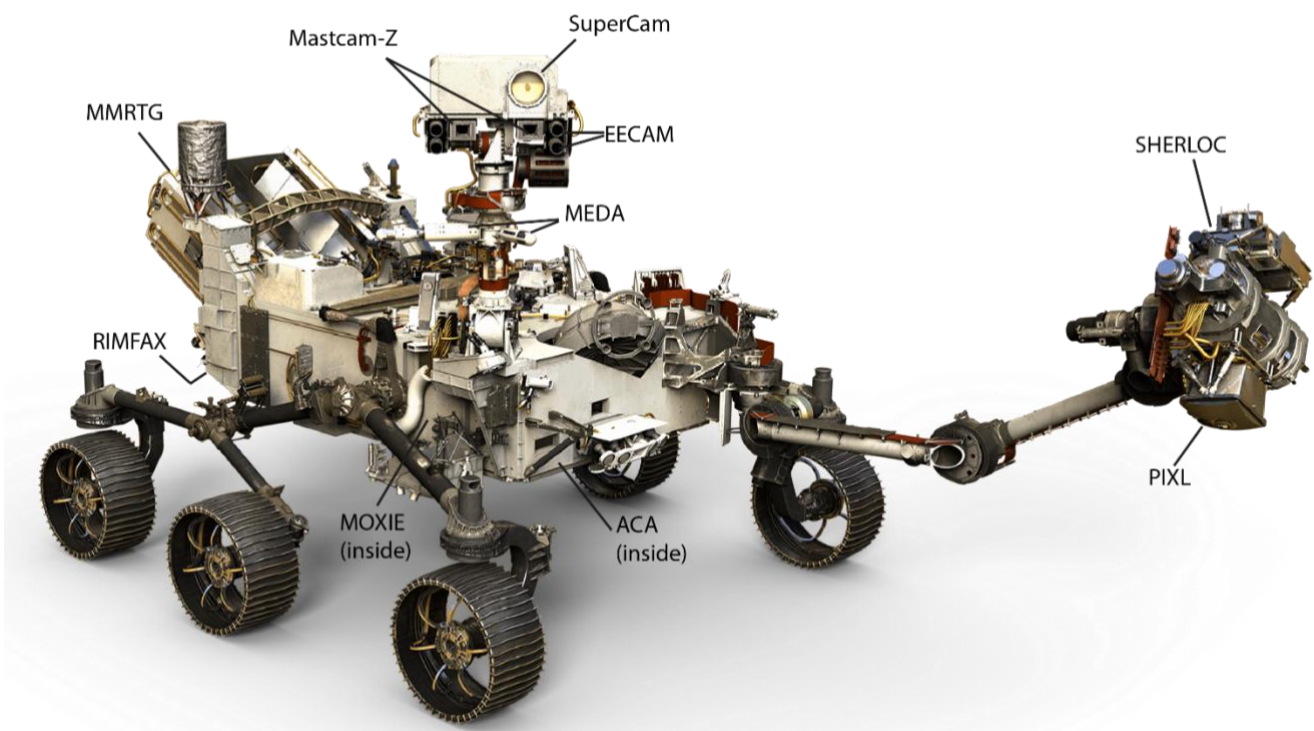
Fig.GI.2: Artist's representation of the Mars 2020 rover with the various instruments, after Williford et al. (2018). See text for instrument details.

Each instrument will respond to one or several objectives of the mission. For instance, the ACA instrument is expected to recover martian samples to be analyzed on Earth. The MOXIE instrument aims to transform the CO_2 present in the martian atmosphere into O_2. This new device will help for future human exploration on the planet. The MEDA instrument will also help for future human mission to Mars by performing environmental measurements (e.g., wind speed, atmospheric pressure, air and ground temperatures).

The SHERLOC instrument is composed of a deep ultraviolet laser for fluorescence emission and a Raman using the same laser frequency. The objectives of SHERLOC are to detect organic materials and some minerals such as carbonates, perchlorates, sulfates and phyllosicitates.

The other instruments will help to characterize the geology on Mars. For instance, the PIXL spectrometer and camera will measure the elemental chemistry of rocks and soils, and will map

the chemical variations related to fine-scale textures and microstructures. The RIMFAX radar can penetrate down to 10 m in surface materials and will permit the relation between surface and subsurface structures.

The Mastcam-Z is close to the Mastcam of Curiosity but is enhanced with new multispectral filters and zoom. Hence, this instrument is equipped of a stereo pair of multispectral and color zoom cameras.

SuperCam instruments

Finally, the SuperCam instrument (Fig.GI.2) is a suite of instrument that can be compared to the ChemCam instrument onboard Curiosity. Two sub-instruments already present on Curiosity have been improved and loaded in SuperCam: a Remote Micro Imager (RMI) with a new color detector and a Laser-Induced Breakdown Spectroscopy (LIBS) coupled with a microphone, to perform element analysis. The additional devices of SuperCam are a Raman and time-resolved fluorescence spectroscopies, coupled to an Infra-Red passive Spectrometer (IRS). Combining these two instruments enable an accurate mineral characterization (detection of silicates, carbonates, sulfates, phosphates, sulfides and organic molecules, if present).

In the Fig.GI.3, the SuperCam instrument can be separated into 3 parts:
1. Mast unit
2. Body unit
3. Calibration targets

The Mast unit is a French contribution (Institut de Recherche en Astrophysique et Planétologie, IRAP) comprising a telescope, a red or green pulsed laser, an infrared spectrometer, a micro-imager and a microphone. An optical fiber will transfer the light emitted on the rock to a unit in the body of the rover.

The Body unit is an American contribution, including three spectrometers covering the ultra-violet, violet, visible and near-infrared frequency range (VNIR) for the LIBS. The VNIR spectrometer is implemented in a way to serve on both Raman spectroscopy and LIBS, but also for passive reflectance spectroscopy. The cables (fiber optic, signal and power) are also part of the Body unit.

Finally, the set of calibration targets is provided by a Spanish lab to perform calibration of the instrument. The set is mounted at the back of the rover.
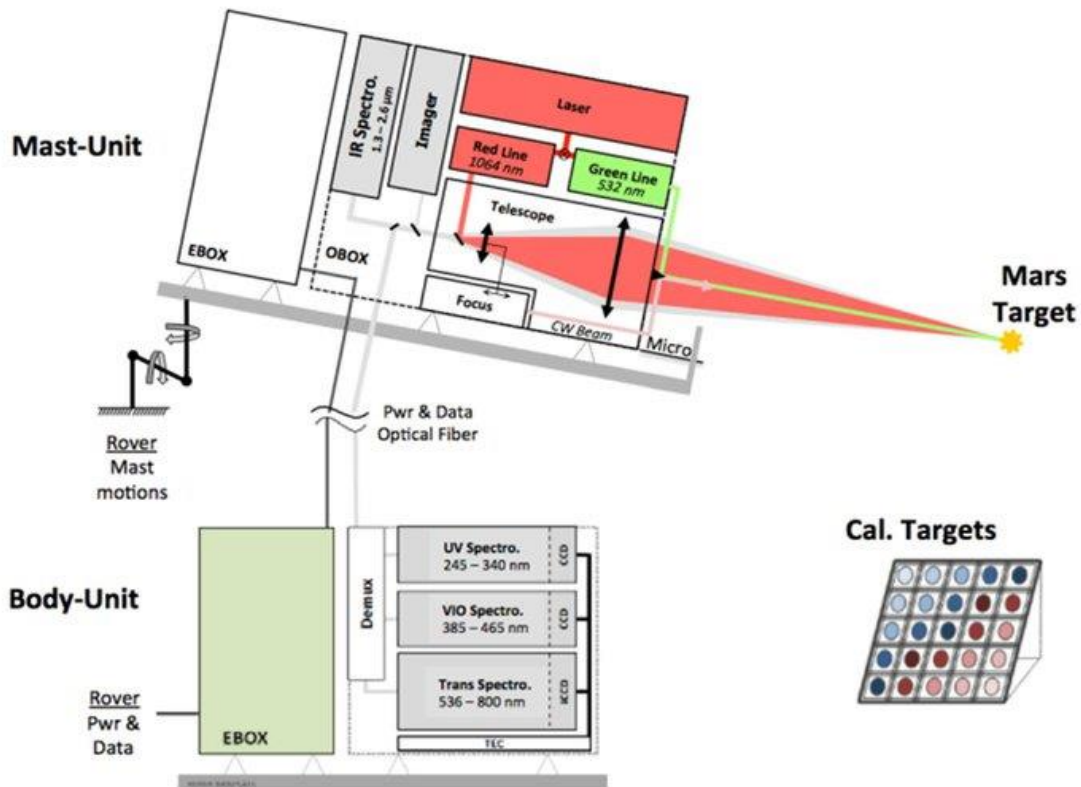
Fig.GI.3 : The SuperCam instrument block diagram. EBOX: electronics-support boxes; OBOX: optics within a single box. Credits from Perez et al. (2017) and Wiens et al. (2017).

This well-equipped rover will land at the Jezero crater due to its geological interest (see location Fig.GI.3). Indeed, Jezero crater contains a fluvial valley inlet linked to delta deposits presenting a wide range of lithologically diverse sediments with carbonate and phyllosilicate mineralogy and provides evidence for subaqueous sediment deposition in a crater-filling lake (Fassett and Head 2005; Ehlmann et al. 2008; Goudge et al. 2015, 2017).

Mars igneous evolution

While the landing site of the Mars 2020 rover will not be a volcanic landscape, the rover should observe volcanic rocks at Jezero crater floor and on its rims due to their presence in the surrounding region of Nili Fossae. Furthermore, the sedimentary rocks dominating the Jezero crater are probably coming from the alteration of igneous rocks after interaction with fluids. Indeed, the martian surface is widely represented by igneous rocks. This is due to the many volcanoes covering its surface. Among them, we can find the biggest volcanoes, Olympus Mons. With its basal diameter of 500 km and 25 km in vertical relief, it is dominating the Solar System volcanoes. Mars presents others large central volcanoes gathered into the Tharsis province as Tharsis Montes, which are including Ascraeus Mons, Pavonis Mons and Arsia Mons (Fig.GI.4). Besides Tharsis Montes and Olympus Mons, Mars central volcanoes are located in Elysium, Syrtis Major and Hellas regions located in Fig.GI.4.
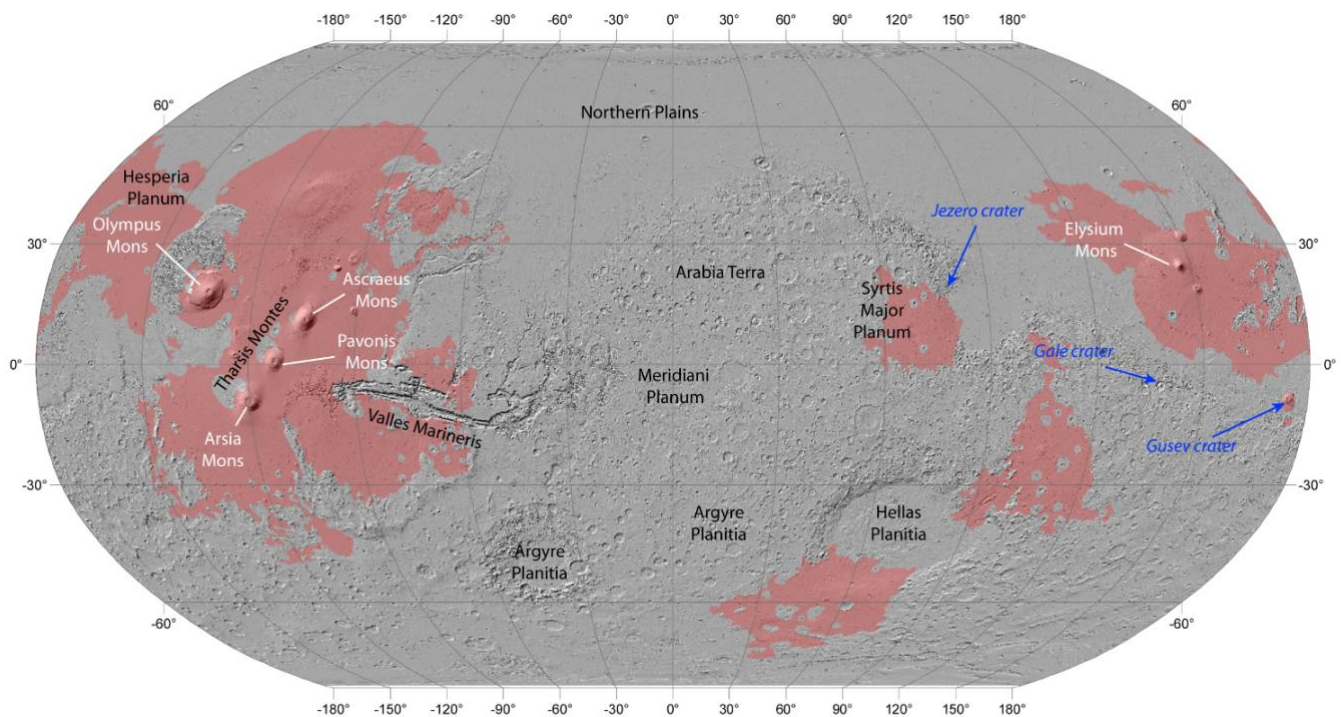
Fig.GI.4: Location of volcanic units on Mars in red, according to Tanaka et al. (2014). The base map is shaded relief of Mars Orbiter Laser Altimeter (MOLA). Major volcanoes are listed in white, and important martian features in black. Important craters are written in blue.

The oldest known volcanic activity dates from back to the Noachian era (> 3.7 Gy). The Tharsis volcanoes display the largest volcanic province observable on Mars with their activity starting in the Noachian (Phillips et al. 2001). During the Hesperian, major volcanoes such as the Syrtis Major Planum, Hesperia Planum and Hellas Planitia regions were formed, and major volcanic plains created by flood volcanism formed around the northern hemisphere and inside the highlands south of the hemispheric dichotomy (Carr 1973; Head et al. 2002; Salvatore et al. 2010); as represented in Fig.GI.4 with the volcanic units. Finally, the Amazonian period displays effusive flows around Tharsis, Elysium and Amazonis Planitia (left side of the Olympus Mons in Fig.GI.4). Last volcanic activities are proposed in the recent times < 100 My, according to Plescia (1990), Neukum et al. (2004), Jaeger et al. (2007), Vaucher et al. (2009). The wide volcanic activity of Mars resulted in large volcanic units at the surface (Fig.GI.4).

Mineralogy of Mars igneous and sedimentary rocks

Mafic minerals were detected at the surface of Mars, notably pyroxenes, olivine, and plagioclase (e.g., Morris et al. 2004; Ehlmann and Edwards 2014). While volcanic products at the surface are predominantly basaltic (e.g., Bandfield et al. 2000; Christensen et al. 2005; McSween et al. 2009; Taylor and McLennan 2009; Ody 2012; Baratoux et al. 2013; Sautter et al. 2016; Cousin et al. 2017); numerous differentiated rocks have been observed from andesite

to trachyte composition (Wray et al. 2010; Stolper et al. 2013; Sautter et al. 2015; Mangold et al. 2016; Udry et al. 2018), questioning the composition of the lower crust.

Another way to characterize the mineralogy of Mars is possible with the use of martian meteorite recovered on Earth. Through SNC investigations, data confirmed the abundances of mafic minerals in various martian meteorites (e.g., Gross et al. 2013; Hewins et al. 2016; Sautter et al. 2016). The martian meteorites are gathered into three groups which are all mafic, at first order:
- Shergotty (S): basaltic or lherzolites/harzburgites composition
- Nakhla (N): clinopyroxenites or wehrlites
- Chassigny (C): dunite

An important outlier is the recently found NWA7533, an ancient 4.4 Gy old breccia, that contains alkali feldspar and lack olivine (Humayun et al., 2011), highlighting the difference between the ancient crust composition and more recent basaltic volcanism.

The crust also displays alteration minerals such as phyllosilicates, carbonates, Fe-oxides, sulfates and chlorides, either as local hydrothermal alteration of the crust, or as sedimentary deposits overlying the igneous crust (e.g., Squyres et al. 2005; Bibring et al. 2006; Carter et al. 2013; Vaniman et al. 2013; Nachon et al. 2017). The analyses of martian meteorites also allow the detection of secondary minerals such as apatite, Fe-oxides, sulfates and to a lesser extent, carbonates (e.g., Dreibus and Wänke 1985; Dann et al. 2001; Filiberto and Treiman 2009; Gross et al. 2013; McCubbin et al. 2013, 2016). Carbonates have been both observed in meteorites analyses and in the surface of Mars; although only a nakhlite meteorite seems to possess such mineral (ALH 84001; e.g., Bridges and Grady 2000; Hicks et al. 2014) with a martian origin. The presence of carbonates at the surface of Mars is mostly due to water-ice-rock-CO_2 interaction. However, no massive deposits of carbonates have been observed, except for one site (Syrtis-Nili Fossae; e.g., Goudge et al. 2017).

The presence of phyllosilicates coupled to sulfate minerals inform the climate evolution of the planet through geological times (see Fig.GI.5). Hence, the era of phyllosilicates is supposed to have dominated the primitive time of the planet, during the Noachian (> 3.7 Gy) (Binring et al., 2006). The sulfate deposits have been dated to the late Noachian to late Hesperian (3.7 to 3.2) from crater counts. The phyllosilicate and sulfate period indicates presence of fluid at the surface of Mars. The occurrence of hydrated minerals such as clays and sulfates, combined with local chlorides or carbonates strongly favors the presence of liquid water in their formation, thus revealing a warmer Mars existed.
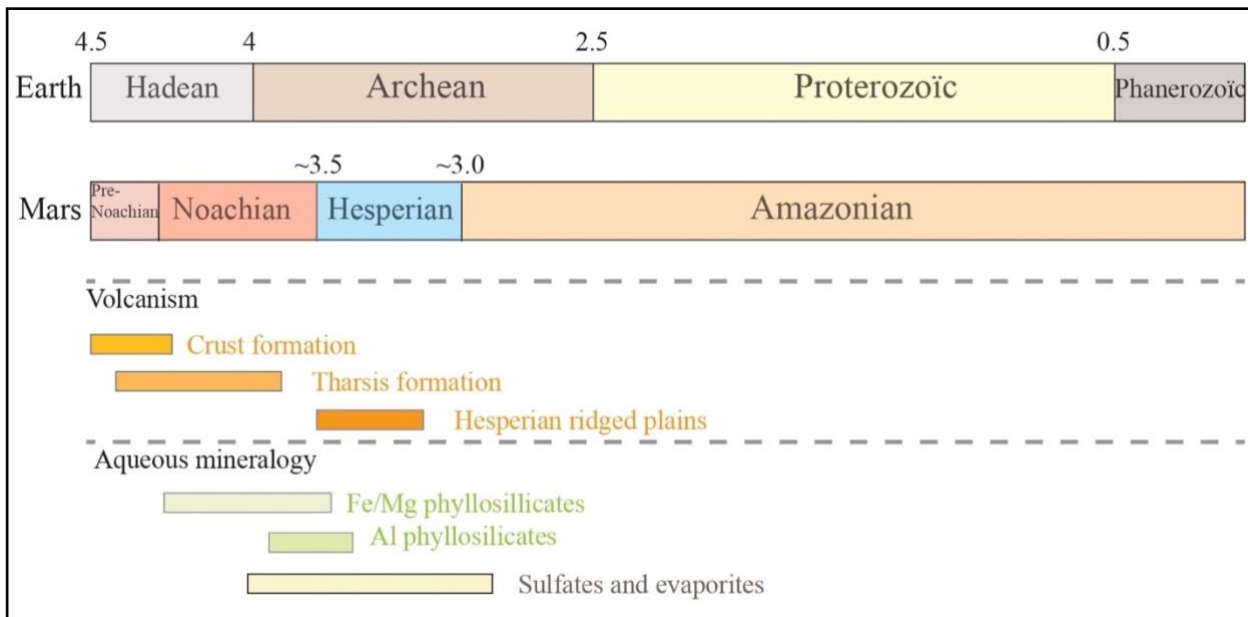
Fig.GI.5: Different geologic era for Mars, compared with Earth. Ages are given in Gy. The associated martian volcanism events are reported in the orange, whereas the different mineralogy categories are reported in green. The schematic representation has been modified after Wordsworth (2016).

Volatiles on Mars

Through SNC investigations, the abundance of mafic minerals is confirmed (e.g., Gross et al. 2013; Hewins et al. 2016; Sautter et al. 2016). The detection of hydrated minerals in these meteorites inform on the presence H_2O. Amphibole especially kaersutite, and apatite are key minerals detected in martian meteorites presenting H_2O. Then, it has been proposed that the H_2O present in those minerals has a magmatic origin (e.g., Hallis et al. 2012; McCubbin et al. 2012; Gross et al. 2013). Halogen-bearing minerals are also observed in martian meteorites, including in chlorides and apatite minerals (Dreibus and Wänke 1985; Treiman 2003; Filiberto and Treiman 2009; Filiberto et al. 2016). S species in pyrrhotite are present in these meteorites with a magmatic origin as inferred in the studies of Lorand et al. (2005, 2018). Finally, only one Nakhlite meteorite show the presence of carbonates (ALH 84001; e.g., Bridges and Grady 2000; Hicks et al. 2014).

Back in the martian surface, H_2O bearing minerals are observed in phyllosilicates and sulfates, as previously mentioned, as well as halogen-bearing minerals. The presence of carbonates at the surface of Mars is mostly due to water-ice-rock-CO_2 interaction. However, no massive deposits of carbonate have been observed, except for one site (Syrtis-Terra Tyrrhena; Goudge et al. 2017).

Hence, Mars exhibits multiple mineralogical features indicating the presence of volatile species such as H_2O, S, Cl, CO_2 but also F and P; as detailed in the previous part with the detection of the different minerals. From orbital observations, the H_2O content at the surface of Mars is suspected to vary from 2 to 7 wt %, whereas the Cl content reaches less than 1 wt %. Finally, the S reaches 3 wt % (Filiberto et al. 2019). The highest abundances of both H_2O and Cl are

located next to the Gusev Crater, but also close to the Tharsis region. On the other hand, S is more important is equatorial latitudes. The occurrence of the volatile species near the volcanic area strongly suggests a magmatic origin. Furthermore, as reported in the Fig.GI.5, the most important volcanic events occurred during the formation of the hydrated and S-rich minerals. Evidence of volatile species in the martian atmosphere, surface and interior are ubiquitous. Presently, H_2O is detected as ice or in subsurface reservoir and in the atmosphere as water vapor. No liquid water is stable in present days, due to the thin CO_2-rich atmosphere. The presence of ancient sulfates and clay minerals favors a thicker early atmosphere that could have stabilized liquid water to create the features observed. The intense volcanic activity during these periods favors this hypothesis: the degassing of volatiles into the primitive atmosphere and may have provided a thicker atmospheric layer (see Fig.GI.6).
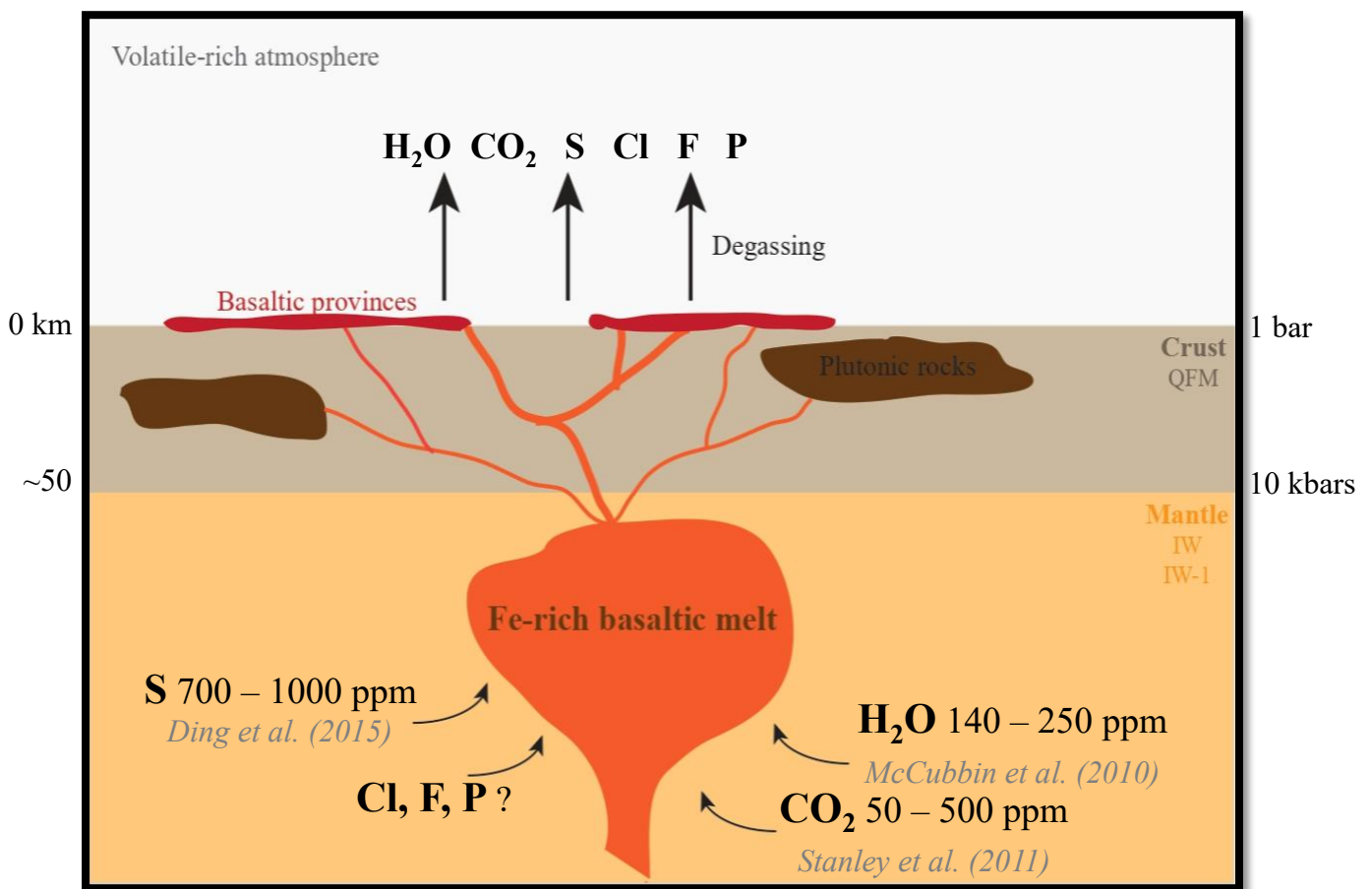
Fig.GI.6: Schematic representation of the martian interior, from the primitive atmosphere enriched in volatiles, the supposed oxidized crust and down to the reduced martian mantle. Here, a Fe-rich basaltic melt is represented as martian magmas, but these compositions are not the only igneous rocks present.

Volatiles budget through experimentation

The current hypothesis to explain the presence of the volatile elements on Mars is a magmatic origin. To constrain a volatile budget on Mars in order to understand the formation of the volatile-rich primitive atmosphere, experimental studies have been conducted. The experimental work aimed at determining the volatile content in the source of the basaltic melts.

This will permit to understand the amount of volatile that have reached the surface and emitted into the atmosphere.

From experimental work, the volatile sources of martian basaltic melt have been calculated (see Fig.GI.6). In the different studies of Stanley et al. (2011, 2012, 2014), the CO_2 in the source can be obtained from their solubility data, hence, they proposed a source content between 50 - 500 ppm CO_2, depending on the redox conditions prevailing in the martian mantle. From the crystallisation sequence obtained in various experimental work, notaly in McCubbin et al. (2010), the H_2O present in the martian interior is supposed to be between 140 to 250 ppm. On the other hand, Ding et al. (2015), supposed 700 to 1000 ppm of S in a reduced martian mantle (in the Iron-Wüstite buffer, i.e., IW). As presented in the Fig.GI.6, the volatiles content in the source of basaltic melt is not really constrained. The volatile dissolve in the melt is even less constrained for such composition.

Most of the studies use a partial melting of a synthetic meteorite chemical composition, to establish the crystallization sequence and quantify the H_2O present in the glass component. Hence, a maximum of 2 wt % H_2O in the source of the martian meteorites has been proposed according to Musselwhite et al. (2006), Filiberto (2008), McCubbin et al. (2010, 2012, 2016), Balta et al. (2013). However, these studies included crystals, which do not permit to determine a solubility of the H_2O inside a martian melts. Solubilities studies using martian composition were performed, but mostly on CO_2, CH_4, and S (e.g., Righter et al. 2009; Stanley et al. 2011, 2012, 2014; Ardia et al. 2013; Armstrong et al. 2015). Their results will be more detailed in the next chapters (Chapter II and Chapter III), however, the expected CO_2 solubility is very low in martian melts (< 2000 ppm).

Consequently, the volatiles content in martian melts is poorly constrained. This thesis aimed to complete those data.

Unanswered questions and present work

The numerous past and future spatial missions to Mars represents the need to answer the unresolved questions on Mars. In the geologic field, the presence of liquid water is ubiquitous. However, the mean to explain how to maintain such phase at the surface of Mars is not trivial. The principal hypothesis is the formation of a thicker atmosphere. The formation of the primitive atmosphere of Mars is far to be clearly understood. The future Mars 2020 rover is a promising mission that should follow the main objectives to detect any past life presence and understand how liquid water was stable. With the new instruments onboard the rover, these objectives can be enlightened. However, data themselves are difficult to interpret without having analogous to compare with. This is the case for the Raman spectrometer. This device is a qualitative instrument that needs calibration to quantify species, for instance, or to mineralogical characterization.

The present study aims to give subsequent Raman spectra in order to compare with the future spectra obtained at the surface of Mars with the SuperCam instrument suite. The main objectives of this thesis were to establish a database of martian analogues in presence of volatile species such as H_2O, S, CO_2, Cl, F, P. The comparison between Raman spectra on martian analogues with the volatile-rich rocks on Mars will help to define a budget of volatiles. The budget represents degassing emissions during eruption transferred to the past atmosphere, the amount of volatiles in igneous and sedimentary rocks and the budget available in the interior of Mars. Then, it would be possible to better understand how a thicker atmosphere was formed in

the primitive time of Mars and has maintained liquid water. In the following chapters, we have investigated the H_2O and S inside martian analogues that have been synthesized and analyzed with Raman spectra. The acquisition of Raman spectra was not the only goal of this thesis. Indeed, the challenge was to create martian igneous rocks analogues in presence of volatiles and understand their behavior.

To better understand the experimental work provided for 3 years, the thesis is divided into four chapters:

1. I have detailed in a first chapter (Chapter I), the high-pressure device coupled to the various analytical instruments, including the Raman spectrometer, used in this study for the three following chapters. The difficulties encountered with the high-pressure experiments are discussed, and some optimizations of the experimental settings are proposed for future experimentalist to possess a new piston-cylinder.

2. Following to the experimental and analytical methods employed, I have chosen to describe the high-pressure results in the two following chapters (Chapter II and III). The readers will first discover the H_2O behavior in martian analogue glasses (Chapter II). Unsuccessful experiments containing high H_2O content are also detailed and some interpretations are proposed at the end of the chapter using both results. These results are a subject of an article, currently in submission in the Journal of Raman Spectroscopy.

3. The third chapter reports the latest experimental work on the S behavior in martian analogue glasses. Saturation experiments were performed which enable us to realize a new solubility law that could be applied on Mars and on various melt compositions on Earth. These results will be soon submitted in the Chemical Geology journal.

4. Finally, the last chapter consists in a Raman calibration to quantify sulfates at the surface of Mars. Sulfate species are likely to be coming from weathered S-rich igneous rocks. Hence, mixtures with sulfate and mafic minerals have been performed and analyzed by Raman spectroscopy. A calibration to quantify sulfate, and especially S, in these mixtures is realized. Coupling the S quantified at the surface with the future Raman of SuperCam, and the amount of S available in martian basalt (Chapter III), can help to determine the budget of S on Mars.

Finally, I will try to summarize our findings in a last part. A degassing model is proposed with the subsequent results obtained in the Chapter II and III. Then, the reader will end the manuscript with the future work that we have considered according to the results obtained in this study.

Chapter I: Description of experimental and analytical methods

I.1: Introduction

Volcanology main field studies are petrology of natural igneous rocks, their chemical compositions and formation processes. However, information such as the path, initial chemical compositions and volatile content cannot be obtained from direct observation of these rocks. Natural igneous rocks can present vitreous inclusions, which are pocket melts trapped in a mineral. The pocket melt will register the condition of formation at depth (i.e., P, T, oxygen fugacity fO_2), but also the volatile content dissolved at pressure and temperature (Dostal et al. 1982; Kamenetsky and Clocchiatti 1996; Della-Pasqua and Varne 1997; Heide and Schmidt 2003; Spilliaert et al. 2006; Saal et al. 2013). However, melt inclusions are not always available and natural volcanic glasses can often loose information with degassing processes.

High-pressure instruments were dedicated to complete the missing information in igneous rocks and to better understand their formation at depth. Nowadays, multiple high-pressure experiments co-exist, from low to very high pressures: Internal High-Pressure Vessel (i.e., IHPV), piston-cylinder, multi-anvil apparatus. The IHPV instrument is dedicated for low pressures (< 0.5 GPa, ~15 km depth), whereas multi-anvil apparatus induces very high-pressures which can go up to 25 GPa (~750 km). Then, the wide range of high-pressure devices created today enable the scientists to retrace the rock history from the Earth upper core to the shallow crust.

The piston-cylinder pressure range is between the IHPV and the multi-anvil apparatus by performing pressures from 0.5 – 4.0 GPa. This high-pressure device enables the reconstruction of igneous rocks evolution from the upper crust to upper mantle (~150 km maximum for the Earth). The piston-cylinder applies a static pressure; thus, it cannot reproduce tectonic movements. However, multiple applications are possible for igneous rocks studies. This high-pressure instrument is mainly dedicated to understand fluid-rock interactions, volatile solubilities, and crystallization sequences (e.g., Faure et al. 2006; Filiberto 2008; Girnis et al. 2011; Bost et al. 2012; Jégo and Pichavant 2012; Sharygin et al. 2015). The starting material can either be a natural glass powder of an igneous rock or a synthetic material with a mixture of oxides. According to the P, T and quench rate conditions, different results are obtained. If the liquidus temperature of the material is reached, coupled to a rapid quench, a glass is obtained. On the other hand, subliquidus conditions permit the growth of crystals and to obtain phase equilibria experiments which enable multiple applications, for instance: mineralogical characterization and element partitioning.

The synthesis of glasses can be used for the understanding the behavior of volatiles dissolved in the material (e.g., Jugo et al. 2005a, b; Kessel et al. 2005; Morizet et al. 2010, 2013; Pichavant et al. 2013; Dalou et al. 2015; Moussallam et al. 2015; Zajacz et al. 2015). The determination of volatile content in various chemical compositions will help to quantify the volatile budget during the transfer of magma from depth toward the surface. Then, degassing models can be obtained in various volcanisc systems and have crucial impact for the global climate on Earth or in other terrestrial planets (Wallace 2003; Grott et al. 2011).

To understand the volcanic processes, the high-pressure experiments are only reproducing the rocks, but the information need to be obtain with different methods. Various instruments are used to characterized synthetized samples. The main characterization lies in the determination of the chemical composition of the sample mostly by microscopic methods. The main method to obtain major and minor chemical species, is the Electron-Probe Microscopic Analysis (EPMA).

While the chemistry is one of the principal information needed, others can be extracted using different methods. Notably, the investigation of volatile solubilities can be obtained with invasive (i.e., bulk analysis) or non-invasive instruments. For instance, bulk analysis such as Karl-Fischer titration has proven its efficiency for the H_2O quantification (Berndt et al. 2002; Keppler 2003; Kessel et al. 2005; Di Genova et al. 2017). Other bulk analysis methods exist to obtain C, H, N, O or S in the sample, but requires a certain amount of material.

Then, different methods have been developed to investigate the volatile content with no destruction of the sample. Spectroscopic instruments were the best choice to obtain such information. However, these instruments were not dedicated to quantification at first, but were mostly qualitative methods. They aimed to determine whether the material presents a crystallization (with the mineral characterization) or a glass spectral signature. Hence, calibrations were established to quantify volatile solubilities in glass obtained at high-pressure. The two spectroscopic methods widely investigated for H_2O, CO_2, S contents are the Raman and Fourier Transform InfraRed spectroscopies (e.g., Stolper 1982; Dixon 1995; Jakobsson 1997; Ohlhorst et al. 2001; Mandeville et al. 2002; Zajacz et al. 2005; Behrens et al. 2006; Mercier et al. 2009; Iacono-Marziano et al. 2012; Le Losq et al. 2012; Morizet et al. 2013a,2017a; Di Genova et al. 2017; Schiavi et al. 2018).

Atomic arrangements and redox speciation are also two important information for the sample characterization. Multiple methods are dedicated to determine those parameters and some of them will be described in the following chapter.

In this study, the high-pressure experiments were essential to re-create martian igneous rocks that are not available on Earth. Understanding the formation processes of martian melts is needed to better constrain the past volcanic activity of Mars. Few experimental studies were dedicated to the synthesis, at high pressure and temperature, of martian analogues in presence of volatiles (e.g., Stanley et al. 2011, 2012, 2014; Ardia et al. 2013; Armstrong et al. 2015). In addition, characterization of the experimental products by spectroscopic methods such as Raman spectroscopy, has also been merely addressed (Di Genova et al. 2016). Hence, to provide new results on such atypical martian melts, various analytical devices were used in the present work. The future 2020 Mars mission will possess new devices onboard the SuperCam instrument, which includes a Raman spectrometer (Wiens et al. 2016). Then, there was a necessity to obtain Raman spectra on martian analogous synthesized at high pressure to compare with the future spectra acquired on martian igneous rocks.

In this chapter, the first part will be dedicated to the description of the experiments setup to perform Fe-rich basaltic glasses. The piston-cylinder apparatus is exposed, along with the sample preparation. Experimental difficulties will be discussed, with various setup optimizations and recommendations for futur experimentalists.

The second part of the chapter will focus on the analytical methods employed. Spectroscopies (IR, X-ray), microscopic and chemical methods will be described. This chapter will be closed with a discussion on the redox conditions in piston-cylinder apparatus and its importance for this study.

I.2: High pressure and temperature experiments
I.2.1. Description of the piston-cylinder equipment

The piston-cylinder apparatus is made of two pistons: the top one called the endload and the bottom one, the sample pressure. The endload is sealing the experimental setting whereas the sample pressure piston is inducing the pressure on the sample. The pressure is reached by compression of a hydraulic liquid (oil) applied on a piston, which will vary according to the required pressure. To reach low pressures, in the range of 0.5 – 2 GPa (i.e., 5 – 20 kbars), a ¾ inch carbide piston is used. For high pressure experiments (> 2 GPa), a ½ inch carbide piston is required instead. Then, the applied pressure on the sample can be described as:

$$F_{applied} = P_i \times \pi \times (\frac{r_2}{2})^2 \tag{1}$$

$$P_{eff} = \frac{F_{applied}}{\pi \times (\frac{r_1}{2})^2} \tag{2}$$

With $F_{applied}$ the force applied on the carbide piston (3/4 or ½ inch)

P_i the wanted pressured of the experiments (in bars)

r_2 the radius carbide piston (3/4 or ½ inch, in cm)

r_1 the radius of the sample pressure piston (in cm)

P_{eff} the effective pressure applied on the carbide piston (in bars)

Since the piston-cylinder apparatus is calibrated for pressures expressed in Pounds per Square Inch (PSI), the effective P (P_{eff}) is then converted into this unit. The pressure applied by the piston cylinder needs correction due to friction into the piston chamber wall interface and flow properties of the pressurized assembly (Green et al. 1966). Here, we applied an error of 10% on the read pressure (McDade et al. 2002).

The piston-cylinder in the Laboratoire de Planétologie et Géodynamique (i.e., LPG) is equipped of a hydraulic pump connected to the sample pressure (Fig.I.1). This instrument permits the program of the increase and decrease in pressure. Coupled to the hydraulic pump, the piston-cylinder is supplied by a liquid to cool down the experiment. The chiller, shown in Fig.I.1, contains a mixture of water and cooling liquid. The liquid temperature can be parametrized with a minimum recommended value at 6°C. The entire chain of elements is shown in the Fig.I.1.

Fig.I.1: A) Chiller with a mixture of water/cooling liquid; B) Piston-cylinder apparatus; C) Hydraulic pump

The piston-cylinder setup exhibited in Fig.I.1, can be decoupled in multiple parts from the base of the sample pressure piston to the endload piston (i.e., from the bottom to the top, Fig.I.2):

- a bottom plate
- a steel piston
- a cupper/steel sleeve
- 3/4 or 1/2 inch pistons made of tungstene carbide
- a perforated anvil with an inner core made of tungstene carbide and the outer part of steel: sample holder
- a Mylar sleeve: is an insulator and enables the current to go only through the middle of the anvil
- a top plate
- a steel piece: links the top plate to the endload piston
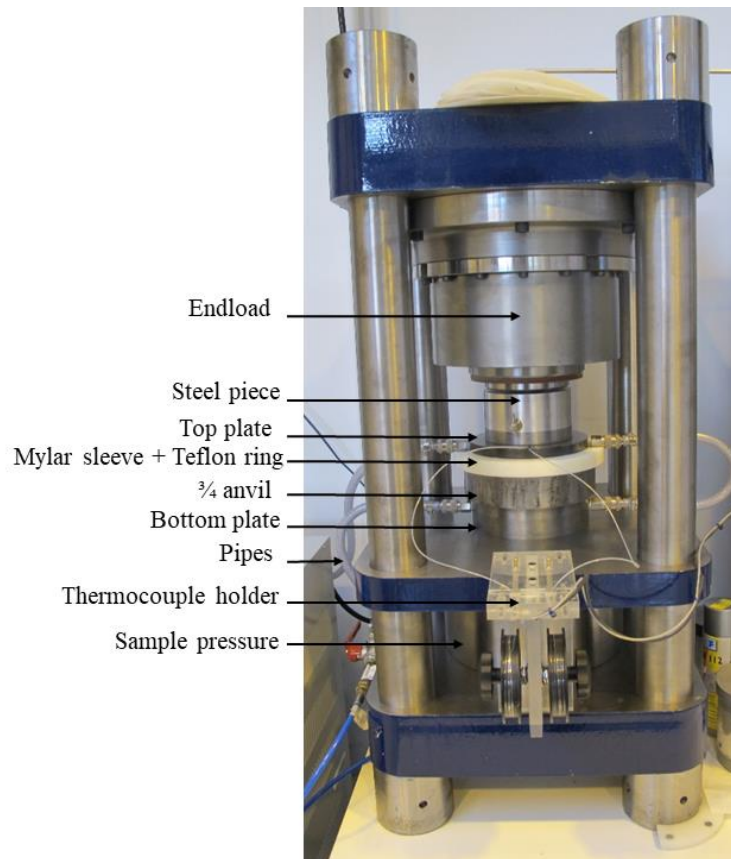
Fig.I.2: Description of the experiment setup in the piston-cylinder

Samples are loaded inside the anvil (¾ or ½) in a ¾ or ½ inch assembly is loaded. A steel plug surrounded by a pyrophyllite ring is on top of the assembly, thus at the top of the anvil. The Milar combined with the pyrophyllite plug will act as insulator to prevent the current to go through the entire anvil.

I.2.2. Description of the ¾ or ½ assemblages

I.2.2.1 Talc-pyrex-graphite assembly

The assemblage where the samples are loaded is made of 3 layers (from the outter part to the inside part): talc, pyrex and graphite.
The talc layer main function is to ensure that the anvil is not heated. It is also a material resistant to high pressures.
The pyrex is present to inhibit H_2 diffusion from the talc to the assembly, i.e., inside the samples.
The graphite will conduct the electrical current through the assembly and convert it into a heat flux. A graphite lid at the bottom of the assembly closes the graphite heater. Inside the graphite heater, three units can be found:
- A plug located at the bottom of the assembly
- A middle perced plug for capsules (2 for ¾ inch and 1 for ½ inch assembly)
- A top perced plug for the thermocouple

Plugs are made of pure MgO and are machinate in the lab. According to the assembly, the length and diameters are different. Indeed, ¾ assembly are larger than ½ and allow experiments with at least 2 capsules. The decomposition of a ¾ assembly is shown in Fig.I.3.
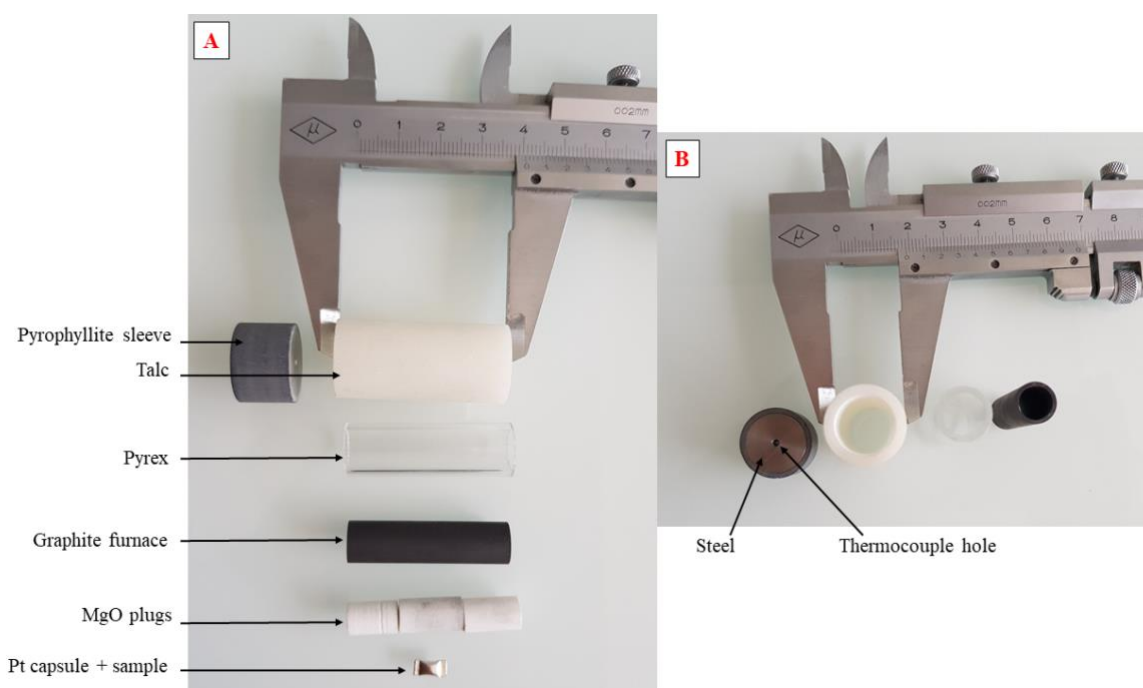
Fig.I.3: A) Description and length of the assemblage; B) Widths of the assembly and pyrophyllite plug

The whole assembly is wrapped into a thin Teflon sleeve to reduce wall friction. The anvil is also greased with Teflon spray.

I.2.2.2 Capsules

For high-pressure experiments, different kind of capsules are available and depends on the experimental settings. At low temperature (< 1200 °C), AuPd capsules is favored due to their low fusion temperature ~1300 °C (Okamoto and Massalski 1985). Beyond this temperature, Pt capsules are necessary with a melting point at >1900 °C below 10 GPa (Kavner and Jeanloz 1998).

For our experiments, we have chosen Pt capsules because high temperatures were reached (> 1400 °C). The tested capsules were either 5.0 mm or 2.9 mm diameters. They were previously cleaned with 2 consecutive heating followed with an ethanol bath.

Fe pre-enrichment of the Pt capsules was tested to prevent any Fe loss during the high-pressure experiment, because of the high Fe content of our samples (> 15 wt % FeO). The Fe-enrichment was performed at the Institut des Sciences de la Terre d'Orléans (i.e., ISTO), using an Adamel furnace powered by a mixture of various gases: H_2-CO_2, $CO-CO_2$ or $CO-CO_2-SO_2$. This technique consists in the addition of Fe powder and Pt capsules in an alumina crucible, exposed in a 1 atm furnace supplied with a $CO-CO_2$ gas-mixture to ensure a fO_2 close to the Quartz-Fayalite-Magnetite -2 buffer (i.e., QFM-2). After few high-pressure experiments using the Fe-

enriched Pt capsules, there was no difference between not-enriched and Fe-enriched capsule, which has also been demonstrated in Brugier et al. (2005) study. Then, no Fe-enriched Pt capsules were used for this study.

Once the capsules are filled with the desire chemical composition and welded shut, they are inserted inside the MgO middle plug (see Fig.I.4). A thin MgO layer is inserted between the capsules to prevent any contact. Indeed, isolating capsules is needed to weight them after the experiments to find any leak.

The capsules are also maintained inside the middle plug by MgO powders to inhibit any deformation during the pressurization (represented with points in Fig.I.4). Then, on top of the capsules, we installed a small lid of MgO to prevent the thermocouple to pierce the capsules during the experiment. The schematic representation of the capsule setting insie the talc-pyrex-graphite ¾ inch assembly is reported in the Fig.I.4.
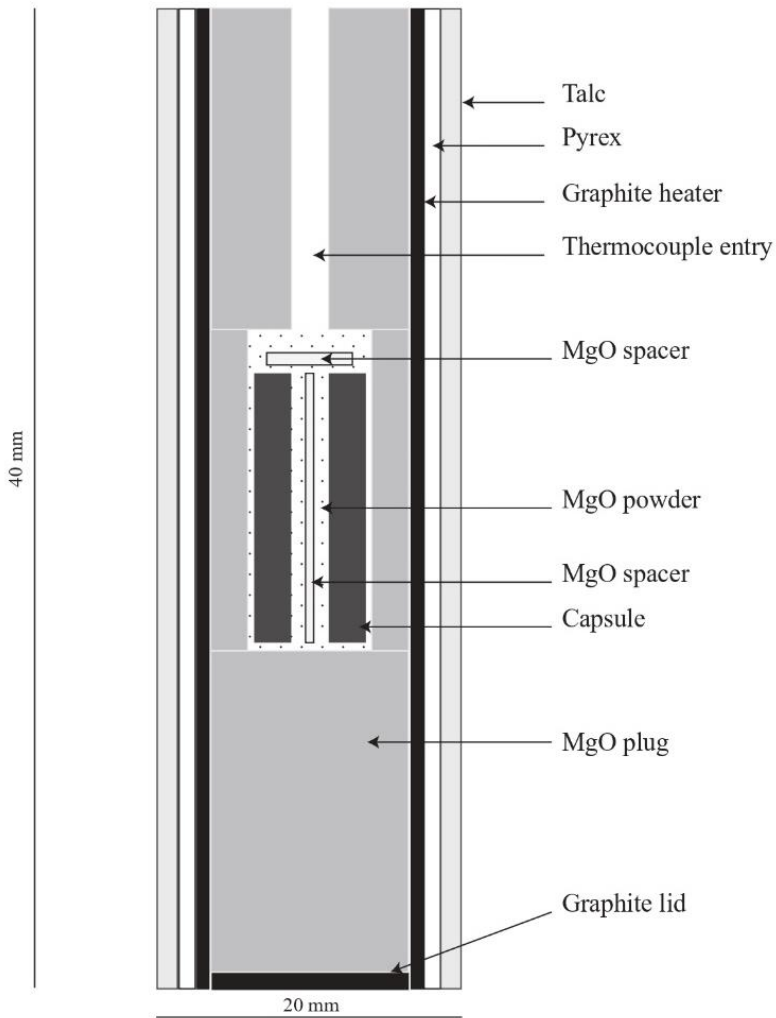
Fig.I.4: Vertical section of the ¾ inch assembly.

I.2.3. Temperature measurements

The heating is produced by a current injected inside the apparatus from the end-load piston to the top of the capsules. The current path will be strictly restricted with the use of the Milar and pyrophyllite sleeves, by only going through the center of the setting. The current flux is closed with a graphite lid located at the bottom of the assembly as shown in Fig.I.4.

The thermocouple used for all experiments was made of a Pt-Rh alloy (i.e., B-type), with 6 and 30 % of Rhodium. This kind of thermocouple allows a temperature measurement up to 1820°C. A 2-holes alumina tube protects the PtRh wires. The intertwining of the two wires at the end of the alumina tube (i.e., at the top of the capsules) permits the temperature measurement. Indeed, the connection of the 2 different wire chemical compositions creates a gradient given in meV. This gradient is measured with a Eurotherm presents on the apparatus. The type B thermocouple calibration equation will depend on the thermocouple voltage (v in meV), p and q coefficients. The equation can be written as follow:

$$T \ (°C) = \frac{P}{Q} + \ T_0$$

Where:

$$P = p_1(v - v_0) + p_2(v - v_0)^2 + p_3(v - v_0)^3 + p_4(v - v_0)^4$$
$$Q = 1 + \ q_1(v - v_0) + q_2(v - v_0)^2 + q_3(v - v_0)^3$$

Parameters T_0, q, p and v_0 are described in Table A1 in the annexes section.

At the beginning of the experiment, the temperature is controlled manually, by increasing the operating power (OP) until the temperature reached 500°C. From this, an increase temperature program was set with a 50 C°/min ramp until the goal temperature is reached (1500 – 1600°C).

I.2.4. Difficulties encountered with high pressure experiments

When the piston-cylinder arrived in our lab, the materials provided did not work properly. During the experiment, the current decreased quickly (from 15 to 10 A) which induced a drop of temperature down to 1200°C, when the temperature was first reaching 1400 °C. This prevented us to increase the temperature above 1100 – 1200°C. Temperature at 1400 °C was rarely reached or with a high OP (70 - 90 %). However, the results were not positive (i.e., no glass). We will discuss of these results in the next chapter.

Few months were dedicated to the optimization of the piston-cylinder to prevent the current drop during the experiment, by optimizing different part of the setup. We first changed the 3/4 anvil and the thermocouple geometries. Almost simultaneously, we focused on the optimization of the assembly containing the samples. Then the quench rate was also modified.

I.2.4.1. Thermocouple optimization

During the first experiments, we have observed a lot of thermocouple broken. It is usual that, during the experiment with the relaxing of the sample, the thermocouple rises up into the steel piece linking the top plate to the endload piston. When the rise is too important, it is likely to break the thermocouple. To prevent the break, the alumina sleeve containing the pair of Pt-Rh

wires, is shorten. The exit of the top plate, i.e. the exit of the thermocouple wires, is very sharp which could also create a fragility at this level. We performed a specific filing of the alumina tube in a beveled shape so that the exit of the wires is smoothen. Coupling these two methods help to keep the temperature measurement for all the experiment duration.

However, the optimization of the thermocouple agency did not remove the issues with the current drop, during our experiments.

I.2.4.2. The talc-pyrex- graphite assemblage

One hypothesis for the current drop was the dehydration of the talc. The chemical formula of the talc is $Mg_3Si_4O_{10}(OH)_2$ which involves H_2O molecules. During the compaction and heating of the assembly, the talc undergoes dehydration. Then, the pyrex is usually working as a shield wall to prevent the H_2O to reach the graphite and the capsules. However, there was a possibility that the talc was more hydrated as usual. Several possibilities for the unusual hydration are available, among them we assume that the assemblies' storage with no moistness control, or manufacture defaults from the enterprise could have such effect. With an unusual high H_2O content of the talc, the Pyrex filter can be overwhelmed, letting H_2O to go through and damage the graphite heater. The damages would have weakened and broke the heater, causing a current decrease.

Thus, Raman analyses were performed to quantify the H_2O content in the talc. The results showed usual content compared to assemblages of another factory. Nevertheless, a dehydration prior experiments was made using a 60°C heat chamber. The assemblages were stored in the chamber one day before the experiment to ensure the dehydration of any extra water.

The initial graphite furnaces used for our experiments presented an internal 3° taper from the center toward both ends of the heater. Previous works have investigated the efficiency of a straight furnace compared to a modeled one (Kushiro 1976). They showed that the latter prevents a large temperature gradient around the samples due to its specific geometry. Only a gradient of 10 °C over 10 mm long is applied on the capsules. On the other hand, the straight heater presents a 50°C gradient over 5 mm in the center of the graphite furnace (Schilling and Wunder 2004).

Another hypothesis for the amperage decreased lied in the heater fragility. If the graphite heater broke during the experiment, the current is still able to go through due to the pressure applied. However, the voltage, hence the resistance, will increase and the amperage decreases. Then, the heater was working but not above 1200 °C. We observed a lot of porosity in the taped furnaces. More interestingly, each furnace had a different porosity. Also, the thickness of the furnace was very small (< 1 mm).

Thus, the taped heater was removed and replaced by straight furnaces of the same factory. However, they still presented visible small grains of charcoal, which evokes a compaction issue in the graphite synthesis.

Consequently, we have chosen to work with straight furnaces from another company, where the compaction and porosity were correct. This change, with the others previously cited, allow us to perform experiments at the temperature wanted, without the current drop.

Our first experiments showed crystallized results instead of a glass that should have been obtained considering the temperature of the experiment (> 1500°C). These results will be discussed in the next chapter.

We measured the temperature of the water circulating inside the setting, prior and during the experiment. We found that during high temperature experiments (> 1500°C), the temperature reached 17°C, where 6°C is usually used to cool down the experiments. Measurements of the quench rate were also performed in that case. From 1500 to 1000 °C, the quench rate was ~70 °C/s and from 1000 down to 10 °C at 30 °C/s. The results show that the quench rate was too slow to obtain a glass. Indeed, the glass transition temperature Tg, i.e., the change from solid (glass) to liquid, will depend on the T, quench rate and chemistry of the sample (Dingwell and Webb 1990). With the actual quench rate of the piston-cylinder (70 °C/s) coupled to the high temperature experiement, Tg cannot be reached.

One possible reason for the slow quench rate observed could be caused by the read temperature of the Eurotherm. Indeed, it is possible that the response of the Eurotherm in comparison with the real temperature drop is shown with a delay. This delay would prevent us to calculate an accurate quench rate. However, the quench rate of 70 °C/s still too low even considering a Eurotherm issue.

Consequently, the piston-cylinder was equipped with a chiller (see Fig.I.1). This instrument permits to cool down the fluid circulating through the anvil. The chiller temperature was set at 6°C, but condensation was observed, which could have provoked some damages during the experiments. Then, the temperature was set at 14 °C for the whole experiment duration and then reduced down to 10 °C for the quench. These modifications increased our quench rate up to ~90 °C/s from 1500 to 1000 °C. The duration time of experiments was also increased from 1 to 6 hours to allow a better homogenization of our sample. Coupling those two techniques permit to obtain a glass. These results will be detailed in the next chapter.

Once the experiments were made, analytical methods were employed to characterize our samples.

I.3. Analytical methods

In this section, the various analytical methods used to characterize our samples will be described. On part is dedicated to the spectroscopic methods, which include the Raman and Fourier Transform InfraRed (i.e., FTIR) spectroscopies. Our samples were also studied by microscopic methods, coupled to X-Ray instruments.

I.3.1. Spectroscopic methods

For our study, spectroscopic measures were essential to characterize our sample. Indeed, multiple applications are possible with these non-destructive methods. In that case, the Raman spectroscopy was used to determine the spectral signature of the Fe-rich glasses, analogous of martian basalts. In addition, we were able to quantify volatile contents according to various calibration method established in the literature, using the Raman spectroscopy. To combine the

values obtained with the Raman calibration, we performed FTIR to quantifiy the H_2O content in our samples. Both methods will be described in the following section.

I.3.1.1. Raman spectroscopy

The Raman phenomenon was discovered in 1928 by Sir Chandrasekhara Venkata Raman using the sunlight as a source, a telescope as a collector and his eyes as a detector. This spectroscopic technique uses a laser source with a specific wavelength to excite molecules present in the samples. InfraRed and Raman spectroscopies are both analyzing the transitions between vibrational levels (i.e., the change of configuration) of molecules. The analyzed frequencies of these spectroscopies are located between microwave and UV-visible, between 3×10^{12} and 3×10^{14} Hz. Three Raman techniques are possible: Normal Raman, Resonance Raman and Fluorescence. In this thesis we used the Normal Raman technique to analyze our samples.
Theoretically, the laser source, with a specific wavelength, is emitted over the sample. The scattered light can be divided in two types:
- the Rayleigh scattering with the same frequency of the incident beam
- the Raman scattering coupling the incident beam and the vibrational frequencies of the molecules
The Raman scattering can also be decomposed:
- the Stokes lines: the incident beam frequency plus the frequency of the molecule vibrating
- the Anti-Stokes lines: the opposite of the Stokes lines
In Raman spectroscopy, the collected spectra exhibit the Stokes lines. Because the Stokes and Anti-Stokes represent an addition or subtraction of the incident beam wavelength, the spectra are represented in the x-axis in Raman shift (cm^{-1}). The covered range by spectroscopy Raman is between 0 and 4000 cm^{-1}.
The molecule, when excited by an incident beam, can vibrate in three dimensions:
- ν_1: the symmetric stretch vibration
- ν_2: the symmetric bending vibration
- ν_3: the anti-symmetric stretch vibration
The representation of vibrations is reported in the Fig.I.5 with an example of a H_2O molecule excited by a laser source and the three kind of vibrations possible.
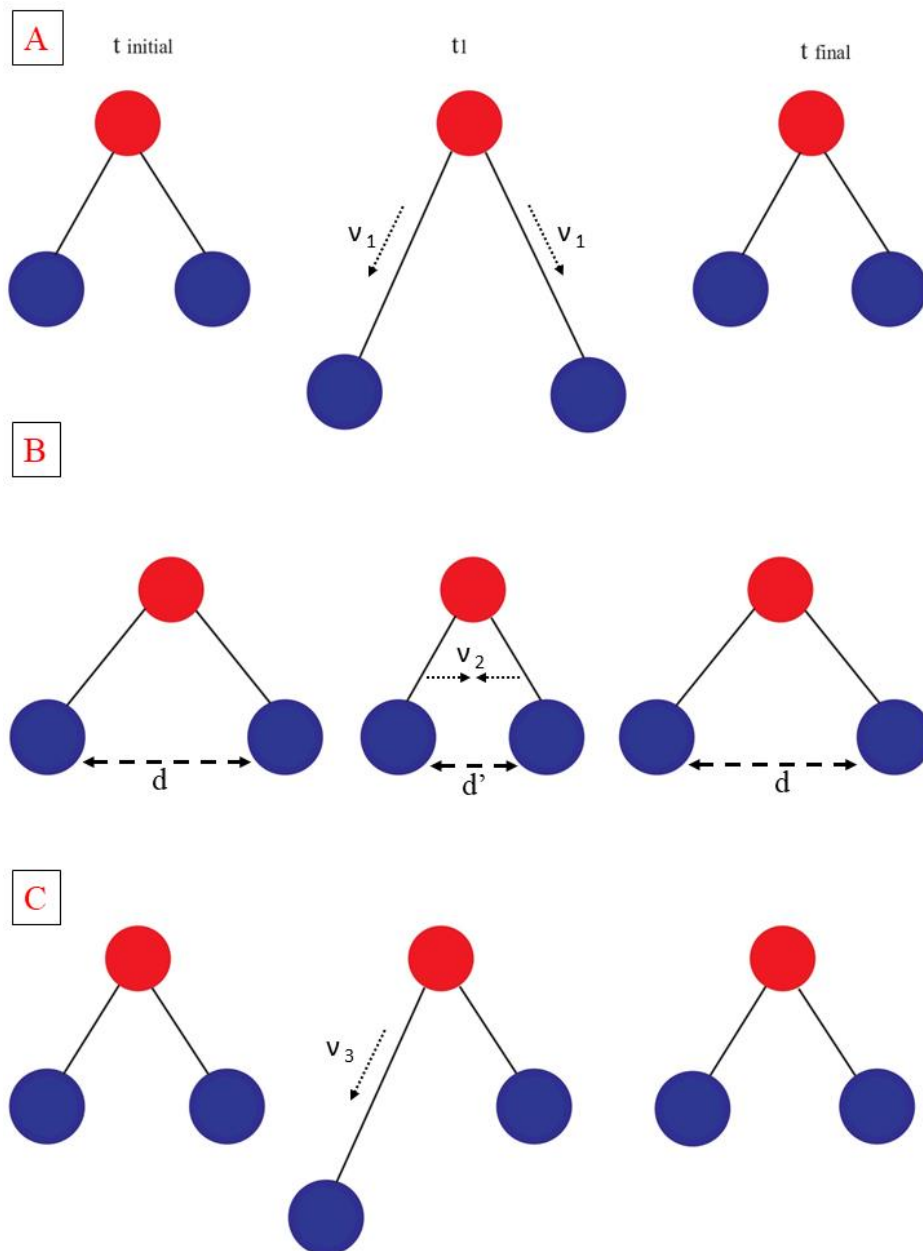
Fig.I.5: Vibration modes with an example of the H_2O molecule (H in red and O in blue) at t initial, t1 when the molecule is excited with a laser source, and t final after the excitation: A) symmetric stretch ν_1; B) symmetric bending ν_2; C) anti-symmetric stretch ν_3. With d refers to the distance between the O atoms, and d' the distance when the molecule is excited.

All three vibrations are not always Raman active and will depend on the polarizability of the molecule. The incident beam will create a distortion between the positive charged nuclei of the molecule attracted to the negative pole, and the electrons attracted by the positive pole. This will induce a dipole moment expressed in the three axis (i.e., x,y,z). The dipole moment can be described as a matrix tensor, representing the polarizability tensor. Hence, if one component of the tensor is modified during the vibration, the vibration is Raman-active.

The LPG laboratory is equipped of a Jobin-Yvon Labram HR800 Raman represented in Fig.I.6A. This Raman can collect data from 100 to 4000 cm-1.

A Raman spectrometer possesses four major components:
- an excitation source: the laser
- a sample illumination and collection system: the microscope/edge filter
- a wavelength selector: gratings
- a detection and computer control/processing systems: Charge-Coupled Device (i.e., CCD)

The LPG possesses currently three solid-state lasers for the Labram HR Raman (Fig.I.6A): 488, 532, 633. The 488 nm is an Ar laser, the 633 nm a laser of HeNe. There is also a IR diode laser at 785 nm. Hence, the wavelength available covers the UV-visible (488, 532, 633) to the Near InfraRed (785 nm) field. In this study, a tunable Nd:YAG solid-state laser up to 200 mW and at 532 nm (mpc6000) was used.

The Jobin-Yvon Labram HR is also equipped of an edge filter with a specific wavelength for each laser. It has two roles:
-   reflect the incident beam emitted from the laser source to the sample
-   filter the incident beam after the excitation of the sample

Multiple gratings are available for the analysis: 300, 1200, 1800 and 2400 grooves/cm. Increasing the number of grooves increases the precision on the spectrum. For our analysis, two gratings have been used: the 300 and 1200 grooves/cm.

Once the Raman scattered light has been collected and filtered, it goes through the Charge-Coupled Device (i.e., CCD) which is a silicon-based semiconductor arranged as an array of photosensitive elements. Each pixel will transform the photon (i.e., the Raman scattered light) into a photoelectron and store it as a small charge. Thus, the pixels on the array can be converted into digital values and transferred to the computer. The LabSpec© software will then exhibit the Raman spectra collected on the samples in Raman shift and intensity.
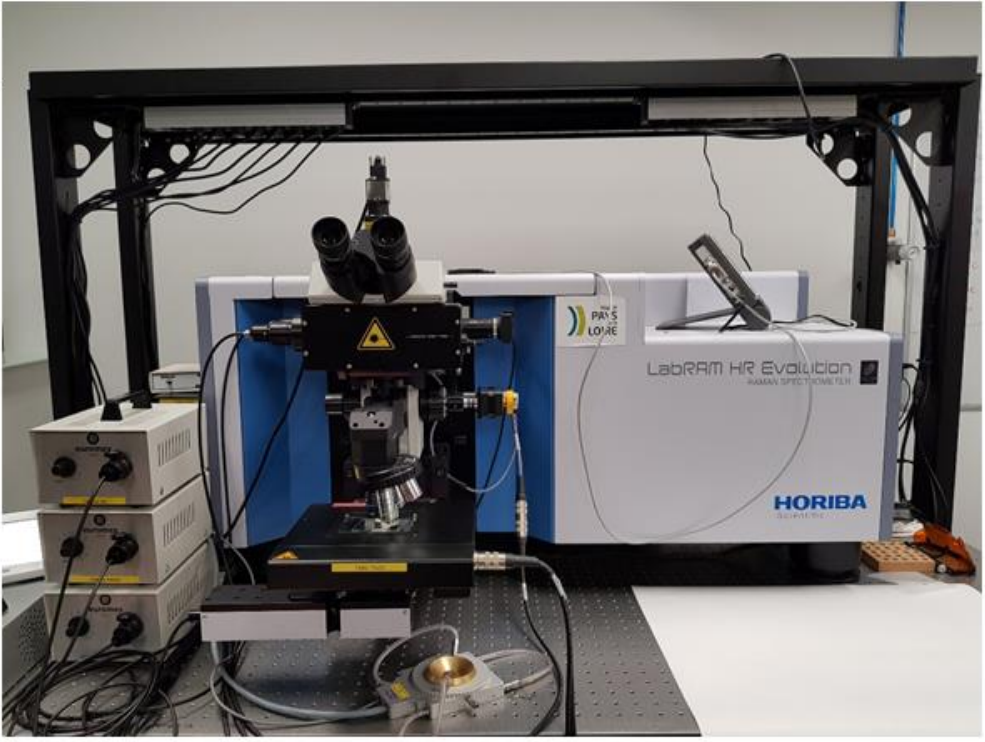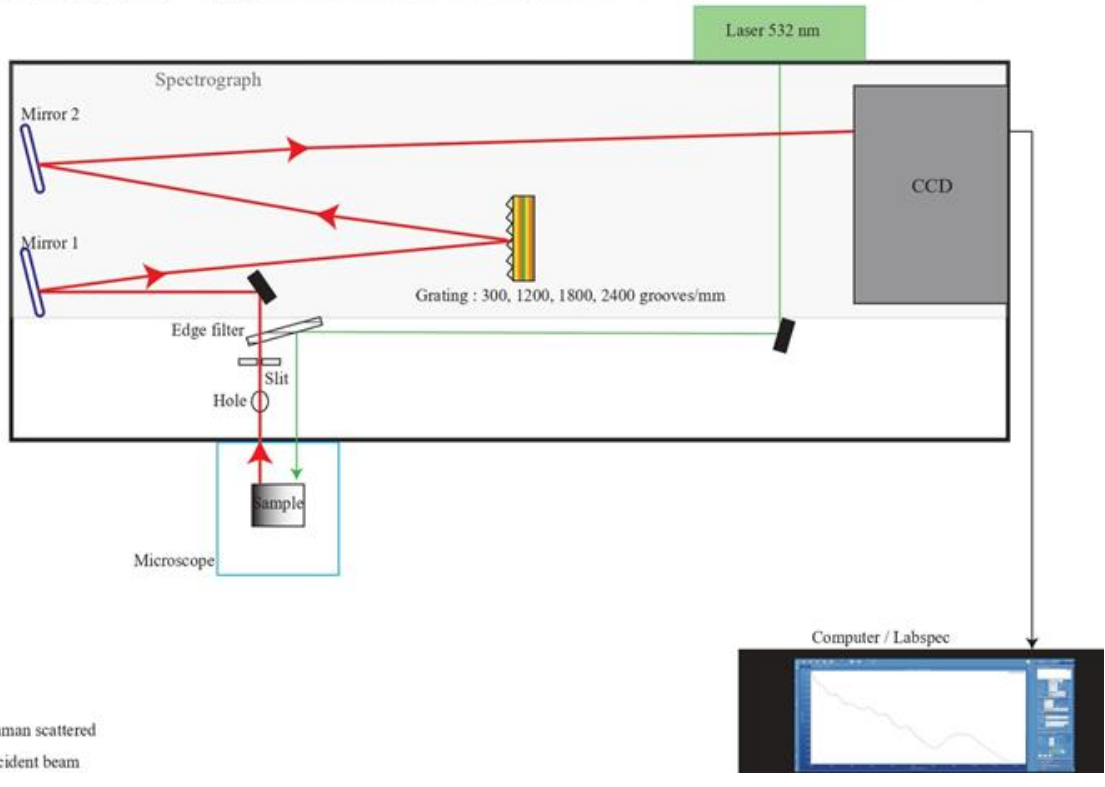
Fig.I.6: A) Jobin-Yvon Labram HR800 Raman spectrometer at the LPG lab; B) Simplified schematic representation of the Raman spectrometer setup when the 532 nm laser is selected. The filled black rectangles are dielectric mirrors reflecting the emitted incident beam.

In Fig.I.6B, an example of the path of the incident beam and the Raman scattered light is represented and simplified. The main steps can be resumed as follow:

1) The incident beam emitted from the laser is transferred through the microscope with the edge filter

2) The sample emits the scattered light (Raman scattered + incident beam) collected by the Raman spectrometer device with a specific hole and slit apertures

3) The scattered light arrives at the edge filter, where only the incident beam is filtered

4) The Raman scattered light goes into the spectrograph, where the grating diffracts the signal with a specific wavelength

5) The diffraction of the signal is collected by a mirror. The latter will reflect the signal toward the CCD device

6) The CCD transforms the photons into a digital signal, exhibited via the Labspec software© on the computer

Samples preparation for Raman spectroscopy is very simple. No specific preparation is required; hence analyses can be performed on a whole rock, powder, liquid, or in sample hold in an epoxy plug.

Using the Raman spectrometer permit the obtention of various information. For vitreous sample, this technique enables the quantification of various volatile content dissolved in the glass through calibration established in previous studies (e.g., CO_2, H_2O and S). Also, the observation of Raman spectra acquired on glassy samples reveal the polymerization degree of the sample, which can be linked to viscosity. In cristallized material, the Raman spectroscopy is an effective tool to characterize the mineralogical assembly in a material.

In our study, the Raman spectrometer was used to quantify volatile dissolved in our synthetic glasses (H_2O and S, i.e., Chapter II and III), to observe the degree of polymerization in the same samples, but also to characterize the mineral present (Chapter IV).

I.3.1.2. FTIR

The Fourier-Transform InfraRed spectroscopy is also based on the observation of vibrational transitions of molecules. Molecules will be excited with an infrared source. The difference between Raman and FTIR is that the latter shows the absorption of the infrared light by the sample. The intensity of the absorption is governed by the Beer-Lambert law:

$$I = I_0 \times e^{-\varepsilon c d}$$

Where I_0 and I are the intensities of the incident and transmitted beams, respectively. ε is the molecular absorption coefficient in L/mol/cm. Here, c and d are the concentration of the sample and the cell length, respectively. It is customary to represent the absorption in transmission percentage, which is the ratio between I and I_0.

The FTIR disposable in LPG is an IR Continuum microscope attached to a Nicolet FTIR 5700, with a X15 Cassegrain objective, shown in Fig.I.7.

Two detectors are available:
- InSb and MCT-B for analysis using the microscope
- DTGS-KBr for powder analysis

Beamsplitters on the FTIR, are CaF_2 or KBr. The CaF_2 beamsplitter enable the spectral range between 2000 and 10 000 cm-1 whereas the KBr detects signal between 400 and 2000 cm-1.

Fig.I.7: A) Nicolet FTIR 5700 spectrometer at LPG; B) IR microscope equipped with the X15 Cassegrain objective

We performed FTIR measurements on glass samples to obtain the H_2O content dissolved (Chapter II). In this study, the analysis conditions were: a white light source, an InSb detector and CaF_2 beamsplitter. The samples were not polished due to their small sizes. In literature, double polishing of the sample is required to get a fixed thickness and better constrain the H_2O quantification. However, this method is possible when samples are not small, which was the case in our study (< 3mm). Then, thickness measurements were realized with a digit meter (with an accuracy of ± 1 µm) to link the absorption to the H_2O content using the Beer-Lambert approximation (Dixon et al. 1995; Morizet et al. 2010). The detailed quantification method is described in the next chapter.

I.3.2. Microscopic methods

I.3.2.1. Secondary Electron Microscopy

Secondary Electron Microscopy (i.e., SEM) is an analytical method allowing the imaging of the sample and its quantification in some cases. To obtain the image of the sample, an electron radiation is sent on its surface which will create principally:
- backscattered electrons from the incident radiation
- secondary electrons coming from external atomic envelops
- X-ray emission
- UV-photons emission
The SEM detector collects a mixture of backscattered and secondary electrons to create the image of the sample. Such microscopy reveals the morphology, the relief and a good resolution (x 10 to X 500 000) of the sample analyzed. However, no structural information beside crystalline shapes can be identified. Two types of images are obtained with this method: backscattered electron image (i.e., BEI) and secondary electron image (i.e., SEI). Adding the two methods gives a complete description of the sample. Indeed, the BEI reveals the relief or the crystalline shapes. On the other hand, the SEI shows the chemical composition of the sample, with various toned of black and white colours. The more the sample is enriched in

heavy elements, for example in Fe, the more the sample is bright on the image. On the contrary, if the sample possesses mostly light elements such as Si, or Al, the sample will be darker.

For instance, SEI method permits to reveal the degree of homogenization of a glass. In the Fig.I.8, we have shown the images obtained by both BEI and SEI methods to constrain the concentration of "dendritic textures" present in one sample and described in the next chapter. As we can see on the Fig.I.8A, the BEI method shows the relief of the bubbles presenting dendritic crystals (i.e., needle-like crystals) and a homogenized area corresponding to the glass. In Fig.8B, the SEI of the same sample exhibits the chemical homogenization. We can see that the center of the bubble with dendritic texture, shown in Fig.8A, are in the same grey tone as the glass component indicating no change in the chemical composition.
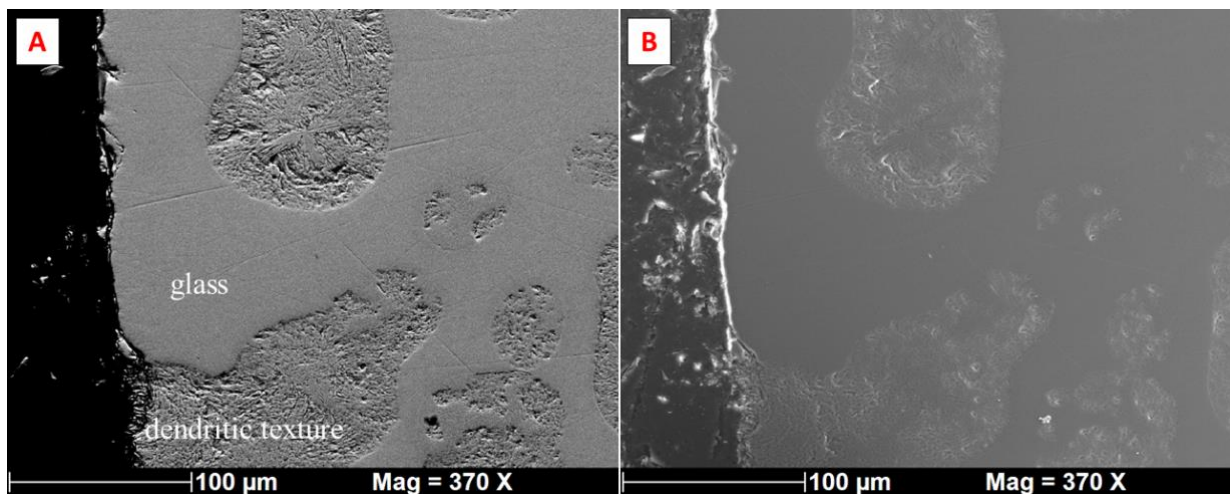
Fig.I.8: A) Backscattered electron image (BEI) of the sample GC-3H-6h; B) Secondary electron image (SEI) of the same sample.

In addition to the standard JEOL JSM 5800 LV available in Institut des Matériaux de Nantes (IMN), the SEM is equipped with Energy Dispersive Spectroscopy to determine the major elements of the samples. However, H_2O and CO_2 are not detected with this method; besides those species, all elements are quantified using the EDS method.

For SEM analysis, the samples need to be in an epoxy pellet that will be polished to a small grain size (down to 1 µm). Then, a thin carbon coating driving the electron through its surface covers the pellet.

I.3.2.2. Electron-Probe Microscopic Analysis

Electron-Probe Microscopic Analysis (EPMA) is a technique working by bombarding a sample with an electron beam with a various energy, between 5 to 30 keV. The X-ray photons emitted by the elemental species present in the sample is collected. Each X-ray wavelength is attributed to an element. The EPMA technique is coupled with a Wavelength Dispersive Spectroscopy (WDS), which identifies the emitted X-ray from the sample analyzed. This is a non-destructive technique analyzing a planned surface to the micron-size. Each element has a detection limit

but the sensitivity of EPMA is down to the ppm level. A schematic representation of the EPMA setup is shown in Fig.I.9.
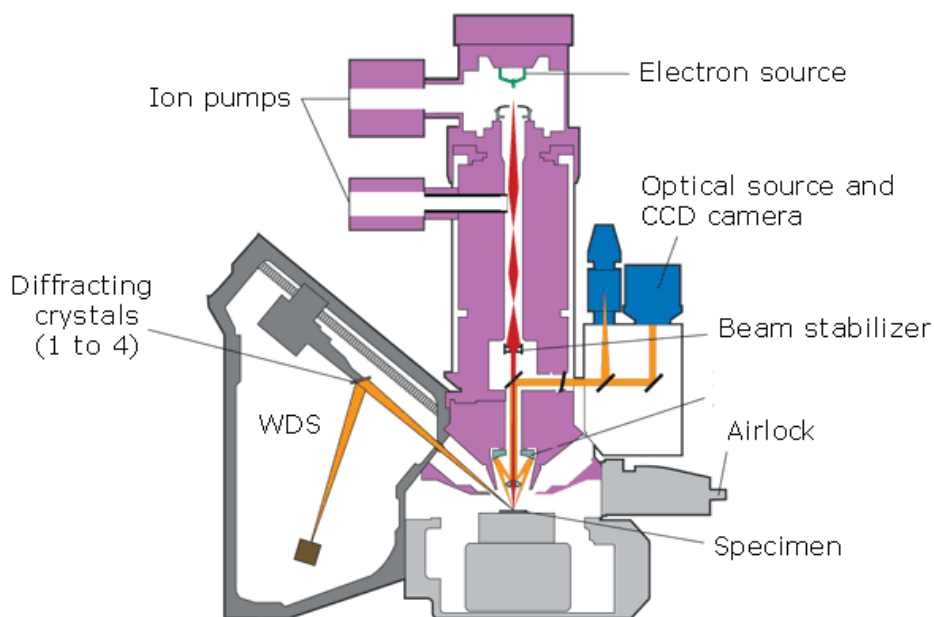
Fig.I.9: Scheme of the Cameca SX 100 device. Provided by CAMECA.

The EPMA analyses were made using a Cameca SX 100 at IFREMER of Brest (France). A spot size of 10 µm, a beam current at 6 nA and a voltage at 15 keV were chosen for the glass components. The acquisition time was 10 s on the sample and 5 s on the background. The standards chosen for our analysis were: wollastonite (Si, Ca), corindum (Al), TiMn oxide, andradite (Fe), NiO, albite (Na), forsterite (Mg), apatite (P), orthoclase (K), Cr_2O_3 oxide. The associated error is about 2 % in relative to the measured value. To obtain the chemical composition by EPMA of our samples, the sample preparation was similar to the SEM analysis: samples in a polished epoxy pellet recovered with a thin carbon coating.

I.3.3. XRD & XPS

I.3.3.1. X-Ray powder Diffraction

The X-Ray powder diffraction (XRD) is a non-destructive technique. Based on powder, solid or even liquid samples, phase composition, structure and texture are the main information, along with others, that can be extracted with this analytical method.

X-rays are electromagnetic waves with associated wavelengths or beams of photons with associated energies. The X-ray exciting atoms in the samples gives a different signal reported into a powder diffractogram. When a crystal is attacked by X-rays, the inter-atomic distance inside the crystal is excited and a diffraction phenomenon occurs. The diffracted intensity of the crystal is reported on the diffractogram versus the Bragg angle (i.e., 2θ, the angle between the incident and the diffracted beam). Each peak is characterized by its position, intensity and profile. The peak position will provide atoms agency in solid matters. The intensity represents the structure, amount and absorption of the material.

Powder diffraction was used on crystallized samples synthesized at high pressures. The use of powder diffraction is to characterize the crystals with no crystal orientation contribution by reducing the sample into a powder. For the present work, the synthesized samples exhibited nanometric crystals, which prevented us to characterize them by spectroscopic or microscopic method. It will be further discussed in the next chapter.

Analyses were realized at IMN with Pierre-Emmanuel PETIT. Less than 20 mg was used, and the sample was grinded into a powder.

Two XRD methods were tested:

- a D8 advance without a Fe fluorescence filter
- a diffractometer D500 (Fig.I.10)

The first one was used to have a rapid diagram to observe the presence of crystals, but the signal was altered by the noise induced by the high Fe content of our sample. The copper tube used in this device has an energy which excites also the Fe atom. The other XRD device has the same tube but coupled to a filter. Then, the D500 was better suited for our Fe-rich samples.

Fig.I.10: XRD D8 at IMN

I.3.3.2. X-ray Photoelectron Spectroscopy

Siegbahn and coworkers discovered the X-Ray Photoelectron Spectroscopy (i.e., XPS) relatively late, during the 1950's and 1960's. This kind of spectroscopy aims to identify the excitation from the core and valence level of electrons present in atoms in the material. The principle of XPS is based on a radiation that ionize the atoms of the material (Siegbahn 1982). The reaction induced follow the equation:

$$A + h\nu \rightarrow A^+ + e^-$$

With A an atom that is excited by an X-ray energy hν, A_+ the ionized atom emitting a photoelectron e_-.

The emitted photoelectron has a kinetic energy (i.e., KE) that will be collected by an analyzer. The KE is corrected from the X-ray energy induced to give a Binding Energy (BE). There are two kinds of photoelectrons produced:

- One that will be collected directly by the analyzer without interaction with the matter: elastically scattered electron
- One that will interact with the solid loosing KE: inelastically scattered electron

The elastically scattered electrons give the narrow peaks observed in XPS graphs (example given in Fig.I.11). The other kind of photoelectron, the inestically scattered, will create the background below the peaks.

For this study, we used an X-ray Photoelectron Spectroscopy available in the IMN lab (Fig.11A). The analyses were performed by Vincent FERNANDEZ and Jonathan HAMON. A Kratos Axis Ultra XPS was used with a monochromated radiation of 1486.6 eV using a source of Al Kα. The instrument was first calibrated according to Seah et al. (1998). Five areas were investigated:

- Fe 2p and 3p at 707 and 55 eV, respectively (Mekki et al. 1996; Nesbitt et al. 2000)
- S 2p and 2s at 164 and 228 eV, respectively (Pratt and Nesbitt 2000; Zhao et al. 2017)
- O 1s ~500 eV (Nesbitt et al. 1995)
- C 1s ~285 eV (Mekki et al. 1996)
- Si 2p 102 eV (Nesbitt et al. 2011)

Some of these features are reported in the graph Fig.I.11B (i.e., C 1s, O 1s, Si 2p, S 2p and Fe 2p). The aims of these analyses were to determine the Fe redox ratio, S redox and the abundance of bridging (BO) and non-bridging oxygen (NBO) in our glasses.

The analyses were performed on glass chips of 2-3 mm long and with a smooth surface. Cleaved and non-cleaved glasses were tested to subtract C pollution. Since the C was not investigated and the cleavage of glass samples were difficult to control, the glasses analyzed were not specifically prepared prior experiments.
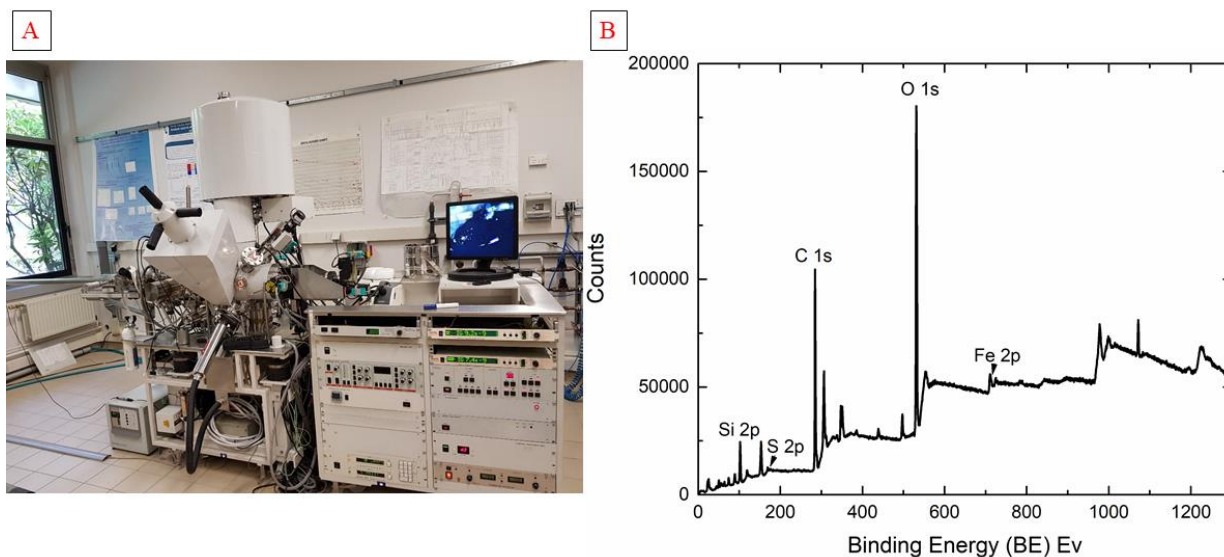
Fig.I.11: A) X-ray Photoelectron Spectroscopy available at the IMN lab; B) GCS-1S-1.5G analyzed by XPS with some peak attributions

I.3.4. Wet chemistry

Another method to determine the Fe redox ratio in our samples is the wet chemistry. This method is destructive and require at least 3 mg of sample.

The Fe_{2+} / $\sum Fe$ ratios were measured using the colorimetric method of Wilson (1960) recently modified by Schuessler et al. (2008). About 3 mg of samples were weighted in 7 mL crystal polypropylene beakers with a precision of 10_{-3} mg and dissolved for 3 days at room temperature in 1 mL of concentrated HF and 1 mL of 0.139 mol. L_{-1} ammonium vanadate (V_{5+}). As the digestion progresses in such low pH solutions, the Fe_{2+} released from the silicate matrix reacts immediately with the V_{5+} to form Fe_{3+} and V_{4+}. This reaction, which prevents any accidental and irreversible oxidation of Fe_{2+} into Fe_{3+} (Wilson 1960), may be reversed if the pH of the solution is raised up to 5. Once the digestions were completed, 5 mL of beryllium sulfate solution (500 g.L_{-1}) was added to the beakers in order to neutralize the excess of HF and breakdown all insoluble fluorides. The final solutions for FeO colorimetric measurement were prepared in volumetric flasks filled with 10 mL of ammonium acetate buffer solution at 500 g.mol$_{-1}$ (to raises pH up to 5), 5 mL of 2:2'-dipyridil solution as the ferrous colorimetric reagent and ultra-pure water to filled up to 100 mL. The FeO$_{tot.}$ analytical solutions were prepared by adding between 5 to 10 mg of hydroxylamine hydrochloride to an aliquot of the ferrous analytical solutions [50]. This strong reducing agent ensure the quantitative reduction of all remaining Fe_{3+} into Fe_{2+}. The colorimetric measurements were made with the UV/VIS spectrophotometer CARY UV500 (Varian). The optical density measurements were done at 525 nm where the ferrous 2.2' -dipyridil complex absorption is maximum (Wilson 1960). The peaks heights were measured relative to the baseline at 700 nm and the Fe_{2+} / $\sum Fe$ ratios were determined by dividing the absorbance ratios corrected for the procedural blanks. The results

of the $Fe_{2+}/\sum Fe$ measurements on the international reference material JB-2 ($Fe_{2+}/\sum Fe = 0.78$ ±0.005, N=19) are in good agreement with the recommended values (i.e., 0.78, Govindaraju 1994).

Each glass synthesized in this study were analyzed according to this method. The determination of the Fe redox ratio gave us information on the fO_2 induced during the experiments and the changes of charges occurring.

I.4. Oxygen fugacity (fO_2) in high pressure experiments

The piston-cylinder is not supplied by a gas mixture controlling the fO_2 during the experiment. However, studies have counteracted this disadvantage by using new techniques to control the fO_2: 1) double capsule coupled to a buffer powder (e.g., Nickel-Nickel-Oxygen buffer, Iron-Wüstite; Righter et al. 2009; Ardia et al. 2013), 2) addition of Fe/Pt/Si inside the Pt capsules (e.g., Armstrong et al. 2013; Namur et al. 2016), 3) reduction of the sample prior the high-pressure experiments with a mixing of gas (e.g., Stanley et al. 2011, 2012), 4) or graphite capsules (Filiberto et al. 2008; Ding et al. 2014, Li et al. 2017). However, the exact fO_2 cannot be controlled properly and back calculations are needed after the experiments using the ratio between Fe_{2+} and Fe_{3+}. Kress and Carmichael (1991) have established calibration equations based on $XFeO/XFe_2O_3$ (i.e., the molar fraction ratio between Fe_{2+} and Fe_{3+}), P and T to determine the fO_2. It is currently the best method to obtain the oxygen fugacity when synthesizing silicate melts at high pressures. However, studies have lately demonstrated that this method cannot be applied for high Fe content (Righter et al. 2012). In this study, the fO_2 calculated with the method of Kress and Carmichael (1991) from the Fe redox measured by wet chemistry were around QFM+6. This value was well above the QFM+1 buffered by the piston-cylinder according to Kägi et al. (2005). Although the Fe was under its oxidized form prior the experiment (i.e., Fe_{3+}), the piston-cylinder apparatus should have buffered the sample. Then, we did not make any fO_2 calculations for this study due to the lack of thermodynamic laws for martian melt compositions.

Our experiments were made in Pt capsules without any buffer to control the fO_2 even though some studies have determined the fO_2 prevailing in the martian mantle to be closed to the IW buffer (Wadhwa 2008). Few studies have been dedicated to the investigation of volatile solubilities in such Fe-rich magmas at high pressures and most of them were established in reduced conditions (Ardia et al. 2013; Armstrong et al. 2015). Then, no data in oxidized conditions of a martian basalt in presence of H_2O or S was available. The syntheses of martian analogues in oxidized conditions were supposed to be the first step before the application into reducing conditions. However, problems encountered with the piston-cylinder setup and the difficulties to obtain a glass in such conditions took more time than scheduled. Results obtained from both crystallized and glassy samples with H_2O and S were very interesting and not expected since no data was available to compare with. These unexpected results will be described in the following chapters.

Chapter II: H$_2$O-bearing martian basalt analogues

II.1. Introduction

II.1.1. The origin of water on Mars

The accumulation of volatiles by a planet can be diverse. For Mars, multiple hypotheses for the presence of H$_2$O are possible:
- Wet accretion of chondrite-like materials
- Dry accretion followed by volatile addition through rich materials (e.g., comets)
- Adsorption of proto-solar nebular during accretion

Drake (2005) demonstrated in his study the arguments in favor and against those three possibilities. Actually, these hypotheses are still in debate for all terrestrial planets, even for the Earth. In Drake (2005) study, they have demonstrated that the last two hypotheses (i.e., dry accretion and the adsorption of proto-solar volatiles) were not in accordance with isotopic measurements in martian meteorites and in its atmosphere. Hence, they favored the possibility of a wet accretion. However, these speculations are debated because of the high temperature during the accretion of terrestrial planets that would have removed any volatiles from the planets prior the accretion. On the other hand, Albarède (2009) postulates a dry accretion, the volatiles being supplied during a late veneer episode few million years after the isolation of the Solar System. The late veneer event would imply a chondritic material, enriched in volatiles. However, these studies were most dedicated to estimate the volatile content present on Earth instead of Mars. Due to the lack of data, it is more difficult to decipher which mechanism has dominated for Mars.

II.1.2. Evolution of water

Nonetheless, we know from numerous spatial missions that Mars is not a dry planet. Many evidences of features related to liquid flows and aqueous phases at the surface of Mars led to the conclusion that water was present during the Noachian epoch (3.7 to 4.5 Ga; e.g., Squyres et al. 2004a,b; Tosca et al. 2009). To stabilize liquid water at the surface of Mars, an atmosphere thicker and denser than the present one is needed (Gross et al. 1966; Dreibus and Wänke 1985; Carr 1989; Mangold et al. 2017). Several studies have demonstrated that such primitive atmosphere could be obtained by volatiles degassing from the interior of the planet through volcanism (Grott et al.2001). Indeed, Mars went through an intense volcanic activity during the Noachian (> 3.7 Ga), resulting in large provinces of igneous basaltic rocks covering the surface (Bandfield et al. 2000; McSween et al. 2009; Baratoux et al. 2013; Sautter et al. 2016; Cousin et al. 2017). Among the igneous rocks, sedimentary bedrocks have also been observed from both orbital and lander spatial missions (e.g., Mustard et al. 2008; Dehouck et al. 2014; Ehlman and Edwards 2014; Gellert et al. 2015). The presence of hydrated minerals inside these sedimentary rocks are another clue to the presence of water on Mars. The hydrated minerals detected were mostly phyllosilicates and hydrated sulfates (Carter et al. 2014).

While water has been detected on the surface and near surface, there are also other evidences for the presence of H in the atmosphere and the interior of Mars. Indeed, three hydrogen reservoirs are identified:
- The primordial water, lies in the mantle
- The crustal water, including subsurface ice and near-surface water
- The atmospheric water

The crustal and atmospheric water reservoirs have widely evolved during the geologic times. The atmospheric water endured strong regional and seasonal variations in the H isotopic composition (Aoki et al. 2015; Villanueva et al. 2015). It will represent the interaction between the surface and near-surface waters.

Young meteorites (~0.2 Ga) such like Shergotty and Los Angeles have served as proxy to determine H content in the crustal reservoir (Greenwood et al. 2008). Other minerals such as carbonates, that could retrace fluid fluxes from the Noachian atmosphere, were used to establish the H content (Borg and Drake 2005; Niles et al. 2013). However, multiple results were obtained, which unable a good constrain on the water content in the crustal reservoir.

On the other hand, the primordial water is supposed to have a more stable H content because it was not submitted to important variation. Indeed, plate tectonics seem not to be present on Mars. Then, the water content in the interior was acquired during the differentiation of the planet. The use of more ancient martian meteorites available on Earth, helped to identify the origin of primordial water. From SNC analyses, Alexander et al. (2012) concluded that the martian primordial water was Earth-like and coming from a carbonaceous chondrite-like material, due to the D/H ratio.

Then, numerous clues are available to postulate that water was available at the surface of Mars and may have contributed to the past dense atmosphere of Mars. However, the amount of H_2O degassed into the atmosphere and the amount present at depth remains an open debate. Cumulating the three H reservoirs, it is possible to constrain the H_2O budget of the planet. Since the H present in both crustal and atmospheric reservoirs come from the primordial water in the mantle, it is needed to retrace the H_2O content in this reservoir.

However, the mean to retrace the H_2O budget on Earth cannot be easily applied for Mars. Indeed, even if the two planets show similarities in their size, global chemical composition, Mars is strongly enriched in FeO compared to Earth (Taylor and McLennan 2012). Hence, the thermodynamical laws of volatile behavior established on Earth are susceptible to be different for Mars. Up to now, such atypical igneous rocks have not be strongly investigated in experimental petrology. Hence, in this chapter, the particular dissolution of H_2O in Fe-rich glasses analogues to martian basalts will be studied and discussed. The method employed to synthesize these glasses will be described as well as their characterization by Raman and FTIR spectroscopies.

The second part of this chapter is dedicated to experiments with high H_2O content (> 3 wt %) for the same chemical compositions used to create Fe-rich glasses. The specific characterization of the dendritic textures formed during these experiments will be described. These atypical features may have a strong impact for martian melts.

The coupling of low and high H_2O content experiments in Fe-rich composition will lead to a discussion at the end of this chapter.

II.2. Particular H_2O dissolution mechanism in iron-rich melt: application to martian basaltic melt genesis.

The following results represent an article submitted in June 2019 in Journal of Raman Spectroscopy.

II.2.1. Abstract

Martian basalts are different from Earth by their iron-rich abundance with 18 wt % FeO_{tot} in average for Mars upper crust. The H_2O dissolution mechanism in this atypical melt composition

is not well understood. We have synthesized H_2O-bearing martian basaltic glass analogues (10 < FeO_{tot} < 16 wt %) under high pressures (0.5-1.5 GPa) and temperatures (> 1500 °C) conditions. We used Raman and FTIR spectroscopies to investigate the effect of H_2O as well as the high FeO_{tot} content on the molecular structure of Fe-rich glasses.

Increasing Fe content appears to inhibit the dissolution of H_2O in the melt. In fact, it appears that Free OH groups are formed at relatively low H_2O content in Fe-rich melts (1 wt %) whereas they only appeared at high H_2O content (~6.5 wt %) for Fe-poor glasses. We suggest that the Free OH are bonded to Fe_{2+} cations in the melt forming isolating clusters of $Fe(OH)_2$. Such configurations are suspected to induce an increase in the melt polymerization. The presence of free hydroxyls dissolved in the melt is likely to have a major impact on the genesis of aqueous fluid phase at the surface of Mars.

II.2.2. Introduction

The quantification of the volatile fluxes from a planetary mantle to its atmosphere depends chiefly on the volatile content at the source and their respective solubility in the magmatic system. During volcanic eruptions, for instance, volatile species such as CO_2, H_2O and SO_2 (for the most important) are degassed into the atmosphere. The behavior of volatile species has been widely investigated for the different terrestrial melt compositions: 1) CO_2, H_2O and SO_{42-} for basaltic melt compositions (e.g., Dixon 1991; Dixon and Soltper 1995; Jugo et al. 2005; Moune et al. 2009; Morizet et al. 2010; Shishkina et al. 2014 and many others); 2) CO_2 and H_2O for silica-poor melts (e.g., Brey et al. 1976; Brooker et al. 2001; Moussallam et al. 2014,2016). These studies have led to subsequent solubility models established on various silicate melts (e.g., Papale, 1999; Newman and Lowenstern 2002; Moretti et al. 2003; Papale et al. 2006; Moretti and Baker 2008). While studies have focused their work on the volatile solubility in Earth magmatic systems, only few of them have focused on the solubility of volatile elements in martian magmas to constrain the volatile geochemical cycle of Mars. From geochemical modeling and meteorite analyses, estimations of the H_2O in a martian melt have been proposed although values are very scattered from thousands of ppm to 2 wt % H_2O (Filiberto 2008; McCubbin et al. 2012; Weis et al. 2017).

Martian interior can be characterized by a wide range of redox conditions: from IW (i.e., Iron Wüstite) to above the QFM buffer (i.e., Quart-Fayalite-Magnetite; Wadhwa 2001; Herd et al. 2003; Schmidt et al. 2013). Experimental studies on martian melt were mainly focused on the C behavior under oxidizing and reducing conditions (e.g., Stanley et al. 2011, 2012, 2014; Armstrong et al. 2015). Studies of the crystallization sequence for martian melt analogues in presence of H_2O have been proposed (Médard and Grove 2006; McCubbin et al. 2008; Nekvasil et al. 2009) and the water content determined. However, the H_2O quantification established in those studies cannot reflect the solubility of H_2O in an iron-rich melt. Up to now, there is no experimental study scrutinizing the H_2O dissolution mechanisms in an iron-rich glass (> 10 wt % FeO_{tot}).

The Raman spectroscopy is a dedicated tool used to investigate qualitatively and quantitatively both crystallized and amorphous materials. Spectroscopic studies were achieved to establish calibrations from Raman spectra in crystallized materials (e.g., Noguchi et al. 2009; Kristova et al. 2013; Larre et al. 2018). Many studies on amorphous materials based on the investigation

of CO_2 and S behaviors in a silicate melt have led to subsequent calibrations (e.g. Morizet et al. 2013a, 2017a; Zajacz et al. 2005). Calibrations to quantify the H_2O in melts by Raman spectroscopy have been proposed in Behrens et al. (2006), Mercier et al. (2009), Di Genova et al. (2017), and Schiavi et al. (2018) studies. Nonetheless, the behavior of volatile species dissolved in an iron-rich melt prevailing on Mars has been merely addressed by Raman spectroscopy.

In the present study, we investigated the dissolution behavior of H_2O in an iron-rich melt. We synthesized Fe-rich basalt glasses ($10 < FeO_{tot} < 16$ wt %) under high-pressure conditions (0.5-1.5 GPa) in equilibrium with a H_2O fluid phase (up to 3 wt % starting H_2O content). The results obtained on Fe-rich glasses are compared to a Fe-poor terrestrial basalt analogue ($\sim$ 6 wt % FeO_{tot}). Experiments at high H_2O content (> 6 wt %) have also been performed on the terrestrial analogue composition. The silicate structure of the obtained glasses has been characterized by Raman spectroscopy. Fe^{2+} and FeO_{tot} (total iron) wet chemistry analyses have been realized in order to discuss the interplay of the Fe coordination state and the H_2O dissolution mechanism. The growth of Free OH molecular groups is observed at very low H_2O content in Fe-rich basaltic glasses and the possible impact of these molecular clusters on element transportation within Mars interiors is discussed.

II.2.3. Methods
II.2.3.1. Starting Material

Investigated synthetic compositions were prepared in the SiO_2-Al_2O_3-FeO-MgO-CaO-Na_2O system from a mixture of oxides and carbonate (Na_2CO_3). The Fe-rich synthetic basaltic compositions were made according to basaltic rocks identified at the surface of Mars by the Spirit and Curiosity rovers at Gusev and Gale craters, respectively (Cousin et al. 2017; Mangold et al. 2017). The two Fe-rich synthetic basaltic compositions were prepared with 15.5 and 23.5 wt % FeO and were referred as GC and CL respectively. A natural Popping Rock $2\pi D43$ glass (i.e., PR, $\sim$10 wt % FeO_{tot}; Bézos and Humler 2005) has also been studied to investigate the H_2O behavior in a terrestrial analogue. The glass chemical compositions are reported in Table II.1.

Oxides (wt %)	PR [a]	GC [b]	CL [b]
SiO_2	50.3	48.1	46.5
TiO_2	1.8		
Al_2O_3	14.8	10.2	8.2
FeO	8.8	15.5	23.5
Fe_2O_3	1.3		
MnO	0.2		
MgO	7.7	13.1	9.8
CaO	10.8	8.1	7.6
Na_2O	2.9	4.9	4.3
K_2O	0.7		
P_2O_5	0.3		
Total	99.6	100.0	100.0
NBO/T [c]	0.38	0.56	0.33
$\dfrac{Fe^{2+}}{\sum Fe}$ [d]		0.03 *(1)*	0.02 *(1)*

Notes :

[a] Natural glass of Popping Rock

[b] Synthetic analogues to Martian basalt (> 15 wt % FeO)

[c] Calculated on the basis of Fe in its tetrahedral coordination (i.e. Fe^{3+}), acting as a network former like Si, Al and Ti tetrahedron. NBO/T parameter ranging from 0 to 4. Calculations made on an anhydrous basis

[d] $\dfrac{Fe^{2+}}{\sum Fe}$ Ratio calculated from wet chemistry analyses for decarbonated powders.

Standards errors (1 σ) are reported in brackets at 10^{-2}

Table II.1: Starting compositions for PR (natural glass of Popping Rock) an Earth basalt analogue, CL and GC synthetic martian basalts.

The natural Popping Rock and the synthetic compositions were crushed in an agate mortar for homogenization. Some powders were decarbonated at 850°C for at least 4 hours in a 1 atm furnace (i.e., GCD and PR samples). The wet chemistry results of the starting materials showed that iron is mostly under Fe^{3+} state, Fe^{2+} / $\sum Fe$ at 0.03 and 0.02 for GC and CL starting powders, respectively (see Table II.1). Prior to the high-pressure experiments, the Fe is almost fully oxidized.

The initial degree of polymerization representing the silicate network tetrahedral unit interconnections and calculated according to Brooker et al. (2001), is represented by the NBO/T parameter (i.e., Non-Bridging Oxygen per Tetrahedron) in the Table II.1. For this calculation, Fe is considered as Fe^{3+} in the mixtures and therefore as a network former cation like Si^{4+} or Al^{3+}. The studied compositions have comparable NBO/T with 0.38, 0.56 and 0.33, for PR, GC and CL, respectively; which represents slightly depolymerized composition. In other words,

there is a relatively strong interconnection between the tetrahedral units forming the silicate network.

II.2.3.2. High pressure experiments

Pure distilled H_2O was added with a micro-syringe in several proportions (1.0 to 6.5 wt %) at the bottom of a 10 mm Pt capsule (2.5 - 2.9 mm in diameter) before loading the starting powder. The capsules were welded shut and weighed to check for mass loss before and after the experiment. It should be stressed out that we did not find evidence for weight loss from the recovered capsules after the high-pressure experiments suggesting that 1) there is no elemental escape from the capsule and 2) there is no elemental gain in the capsule; which could be ascribed to elemental diffusion through the capsule walls. Reports of capsule preparation, H_2O content and powder added are listed in the Annex Section of this chapter (Table II.A1).

The experiments were carried out using piston-cylinder apparatus in the pressure range of 0.5-1.5 GPa (equivalent to ~80 – 120 km in depth for Mars) and 1500 – 1600 °C for temperature range. The pressure is applied and transmitted through the assembly and therefore on the sample capsule in an isotropic way. A ¾ inch talc-pyrex assembly was used. Previous work (Kägi et al. 2005) showed that using talc-pyrex assemblies apply intrinsic fO_2 conditions close to QFM+1 buffer. The fO$_2$ was not controlled with a specific buffer in the capsule to simplify the experiment and the resulted products. Temperature was controlled with a B-type thermocouple (PtRh$_6$—PtRh$_{30}$) with an accuracy of ±5°C. The accuracy on pressure was ±10 % and a 10 % friction correction was applied during the experiment (McDade et al. 2002). The run duration varied between 1 and 6 hours. Quenching was achieved by cutting off the power and the quench rate was measured and estimated to be above 80°C/s between 1600 down to 1000 °C. We conducted an isobaric quench resulting in a glass free of bubbles. The excess fluid phase (if present) will be located at the top of the capsule in the case of isobaric quench (Morizet et al., 2002). Several experimental charges did not produce a hiss at capsule opening indicating that these experiments were probably H_2O-undersaturated.

H_2O content and experimental conditions of each experiments are reported in the Table II.2.

II.2.3.3. Analytical methods
Spectroscopic methods

Acquisitions of spectra using the FTIR, were performed in the near IR area between 3000 – 6000 cm$_{-1}$ with a spectral resolution of 4 cm$_{-1}$. Each sample is an accumulation of 100 repetitive scans. The detailed technique of FTIR analyses has been previously addressed in Chapter I.

We used a Jobin-Yvon Labram HR800 Raman spectrometer equipped with a 532 nm solid-state laser. The output power was set at 50 mW to prevent sample damage. The laser power at the sample was estimated at 10 % of the output power, hence at 5 mW. This low power has prevented the degradation of the sample through oxidation, according to Di Genova et al. (2017). We used a grating of 1200 grooves/mm corresponding to a spectral resolution of ~0.8 cm$_{-1}$. The acquisition time was typically 30 sec with 6 repetitive scans. Spectra were acquired

in a non-confocal mode with a slit aperture of 200 µm and a spot size estimated ~1 µm in diameter. A X50 Olympus objective was used. At least 5 spectra were acquired on each sample to investigate the homogeneity of the recovered sample with respect to the dissolved H_2O. The studied spectral range was between 200 and 1250 cm$_{-1}$ and between 2600 and 4000 cm$_{-1}$, covering the area of the silicate network and the H_2O vibrations, respectively.

H_2O dissolved in silicate glasses exhibits Raman vibrations corresponding to the symmetric and anti-symmetric stretch vibrations (v_1 and v_3) of H_2O_{mol} and OH$_-$ represented by an envelope with a peak maximum at ~3550 cm$_{-1}$. A shoulder at 3660 cm$_{-1}$ can be observed and is attributed to Free OH groups vibrations (Mysen and Virgo 1986; Mysen and Cody 2005; Corridoni et al. 2007). We tested several calibrations to quantify H_2O in glasses: Behrens et al. (2006), Mercier et al. (2009), Di Genova et al. (2017) and Schiavi et al. (2018); using the ratio between the HF area (i.e., high wavenumbers) band in the 800 – 1200 cm$_{-1}$ and the H_2O band at 3550 cm$_{-1}$ (Behrens et al. 2006; Di Genova et al. 2017; Schiavi et al. 2018) and the intensity of the same band Mercier et al. (2009). Although, these calibrations were not fully tested to quantify H_2O in Fe-rich basaltic glasses, at a given composition the H_2O content can be compared from one sample to another.

SEM and EPMA analysis

The SEM analyses were performed with a JEOL JSM 5800LV with a beam current at 5 nA and a voltage at 15 kV, at Institut des Matériaux Jean Rouxel of Nantes (IMN, France).

The EPMA analyses were made using a Cameca SX 100 at IFREMER of Brest (France). A spot size of 10 µm and a beam current at 6 nA were chosen for the glass components. The acquisition time was 10 s on the sample and 5 s on the background.

Chemical compositions obtained with both microscopic methods on each sample are reported in the Table II.2. Images from SEM analysis on several samples are exhibited in Annex Section (Fig.II.A1).

We can see in the Table II.2, that the PR-3H-6h sample has experienced a strong Fe loss (2.7 wt % FeO$_{tot}$) during the experiment considering that the FeO$_{tot}$ in the PR composition is ~10 wt %. This Fe-loss has previously been observed (Brugier et al. 2015) and it is known from experimental study that the Fe can form an alloy with the Pt capsule. Even knowing the loss of Fe during experiments, the Fe-enrichment of the capsules has not proven its efficiency either. Then the Fe-loss cannot be accurately controlled in high pressure and temperature experiments. However, all the experiments have experienced depletion with respect to Fe. The following results are then considering the FeO$_{tot}$ after the experiments.

II.2.4. Results
II.2.4.1. Raman spectra

The Raman spectra obtained on H_2O-bearing glasses synthesized at 1 GPa are represented in Fig.II.1A. The Raman spectra were treated with Labspec 6© software and a 5-degree polynomial fit which goes through entrenched points (200 – 250 cm$_{-1}$, ~600, ~800 and > 1150 cm$_{-1}$) to subtract the baseline is used Mercier et al. (2009). The spectra are arranged according to their FeO$_{tot}$. We distinguish two spectral regions: the HF region 800 – 1200 cm$_{-1}$ and the LF

region 200 – 600 cm^{-1}. The 800 – 1200 cm^{-1} region represents the stretching of the silicate network (ν_1). The region between 200 and 600 cm^{-1} in amorphous material is still not well constrained owing to the complexity of the many vibrations occurring and overlapping together. Previous studies (McMillan and Piriou 1982; Mysen et al. 1982: Mercier et al. 2009; LeLosq et al. 2012; Di Genova et al. 2017; Schiavi et al. 2018) have shown that the LF region is a complex combination of several vibrations: bending of tetrahedron from the silicate network (e.g., Al, Si, Ti or Fe in tetrahedral coordination), bending of tetrahedron in relation to cation network modifiers (e.g., Mg, Ca, Na, K and Fe in octahedral coordination), and ring or rocking of tetrahedral structural units.

In Fig.II.1A, we observe that the LF region is more intense than the HF region for the PR-6Hb and PR-3H-6h, with 4.5 and 2.7 wt % FeO$_{tot}$ respectively. On the contrary, the Fe-rich synthetic glasses (e.g., GC-3H-6h, GC-H$_2$O-4h, GCD-3H-6h, CL-3H-6h) show the opposite behavior. In the PR samples (PR-3H-6h and PR-6Hb), the HF region is asymmetric and exhibits three main features: 850, ~1000 and 1050 cm^{-1}. The most intense peak is localized around 1000 cm^{-1}. In the GC samples (GC-H$_2$O-4h and GCD-3H-6h) peaks at 850 and 1050 cm^{-1} are smoothen but distinguishable. An intense peak around 950 cm^{-1} is present for GC synthetic glasses. Finally, for CL-3H-6h, the HF region shape is almost symmetric with an intense peak centered at 950 cm^{-1}. A Lorentzian-shape peak is observed between the LF and HF region a 670 cm^{-1} for the H$_2$O-bearing iron-rich sample CL-3H-6h and the Popping Rock PR-6Hb.
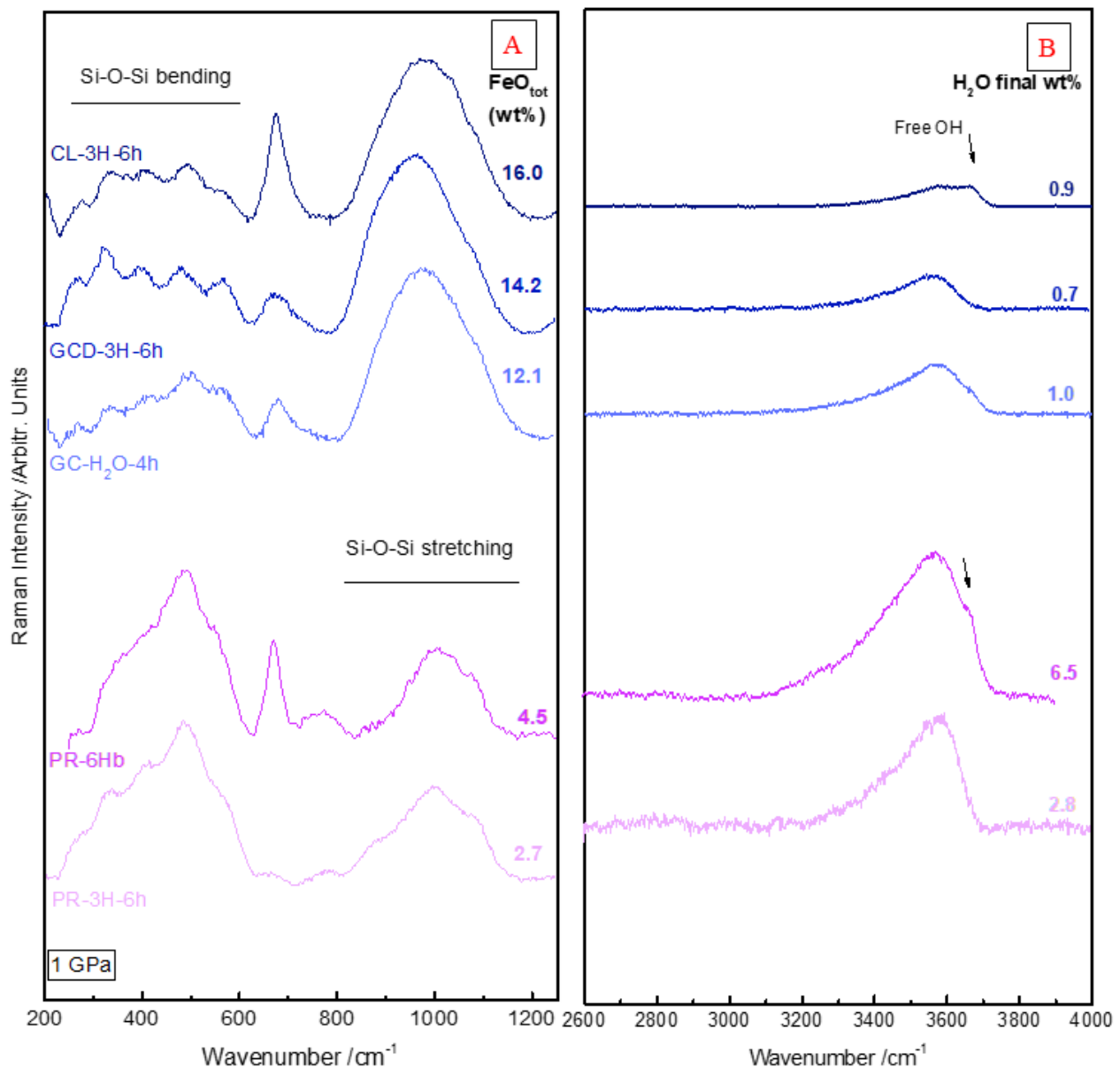
Fig.II.1: A) Raman spectra of the 200 – 1250 cm-1 region for the Fe-poor glasses (PR) and the synthetic Fe-rich glasses obtained at 1 GPa; B) Raman spectra of the same samples in the high frequency region (2600 – 4000 cm-1). Spectra are ranked according to the FeOtot content in the samples. Spectra are normalized to the most intense peak (arbitrary units).

II.2.4.2. H2O quantification by Raman spectroscopy

Raman spectra of glasses synthesized at 1 GPa are shown in Fig.II.1B in the H2O vibration region between 3400 and 3700 cm-1. Raman acquisitions were also performed between 4000 and 4300 cm-1 to investigate the possible presence of H2 at 4135 cm-1 (Freund et al. 1982) but no signal was found. A main broad feature is observed at 3550 cm-1. At 3660 cm-1, we can observe a shoulder only presents for the CL-3H-6h and PR-6H-b samples and is attributed to Free OH species.

The quantification of H_2O in our samples was performed using the calibration of Mercier et al. (2009) and according to the following equation (1):

(1) $H_2O \ (wt \ \%) = \frac{I \ H_2O_{tot}}{I \ HF} \times \frac{1}{a}$

With I H_2O_{tot} the maximum peak intensity at 3550 cm$_{-1}$, HF the intensity taken at 960 cm$_{-1}$ and a the correlation coefficient chosen for a basaltic composition (i.e., 0.26).

Quantifications have been done on at least 5 spectra collected at different location on the sample and on several glass chips. The estimated error on the quantification method is ± 0.4 wt % H_2O Mercier et al. (2009). Therefore, the H_2O errors mentioned in Table II.2 are a combination of 1) the error relative to the H_2O homogeneity in the glass if above the error calibration provided by Mercier et al. (2009), 2) the calibration error (0.4 wt %) if H_2O homogeneity is lower than this value.

In Fig.II.1B, spectra are normalized according to the concomitant HF peak intensity in Fig.II.1A. Hence, we can provide a direct comparison of the H_2O content from one sample to another. The PR glass with 4.5 wt % FeO_{tot}, dissolves 6.5 wt % H_2O and shows the highest peak at 3550 cm$_{-1}$ (i.e., PR-6Hb). The peak intensity is decreasing towards higher FeO_{tot} contents: for the CL-3H-6h (with 16.0 wt % FeO_{tot}) 0.9 wt % H_2O is recovered. The highest 3550 cm$_{-1}$ peak intensity corresponds to the highest H_2O content.

The derived H_2O contents are reported in Table II.2. High water content experiments at 1 GPa have been measured for the PR composition with 4.1 and then 6.5 wt % H_2O dissolved in the melt, with 5.7 and 6.5 wt % H_2O_{ini}, respectively (i.e., PR-6H-4h and PR-6Hb). Experiment with 0.9 wt % H_2O_{ini}, at 1 GPa, has been tested for the GC composition (i.e., GC-1H-4h sample). Almost all the H_2O initially added is recovered in the melt: 0.8 wt % H_2O. Experiments with more than 3 wt % H_2O for the synthetic martian basalt compositions were performed at 1 GPa but no quenched glass could be obtained. At 1.5 GPa, 0.8 wt % H_2O is determined in GCD-3H-6h-1.5GPa, with ~3 wt % H_2O_{ini}. Finally, at low pressure 0.9 wt % H_2O is dissolved in the same starting composition (i.e., GCD).

Samples	GC-H2O-chiller	GC-H2O-4h	GC-3H-6h	GC-1H-4h	GCD-3H-6h	GCD-3H-6h-1.5GPa	GCD-2H-0.5GPa [a]	CL-3H-6h	PR-3H-6h	PR-6H-4h	PR-6Hb [a]
H_2O_{ini} (wt %)	2.6	2.6	2.4	0.9	2.7	3.0	1.9	2.9	2.9	5.7	6.5
$CO_{2\,ini}$ (wt %)	3.5	3.5	3.5	3.5				3.1			
P (GPa)	1	1	1	1	1	1.5	0.5	1	1	1	1
T (°C)	1600	1600	1600	1600	1600	1600	1600	1600	1600	1600	1500
t (h)	1	4	6	4	6	6	6	6	6	4	1
SiO_2	48.6 (8)	50.1 (3)	50.9 (3)	51.1 (3)	48.5 (2)	47.8 (4)	49.4 (2)	50.9 (2)	54.8 (3)	51.2 (3)	51.1 (2)
TiO_2									1.9 (1)	1.7 (1)	1.5 (1)
Al_2O_3	11.5 (5)	10.7 (4)	10.8 (2)	10.6 (2)	10.2 (2)	10.4 (20)	10.9 (1)	8.7 (2)	15.2 (3)	14.5 (3)	14.5 (1)
FeO_{tot}	13.4 (4)	12.1 (3)	10.6 (3)	11.6 (3)	14.2 (3)	14.1 (3)	13.4 (1)	16.0 (4)	2.7 (1)	5.8 (2)	4.5 (1)
MnO									0.1 (0)	0.1 (0)	0.1 (0)
MgO	12.7 (1.0)	12.7 (4)	12.8 (3)	12.9 (3)	12.3 (3)	12.0 (3)	11.3 (1)	10.0 (1)	7.9 (2)	7.4 (2)	8.4 (2)
CaO	5.9 (1)	5.6 (3)	5.9 (2)	6.0 (1)	6.9 (3)	6.6 (2)	7.6 (1)	5.6 (2)	10.7 (2)	10.1 (3)	10.7 (2)
Na_2O	3.6 (3)	4.0 (6)	4.3 (2)	4.5 (1)	4.2 (3)	3.7 (3)	5.1 (1)	4.0 (2)	3.0 (1)	2.5 (1)	3.1 (1)
K_2O									0.7 (0)	0.7 (0)	0.6 (0)
P_2O_5									0.3 (1)	0.3 (1)	0.3 (0)
Total	95.6	95.2	95.3	96.8	96.4	94.7	97.8	95.3	95.2	92.8	93.6
H_2O_{final} (wt %)	1.0 (4)	1.0 (4)	1.5 (4)	0.8 (4)	0.7 (4)	0.8 (4)	0.9 (4)	0.9 (4)	2.7 (4)	4.1 (4)	6.5 (4)
Free OH (%)	6.0	3.0				6.6		17.1			2.0
$\frac{Fe^{2+}}{\sum Fe}$ [b]	0.47	0.49	0.53	0.57	0.37	0.46	0.44	0.58	0.83	0.70	0.82
NBO/T [c]	0.51	0.48	0.52	0.52	0.50	0.46	0.49	1.08	0.53	0.63	0.68

Notes:

[a] Final chemical composition determined by SEM only

[b] $\frac{Fe^{2+}}{\sum Fe}$ Ratio calculated from wet chemistry analyses

[c] NBO/T calculated according to Brooker et al. [18] on an anhydrous basis

Table II.2: Experimental settings for the different samples (P, T, t, H$_2$O content). Chemical compositions of the samples determined by EPMA and SEM analyses. Final content of H$_2$O and FeO$_{tot}$ are also reported, associated with wet chemistry results. The Free OH percentages are added for samples presenting the features at 3660 cm$_{-1}$. The calculation of Free OH percentages is made on the deconvolution of the H$_2$O area. Detailed of deconvolutions are reported in the Table II.A2 (Annexes section). Standards errors (1 σ) are reported in brackets at 10$_{-1}$. The associated standard errors of wet chemistry measurements are 0.01.

II.2.4.3. FTIR versus Raman for H$_2$O quantification

FTIR spectroscopy has been conducted on several glass samples in order to investigate the applicability of the Mercier et al. (2009) calibration on Fe-rich basalts. Not all samples could be analyzed by FTIR because of 1) sample size (small glass chips < 1mm); 2) quenched crystals at the rim of the samples. Only pure glass chips with a size > 2 mm have been analyzed: GC-3H-6h, GC-1H-4h, GCD-3H-6h, PR-3H-6h, PR-6H-4h and PR-6Hb. The determination of water content by FTIR follows the Beer-Lambert equation (Dixon and Stolper 1995; Morizet et al. 2010):

$$(2)\ C_{H_2O} = \frac{100 \times MM \times A}{d \times \rho \times \varepsilon}$$

Where C is the H$_2$O$_{mol}$ or OH$_-$ content in wt %, A the height of the band for OH$_-$ (4500 cm$_{-1}$) or H$_2$O$_{mol}$ (5200 cm$_{-1}$), MM the molar mass in g/mol for H$_2$O, d the thickness in cm, ρ the density in g/L and ε the linear molar absorption coefficient in L/mol/cm.

In the Fig.II.2, an example of a IR spectrum is showed. In this spectrum, the 4500 and 5200 cm$_{-1}$ bands are exhibited for GC-3H-6h sample.
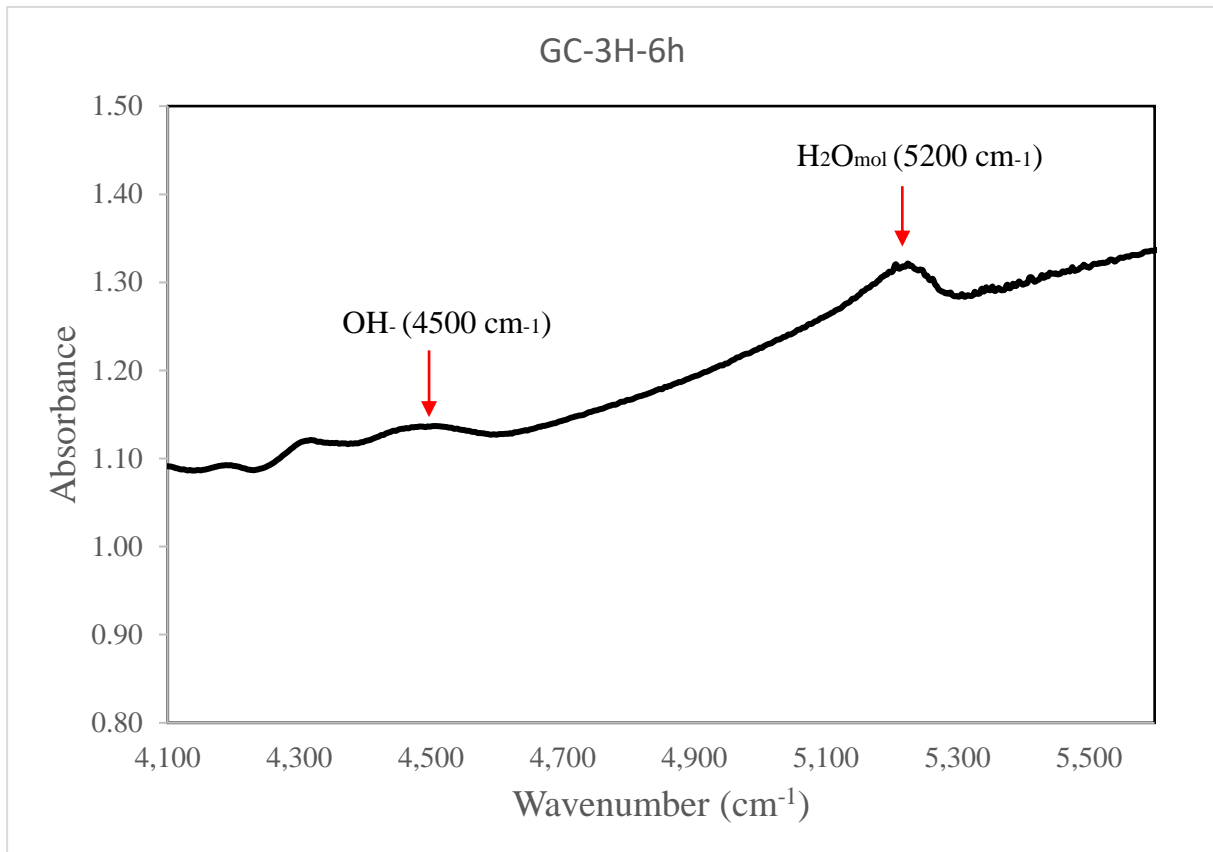
Fig.II.2: IR spectrum obtained on GC-3H-6h sample showing the OH$_-$ and H$_2$O$_{mol}$ bands used for H$_2$O quantification.

Coupled to the H$_2$O signal between 4500 and 5200 cm$_{-1}$, no H$_2$ was detected at 4100 cm$_{-1}$ (Colomban et al. 2013; Schmidt et al. 1998), which is consistent with the absence of H$_2$ signal in Raman spectra.

For PR samples, we used the extinction coefficients derived from Ohlhorst et al. (2001) 0.56 L/mol/cm for both the peak at 4500 and 5200 cm$_{-1}$. For our Fe-rich we used the extinction coefficient given by Stolper (1982) considering that the studied basalts are closer in composition to ours. The molar absorptivity coefficients are 0.98 and 1.76 L/mol/cm for 4500 and 5200 cm$_{-1}$, respectively.

Glass density measurements were not possible considering the size of our glass chips. It was calculated using the calibration of Schiavi et al. (2018); which takes into account the chemical composition and is applicable to Fe-rich glass compositions. Results from subsequent measurements are shown in Fig.II.2 and in Table II.3.

In Fig.II.2A, we observe that the H$_2$O quantified with Mercier et al. (2009) provided better correspondence to the FTIR results. At low H$_2$O content, for Fe-rich glasses, the H$_2$O quantification by Mercier et al. (2009) is close to the 1:1 line (see Fig.II.2B). As an example, for the GC-3H-6h sample, 1.4 wt % and 1.5 wt % H$_2$O are determined by FTIR and Raman, respectively. At higher H$_2$O content (> 2 wt %), the results are more scattered, but still in reasonable agreement with the FTIR results. For the water-rich sample (PR-6Hb), 6.9 wt % H$_2$O is determined by FTIR, where 6.5 is calculated by the method of Mercier et al. (2009).

There is a strong discrepancy for PR-6H-4h with 4.1 wt % H_2O determined by Raman whereas 6.1 wt % is determined by FTIR. However, this sample has the highest error bar due to possible heterogeneity in the H_2O distribution with the glass, even though no crystallisation is observed in SEM analyses (see Fig.II.A1, representing PR-6H-4h sample in the Annex Section).

In Fig.II.3, the calibration provided by Behrens et al. (2006) slightly overestimates the water content for Fe-rich glasses at low H_2O content. For GC-1H-4h, 1.1 wt % H_2O is quantified with Raman and 1.0 wt % by FTIR; although 0.9 wt % H_2O was initially added before the experiment. The discrepancy becomes more important at high H_2O content in PR-6Hb glass: 8.1 wt % H_2O by Raman with 6.5 wt % H_2O_{ini}. However, it should be emphasized that the calibration is accurate to 4.7 wt % H_2O; and at higher content, the error in determining the amount of H_2O will be larger.

The calibration established by Schiavi et al. (2018) shows good results for low H_2O content in Fig.II.3A with 0.7 wt % for GC-1H-4h against 1.0 wt % H_2O by FTIR. However, with increasing H_2O content (Fig.II.2B), there is an increasing deviation with the FTIR results. This difference can be ascribed by the high Fe content of basalts in Schiavi et al. (2018) (FeO_{tot}, > 7 wt %) compared to our Fe-poor basalts (< 6 wt % FeO_{tot}).
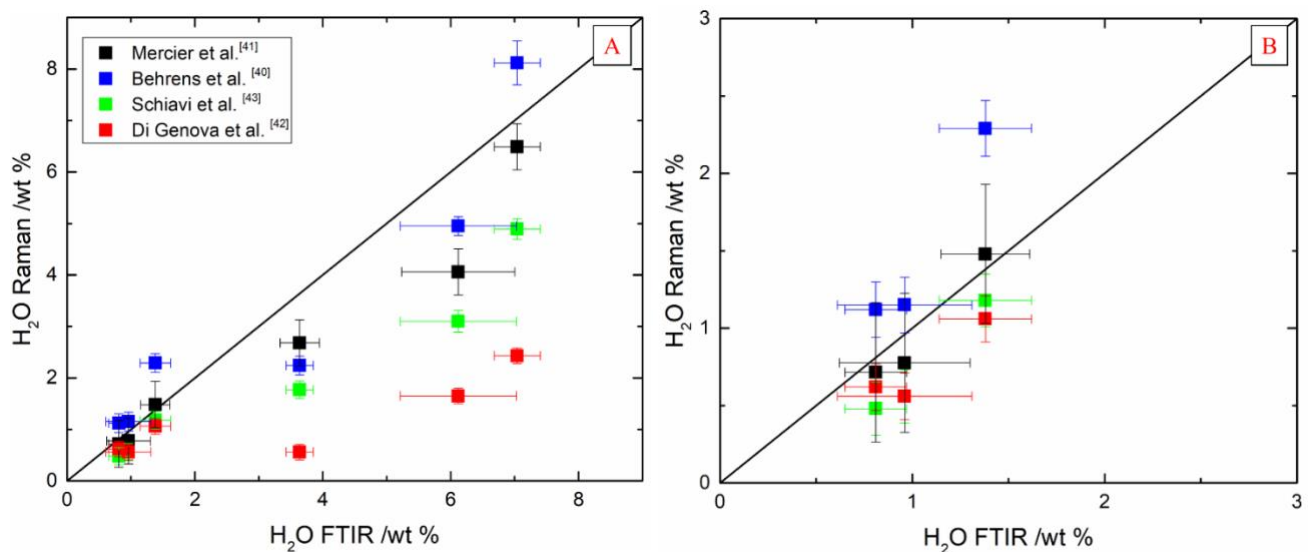
Fig.II.3: A) H_2O quantifications by FTIR against calibrations established by Raman spectroscopy for Mercier et al. (2009) in black, Behrens et al. (2006) in blue, Schiavi et al. (2018) in green and Di Genova et al. (2017) in red. Error bars reported are the error from the homogenization of the sample when it is above the calibration error of each study; B) Zoom of the Fig.II.3A at small H_2O content (< 3 wt%) for the Fe-rich samples.

We also compared the FTIR results with the calibration established by Di Genova et al. (2017) for Fe-rich glasses. We can see that the calibration does not seem accurate for terrestrial basalt glasses as shown in Fig.II.3A, where the results are at least 2 wt % below the FTIR results (see Table II.3). On the other hand, in Fig.II.3B we can see that the calibration is better suited for Fe-rich glasses; however, the results are still less in accordance with the FTIR compare to Mercier et al. (2009).

The comparison provided in Fig.II.3 suggests that we can reasonably assess that the Raman calibration established by Mercier et al. (2009) is more appropriate to quantify H_2O in our Fe-rich and Fe-poor basaltic glasses. The results from all H_2O quantifications by IR and Raman spectroscopies are reported in the Table II.3. However, there is still a matter of discussion on whether one calibration is applicable to a given composition (i.e. Fe-rich glasses) or not. At low H_2O content (< 2 wt %), as shown in Fig.II.3B, all calibrations are in reasonable agreement and can be used to determine the H_2O content in Fe-rich silicate glasses.

	PR-3H-6h	PR-6H-4h	PR-6Hb	GC-3H-6h	GC-1H-4h	GCD-3H-6h
ε_{4500} *	0.56 a	0.56	0.56	0.98 b	0.98	0.98
ε_{5200}	0.56	0.56	0.56	1.76	1.76	1.76
Density ** (g/L)	2789	2765	2722	2815	2832	2833
H_2O wt % (FTIR)	3.6 (3)	6.1 (9)	6.9 (4)	1.4 (2)	1.0 (3)	0.8 (2)
Analysis number	8	6	7	3	4	5
H_2O from Raman spectroscopy (% wt):						
Mercier et al. (2009)	2.7 (4)	4.1 (4)	6.5 (4)	1.5 (4)	0.8 (4)	0.7 (4)
Behrens et al. (2006)	2.2 (2)	5.0 (2)	8.1 (4)	2.3 (2)	1.1 (2)	1.1 (2)
Di Genova et al. (2017)	0.6 (2)	1.7 (2)	2.4 (2)	1.1. (2)	0.6 (2)	0.6 (2)
Schiavi et al. (2018)	1.4 (1)	3.0 (1)	4.9 (3)	1.4 (2)	0.7 (2)	0.7 (2)

Notes :

* : extinction coefficient L/mol/cm

** : calculated according to Schiavi et al.(2018)

a: From Ohlhorst et al. (2001)

b: From Stolper (1982)

Table II.3: FTIR and Raman H_2O quantifications. Description of the parameters chosen for FTIR calculations. Standard deviations on H_2O quantification are attributed to either: 1) the error on the Raman calibrations or 2) the H_2O homogeneity in the sample (i.e., when the standard deviation in H_2O quantification is higher than the error from the calibration)

II.2.5. Discussion
II.2.5.1. H_2O content in Fe-rich basalts

Differences between H_2O dissolved in the melt and H_2O_{ini} can be observed for PR samples (Table II.2). For 5.7 wt % H_2O added in PR-6H-4h experiment, less than 4 wt % H_2O is dissolved. For 6.5 wt %, ~6.5 wt % H_2O is recovered in the PR glass. Under these conditions (i.e. 1 GPa), H_2O solubility is close to 7 wt % (Newman et al. 1999). The difference between initial and final amount of H_2O for PR glasses can be explained by the thermodynamic equilibrium of the H_2O species in the liquid and fluid phase (Papale 1999); by extension, there is a partitioning of H_2O between the fluid phase and the melt phase.

Some mixtures were not decarbonated and CO_2 was present in the fluid phase during the experiments. However, after the experiments, no CO_3^{2-} signal at 1080 cm^{-1} was observed with Raman spectroscopy (Morizet et al. 2013a), implying that only hundreds ppm of CO_2 could be dissolved. It is consistent with previous studies that estimated the CO_2 solubility in these iron-rich melt at ~0.3 wt % under oxidized conditions (Stanley et al. 2011, 2012).

The presented results in Fig.II.1B and Table II.2, suggest that increasing Fe content will induce a substantial decrease in the H_2O dissolution. For instance, if we compare the PR-3H-6h and GCD-3H-6h samples with 2.9 and 2.7 wt % H_2O_{ini}, the total H_2O dissolved in the melt is 2.8 and 0.7 wt % H_2O, respectively. For those two experiments made at identical intensive conditions and with no CO_2 present, there is a difference of ~2 wt % between H_2O dissolved, and the H_2O initially loaded in the sample charge. The most likely hypothesis to explain this difference is the change in the Fe content: ~13 wt % for GC samples and 5 wt % FeO_{tot} for PR. We have presented the H_2O dissolved as a function of the FeO_{tot} for 1 GPa experiments in Fig.II.4. We observe a decrease of the H_2O content from 6.5 wt % H_2O at 5 wt % FeO_{tot} for PR-6Hb, to less than 1 wt % at 16 wt % FeO_{tot} for CL-3H-6h (see Table II.2). Hence, increasing the FeO_{tot} in the melt composition seems to hamper the H_2O dissolution. Even though the studied melt compositions of Hou et al. (2018) are richer in Fe than ours, they investigated the immiscibility of an Fe-rich melt in presence of H_2O and observe a subsequent decrease of H_2O dissolution with increasing Fe content.
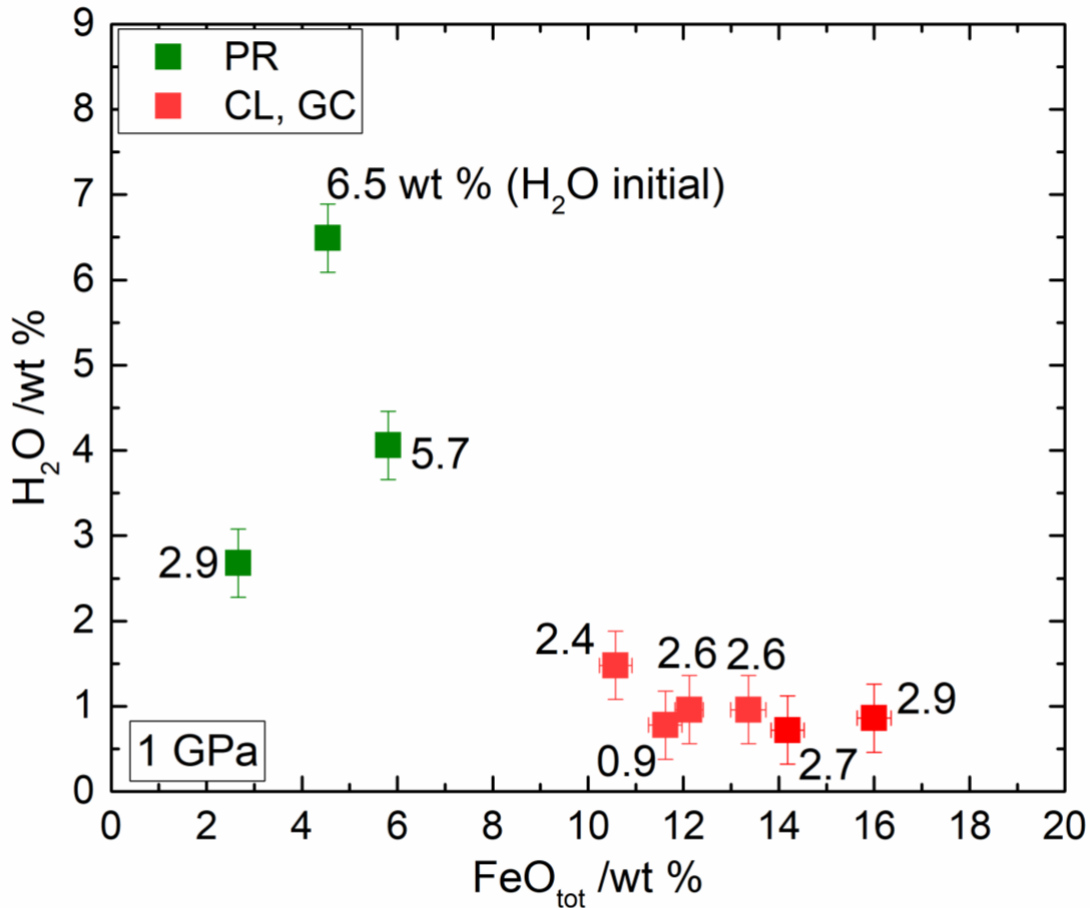
Fig.II.4: H_2O dissolved in the melt versus the FeOtot measured by EPMA analysis in our samples at 1 GPa. The H2Oini content is also reported.

The calibration established by Raman spectroscopy to quantify H_2O can be user- and composition-dependent. However, we suggest that our values can be representative of the real H_2O dissolved in our glasses; especially at the lowest H_2O content. Indeed, Di Genova et al. (2017) have shown that the presence of nanolite of Fe^{3+} in Fe-rich composition can provoke some differences in the H_2O quantification compared to nanolite-free samples. In this study, small quench crystals were observed in the rim of glasses for the following samples: CL-3H-6h, GCD-3H-6h, GC-H2O-chiller, GC-3H-6h. From the Fig.II.3, we can see that the FTIR measurements are in good accordance with the method of Mercier et al. (2009) to quantify H_2O. Then we can assume that quantifications established on the FTIR samples are correct. We performed FTIR on two samples presenting rims quenched crystals. We can see from Fig.II.3 that the results are still good and in accordance with the Raman spectroscopy calibration. Since there is currently no study attesting that the H_2O quantification can be underestimated for such glasses by FTIR, we can assume that our H_2O content is correct with this method. According to Di Genova et al. (2017), an underestimation of H_2O content can be expected due to the presence of nanolites. During our Raman acquisitions, we make sure to investigate only glass component. Coupled to SEM images, were the crystals are almost invisible, we obtained a homogenized chemical composition. Then, partitioning of H_2O between crystals and the melt

seems unlikely. In addition, the small needle-shape size (nm) of the crystals make their identification impossible by Raman spectroscopy. This peculiar shape is characteristic of quench phases; that should not alter the glass composition. Then, we can postulate that the H_2O content obtained in the four samples (CL-3H-6h, GCD-3H-6h, GC-H_2O-chiller, GC-3H-6h) are reliable.

Although we did not observe any variation in the mass of the Pt capsules after experiments, there is a possibility for additional H_2O to be formed from the diffusion of hydrogen through the capsule walls. In that case, the formation of H_2O during the experiment could be possible due to O_2 produced by reduction of Fe_{3+} to Fe_{2+} during the experiment. From wet chemistry measurements, we can see that part of the initial Fe_{3+} is converted into Fe_{2+}. Hence, following the reaction below, O_2 will be formed in the fluid phase:

(3) $Fe_2O_3^{melt} = 2FeO^{melt} + \frac{1}{2}O_2^{fl}$
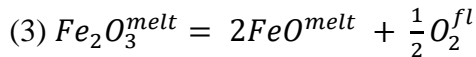
It is possible that H_2 diffuses into the Pt capsule, even though the pyrex of the talc-pyrex assembly is supposed to prevent it acting as a shield (Brooker 1998). The H_2O formation with H2 diffusion follow the reaction:

(4) $H_2^{fl} + \frac{1}{2}O_2^{fl} = H_2O^{melt}$
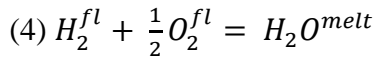
This H_2O could contribute to total H_2O dissolved in the glass. Therefore, the total available H_2O during the experiment would be higher. Such a case will reflect an even lower capability for Fe-rich glasses to dissolve within its structure. A simple calculation based on the change in Fe redox state leads to a possible increase in the H_2O content of less than 0.5 wt %, which is within the possible error in the H_2O determination.

II.2.5.2. Peculiar H_2O dissolution mechanisms in Fe-rich basalt

Previous spectroscopic investigations (Mysen and Virgo 1986; Dixon and Stolper 1995; Mysen and Cody 2005; Ohlhorst et al. 2001) have shown that H_2O can dissolve in silicate glasses as two main species: 1) hydroxyl groups (i.e., OH) or 2) molecular H_2O (i.e., H_2O_{mol}). At low H_2O content, OH is the predominant species to be formed in silicate glasses owing to the water dissociation reaction:

(5) $H_2O^{melt} + O^{2-melt} \rightarrow 2OH^{-\ melt}$
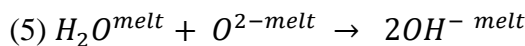
For instance, this dissolution mechanism induces a depolymerization of the silicate network through the formation of silanol groups (SiOH):

(6) $Si - O - Si^{melt} + H_2O^{fl} \rightarrow 2\ SiOH^{melt}$
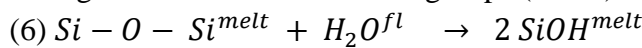
At higher H_2O content, the H_2O dissolves as a molecular species (H_2O_{mol}) and becomes the predominant species (i.e., OH species remain almost constant) according to the following reaction:

(7) $H_2O^{fl} = H_2O^{melt}$
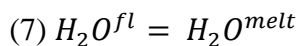
An additional H_2O dissolution mechanism has been inferred in recent studies based on Raman and NMR spectroscopic results (Xue et al. 2004; Mysen and Cody 2005) and corresponds to the formation of Free OH groups. With opposition to the first mechanism, the formation of Free OH will induce a polymerization of the silicate melt structure as the network modifying cation charges are consumed by the OH- negative charges according to the following equation (8):

(8) $2Si - O^- M^{n+} + H_2O^{fluid} \rightarrow Si - O - Si + M^{n+}OH^n$
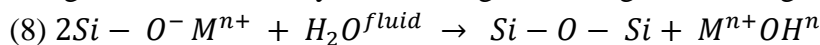
With M for cations (i.e., Ca, Mg, Fe) and n representing the charge of the cation. It has to be noted that, the example of Si has been taken to simplify the changes occurring with H_2O dissolution mechanism. The equation (8) could easily be rewritten using the others network former cations (i.e., Al_{3+}, Fe_{3+}).

A shoulder at 3660 cm-1 corresponding to Free OH vibrations (Mysen and Virgo 1986; Corridoni et al. 2007) is observed for the Fe-rich glass (CL-3H-6h) and the water-rich terrestrial analogue (PR-6Hb) in Fig.II.1B. Coupled with the shoulder at 3660 cm-1, a peculiar peak at 670 cm-1 has been detected for those two spectra (Fig.II.1A) with a Lorentzian shape. The occurrence of the 3660 and 670 cm-1 peaks appear correlated, although the assignment of the 670 cm-1 peak to a peculiar vibration remains to be determined. In the study of Di Genova et al. (2017), Raman spectra acquired on Fe-rich basaltic glasses exhibit a specific peak at ~690 cm-1 that is correlated with nanolite particles due to high Fe content, but also due to high H_2O content. Furthermore, we have noticed that some other experiments showed the same peaks: GC-H_2O-chiller, GC-H_2O-4h and GCD-3H-6h-1.5GPa.

To determine the proportion of the 3660 cm-1 peak, we carried out spectrum simulation using 4 peaks: 3 Gaussians and one Voigt (combination of a Gaussian and a Lorentzian component). Values of simulations are reported in the Supporting Information in Table II.A2. Typical simulations for PR-6Hb and CL-3H-6h are shown in Fig.II.5. In the simulations in Fig.II.5, CL-3H-6h sample exhibits ~17 % of Free OH and only 2 % is calculated for PR-6Hb.
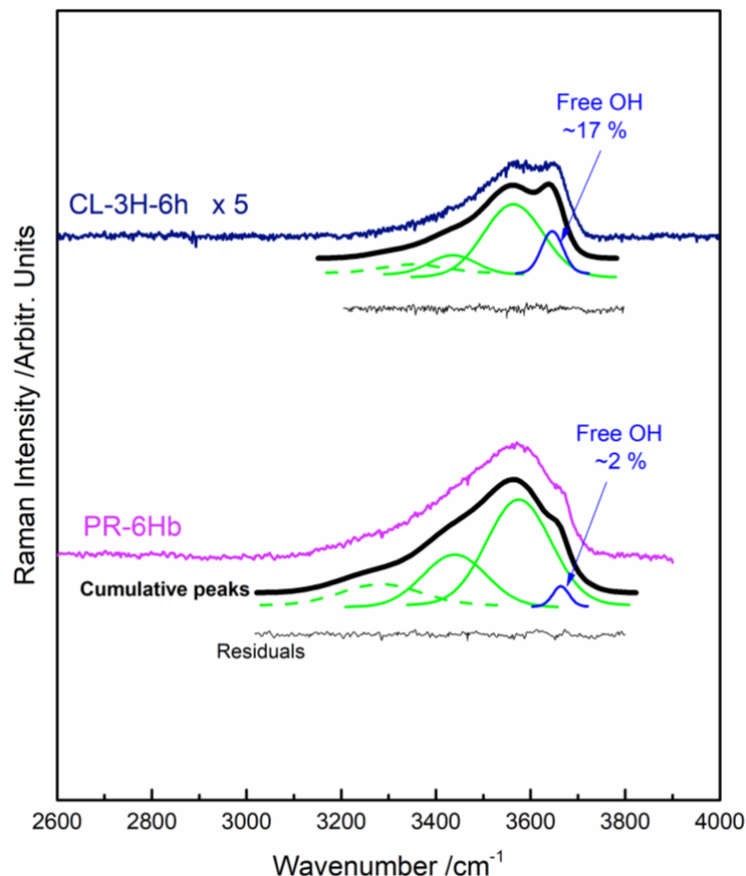
Fig.II.5: Deconvolution of the H_2O region (2600 – 4000 cm-1) for CL-3H-6h and PR-6Hb samples. In blue is highlighted the Free OH area. The CL-3H-6h sample has been increased x5 for clarity.

In Fig.II.6A, we have reported the proportions of Free OH as a function of the proportion of the 670 cm$_{-1}$ peak (i.e., 670* corresponding to the ratio between the 670 cm$_{-1}$ area and the total area of H_2O) for the samples: CL-3H-6h,PR-6Hb, GC-H_2O-chiller, GC-H_2O-4h and GCD-3H-6h-1.5GPa. Each data reported in this graph corresponds to the proportion determined from the simulation of a given spectrum. In Fig.II.6A, we observe a correlation between the percentage of Free OH and the 670 cm$_{-1}$ peak. The increase of the 670 cm$_{-1}$ is correlated to an increase in Free OH. For PR-6Hb, we measure the 670*= 6 % and Free OH= 2 %. For CL-3H-6h, we obtain 670* ~60 % and 20 % of Free OH.

In Fig.II.6B, the Free OH percentages are represented against the FeO$_{tot}$. The Free OH fraction appears also correlated to the FeO$_{tot}$ in the sample. The Fe-rich sample, CL-3H-6h with 16.0 wt % FeO$_{tot}$, presents ~17 % of Free OH. The GC and GCD samples exhibit values from 3 to 7 % of Free OH, with ~12 and ~14 wt % FeO$_{tot}$, respectively. On the other hand, PR-6Hb with 4.5 wt % FeO$_{tot}$, shows only 2 % of Free OH.

Di Genova et al. (2016) demonstrate that the 690 cm$_{-1}$ peak is attributed to magnetite nanolites. For instance, the Raman spectra of magnetite (Fe-OH component) and portlandite (Ca-OH) taken from the RRUFF database exhibit the same Raman signature at ~670 cm$_{-1}$ as in our glass samples. It seems that multiple parameters are controlling the occurrence of these two correlated peaks (i.e., 670 and 3660 cm$_{-1}$), such as the H_2O and FeO content, but also the Fe redox state. Further investigation is needed to understand these atypical features developing at low H_2O content in Fe-rich glasses.
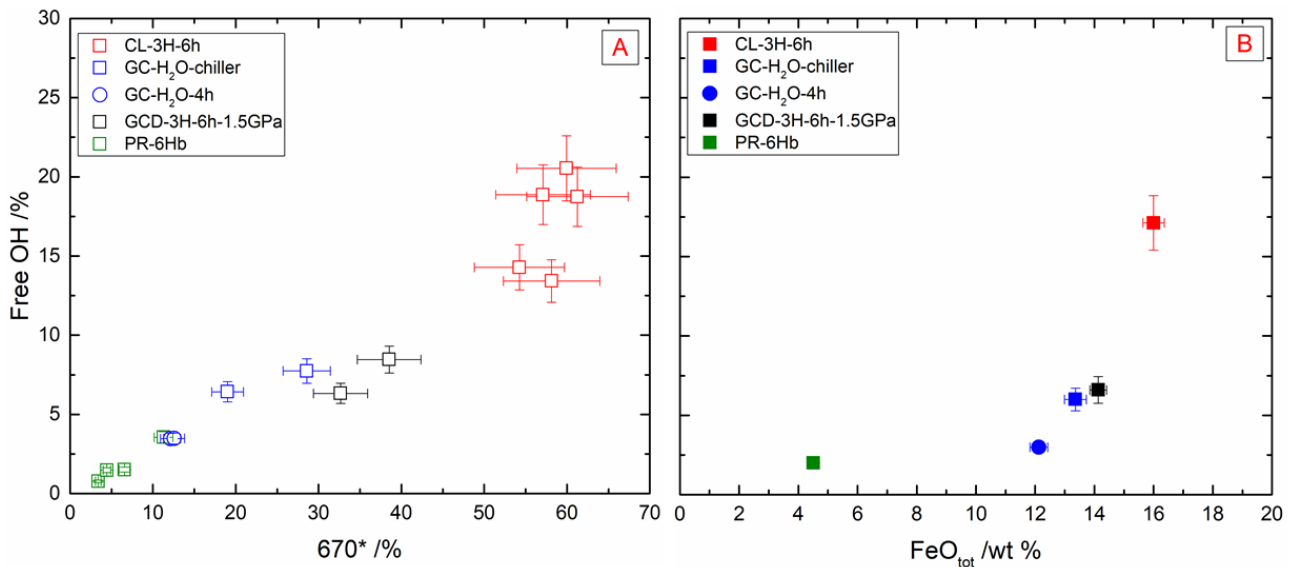
Fig.II.6: A) Percentage of Free OH (i.e., A$_{3660}$/A$_{H2Otot}$; with A the area from deconvolution of the 3660 cm-1 and the water band from 3000 to 4000 cm$_{-1}$) versus the percentage of the 670 cm$_{-1}$ peak (i.e., 670*) normalized by the total H_2O area (A$_{H2Otot}$); B) Free OH percentages in function of the total iron content (FeO$_{tot}$).

Previous works have shown that the formation of Free OH is observed 1) when H_2O is dissolved in a strongly depolymerized composition (Hou et al. 2018), 2) with high H_2O concentrations (Mysen and Virgo 1986), and 3) in aqueous solutions (Corrdioni et al. 2007).

The presence of Free OH is rather surprising in Fe-rich glasses investigated here. This glass composition is not strongly depolymerized (i.e., NBO/T <1) and the total H_2O content does not exceed 1 wt %. One possible reason for the existence of Free OH groups in Fe-rich glasses could be ascribed to the structural role of iron within the glass. Recovered Fe-rich glasses (i.e., GC and CL) from high pressure experiments have a Fe ratio between $Fe^{2+} / \sum Fe = 0.4$ and 0.6, respectively (see Table II.2) suggesting that Fe plays a network modifying role (Mysen 1991) within the glass when under its Fe^{2+} state. Although additional work is clearly needed to better characterize the correlation between the Free OH groups and Fe redox state; it is possible that Fe^{2+} has a high affinity to form isolated complexes with OH^-.

The observation of Free OH in Fe-rich melt at low H_2O content (~1 wt %) has implications on the mineralogical composition at the Mars surface. The formation of Free OH molecular clusters could constitute a precursor for an immiscible Fe-rich phase; in a similar manner to the immiscibility observed between carbonatite and silicate melts owing to the formation of Free carbonates (Morizet et al. 2017b). Previous spatial missions identified multiple forms of Fe-oxides, mostly hematite and magnetite at the surface of Mars (Morris et al. 2004; Bribing et al. 2006; Le Deit et al. 2008). The separation of $Fe-(OH)_2$ rich phase could favor the formation of Fe-oxides by weathering of the basalt at the surface.

II.2.5.3. Evolution of the silicate network signature as a function of the Fe redox state estimation

The presence of Free OH should induce a change on the overall silicate network considering that Fe^{2+} cations are scavenged by the OH species. Therefore, the deficit of positive charges from the network modifying cations should induce an increase in the degree of polymerization according to the reaction (9):

(9) $2O^{NBO\ melt} + Fe^{2+melt} + H_2O^{melt} = 1O^{BO\ melt} + Fe(OH)_2^{melt}$
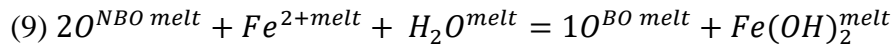
Where O_{NBO} and O_{BO} are a Non-Bridging Oxygen and Bridging Oxygen from a tetrahedral Q_n species, respectively. This reaction is equivalent to Eq. 8 and shows that Q_n species proportions should decrease in proportion due to the formation of Free OH clusters that uses an available NBO and a more polymerized Q_{n+1} species is formed. For instance, Q_3 species should merge to form Q_4 species upon the dissolution of water as Free OH clusters. This change is likely to be observed by Raman spectroscopy.

The HF region is a composition of several Gaussians peaks (Mysen et al. 1982) referred to a Q_n species with, n the number of bridging O varying from 0 to 4. Each Q_n species will represent a network former cation (Si, Al, Fe^{3+}) linked to an oxygen. We conducted spectrum deconvolution of the HF region that are exhibited in Fig.II.7. The results from the deconvolutions are reported in the Table II.A2 (Annex section). The deconvolutions of the Raman spectra for PR-6H-4h, GCD-3H-6h and CL-3H-6h (i.e. synthetic martian basalts) are reported in Fig.II.7. Although the attribution of Q_n species can be debated, we assumed these positions according to Rossano and Mysen (2012) and references therein. Hence, we attributed: Q_4 at 1080 cm-1, $Q_{Si-O-Si}$ at ~1020 cm-1, Q_3 at ~950 cm-1 and Q_2 at ~880 cm-1. The $Q_{Si-O-Si}$ corresponds to the vibration of the interconnected oxygen between two tetrahedral Q_n units as stated in previous studies (Mysen and Frantz 1994; Frantz and Mysen 1995); although, Trcera et al. 2010 assigned it to Q_3 species. Considering the work of Micoulaut et al. (2005) and Mysen

(2014), and the low NBO/T of our glasses (i.e., < 1), Q_1 species cannot be present. Indeed, all the Q_n species that can be present are following the equilibrium (Mysen and Frantz 1994):

(10) $2Q^{n\ melt} = Q^{n+1\ melt} + Q^{n-1\ melt}$

Hence, with the calculated NBO/T and H_2O present in our basaltic glasses (both Fe-rich and Fe-poor), Q_1 species cannot be attributed in the deconvolution shown in Fig.II.6.
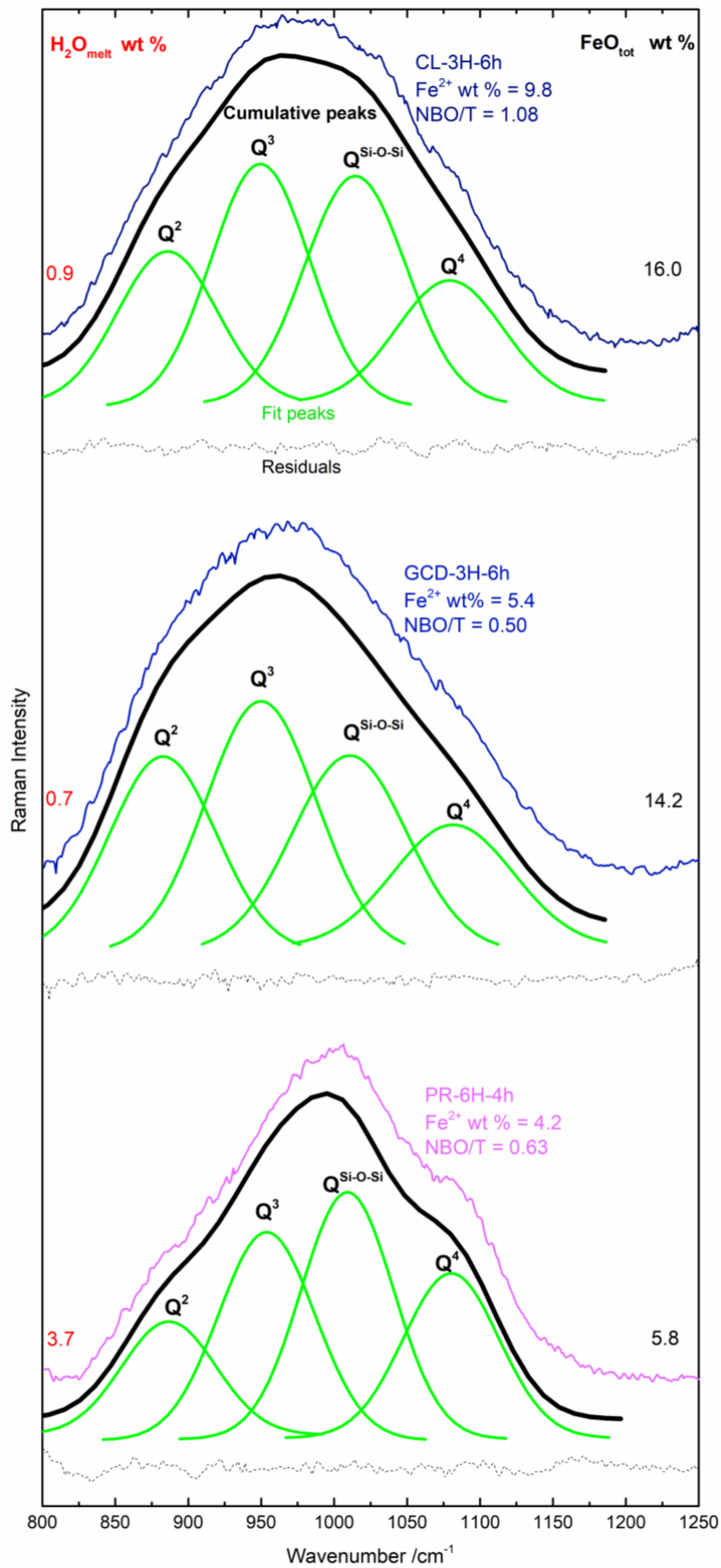
Deconvolution of the high frequency region (i.e., HF; silicate matrix signal) for CL-3H-6h, GCD-3H-6h and PR-6H-4h. Gaussian lines are in green, cumulative peaks of the Gaussian lines are the black and the residuals from simulations is the black dotted lines. H_2O and FeO_{tot} final content for each experiment are localized next to their respective spectrum. The Fe_{2+} content is given for each sample. Spectra are normalized to the most intense peak (arbitrary units).

For the PR-6H-4h sample, the deconvolution shows that the Q_4 (~1080 cm-1) is the most intense peak compares to the same Q_n species for GCD and CL samples. On the opposite, Q_2 species is more intense for GCD and CL. Di Genova et al. (2016) have experimented Fe-rich glasses obtained at 1 atm. In the Raman spectra analyses of these glasses, they stated that the 950 cm-1 peak is attributed to the occurrence of Fe_{3+} in the melt. Our Fe-rich glasses exhibit ~50 % of Fe_{3+}. Then, it is possible that the 950 cm-1 peak is the vibration of Fe_{3+} tetrahedron.

The presence of high Fe_{2+} content should enhance the depolymerization on the structure considering Fe_{2+} cation as a network modifier. It is confirmed with the deconvolution of the GCD glass in Fig.II.6. We can see that the iron-rich composition (CL sample) is richer in Fe_{2+} species (9.8 wt %) in comparison with the PR sample at ~4.2 wt % Fe_{2+}. The decrease of Q_4 intensity with respect to Q_2 species when increasing Fe_{2+} is observed from PR to GC and CL. Hence, a depolymerization is observed with the deconvolutions for the Fe-rich composition (Fig.II.7).

When looking at the calculated NBO/T (anhydrous basis), and whether Fe_{2+} or Fe_{3+} is the major component (according to wet chemistry) exhibited in Fig.II.6, there are some differences. PR-6H-4h is the most reduced compared to GCD and CL (the NBO/T considers Fe_{2+} as the main specie of Fe); hence the NBO/T = 0.6. For the GCD sample, Fe_{3+} is predominant and NBO/T = 0.5. Finally, CL-3H-6h is more reduced than GCD with $Fe_{2+}/\sum Fe = 0.6$; thus NBO/T = 1.1. It is rather surprising that the CL sample has the most depolymerized structure according to the NBO/T (more depolymerized than GCD) compared to the opposite observation on deconvolution in Fig.II.7. Indeed, there seems to have a decrease in Q_2 intensity with the increase of Q_3 and $Q_{Si-O-Si}$, even though the latter cannot traduce the polymerization degree of the melt. The polymerization observed could be ascribed to the formation of Free OH clusters in this sample.

From Fig.II.8, we wish to discriminate the possible effect of Free OH and in relation with Fe_{2+} local environment on the degree of polymerization. We expected a measurable effect of the Free OH on the polymerization degree: increasing the Free OH will increase the degree of polymerization according to Eq. 9. As observed in Fig.II.8, the presence of Free OH species seem to have a limited effect on the degree of polymerization. The data points in Fig.II.8A for Free OH bearing sample are aligned to the general trend of the effect of Fe_{2+} on the degree of polymerization. For instance, for GCD-3H-6h without Free OH and GCD-3H-1.5G with Free OH, we observe a Q_4 proportion of 0.18 and 0.19, respectively. The same applies for the Q_2 proportion in Fig.II.8B. Deconvolutions of the Q_3 and $Q_{Si-O-Si}$ represented in function of the Fe_{2+} content are reported in the Annex Section in Fig.II.A2.

Several aspects could explain the absence of effect shown in Fig.II.8: 1) the abundance of Free OH is too low for an effect to be seen on the degree of polymerization, 2) it is also possible that the Free OH species are not exclusively linked to Fe_{2+} and other cations such as Mg_{2+} and Ca_{2+} form Free OH clusters.
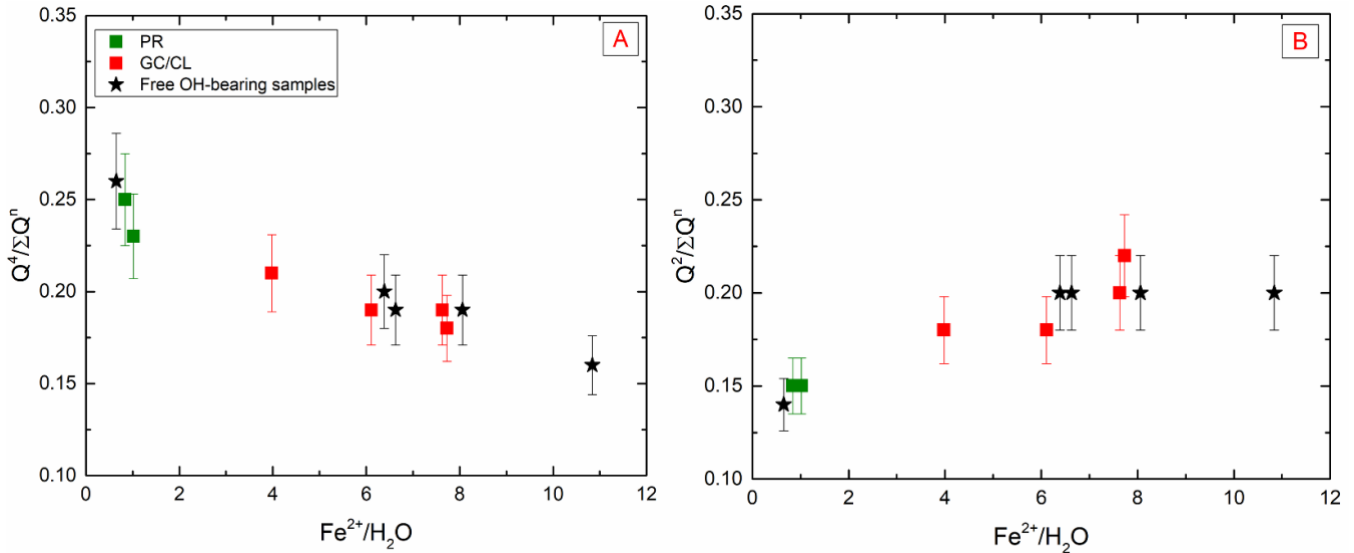
Fig.II.8: A) Ratio of $Q_4/\sum Q_n$ species versus the Fe_{2+} normalized by the H_2O content for all samples; B) Q_2 ratio for the same samples. PR samples are in green, where synthetic Fe-rich experiments are represented in red. The black stars are samples presenting Free OH molecular groups. A relative error of 10 % has been applied.

II.2.6 Summary

In the present work, we have shown that Fe concentration in glass has a non-negligible effect on the H_2O dissolution within the melt structure. Increasing the Fe content appears to induce a decrease in the H_2O dissolution. We inferred the formation of Free OH in Fe-rich glasses (i.e., martian basalt analogues) at relatively low H_2O content (~1 wt %) whereas such molecular groups appear at very high H_2O content for terrestrial basaltic glasses (> 6 wt %). The presence of Free OH molecular clusters seems to be dependent on the Fe content with increasing the FeO_{tot}. In detail, Free OH species are likely to be correlated to the Fe_{2+} in Fe-rich composition. Free OH are supposed to induce a polymerization effect on the silicate network; although further work is currently needed to investigate the exact molecular configuration in the surrounding of cations forming Free OH groups. The possibility for Free OH in the vicinity of Fe_{2+} cations represents a precursor for producing Fe-rich mineral phases through weathering of the erupted Fe-rich basalts, which will be consistent with Fe-oxides found at Mars surface.

While low H_2O-content Fe-rich glasses exhibit atypical signatures and low dissolution, high H_2O content needs to be investigated in these melts to fully understand the H_2O behavior.

II.3. High H_2O contet experiments in Martian basalt analogues

New data were obtained on Fe-rich glasses obtained at high pressure with low H_2O content. Experiments containing > 3 wt% H_2O were also tested in these chemical compositions (i.e., GC and CL). However, even with the optimization of the experimental setup described previously in this chapter, these experiments were not quenched fast enough to successfully obtain a glass. The results are discussed hereafter.

II.3.1 Dendritic textures

Several experiments have shown difficulties to be quenched into a glass. Indeed, some issues were coming from the materials used in the experiments such as the assembly (i.e., graphite furnace flawed), as described in the previous chapter (see Chapter I, section I.2.4.2). However, after further optimization of the material, the crystallized samples have persisted.

In Fig.II.8, various dendritic textures can be observed in different samples. The dendritic texture represents needle-like crystals of few nanometers scale. In Fig.II.9A and Fig.II.9B, a variation of the dwell time was tested. For the Fig.II.9B the duration for the GC sample with less than > 3 wt % H_2O was at set to 1h, when 6 hours was experimented in Fig.II.8A. We observe on these two figures that increasing the duration time permits the quench to a glass, which was not possible in only one hour of experiment.

Dendritic textures can still be observed in Fig.II.9A, but EPMA and SEM measurements show that the chemical composition is close to the glass composition. Hence, this sample in Fig.II.9A is included in the previous results for H_2O behavior in Fe-rich glasses (section II.2).

On the other hand, the results described in the previous section involved experiments with only < 3 wt % H_2O for the Fe-rich composition. In Fig.II.9C and 9D, two experiments with CL and GC compositions (i.e., 23.5 and 15.5 wt % FeO_{ini}) containing higher H_2O are exhibited: 3.9 and 5.9 wt % H_2O_{ini}; respectively. We can see that the two samples show a clear dendritic texture. The sample in Fig.II.9C (i.e., CL composition) has been obtained after 1h of experiment. In this sample, we can distinguish crystals in the needle-like shape, representing the dendritic texture, coupling to a darker material in between the crystals: the melt. According to SEM analysis, the crystals possess the same chemical composition as the bulk starting material (i.e., CL, see Table II.1). However, the melt, that is darker and indicating the predominance of light elements, is strongly depleted with respect to Fe and Mg (~3 wt% FeO_{tot} and 1 wt% for MgO). The chemical composition of this melt is close to a trachy-dacitic composition with an average of 63 wt% SiO_2, 15 Al_2O_3, 4 FeO_{tot}, 2 MgO, 2 CaO and 7 Na_2O. The proportion of the glass represents less than 10 % of the sample.

The chemical composition obtained for the interstitial melt between crystals is difficult to constrain, as well as the dendritic crystal composition. Indeed, their compositions have been determined with quantitative method with the SEM instrument. However, as represented in the Fig.II.8, the crystals and the melt are very small, below the nanometric scale. Hence, a strong magnification is necessary to isolate the crystals from the melt, but it is not entirely enough to prevent any crystals contaminating the melt composition. Hence, the chemical compositions of the dendritic crystals and the melt have to be considered with precaution. However, it is clear that the melt composition is depleted in Fe and Mg compared to crystals.
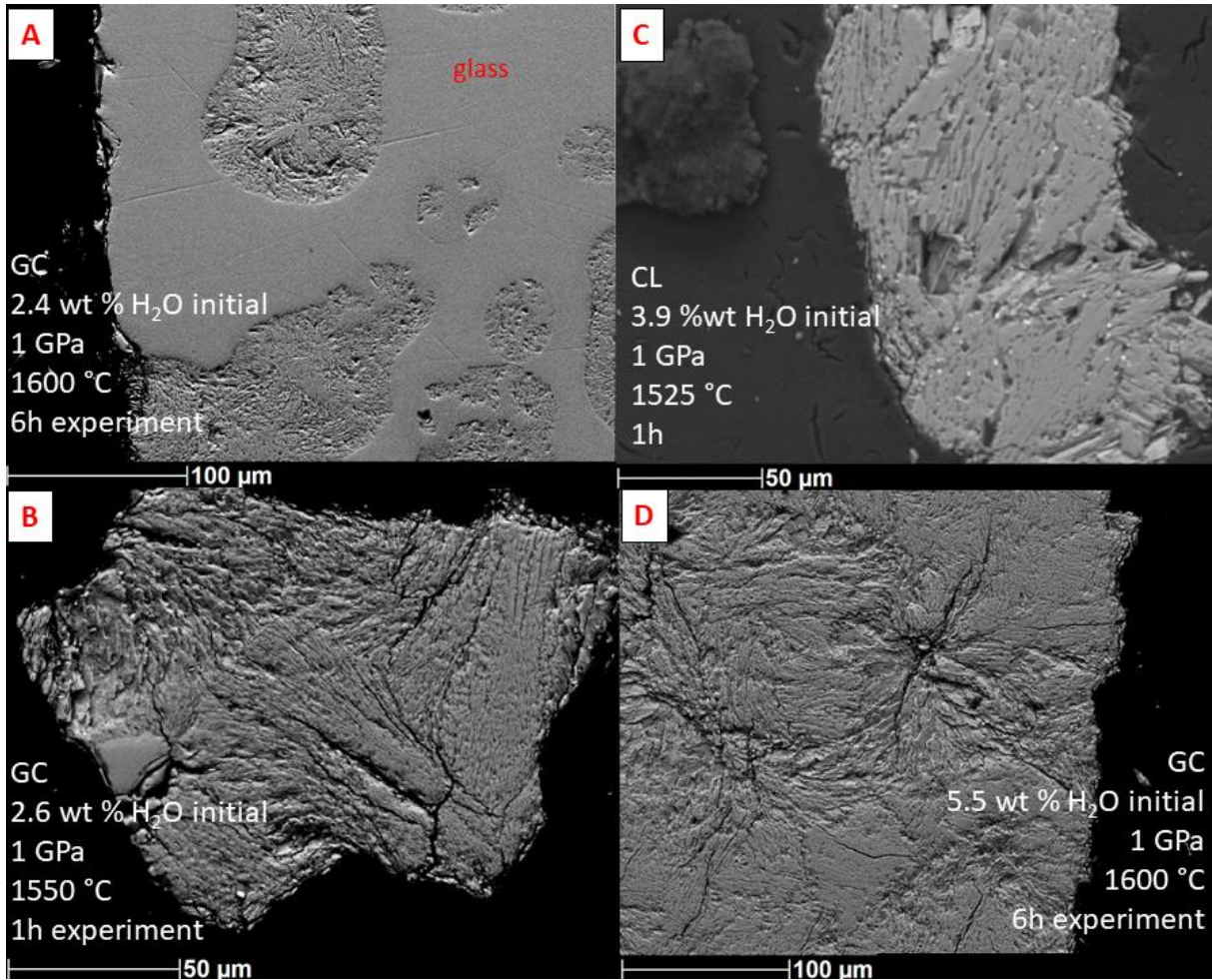
Fig.II.9: SEM assemblage of various samples presenting dendritic texture: A) GC composition with 2.4 wt % H_2O_{ini} after 6 hours of experiments, B) GC composition after 1 hour of experiment, C) CL composition 3.9 wt % H_2O_{ini} and 1 hour experiment; D) GC with 5.5 wt % H_2O_{ini}, 6 hours.

The dendritic textures observed in various samples containing > 3 wt% H_2O or with a low run duraction, can be described as crystals in a needle-like shape of < 1µm in width. Due to their small sizes, their identification was difficult. EPMA and SEM combined did not succeed to obtain the chemical composition of the dendrite only; but a mixture of crystals and melt was obtained.

II.3.2 Characterization of the dendritic samples

Spectroscopic methods were then necessary to characterize the crystals. Raman spectroscopy results for the GC-6H-6h sample is exhibited in Fig.II.10. In Fig.II.10A, the silicate matrix of the sample is shown, whereas the H_2O signal is reported in Fig.II.10B. From the Fig.II.10A, we can see that a glass signal is detected between 800 and 1200 cm-1 with a small peak around 1000 cm-1, that can be attributed to the crystallization of the sample. Added to the glass signature, a Lorentzian shape peak at 670 cm-1 is observed. Coupled to the 670 cm-1 peak, we can see the peak at 3660 cm-1 in Fig.II.10B, in the H_2O vibration. We have seen in the previous

section (i.e., Chapter II, section II.2.5.2) that the 670 and 3660 cm-1 peaks were correlated and attributed to the formation of Free OH. These Free OH would probably bond with Fe_{2+} presents in the sample. With the high H_2O content of the sample (5.5 wt % H_2O_{ini}) and with the probable low dissolution of H_2O in these Fe-rich melt, the amount of Free OH dissolved is increased with increasing H_2O initial content. No more than 0.4 wt % H_2O has been quantified for this sample according to the method of Mercier et al. (2009).
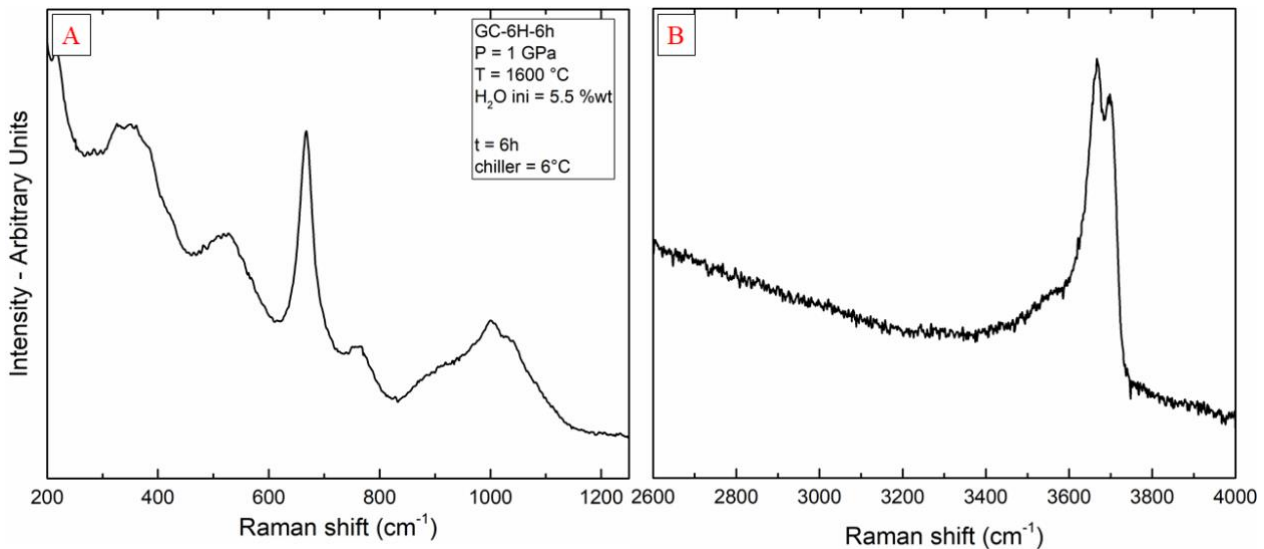
Fig.II.10:A) Raman spectra of the 200 - 1250 cm-1 region for GC-6H-6h; B) H_2O region (2600 – 4000 cm-1) for the same sample.

While the Raman spectroscopy gave us the spectral signature of the sample, we were not able to characterize the dendritic crystals because the spot size of the laser was of 1 µm, which is too large for the nanometric crystals. Then, we used the X-Ray powder Diffraction, which method has been detailed in the previous chapter (i.e., Chapter I, section I.3.3). Only one sample was analyzed with this technique. We have chosen a sample presenting the dentritic textures: GC-1.5GPa. This sample was loaded with 4.5 wt % H_2O_{ini}, experimented at 1.5 GPa at 1550°C for 1 hour.

After XRD analyses, we can see on Fig.II.11 the peak attribution on the diffractogram. Four minerals have been chosen to represent the peaks of our sample: pyroxene, carbonate and two amphiboles (ferroglaucophane and magnesiohornblende). The presence of carbonate is a possibility since this sample was not decarbonated and almost 3 wt % CO_2 was added along with the Na_2O. Moreover, the formation of amphiboles can be expected in high H_2O content. Due to the relatively high MgO and FeO content in GC samples, it is also possible to form pyroxenes. In Fig.II.11, we can see that among the four minerals, the amphiboles peaks are closer to those of the sample, followed by the pyroxene signal. The carbonate component is less in agreement with the peaks observed on GC-1.5GPa.

Then, we can propose that the major components representing dendritic crystals are a mixture of amphiboles and pyroxenes; although the analysis was performed only one sample. While we were finally able to determine the crystals created in high H_2O content experiments, we still have to understand how they formed.
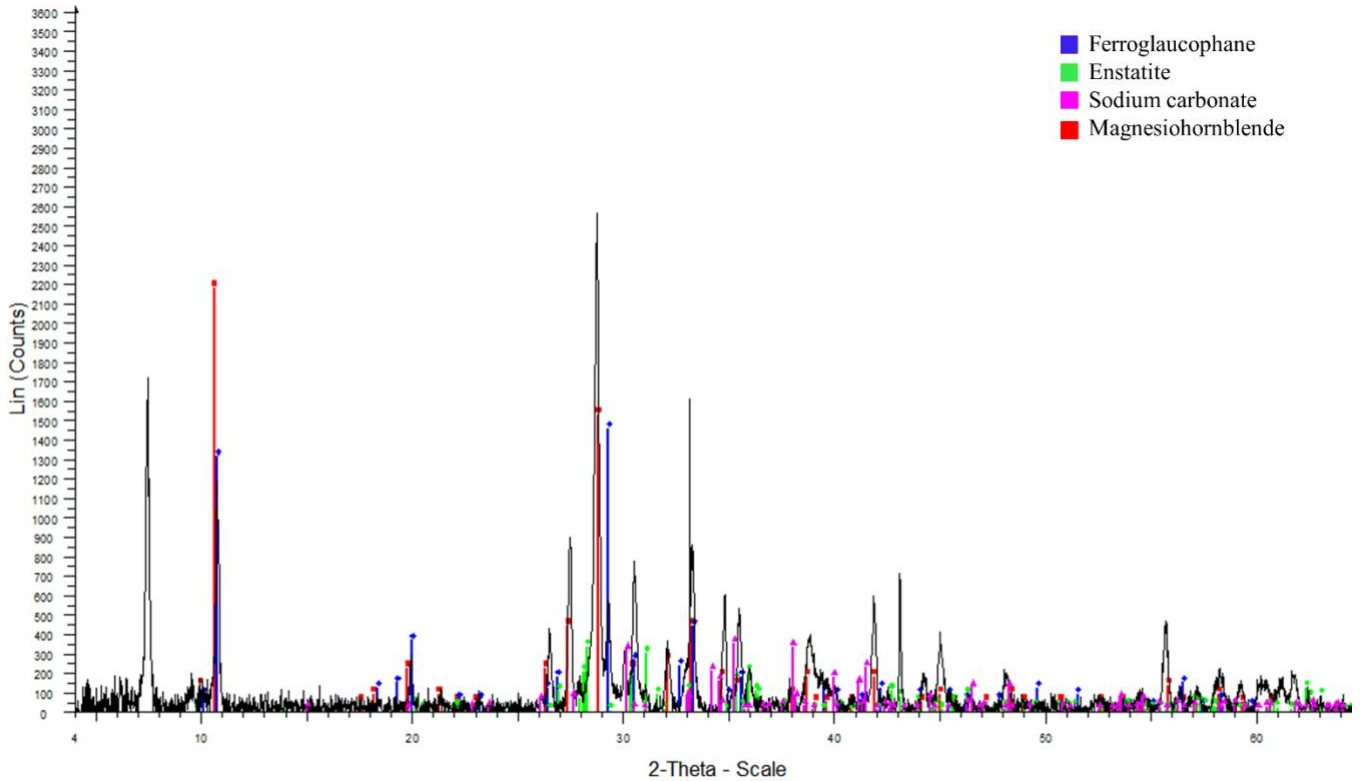
Fig.II.11 : XDR diffractogram for a sample presenting dendritic texture: GC-1.5GPa. In blue: ferroglaucophane $Na_2(Al,Fe,Mg)_5Si_8O_{22}(OH)2$; in green, a signal of enstatite $Mg_{1.83}Fe_{0.17}Si_2O_6$; in pink: sodium carbonate Na_2CO_3; and in red: magnesiohornblende $(Ca,Na)_{2.26}(Mg,Fe,Al)_{5.15}(Si,Al)_8O_{22}(OH)_2$.

II.3.2 Glass transition temperature and viscosities

We know from the literature that the H_2O lower the viscosity and the glass transitional temperature (Tg) of the melt (Dingwell 1987,1990). As described in the study of Dingwell (1990), the glass transition represents a barrier between the liquid and glass behavior in a silicate melt. This parameter depends on the chemical composition, pressure, temperature, and quench rate.

The piston-cylinder apparatus can reach a quench rate up to 100 °C/s. We first consider the point A in Fig.II.12, corresponding to the sample at the fusion temperature for a specific dwell time. The quenching of the point A with a quenching rate of a piston-cylinder at 100°C/s will result in the point B in Fig.II.12. The Tg is reached according to the quench rate of the piston-cylinder at T1. On the contrary, with the same point A at fusion temperature, the resulting Tg with a fast quench rate (500 °C/s), will result in point C at T2. Hence, the Tg of point B is lower than for point C (i.e., T2 > T1).

93

Glass samples obtained in the previous section (II.2) are then obtained following the path of point B in Fig.II.12.
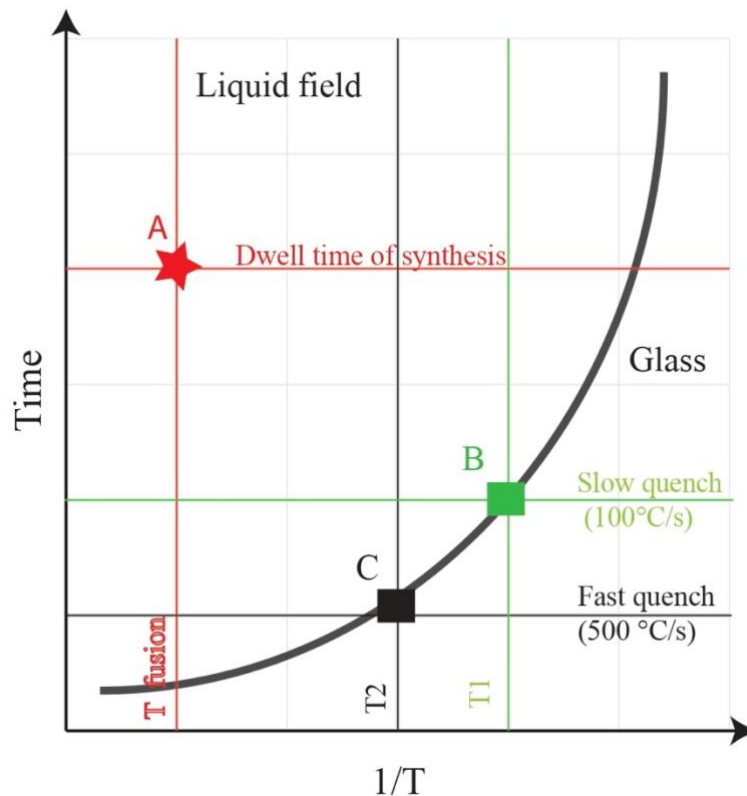
Fig.II.12: Representation of the transitional glass temperature relationship in function of time and temperature, after Dingwell and Webb (1990).

Chevrel et al. (2013) have shown from their experiments that increasing the FeO content in the melt increases the density and lower the viscosity. Indeed, their experiments at 1 atm and high temperatures (> 1200 °C), on anorthite-diopside doped in Fe_2O_3 up to 30 wt%, have shown that the more iron is added in the system, the more the viscosity decreases by at least 2 log units, hence the Tg of the melt. This study reflects the same results than the study of Botcharnikov et al. (2005) who have also investigated the effect of both the Fe and H_2O content on the viscosity of the melt.

Hence, in our Fe-rich samples, both the FeO and H_2O content have to be taken into account. Increasing the H_2O content in the melt (> 3 wt %), coupled to the high FeO (> 15.5 wt %) have drastically decreases the viscosity of the melt, and increased the crystallization cinetic. To quench this melt, a faster quench rate is required. However, the quench rate cannot be modified with the piston-cylinder; hence we can suppose that the quench rate is not fast enough compared to the cinetic crystallization. Instead, needle-like crystals were able to develop. Then, obtaining a Fe-rich glass with high H_2O content (> 3 wt %) is not possible with our experimental device (i.e., with the piston-cylinder). It implies that solubility laws cannot be obtained at high pressure, with high H_2O content in Fe-rich melt.

II.3.3 Discussion

Our results show that a dendritic texture was formed in several experiments and was likely caused by the high FeO and H_2O contents (>15 wt%, > 3 wt % respectively). This dendritic texture is made of a mixture of pyroxene and hornblende crystals coupled with a trachy-dacitic liquid. The recurrent occurrence of this texture suggests that the same phenomenon may occur in the interior of Mars; even though no amphibole has been detected yet. Indeed, depending on the partial melting of the martian mantle, more than 3 wt% of H_2O could be dissolved in the basaltic magma. If so, the ascent of this water-rich magma will be followed by a fractional crystallization of a trachy-dacitic liquid and crystallization of the basaltic melt. By difference of buoyancy and density, the depleted liquid will be able to reach the surface or crystallize in the shallow crust. Yet, the presence of trachyte and dacite rocks has been found locally in the martian crust (Christensen et al. 2005; McCubbin et al. 2008; Sautter et al. 2016), which potentially link our results to these observations.

The formation of trachy-dacitic rocks from a basaltic source has also been observed on Earth, for instance in Chili, in the Purico domain. From the different ignimbrites found, andesite, rhyolites and dacite have been characterized by Schmitt et al. (2001). From this study, it is implied that one mantle source, with a basaltic composition, is at the origin of ignimbrites at various degree of differenciation. In addition, the recent study from Udry et al. (2018) has shown that a crystallization of a basaltic melt can lead to several differentiated melts. Indeed, they tested different parameters such as P, T, fO_2 and H_2O content with a martian basalt composition. From their simulations with Rhyolite-MELTS, they have concluded that all the differentiated magmatic rocks observed at the surface of Mars (i.e., trachyte, trachydacite, trachyandesite) can be explained by crystallization of a basaltic source. Then, as this phenomenon is observed on Earth, and can also be simulated for Mars mantle composition, the formation of trachydacite may happen on Mars caused by the crystallization of a hydrated basaltic melt. The extend of those trachytes and dacite rocks on Mars is currently unknown, limiting the implication of our findings; but the possibility of a martian crust with a lower density opens the door for a more widespread occurrence of such rocks at depth (Baratoux et al., 2014).

Nonetheless, our results only show a picture of the quenched crystals formed at depth in such composition. It does not reflect a fractionnal crystallization, hence, the products of crystals and the composition of the melt during its ascent. The above proposed outcomes of a H_2O-rich martian basaltic melt rely only on our quenched phases observed in our high-pressure experiments. To constrain the future of this kind of melt with high H_2O content, it would be interesting to perform temperature-controlled experiments, enabling the crystal growth in the melt.

II.4. Perspectives

The H_2O behavior in Fe-rich glasses has demonstrated that further investigations are needed. Indeed, at low H_2O content, Free OH are observed and tend to polymerize the melt, which will affect the viscosity. On the other hand, at high H_2O content, dendritic textures are observed

with a mixture of trachy-dacitic liquid and pyroxene and horblende crystals. The high H_2O coupled to high Fe content will also influence the viscosity of the martian basaltic melts.

The polymerization effect of Free OH is of interest for martian melt. Effusive flows have been proposed for most basaltic eruptions on Mars (Greeley et al. 2005; Hiesinger et al. 2007; Baratoux et al. 2009; Vaucher et al. 2009) according to rheologic data. Experimental data of Chevrel et al. (2014) have demonstrated that Fe-rich martian basalts are would possess a viscosity around 10_5 - $10_{5.2}$ Pa.s, which is in accordance with the effusive flow morphologies observed at the surface of Mars.

However, it is most probable that the martian basaltic melt contains Free OH and will be more viscous than a basalt without Free OH; although we suspect that the difference is very low due to the small effect on the polymerization degree observed in the previous section (Chapter II, section II.2.5.3). On the other hand, the investigation of high H_2O content in Fe-rich basalts has led to the interpretation that the Tg is very low in these compositions, which invokes a strongly depolymerized melt. Chevrel et al. (2014) have also investigated melts that would crystallize needle-like crystals. The apparent viscosity of such melts would go down to $10_{3.5}$ Pa.s at 1150 °C. This low viscosity has already been observed of lava flow features at the surface of Mars in the Central Elysium Planitia (Vaucher et al. 2009) with a calculated viscosity at 10_2 Pa.s. This would suggest that potentially high H_2O-bearing basaltic melts erupted in this area.

Although the study of Chevrel et al. (2014) proposed viscosity that could be appropriate with the observed polymerization structure of our present work, their experiments were made on melts at 1 atm. The pressure will impact the alumino silicate-network, hence the viscosity of the melt. As we have seen in the previous sections, the H_2O dissolution in Fe-rich composition impacts strongly the physical parameters of the melt by modifying the viscosity, but also the electrical conductivity. It would be of interest to perform physical properties experiments (determination of Tg, viscosity and electrical conductivity) at high-pressures in Fe-rich basaltic composition in presence of H_2O.

We have notably studied the effect of the H_2O dissolution in Fe-rich melts at high pressure in this study, which was not done until then. Even if we were not able to perform H_2O-saturated experiments, we can suppose that the H_2O content at high pressure (> 1 GPa) will not exceed 2 wt %. Indeed, low pressure experiment in composition close to ours such as the study of Shishkina et al. (2014) have demonstrated that more than 8 wt % H_2O can be dissolved in 13 wt % FeO_{tot} ferrobasalt at 500 MPa. These experiments were performed using a IHPV instrument, with a quench rate 500°C/s. Hence, as discussed above, the fast quench rate enables the quenching of a high H_2O content Fe-rich glass. However, in our study, we used the piston-cylinder apparatus. The quench rate is much slower (five times below IHPV quench rate), which prevent us to obtain high H_2O content Fe-rich glass. Nonetheless, if we consider a magma ascent, it never reaches 500°C/s. Then, the experiments performed in this work could be more representative of the H_2O behavior at depth in martian melts. Considering this, we have seen that a small amount of H_2O is dissolved at 1 GPa, which corresponds ~90 km in martian depth. Hence, it implies that a small content of H_2O can be degassed in the atmosphere of Mars if the melt reaches the surface. The formation of Free OH would, although, contributes in the H_2O content degassed with the magma ascent, but the fraction of Free OH is very small. On the other hand, we have seen that higher H_2O-content will favorize the crystallization of the melt, which prevent it to degas.

In conclusion, we can wonder about the formation of the primitive atmosphere of Mars that needs high volatile content to be dense and stabilize liquid water. While the H_2O alone can probably not contribute to the amount of volatiles degassed, others should be considered. In the following chapter, we will perform high-pressure experiment on Fe-rich chemical composition (the same used in this chapter) in presence of S but also H_2O.

Chapter III: S-bearing basalt analogues

This chapter represents an article in preparation to be submitted in Chemical Geology.

III.1. Abstract

The large amount of S detected at the surface, coupled to the 5 wt % bulk S, indicates that this volatile is important on Mars. The sulfates dominating the surface are probably resulting from subsequent volcanism degassing. The past atmosphere of Mars is thought to be dense and enriched in volatiles. S emitted as SO_2, could be a good candidate to contribute to the densification of the past atmosphere of Mars allowing liquid water at the surface during the Noachian.

We have performed high pressures experiments (0.5 – 2 GPa) on Fe-rich basaltic composition (9 to 23 wt % FeO_{tot}) in presence of S. Piston-cylinder experiments were S-saturated with $CaSO_4$ and elemental S_0 in the starting material. Analyses were performed using Raman and XPS spectroscopies. Measurements of Fe redox ratio were realized by wet chemistry. S_0 glasses show only S^{6+} species at the end of the experiment, with possible FeS species as inferred by XPS spectroscopy. The fO_2 investigated are estimated between QFM and QFM+1. The solubility of S do not strongly differs from $CaSO_4$ and S_0 experiments, and a maximum of 1.4 wt % is reached. New solubility data on Fe-rich compositions are then proposed.

We have developed a new solubility model with 186 data, coupling reduced and oxidized conditions (both sulfide and sulfate saturated experiments). This model depends on P, T, fO_2, S_{ini} and H_2O contents, the Ionic Field Strength (IFS) and the Non-Bridging Oxygen Per Tetrahedron (NBO/T). The IFS will characterize the interaction between the cations of the melt, whereas the NBO/T represents the degree of polymerization. This model can be applied to various melt composition spanning from basalts to rhyolites. The fO_2 investigated are from extremely reduced (NNO -2.3; Nickel-Nickel-Oxygen) to oxidized (NNO + 0.6) compositions. Then, the model can be applied on both terrestrial and extraterrestrial melts, such as Mars.

III.2. Introduction

Mars is a S-rich planet. Studies have estimated the S bulk content for Mars to raise up to 5 wt % (Wänke and Dreibus 1997), where only 0.5 wt % is quantified for Earth (Dreibus and Palme 1996). Contrary to the Earth, it has been proposed that the accreted material for Mars was not volatile depleted. Indeed, S was first an abundant volatile in the solar nebula as H_2S (Lodders et al. 2009; Ebel 2011) but the chondrites that formed during fractionation contained various volatile contents. Then, due to the high S content of Mars compared to Earth, a volatile-rich chondrite could be at the origin of Mars, whereas depleted chondrites could be at the origin of the Earth and the Moon. Then, Gaillard et al. (2013) proposed that Mars is mainly controlled by the S cycle in analogy to the C cycle prevailing on Earth. The large amount of S detected at the surface of Mars was initially stored in its interior. In addition, Mars is also enriched with respect to Fe compared to Earth with ~18 wt % FeO_{tot} in average (Taylor and McLennan 2009). The first space missions having detected S on Mars were the Viking spacecrafts which discovered 4 wt % of sulfur at the surface (Clark et al. 1977, 1993). It was followed by other

orbital detections, notably with the OMEGA instrument onboard the Mars Express spacecraft, which was the first to inform on the evidence for sulfate minerals on Mars (Gendrin et al. 2005; Langevin et al. 2005). From orbital and lander missions, it is clear that Mars crust is riched in S. The main form of S at Mars' surface is oxidized, as sulfate (i.e., S_{6+}). The most represented sulfate species are Fe and Mg-sulfates, with also the presence of Ca-sulfates. They are mostly found intertwined in sediment layers over the igneous bedrock or rarely in crustal outcrops exhumed by impact craters (e.g., Squyres et al. 2004; Gendrin et al. 2005; Wray et al. 2010; Carter et al. 2013). In the regolith, it has been determined from previous spatial missions, that the SO_3 content is up to 7 wt % which translates to 5 - 10 % sulfate minerals (King and McLennan 2010; McSween et al. 2010). Even if sulfates have been widely detected on the surface, the mineralogical characterization is still imprecise (due to absorption bands in near infrared) sulfates are mostly separated in two groups: monohydrated and polyhydrated; which both contain Ca, Mg or Fe-sulfate species.

It is currently assumed that the large amount of S at the surface of Mars is coming from subsequent volcanism degassing (King and McLennan 2010). The aim of the various spatial mission toward Mars is the understanding of the past geologic activity of the planet that is reflected at the present surface. Many features at the surface of Mars indicate the presence of past liquid water followed by sulfur-rich solutions that would have formed the sulfates in sedimentary rocks from the Noachian to Hesperian epochs (e.g., Squyres et al. 2004a,b; Gendrin et al. 2005; Tosca et al. 2009). To maintain liquid water, the scientist agreed that the past atmosphere of Mars should have been enriched in volatiles (Elkins-Tanton 2008, Craddock and Greeley 2009). However, there is still a debate on whether the past atmosphere was warm and wet (Carr 1983; Pollack et al. 1987; Carter et al. 2015) or if it was only episodic events in a generally cold climate (King et al. 2004; Johnson et al. 2008, 2009; Halevy and Head 2014). A volatile-rich primitive atmosphere would have probably been fed by volcanic degassing. Hence, to understand the amount of volatile degassed into the atmosphere, the investigation of volatile content at the surface and in the interior of Mars is needed. Furthermore, the determination of the budget of S dissolved in atypical melts such as martian basalts has crucial impact for the future spatial mission. The Mars 2020 rover will investigate the Mars surface through multiple analytical devices, notably the Raman spectroscopy onboard the SuperCam instrument (Wiens et al. 2016). The current analytical instruments onboard Curiosity such as ChemCam, as a very low S resolution, which prevents the quantification of this element < 10 wt % (Wiens et al. 2012). Recently, Larre et al. (2018) have developed a calibration to quantify S in sulfate mixtures using the Raman spectroscopy (see the following Chapter IV). The calibration enables the detection down to 1 wt % S. However, rovers and orbital missions on Mars permits only the quantification of S already degassed and transferred into sulfates or within igneous rocks. Then, it cannot retrace entirely the amount of S degassed into the atmosphere and what was present at depth within the martian melt.

Nowadays, experimental studies have mostly looked at the CO_2 and CH_4 solubility (Stanley et al. 2011,2012,2014; Ardia et al.2013; Armstrong et al. 2015) in martian analogous melt compositions. Recently, Larre et al. (subm) have observed the H_2O behavior in Fe-rich glasses in application for Mars (Chapter II). Righter et al. (2009) performed an experimental study to determine the S solubility in primary martian basalts at 4000 ppm. Alternatively, solubility models were created to estimate the S solubility in martian interior by Gaillard and Scaillet

(2009). They have calculated a minimum S content in martian basalts to be at least at 4000 ppm. Hence, there is currently few experimental studies investigating the S behavior in Fe-rich basaltic melts to constrain the S solubility.

The S is abundant is volcanic systems with its presence withing fumaroles, volatile degassed or in the erupted igneous rocks. Sulfur is also associated with the formation of ore deposits (Simon and Ripley 2011), which makes this volatile element important for scientists. In silicate melts, S will be dissolved either as S^{2-} or S^{6+} species (Jugo et al. 2010), whereas it mainly dissolved as S^0 in metals. In the vapor phase, S will be present notably as H_2S, S_2 or SO_2 (S^{2-}, S^0 and S^{4+} oxidation state of S) according to Gaillard et al. (2011). The behavior of S in various silicate melts has been widely investigated for terrestrial melt composition: from Si-poor silicate melts (Morizet et al. in prep), basaltic melts (e.g., Haughton et al. 1974; Mavrogenes and O'Neill 1999; Jugo et al. 2005a,b; Liu et al. 2007; Beerman et al. 2011;), to Si-rich compositions (e.g., Clemente et al. 2004; Klimm et al. 2012; Jégo and Pichavant 2012). It resulted in multiple solubility laws established for Earth silicate melts. In the previous S solubility investigations, several factors have been enlightened to impact on the S solubility: the fO_2, fS_2, FeO content, and melt composition (Haughton et al. 1974; Liu et al. 2007). The redox condition on Mars interior is still debated. However, there is a consensus to estimate the fO_2 of the martian mantle to be between the Iron-Wüstite buffer (i.e., IW) -1 up to IW +1 (Wadhwa 2008). According to the Martian S cycle, it has been established that the amount of sulfur dissolved in silicate melts is limited by its partitioning with other coexisting phases, such as metal, sulfide, sulfate and vapor, from the core formation to the magma degassing.

In the present study, we have investigated the S solubility considering two starting redox state of S (S^0 and S^{6+}), at high pressures (0.5 - 2 GPa) and temperatures (1400 - 1500 °C). Spectroscopic analyses were performed to obtained Raman spectra on Fe-S-rich glasses obtained at high pressures. XPS measurements were also made to observe the S and Fe redox state, as well as the number of bridging oxygen in the alumino-silicate matrix to potentially discuss the effect of S on the melt structure and melt physical properties. In our work, we determined a S dissolution in two S_{ini} redox state (S^0 and S^{6+}). In addition, we have made a review of S-saturated experiments, at various fO_2, P, T, H_2O contents and in various melt compositions. We proposed a new solubility model depending on the Ionic Field Strength (IFS) and Non Bridging Oxygen per Tetrahedron (NBO/T) parameters. In this new solubility model, we have implemented the S solubility data experimented in this study for Fe-rich composition. The model is then valid for various melt compositions on Earth (from basaltic to rhyolitic melts) and Mars.

III.3. Material and methods

III.3.1. Starting material

The chemical compositions chosen in this study are based on average chemical composition of basalts detected by the rover Curiosity on Mars. The GC and CL chemical compositions used in this study are detailed in Larre et al. (subm) and contain 15.5 and 25.5 wt % FeO_{ini}, respectively (see Table II.1, chapter II). The synthetic mixtures are prepared with a mixture of oxides and carbonate powders (Na_2CO_3). The starting materials, GC and CL compositions, were previously decarbonated in a 1atm furnace at 800 °C for at least 2 hours, before the mixing

with the S components. The mixtures were prepared in order to obtain an initial S content at: 0.4, 1 and 2 wt % S.

Two species of S were investigated in this study and added into GC and CL:

- As $CaSO_4$, for oxidized experiments (i.e., starting with S_{6+}), referred as GCS and CLS in Table III.1
- As S_0, for reduced experiments, referred as $GCS°$ in Table III.1

III.3.2. High pressure experiments

The investigated iron-rich composition with S were loaded into a Pt capsule. Details of sample preparation are reported in the Annex Section in the Table III.A1.

In order to investigate the S solubility at high pressure, we performed experiments between 0.5 – 2 GPa, and 1400 – 1500°C using a piston-cylinder, similar to the method employed in Chapter II (section II.2.3.2). A ¾ inch talc-pyrex assembly was used for experiments below 2 GPa, and a ½ inch talc-pyrex assembly for the experiments above this pressure. Previous work (Kägi et al. 2005) showed that using talc-pyrex assemblies apply intrinsic fO_2 conditions close to QFM+1 buffer. The experiments were performed with no fO2 control and in oxidized conditions buffered with the S redox state and the piston-cylinder apparatus. According to various fO2 conditions in the martian interior, the ascending melt can be in equilibrium with oxidized layers. Also, these experiments were first prepared with no buffer to simplify the experiments. Experiments were planned in reduced conditions using graphite capsules, but the schedule of experiments with H_2O (Chapter II) and S took more time, and reduced expeirments are then considered as future work after this thesis.

The run duration was set at 6 hours to ensure the solubilization of S in the melt. Quenching was performed by cutting off the power and the quench rate was measured and estimated to be above 80°C/s.

III.3.3. Analytical methods
III.3.3.1. Raman spectroscopy

For our study, we used the Jobin-Yvon Labram HR800 Raman spectrometer equipped with a 532 nm solid-state laser of the Laboratory of Planetology and Geodynamic (LPG, Nantes University, France). The output power was set at 50 mW to prevent sample damages. We used a grating of 1200 grooves/mm corresponding to a spectral resolution of ~0.8 cm-1. The acquisition time was typically 30 sec with 3 or 6 repetitive scans. Spectra were acquired in a non-confocal mode with a slit aperture of 200 µm and a spot size estimated ~1 µm in diameter. A X50 Olympus objective was used. At least 5 spectra were acquired on each sample to investigate the homogeneity of the recovered sample with respect to the dissolved S. The studied spectral range was between 200 and 1250 cm-1 and between 2500 and 3900 cm-1, covering the area of the silicate network and the H_2O vibrations (for H_2O-bearing samples, see Table III.1), respectively.

The dissolution of S in silicate melts is multiple. Indeed, according to the fO_2 prevailing in the system, the S can be present in S^{2-}, S^0 and S^{6+}. Intermediate valence of S can also be expected (S^+, S^{2+} and S^{4+}), although S^2 and S^{6+} are the most common species found in silicate melts. The Raman spectroscopy is an accurate tool to observe S^{6+} species in silicate melts with its symmetric stretch vibration v_1 at ~1000 cm^{-1}, representing SO_4^{2-} species (Bény et al. 1982; Burke et al. 2001; Klimm and Botcharnikov; 2010; Wilke et al. 2011; Morizet et al. 2017). The other reduced valence of S can be detected by Raman spectroscopy at low Raman shifts. S^{2-} species can be observed between ~300 and ~400 cm^{-1} when bounding with metallic cations, especially Fe to form FeS species at 375 cm^{-1} (Wilke et al. 2011; Klimm et al. 2012b). At very reduced conditions and in Fe-free experiments, HS^- species can also be detected 2574 cm^{-1} (Klimm et al. 2010, 2012b). However, vibrations of S^0 species by Raman spectroscopy, and the other intermediate redox states are currently not well constrained.

III.3.3.2. SEM analysis

Secondary Electron Microscopy (SEM) analyses were performed according to the method described in Chapter I and Chapter II. Sulfur quantification is possible by SEM using a pyrite standard (FeS). The latter has been calculated for all samples with 5 to 10 runs on each sample to obtain a standard deviation reported in Table III.1.

III.3.3.3. Colorimetric determination of the Fe_{2+} / $\sum Fe$ ratio

The colorimetric determination of the Fe ratio has been previously described in Larre et al. (subm) study and is based on the modified method of Schuessler et al. (2008) after Wilson (1960). This method aims to quantify the FeO_{tot} and FeO in the samples (see Chapter I for further information).

The results of the Fe_{2+} / $\sum Fe$ measurements on the international reference material JB-2 (Fe_{2+} / $\sum Fe$ = 0.78± 0.005, N=19) are in good agreement with the recommended values (i.e., 0.78, Govindaraju 1994).

III.3.3.4. XPS

The X-Ray Photoelectron Spectroscopy (XPS) was used on several samples to investigate the Fe and S redox state prevailing, as well as the polymerization degree of the melt. Five samples were analyzed: GCS-1S-1G, GCS0-2S-1G, GCS-2S-1G, GCS0-2SH-1G and GCS0-2S-2G. The method is described in Chapter I.
Five areas were investigated:
- Fe 3p at 55 eV, (Mekki et al. 1996; Nesbitt et al. 2000)
- S 2s at 228 eV (Zhao et al. 2017)
- O 1s ~500 eV (Nesbitt et al. 1995)
- C 1s ~285 eV (Mekki et al. 1996)
- Si 2p 102 eV (Nesbitt et al. 2011)

III.4. Results and Discussion
III.4.1. S quantification

All the experiments obtained in this study were not glassy. Indeed, the Fe-rich composition CLS always showed a crystallized texture at different pressure. SEM images showed nanometric needle-like crystals that could not be characterized and were almost not detectable. This specific size indicates that the crystals are probably coming from the quench (see Chapter I, section I.2.4). Also, the H_2O-rich sample in GCS composition (i.e., S added as $CaSO_4$ initially) was not glassy either. This sample presented the same characteristics as CLS experiments with very small crystals.

The S determined for those crystallized experiments were determined on several chips considering the nanometric crystals. Hence, the S estimated by SEM analyses represent the bulk S content on these samples.

In addition, no sulfide melt phase was observed for the most reduced samples (i.e., starting with S_0). Various SEM images are reported in the Annex Section in Fig.III.A1.

In Fig.III.1, S results from SEM analyses are reported in function of the pressure tested in this study. Detailed values are also reported in Table III.1. It is shown in Fig.III.1 that pressure has no effect on the S solubility. For GCS glasses (i.e., S added as $CaSO_4$) with 1 wt % S_{ini}, ~0.4 wt % S is dissolved at 1, 1.5 and 2 GPa. With 1 wt % S added as S_0, (GCS_0), the S final content is not varying (~ 1.1 wt %) between 1 and 1.5 GPa. For glasses with 2 wt % S_{ini} in GCS_0 composition, a small decrease of S is observed with 1.4 wt % at 1 GPa against 1.0 wt % at 1.5 GPa, followed by an increase at 2 GPa with 1.2 wt % S_{tot}. Then, no trend is observed for the S dissolved with increasing pressure.

However, we can see an increase of S dissolution between 1 and 2 wt % S_{ini} in GCS composition in Fig.III.1: 0.4 wt % and 1.4 wt %, respectively at 1 GPa (i.e., GCS-1S-1G and GCS-2S-1G; see Table III.1). However, for GCS_0 samples at 1 GPa, there is ~1.1 wt % dissolved with 1 wt % S_{ini} and 1.2 with 2 wt % S_{ini}. Hence, there is an effect of the S initially added for oxidized experiments (GCS) that is not clearly observed for S_0 samples (GCS_0).
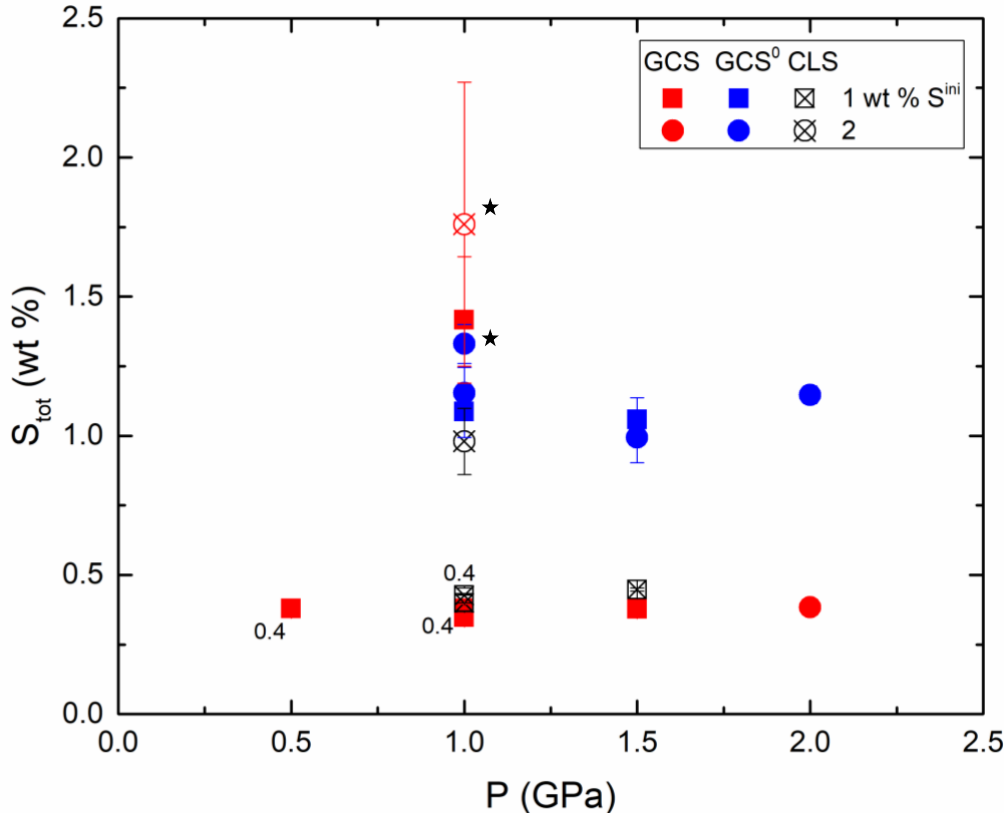
Fig.III.1: Sulfur determined by SEM in function of pressure. In red are data with S added as $CaSO_4$ for the GC composition, when blue represents the S added as S_0. In CLS samples, S was added only as $CaSO_4$. Distinction between squares and round markers identify when 1 or 2 wt % of S is added initially, except 3 samples where 0.4 wt % of S was added and notified in the graph. Open crossed symbols are for crystallized samples. Dark stars represent experiments with 2 wt % H_2O initially added.

In Fig.III.2, the total S dissolved is reported in function of FeO_{tot} determined by SEM and wet chemistry analyses, respectively. From the Fig.III.2, we can see that the FeO_{tot} content does not play a significant role in the S solubility when looking at our data GCS, GCS_0 and CLS. For GCS_0-2S-1.5G sample with the lowest FeO_{tot} (9.2 wt %) there is ~1.0 wt % S dissolved. In GCS glasses, a maximum at 1.4 wt % S is reached for GCS-2S-1G with ~14.6 wt % FeO_{tot}. For the Fe-rich composition (CLS), that is crystallized, a maximum of 1.0 wt % S is dissolved at ~23 wt % FeO_{tot}. We can see that GCS_0 samples with 2 wt % S_{ini} exhibit a strong Fe-loss compared to the initial Fe content (i.e., 15.5 wt %), with the lowest value at ~9 wt % FeO_{tot} (GCS_0-2S-1.5G, see Table III.1). This decrease with respect to Fe may be due to the reduced S species at the beginning of the experiment that enables some Fe_{2+} species to create an alloy with the Pt capsule.

However, when looking at the Fig.III.2, the FeO_{tot} seems to play a role in the S dissolution when terrestrial basalts are added into the trend. Indeed, the S-rich basaltic experiments from Tsay and Zajacz (2019) are FeO-poor compared to GCS, GCS_0 and CLS samples. Indeed, the terrestrial basalts are varying between 3 and 7 wt % FeO_{tot}. The S solubility seems to be impacted with this low FeO content which varying from 0.1 to 0.7 wt % between 3 and 7 wt % FeO_{tot}, respectively. Hence, when increasing the FeO_{tot}, starting at 3 wt % with terrestrial basalt

of Tsay and Zajacz (2019), to 15 wt % with the GCS composition, the S dissolution is increasing from 0.1 to nearly 1.5 wt % S_{tot}.
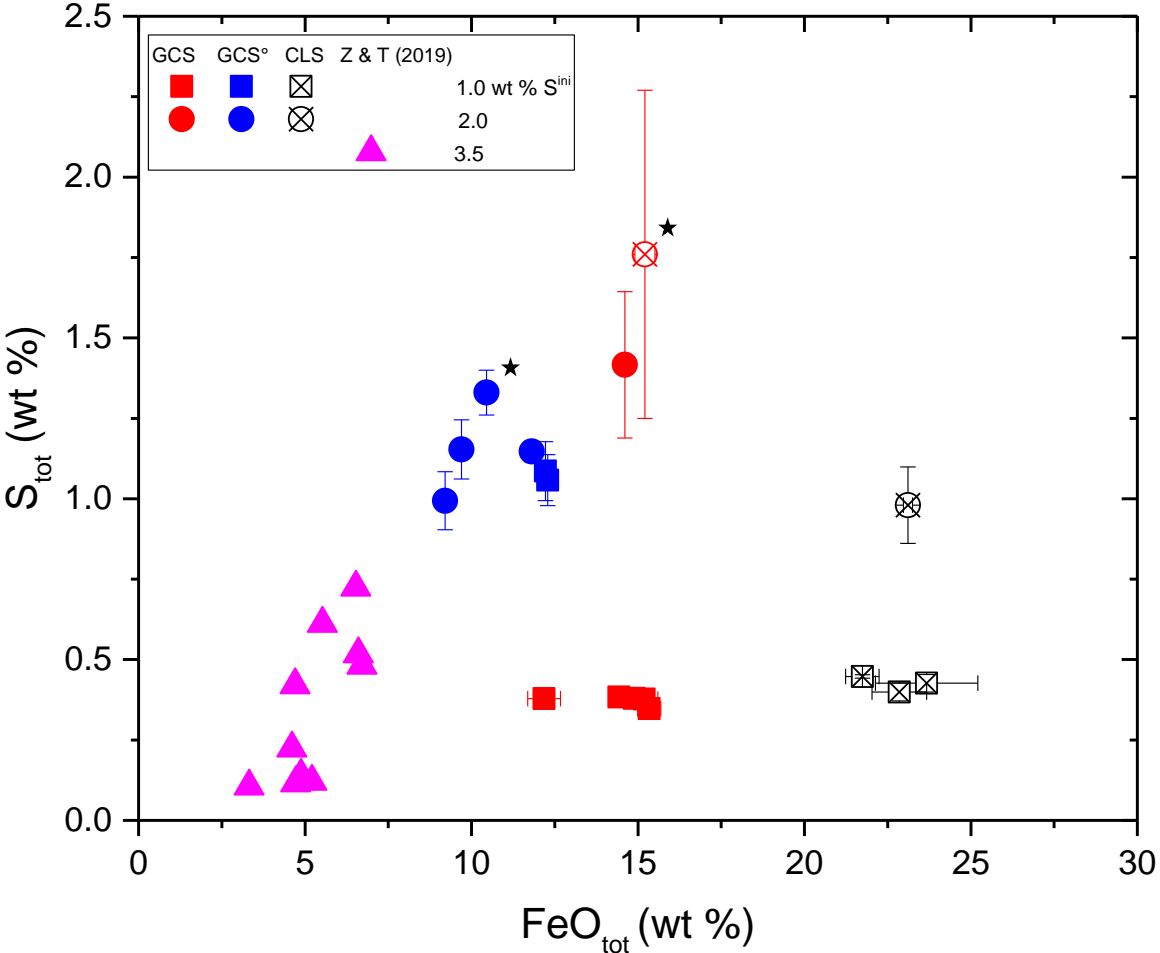
Fig.III.2: S_{tot} in fonction of the FeO_{tot} both determined by SEM analyses. In red are data with S added as $CaSO_4$ for the GC composition, when blue represents the S added as S_0. In CLS samples, S was added only as $CaSO_4$. Distinction between squares and round markers identify when 1 or 2 wt % of S is added initially, except 3 samples where 0.4 wt % of S was added and notified in the graph. Open crossed symbols are for crystallized samples. Pink data are S-saturated basaltic experiments from Tsay and Zajacz (2019). Dark stars represent experiments with 2 wt % H_2O initially added.

Samples with 2 wt % H_2O were also synthesized in both GCS and GCS_0 starting composition. They are reported in Fig.III.1 and III.2. From the GCS composition, no glass could be obtained, which explained the large error bars reported on Fig.III.1 and Fig.III.2 (GCS-2SH-1G, see Table 1) characterizing the heterogeneity of the sample. With the GCS_0 composition and 2 wt % H_2O_{ini}, a glass was obtained (GCS_0-2SH-1G).

Samples	P (GPa)	T (°C)	S_{ini} [a]	SiO_2	σ	Al_2O_3	σ	FeO_{tot}	σ	MgO	σ	CaO	σ	Na_2O	σ	Total [b]	S_f (Raman)	$σ_d$	S_f (SEM)	σ	$Fe^{2+}/\sum Fe$	IFS
GCS-4000S	0.5	1 500	0.40	53.43	54	11.62	16	12.18	49	9.18	37	7.07	5	6.04	11	100	0.11	6	0.38	3	0.43	9.0
GCS-4000-1G	1.0	1 500	0.40	49.42	31	9.99	9	15.34	35	13.58	11	6.04	14	5.13	5	100	n.d	0	0.35	2	0.26	8.8
GCS-1S-1G	1.0	1 500	1.00	49.58	33	10.52	16	14.89	16	13.52	7	6.23	9	4.94	9	100	0.43	6	0.38	2	0.43	8.9
GCS-1S-1,5G	1.5	1 500	1.00	49.40	38	10.46	9	15.19	41	13.47	17	6.17	12	5.00	8	100	0.39	6	0.38	1	0.33	8.7
GCS-1S-2G	2.0	1 500	1.00	49.91	23	10.59	11	14.43	23	13.45	9	6.23	10	5.06	8	100	0.48	6	0.38	2	0.53	8.8
GCS-2S-1G	1.0	1 500	2.00	50.80	22	10.22	9	14.61	10	13.47	10	4.62	10	6.28	9	100	0.83	12	1.42	23	0.53	9.5
GCS-2SH-1G *c	1.0	1 400	2.00	50.37	47	10.04	13	15.21	30	13.15	13	4.73	26	6.50	34	100	n.d		1.76	51	0.37 c	8.8
GCS°-1S-1G	1.0	1 500	1.00	52.15	16	10.43	10	12.22	13	13.92	9	5.24	7	6.03	10	100	0.66	6	1.09	9	0.64	9.2
GCS°-2S-1G	1.0	1 500	2.00	53.53	22	10.70	11	9.70	19	14.46	10	5.34	9	6.27	13	100	0.88	7	1.15	9	0.81	9.2
GCS°-1S-1,5G	1.5	1 500	1.00	51.95	30	10.41	8	12.29	17	14.07	13	5.22	5	6.06	7	100	0.82	13	1.06	8	0.70	9.2
GCS°-2S-1,5G	1.5	1 500	2.00	54.04	55	10.76	15	9.21	28	14.31	25	5.37	9	6.30	7	100	0.92	6	0.99	9	0.82	9.6
GCS°-2S-2G	2.0	1 400	2.00	52.61	30	10.49	8	11.81	16	13.72	11	5.27	6	6.10	17	100	0.81	6	1.15	3	0.80	9.2
GCS°-2SH-1G c	1.0	1 400	2.00	53.45	33	10.46	11	10.45	17	13.90	14	5.67	9	6.07	6	100	1.08	6	1.33	7	0.79	9.2
CLS-4000S*	1.0	1 500	0.40	47.44	53	8.56	11	23.67	154	9.97	18	5.38	35	4.46	13	100	n.d		0.43	3	0.31	8.1
CLS-1S-1G*	1.0	1 500	1.00	47.83	53	8.62	17	22.85	82	10.05	16	5.90	7	4.47	14	100	n.d		0.40	3	0.38	8.2
CLS-1S-1,5G*	1.5	1 500	1.00	48.66	36	8.70	15	21.74	50	9.97	14	5.98	15	4.59	5	100	n.d		0.45	1	0.22	8.2
CLS-2S-1G*	1.0	1 500	2.00	50.19	32	8.01	6	23.11	77	9.78	14	4.03	7	4.88	19	100	n.d		0.98	12	0.44	8.5

Notes:

a : Chemical composition given in wt %

b : Normalization calculated without SO_3

c : Experiments containing 2 wt % H_2O initially

σ : Standard deviation at 10^{-2}

$σ_d$: Error on the homogeneity of the sample or 0.06 wt % (Morizet et al. (2017), see text

S_{ini}: Initial amount of S

S_f: Final amount of S

*: Crystallized experiments, quenched crystals

n.d.: Not determined

Table III.1: Experimental conditions for each sample and the chemical compositions after experiments obtained by SEM analyses. S quantifications determined by Raman spectroscopy according to Morizet et al. (2017) study and by SEM. Fe$_{2+}$/∑Fe obtained by wet chemistry measurements. The NBO/T is calculated considering the major redox state of Fe according to the wet chemistry results. The Ionic Field Strength (IFS) is using the molar fraction of cations calculated in a volatile-free case. See text for the calculation of IFS.

III.4.2. Raman spectroscopy: S quantification and speciation; insight into the degree of polymerization
III.4.2.1. S quantification

A S calibration using Raman spectroscopy has been proposed in the study of Morizet et al. (2017). The calibration is based on measuring the SO_4^{-2} species which is related to S^{6+} content. Prior quantifications, each Raman spectrum needs to be corrected according to the following procedure: 1) the subtraction of the baseline with a 4-order-polynomial degree, with entrenched points between 200 and 220, 800 and from 1150 to 1250 cm$_{-1}$, 2) the attribution of 4 Gaussian peaks is necessary to simulate the silicate matrix of the glass plus 1 Gaussian representing the SO_4^{2-} species. The starting conditions of the simulation (positions and width) for the peaks are:

- Q_2: ~895 cm$_{-1}$, width = 50
- Q_3: ~950, 50
- $Q_{Si-O-Si}$: ~1040, 50
- Q_4: 1090, 50
- QS_{6+}: 1000, 30

The Q_n species represent the number of bridging oxygen with a tetrahedron (Si, Al, Ti of Fe$_{3+}$). The degree n will evolve between 0 and 4; with 0 bridging oxygen describing a depolymerized structure, to 4 bridging oxygens representing a fully polymerized melt. Although the attribution of Q_n species can be debated, we considered these positions according to Rossano and Mysen (2012) and references therein. The $Q_{Si-O-Si}$ is attributed according to Mysen and Frantz (1994) and Frantz and Mysen (1995) studies.

After considerations of this procedure, peak optimization is made until the Chi-square parameter (i.e., the difference between the simulated peaks and the initial spectrum) has reached the lowest possible value (~10$_{-6}$). The S quantification is then possible following the calibration equation proposed by Morizet et al. (2017):

$$(1) \; S^{6+} = 34371 \times \frac{A\,SO_4^{2-}}{A\,Q^n}$$

Here S$_{6+}$ expressed in ppm, A SO$_{4-2}$ (i.e., QS$_{6+}$ species) corresponding to the area of the ~1000 cm$_{-1}$ peak, and A Q$_n$ the total area of the Q$_n$ peaks. The error on the S estimation considering Morizet et al. (2017) calibration is estimated at $\pm$609 ppm S (i.e., 0.06 wt % S). Error values reported in Table III.1 either corresponds to the homogeneity of the sample when > 0.06, or the error determined by Morizet et al. (2017).

The results of the quantification are exhibited in the Table III.1.

Raman spectra of GCS and GCS$_0$ samples are reported in Fig.III.3. A peak at 1000 cm$_{-1}$ is observed, overlapping the glass alumino-silicate network between the 800 and 1200 cm$_{-1}$. The presence of the 1000 cm$_{-1}$ peak indicates the presence of S$_{6+}$ species (Bény et al. 1982; Burke

et al. 2001; Klimm and Botcharnikov; 2010; Wilke et al. 2011; Morizet et al. 2017). We had difficulties to identify reduced S redox state such as S^{2-} which would be bound with metallic cations in low wavenumbers (i.e., 300 - 600 cm^{-1}). Since this region is complex and attributing to multiple vibrations, we cannot decipher the presence of FeS species at 375 cm^{-1} (Wilke et al. 2011; Klimm et al. 2012b). This could be due to the absence or a small amount of such species, which does not permit to identify a specific peak.

For the GCS composition (i.e., initially oxidized), the maximum of S^{6+} species detected in the glass is at 0.8 wt % S^{6+}, for GCS-2S-1G (at 1 GPa and with 2 wt % S_{ini}). The lowest content of S dissolved is for GCS-4000S, at 0.5 GPa and with 0.4 wt % $S_{ini,}$ and 0.1 wt % S^{6+}. Experiments with S^0 as starting material do not show strong differences with oxidized experiments. The highest S^{6+} content is for the experiment in presence of H_2O, with 1.1 wt% S^{6+} (GCS°-2SH-1G) at 1 GPa. For anhydrous S^0 experiments, the maximum S^{6+} obtained is for GCS0-2S-1G and GCS0-2S-2G with ~1.2 wt % S^{6+}
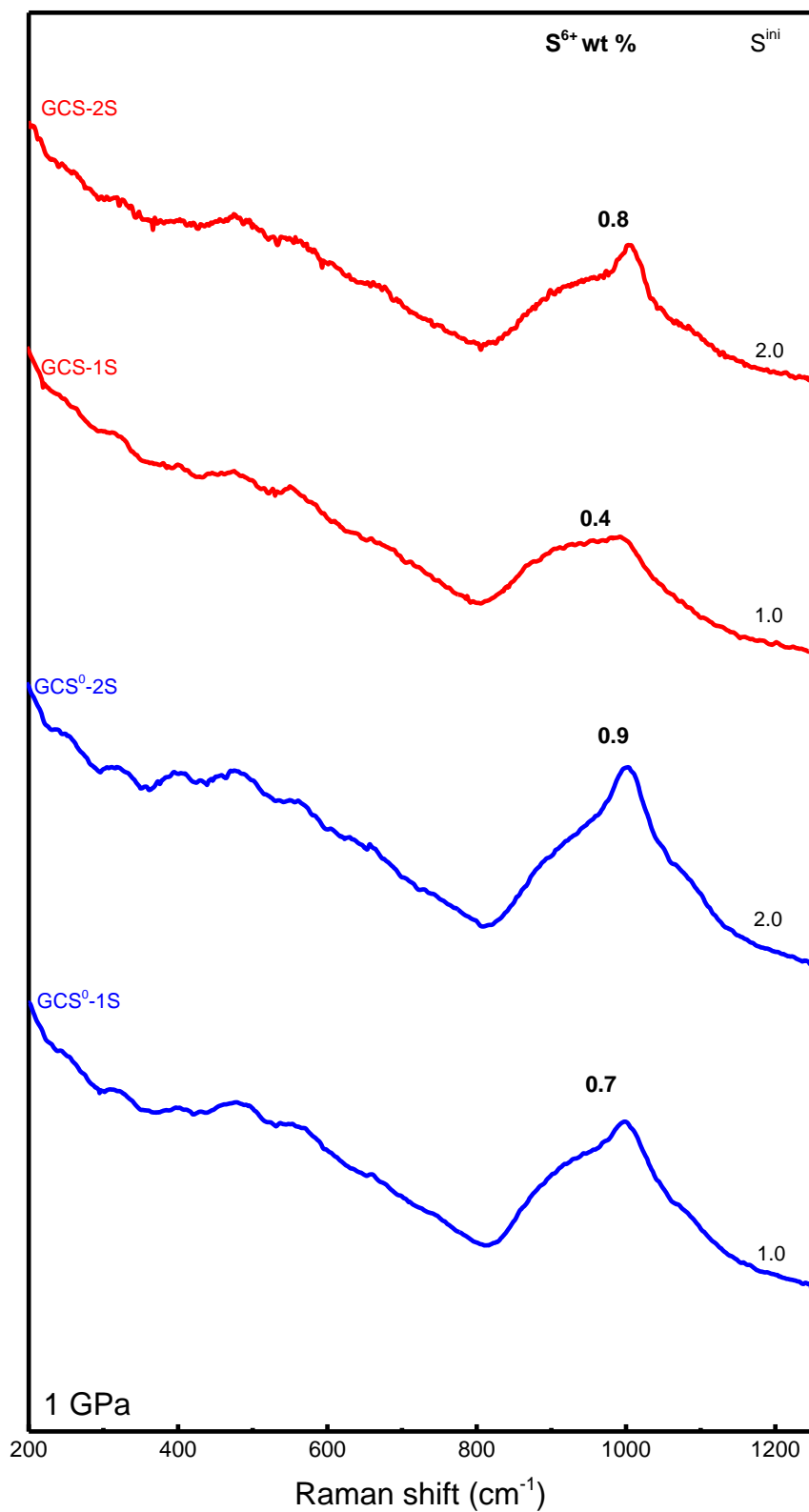
Fig.III.3: Raman spectra of 1 GPa samples in the area of 200 – 1200 cm-1, for samples with S_0 added initially in blue, and $CaSO_4$ in red. Initial content of S is reported on the right side of the graph, and the quantification of S_{6+} has been determined according to Morizet et al. (2017)

In Fig.III.4, the S quantifications by Raman spectroscopy correlated to S determined by SEM are reported. As previously mentioned, the calibration established by Morizet et al. (2017) allows only the quantification of S under its oxidized form, i.e., S^{6+}. We can see from the Fig.III.4 that the glasses have only S^{6+} species. Indeed, for GCS samples with 1 wt % S_{ini}, 0.4 wt % S^{6+} is calculated by Raman and 0.4 wt % S_{tot} by SEM for GCS-1S-1G. For the GCS_0 composition, the results are a bit more distant from the 1:1 line: 0.7 wt % S^{6+} and 1.1 wt % S_{tot}, in GCS_0-1S-1G by Raman and SEM, respectively. The difference between SEM and Raman spectroscopy results can be attributed to the Raman calibration that can be less accurate than SEM analyses. It could also imply a presence of another S redox state.
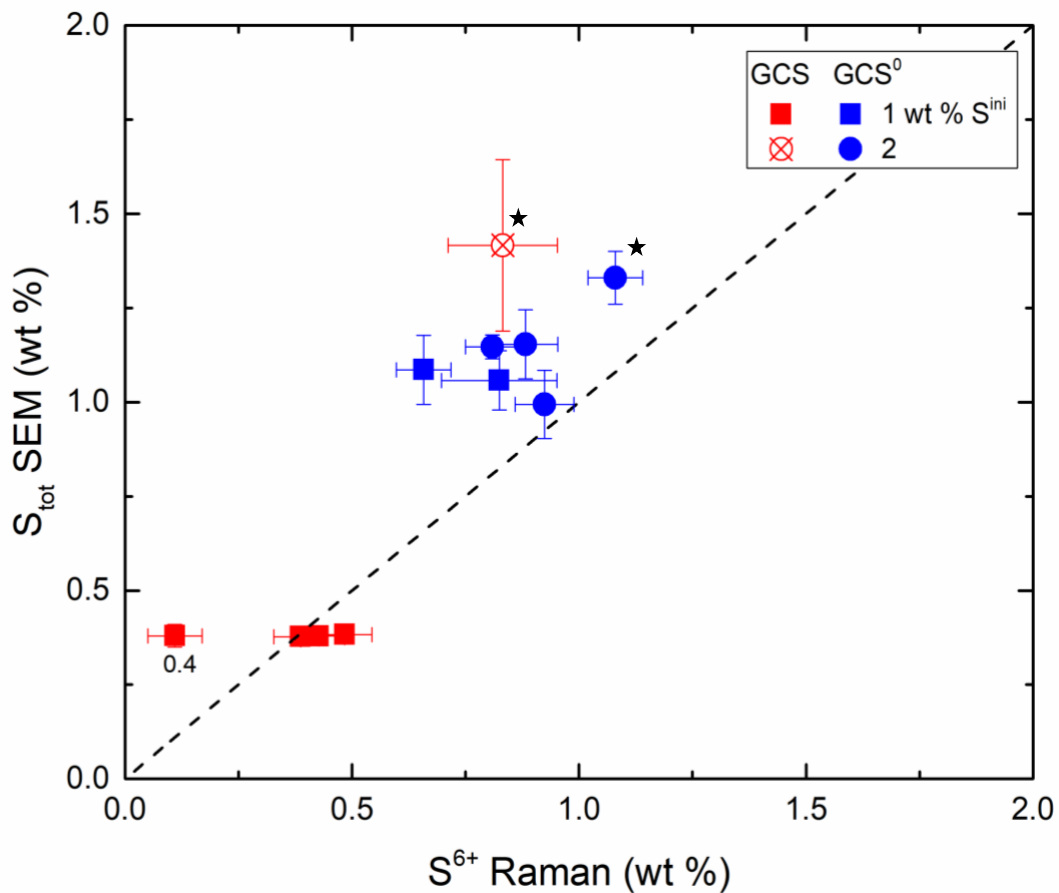
Fig.III.4 : Quantification of S by SEM versus Raman spectroscopy. Results by Raman spectroscopy indicate the S quantification as S^{6+}. In red are data with S added as $CaSO_4$ for the GC composition, when blue represents the S added as S_0. Distinction between squares and round markers identify when 1 or 2 wt % of S is added initially, except 3 samples where 0.4 wt % of S was added and are notified in the graph. Open crossed symbols are for crystallized samples. Dark stars represent experiments with 2 wt % H_2O initially added.

III.4.2.3. Polymerization degree

Typical deconvolutions of the silicate matrix of 1 GPa samples are represented in Fig.III.5. Although the attribution of Q_n species is still debated, we postulate that the Gaussian at the lowest wavenumber is probably coming from Q_2 species vibrations. Indeed, due to the apparent high polymerization degree of the melt, it is unlikely that Q_1 species are present (i.e., 1 bridging oxygen; Mysen et al. 1982). Furthermore, Q_1 species are vibrating at lower wavenumbers (800 – 850 cm$_{-1}$) according to Rossano and Mysen (2009), although our we seemed to be at the limit between the two species (i.e. Q_1 and Q_2) at ~895 cm$_{-1}$. Since we know that an equilibrium is present between Q_n species (Mysen and Frantz 1994), we proposed Q_2 species ~895 cm$_{-1}$, followed by Q_3, $Q_{Si-O-Si}$ vibrations (Mysen and Frantz 1994; Frantz and Mysen 1995), and Q_4 for the highest wavenumber, considering:

(2) $2Q^n = Q^{n+1} + Q^{n-1}$

From the Fig.III.5, we cannot distinguish different behaviors of the Q_n organization inside the silicate matrix for GCS and GCS$_0$ samples. Indeed, deconvolutions of GCS$_0$-2S-1GPa and GCS$_0$-1S-1GPa, exhibit the Q_3 species more abundant compared to Q_4 species height. For the same Q_n species in GCS-1S-1GPa and GCS-2S-1GPa, the same trend is observed; although one could argue that the difference is higher. The intensity between Q_2 and Q_4 although, seems at the relatively same heigh in GCS$_0$ samples, where GCS showed more difference between the two species.

Di Genova et al. (2016) have demonstrated in Fe-rich glasses that the 950 cm$_{-1}$ peak can be attributed to the presence of Fe^{3+} species. Hence, the Q_3 peaks observed can be attributed to Fe^{3+} abundance in Fig.III.5. This will be in accordance with the deconvolution of GCS samples which express a higher 950 cm$_{-1}$ peak. Since wet chemistry indicates a range between $Fe_{2+}/\sum Fe$ = 0.3 - 0.5 for GCS samples and 0.6 - 0.8 for GCS$_0$, it implies more Fe^{3+} species in GCS experiments; hence a 950 cm$_{-1}$ peak higher than for reduced samples (i.e., GCS$_0$).
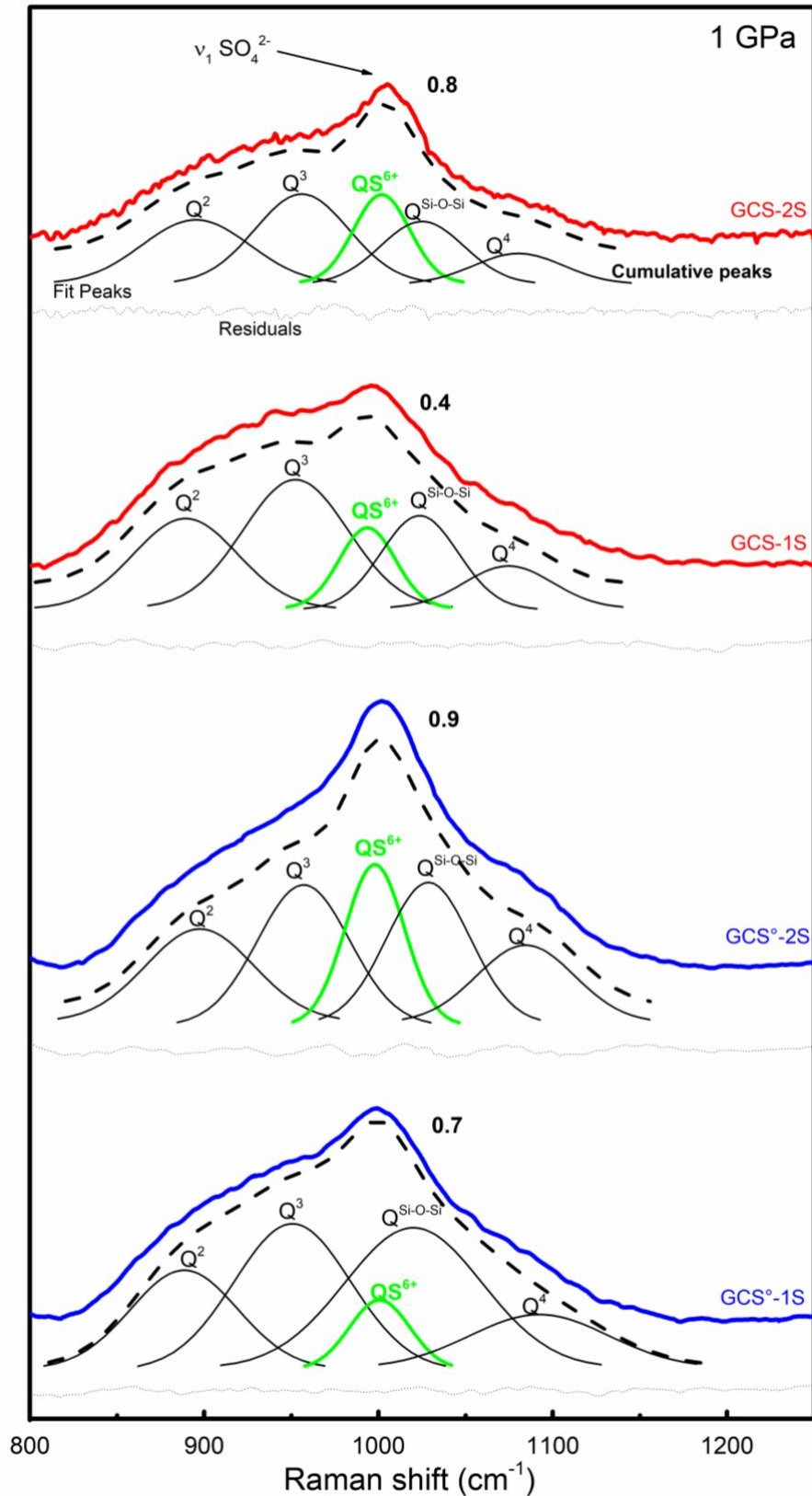
Fig.III.5: Deconvolution of the silicate matrix (800 – 1250 cm-1) of GCS0-1S, GCS0-2S-GCS-1S and GCS-2S samples at 1 GPa. The peaks simulated are in black and the S peak is outline in green. The cumulative peaks of all simulations are black dashed lines and the subsequent residuals are in the black dotted lines.

III.4.3. XPS spectra for elemental speciation: S, Fe and O species

XPS analyses were performed on 5 samples: GCS_0-2SH-1G, GCS-2S-1G, GCS-1S-1G, GCS_0-2S-1G, GCS_0-2S-2G. The area of Fe 3p, O 1s, S 2p and S 2s were investigated and reported in Fig.III.6.

III.4.3.1. Polymerization degree by XPS

The simulations of the O 1s region are reported in Fig.III.6A. Looking at the O 1s signatures for all experiments, we can see that the proportion of Bridging Oxygen is predominant over the Non Bridging Oxygen with the BO and NBO at ~531 and 530 eV, respectively (Nesbitt et al. 2011; Nesbitt and Bancroft 2014). The calculations from simulations show very strong polymerized structure especially for GCS_0-2S-1G with 0.18. The GCS_0-2SH-1G sample exhibits a more depolymerize structure with NBO/T = 0.80, which seems in accordance with the addition of 2 wt % of H_2O_{ini}. For GCS experiments (GCS-2S-1G and GCS-1S-1G) the XPS deconvolutions show a NBO/T= 0.30 and 0.20, respectively (see Fig.III.6A).

In Fig.III.5, we have seen a polymerized structure for GCS_0 and GCS samples. Then, the XPS determination of NBO/T= 0.18 (i.e., polymerized network, see Fig.III.6A) are in accordance with the deconvolution for GCS_0-2S-1G shown in Fig.III.5. For GCS samples, the XPS deconvolutions also tend in favor of Raman simulations with a NBO/T at 0.20 – 0.30 (see Table III.2).

When comparing the NBO/T calculated from XPS deconvolution and theoretical calculations with wet chemistry results, we can see some discrepancies. The results are reported in the Table III.2. The theoretical calculation of the NBO/T will consider either Fe^{2+} or Fe^{3+} as the main species (Brooker et al. 2001). Our calculations are made according to wet chemistry results which indicate the Fe dominant species in our samples. When looking at the theoretical calculations, GCS-1S-1G is the most polymerized at 0.79. GCS-2S-1G shows a more depolymerized structure with NBO/T= 1.06. The GCS_0 samples, on the contrary are all more depolymerized according to the theoretical calculations with a NBO/T~1.10.

We can see from Table III.2 that the difference is marked for GCS_0-2S-1H and GCS_0-2S-2G where 1.12 and 1.10 are calculated theoretically, whereas 0.18 and 0.29 are obtained by XPS, respectively. However, the XPS results seemed in accordance with the theoretical calculation for GCS samples (Table III.2).

III.4.3.2. Fe speciation

For Fe 3p analyses, the Fe^{2+}/Fe^{3+} ratio can be calculated from the peaks attributed in Fig.III.6B, with: Fe^{3+} at ~56 eV and 54 for Fe^{2+} (Mekki et al. 1996). Subsequent deconvolutions of those two peaks are exhibited in Fig.III.6B and the ratios are reported for comparison with wet chemistry results in the Table III.2. GCS_0-2S-2G shows the most intense ratio with Fe^{2+}/Fe^{3+} ~2.0, whereas GCS-1S-1G is at 0.9, favoring the presence of high Fe^{3+} in GCS samples. These results indicate the same trend as wet chemistry since with GCS_0 samples more reduced with GCS_0-2S-1G (Fe^{2+}/Fe^{3+} ~4.1), and GCS-1S-1G, the most oxidized (0.8). However, values are in disagreement for GCS_0 experiments. Indeed, for GCS_0-2S-1G, the ratio by wet chemistry is

at 4.2; where 1.9 is calculated according to XPS deconvolutions. GCS0-2S-2G and GCS0-2SH-1G exhibit the same trend, with 4.1 and 3.7 determined by wet chemistry, against 2.0 and 1.9 calculated with XPS, respectively. On the contrary, GCS experiments do not show the same discrepancies between XPS and wet chemistry results, as seen in Table III.2. The obtained results are quite similar with $Fe_{2+}/Fe_{3+} = 0.8$ and 1.1 for GCS-1-1G and GCS-2S-1G by wet chemistry, and 0.9 and 1.3 with XPS, respectively.

	NBO/T			Fe speciation		
	Initial	Wet chemistry**	XPS	$Fe_{2+}/\sum Fe$ *	Fe_{2+}/Fe_{3+} *	Fe_{2+}/Fe_{3+} XPS
GCS-1S-1G		0.79	0.20		0.76	0.91
GCS-2S-1G		1.06	0.30	0.53	1.11	1.26
GCS0-2S-1G	0.56	1.12	0.18	0.53	4.23	1.95
GCS0-2S-2G		1.10	0.29	0.70	4.09	2.04
GCS0-2SH-1G		3.71	1.87	0.80 0.79	3.71	1.87

Notes:
* Obtained from wet chemistry analyses
** Calculated according to Brooker et al. (2001) considering the major species of Fe obtained by wet chemistry

Table III.2: Comparison between NBO/T and Fe_{2+}/Fe_{3+} parameters calculated with XPS deconvolutions and the wet chemistry. The initial NBO/T calculation (see Brooker et al. 2001) considers Fe as Fe_{3+} due to decarbonation prior the experiment.

III.4.3.3. S speciation by XPS

In Fig.III.6C, the S 2s signatures are reported for 4 samples: GCS-2S-1G, GCS-1S-1G, GCS0-2SH-1G and GCS0-2S-2G. Two peaks can be simulated under the envelope between 220 and 250 eV. The main peak at ~232 eV indicates S_{6+} species (Zhao et al. 2017). For the GCS composition, a second peak is at ~229 eV. For GCS0-2SH-1G and GCS0-2S-2G, the second peak is a little bit lower, ~226 eV. The latter could be attributed to Fe-S species according to Panzner and Egert (1984), Laajalehto et al. (1994), although these studies were not established on Fe-rich glasses in presence of S. On the other hand, the 229 eV peak could be attributed to a lower oxidation state of S such as S_{4+} since it does not correspond to S_{6+} signatures. However, there is currently few XPS study on silicate glasses in presence of S; hence the peak attribution can still be debated.
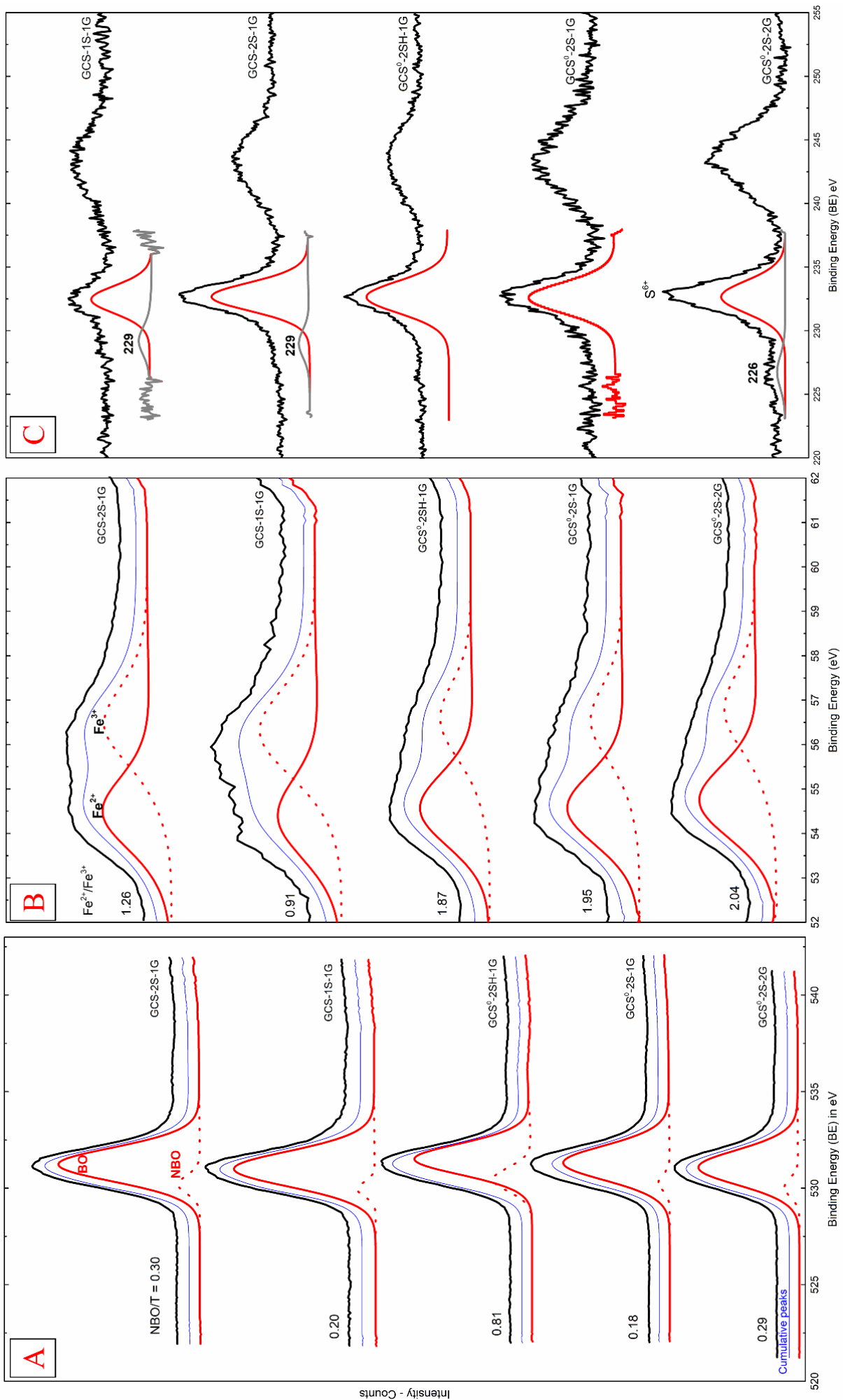
Fig.III.6: A) Spectra from the O 1s area for each sample. Deconvolution of the NBO (red dotted line) and BO (red straight line) are represented along with the cumulative peaks; B) Fe 3p area for the same sample. The red dotted line is attributed to Fe_{3+} contribution whereas the red straight line is Fe_{2+}; C) Spectra of the S 2s region for the same samples as A and B. The main S species is represented in the red peak (S_{6+}) with another specified peak in grey, at lower binding energy (eV), for three samples: GCS-1S-1G, GCS-2S-1G and GCS$_0$-2S-2G.

III.4.3.4. Limits of wet chemistry and XPS analyses

The XPS results have shown strong discrepancies with wet chemistry analyses, notably with the Fe_{2+}/Fe_{3+} ratio for GCS$_0$ samples. These differences could be ascribed to the wet chemistry calibrations. Indeed, this method has been well established for samples containing S_{6+}. However, GCS$_0$ experiments contained at the beginning of the experiment S_0 species, which could flawed the results of wet chemistry. Even if there are only S_{6+} species at the end of the experiments, according to Raman and XPS spectroscopies, it is possible that S_0 species are present at the rim of the samples. On the other hand, few XPS studies have been made on silicate glasses, especially on Fe-rich basalt in presence of S. Since there is clearly a lack of study on silicate glasses containing S by XPS, but also in wet chemistry for these chemical compositions, it is difficult to decipher which methods give the best results.

Furthermore, the NBO/T calculated according to Brooker et al. (2001) considering wet chemistry results, and the XPS calculations are also distant for reduced glasses (GCS$_0$). Indeed, the theoretical method will consider the main Fe species (i.e., Fe_{2+} or Fe_{3+}) as the only Fe presents in the glass. However, it is known from previous studies that both redox states can coexist in the melt. These differences can be due to the role the Fe plays in the melt. Indeed, previous studies have shown that Fe_{2+} could play the role of both network modifier and former; which is also the case for Fe_{3+} (Mysen et al. 1982). The XPS results for GCS$_0$ experiments show that melts are strongly polymerized compared to the theoretical calculation considering Fe_{2+} as a network modifier. The calculated polymerization by XPS is also observed in the deconvolution of GCS$_0$ spectra in Fig.III.5. Then, Fe_{2+} may play a role of network former in GCS$_0$ sample. On the other hand, Fe-S species may be present for GCS$_0$-2SH-1G and GCS$_0$-2S-2G, according to XPS measurements. The formation of Fe-S clusters could be at the origin of the polymerization of the melt. However, such signatures were not observed for GCS$_0$-2S-1G. Further investigation on the Fe environment is required to better characterize the species formed in GCS$_0$ experiments.

On the opposite, GCS samples do not show a great difference between the two NBO/T methods, which indicate that the Fe_{3+} may have the solely role of network former and Fe_{2+} network modifier.

III.4.4. S and Fe redox speciation

The combined results by wet chemistry and XPS have shown that the GCS$_0$ have endured significant reduction with respect to Fe. Indeed, the initial Fe redox state was Fe_{3+}, due to decarbonation prior the experiments. According to Kägi et al. (2005), the piston-cylinder

buffers the experiment around QFM +1 (i.e., Quartz-Fayalite-Magnetite). However, GCS composition does not exhibit the same redox results. Instead, the Fe ratio favors the Fe^{3+} as the predominant species with the $Fe^{2+}/\sum Fe$ varying from 0.3 – 0.5 for GCS (Table III.1), whereas GCS_0 range is between 0.6 – 0.8. For GCS experiments, the piston-cylinder apparatus must induce the presence of some Fe^{2+}, since Fe^{3+} was the started Fe redox state. However, the buffering of the device is not enough to reduce S^{6+} which was the initial redox state of S for GCS samples; although S^{4+} species may be present according to XPS spectra (i.e., ~229 eV, Fig.III.5C).

Since the Fe redox state is even more reduced for GCS_0 samples, another phenomenon must reduce the conditions in the experiment. GCS_0 samples were prepared with S^0 as initial S. We were expecting to observe reduced S species by XPS analyses. However, according to Fig.III.6C, S^{6+} is the main species for all GC experiments (including both GCS and GCS_0). In addition, Raman spectra exhibit the 1000 cm$_{-1}$ peak which correspond to $SO_{4^{2-}}$ species in Fig.III.5 (i.e., S^{6+}). Comparisons with SEM and Raman S results (see Fig.III.4) also show the same conclusion: S^{6+} is the only S species presents in the Fe-rich glassy samples. No other S redox state has been detected by both Raman and XPS spectroscopies.

Then, the S has been strongly oxidized for GCS_0 experiments, which permits to go from 0 to +6 redox state. Then, the reduction occurring during the experiment could be described as:

(3) $\frac{1}{2}O_2 + Fe_2O_3 + S^0 \rightarrow SO_4^{2-} + 2Fe^{2+}$
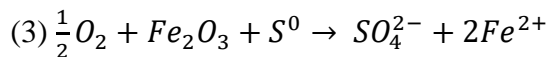
This chemical reaction could explain the large amount of Fe^{2+} in GCS_0 species detected by wet chemistry and XPS (Fig.III.6B and Table III.2). Raman deconvolutions of GCS_0 experiment do show a smaller Q_3 peak (i.e., Fe^{3+} abundance according to Di Genova et al. 2016) which favors the high Fe^{2+} content in these samples. However, there is still an uncertainty for a lower binding energy peak detected by XPS (Fig.III.6C), which could be related to FeS species for GCS_0-2S-2G. This peak could imply that there is also a reduced species of S in this high pressure and reduced sample.

III.5. A new S-solubility model
III.5.1. Introduction to the S solubility

From both SEM and Raman S quantifications, we observe that the S solubility is different for oxidized (i.e., GCS) and reduced compositions (i.e., GCS_0). The maximum of S solubility is measured at 1.4 wt % with the SEM for GCS-2S-1G when 2 wt % S was initially added. Since these experiments possessed sulfate crystals, the quantification by Raman spectroscopy was not possible. The presence of sulfate crystals indicates the sulfate saturation. Alternatively, the maximum solubility for reduced samples is at 1.1 wt % for GCS_0-2S-2G and GCS_0-2S-1G, with 2 wt % S_{ini}. The same experiment with 1 wt % S_{ini} also dissolves ~1.1 wt % S, according to SEM analyses, for GCS_0-1S-1G. Then, we can reasonably assume that the GCS_0 with 2 wt % S_{ini} were S-saturated, although no sulfate crystal was found. However, further experiments are required, with higher S_{ini} to better constrain the S solubility in these compositions. Interestingly, the GCS_0-2SH-1G sample, with 2 wt % H_2O_{ini} and S_{ini}, possesses the highest S content with 1.3 wt % (see Table III.1); although it can be considered close to GCS_0-2S-1G and GCS_0-2S-2G within analytical errors.

Since we obtained new results on S solubility in Fe-rich experiments at high pressure, we performed a solubility model. Many S solubility models have been proposed in the past 50 years. Baker and Moretti (2011) have described the main models established in their review.

In Fincham and Richardson (1954) experimental study on S behavior in silicate melt, they have defined the dissolution mechanism of S according to the oxygen fugacity prevailing in the system. Hence, at low oxygen fugacity, S is dissolved mainly as S_{2-} according to the following equation:

$$(4) \frac{1}{2} S_2^{fl} + O^{2-\,melt} = \frac{1}{2} O_2^{fl} + S^{2-\,melt}$$
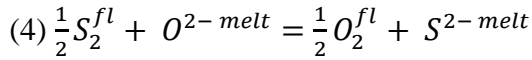
With S_2 presents in the fluid phase at the beginning of the experiment.

On the contrary, at high oxygen fugacity, the S will preferentially dissolve as S_{6+}:

$$(5) \frac{1}{2} S_2^{fl} + \frac{3}{2} O_2^{fl} + O^{2-\,melt} = SO_4^{2-\,melt}$$
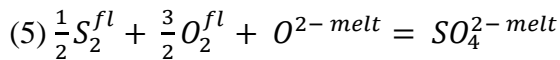
Rosenqvist (1951) introduced in this study the notion of S maximum capacity, which is also described in the study of Fincham and Richardson (1954). This notion infers to the maximum amount of S dissolved considering either oxidized, or reduced conditions. In that way, at high oxygen fugacity the S capacity is controlled by the Sulfur Concentration at Anhydrite Saturation (i.e., SCAS), or Sulfur Concentration at Sulfide Saturation (i.e., SCSS) at low oxygen fugacity. Following the previous equilibrium (eq. 4 and 5), the SCSS and SCAS laws can be written as:

$$(6) S_{SCSS} = Cs \times \frac{fO_2^{1/2}}{fS_2^{1/2}}$$

$$(7) S_{SCAS} = Cs \times \frac{1}{fO_2^{3/2} \times fS_2^{1/2}}$$

Cs defines the maximum S Capacity dissolved in the melt, which could approximatively describe the S solubility. According to the previous equations, it is clear that the solubility of S is recorded, in part, by the oxygen fugacity and the fugacity of S_2 prevailing in the system. This has been already attested in the study of Haughton et al. (1974).

Mavrogenes and O'Neill (1999) introduced in their S solubility law, the Fe content parameter for their sulfide saturation experiments in anhydrous basaltic and picritic melts at high pressures. Holzheid and Grove (2002) improved this model by the addition of the melt compositional parameter implemented as the NBO/T. Models were also developed in various melt composition and in hydrous conditions such as the work of Clemente et al. (2004) on sulfide and sulfate saturation in hydrous rhyolite melt composition. Liu et al. (2007) developed a SCSS model considering T, P, XH_2O, XFeO and the MFM parameter. The latter is a compositional parameter taking into account cation mole fractions such as Na, K, Ca, Mg, Fe_{2+}, Si, Al and Fe_{3+}. Recently, Zajacz et al. (2019) have created a new solubility model at sulfate saturation. In this computational study of 189 sulfate-saturated experiments, they have developed a model based on the NBO/T parameter to implement the chemical composition impact. Since it is only based on SCAS results, the model does not depend on the fO_2 and fS_2, but only on T, P, NBO/T and H_2O content. If this recent model predicts with a very good accuracy the SCAS from basaltic to rhyolitic composition, it cannot be applied for reduced conditions. Hence, up to now, there is no S solubility model considering both SCSS or SCAS results.

III.5.2. Model parameters

To establish our S solubility model, a database made on 156 S-bearing glasses were tested including the 6 S-saturated samples in this study: GCS°-2S-1SG, GCS°-2S-1.5G, GCS°-2SH-1G, GCS°-2S-2G and GCS-2S-1G, GCS-2SH-1G. CLS experiment were not added to the model because of the complete crystallization of the samples. S-saturated data were chosen to complete the experiments of this study: Luhr (1990), Clemente et al. (2004), Liu et al. (2007), Costa et al. (2008), Lesne (2008), Morizet et al. (2013), Masotta and Keppler (2015), Zajacz et al. (2015), Zajacz (2019). Then, the range of pressure and temperature implemented in the model are between ~0.3 – 20 kbars and ~800 – 1500 °C, respectively. The S and H_2O content varied from ~70 – 20 000 ppm S and ~0 – 100 000 ppm H_2O (i.e., from 0.007 – 2 wt % S and 0 – 10 wt % H_2O, respectively). We have limited the experiments with $S_{ini} > 6$ wt %. This wide database allows us to span from NNO - 2.3 to + 0.6 (i.e., Nickel-Nickel-Oxygen) in fO_2 (or QFM – 2.8 to +1).

The model is based on nine parameters, which includes: P, T, H_2O content, S_{ini}, fO_2 and compositional parameters.

We have calculated the Ionic Filed Strength of each sample, which refers to interaction between cations within the melt (see Morizet et al. 2017). It is defined as:

$$(8)\ IFS = \frac{\sum(X_i \times \left(\frac{z}{r^2}\right)i)}{X_O \times \frac{z_O}{r_O^2}}$$

Where X represents the molar fraction of a cation i, z and r the charge and radius of the cation respectively, and X_O the molar fraction of oxygen. At a given cationic charge, the more the IFS is high, the more the composition is enriched in small ionic radius such as SiO_2. Typically, rhyolites possess a high IFS (i.e., > 13) where kimberlites (Si-poor melt composition) are < 9. Our GC experiments varied from IFS = 8.1 to 9.6, which does not represent a wide chemical composition variation (see Table III.1). We have chosen to use the IFS parameter to implement each cation and its coordination state in the melt composition. With this, it allows us to have a better investigation of the melt composition impact on the S solubility. From the Fig.III.7A, we represent the impact of the IFS on the S solubility. As we can see from this figure, there is a strong increase in the S solubility with decreasing the IFS, toward silica-poor melts. From the results exhibited in Fig.III.7A, we can see that the trend is not linear.

The polymerization degree could also be a parameter impacting the S solubility. As shown in previous studies, and recently in Zajacz (2019), the S is strongly dependent on the polymerization of the melt. We reported the calculated NBO/T of each data in Fig.III.7B. From it, a clear trend is observed with an increase of S solubility with increasing NBO/T, i.e., with increasing the depolymerization. However, the trend exhibited is non-linear and another fit could be better appropriated.

The initial S added in oxidized samples had a strong effect on the S dissolved. Indeed, the addition of 1 wt % S resulted in ~0.4 wt % S in GCS experiments. Increasing the S_{ini} at 2 wt %, permits the dissolution of > 1 wt % S (see Table III.1). However, this trend was not observed for experiments with S_0 as starting material. In the Fig.III.7C, we have plotted the initial S content compared to the ln S measured in the samples. From the results of Clemente et al. (2004), we can observe a non-linear trend which show a small increase in S dissolved with

increasing intial S content; although a flat is appearing around 30 000 ppm S_{ini}. On the other hand, this trend is not clear from the other data.

The redox conditions play also a role as demonstrated by Haughton et al. (1974) study. In Fig.III.2B, we have seen that the same amount of S can be dissolved in reduced sample with high $Fe_{2+}/\Sigma Fe$ (0.6 - 0.8) compared to oxidized glasses (0.3 - 0.5). This could be the S dissolved mainly as S_{6+} in our glasses. When looking at the Fig.III.7D on the various fO_2 investigated in our model, we can see a sigmoïdal trend. The redox conditions were calculated according to Kress and Carmichael (1991) law for the literature data. In our experiments, the proposed fO_2 calculations cannot be applied on our Fe-rich compositions according the work of Righter et al. (2012). Hence, we have postulated that the saturated GCS experiments were buffered by the piston-cylinder apparatus, hence at QFM +1 according to Kägi et al. (2005). Since, the GCS_0 experiments showed a Fe redox state more reduced, we proposed a fO2 around QFM. Toward reduced conditions (to $\ln fO_2 – 25$) the S solubility decreases with decreasing fO_2. Then, below $\ln fO_2 = -25$, the S solubility increases again. This trend has already been seen in previous works such as in Nilsson and Peach (1993) and Moretti and Ottonello (2003).

We have seen that P have little effect on S solubility in Fig.III.1. Several studies have experimented the S solubility with pressure, which showed that the results vary with the melt composition, and experimental settings. Where Mysen and Popp 1980 and Zajacz (2019) observed an increase of solubility with pressure, Wendlandt (1982) and Mavrogenes and O'Neill (1999) determined the opposite behavior in their studies. From Fig.III.7E, the trend is not clear. When looking at our results coupled to Lesne (2008), Morizet et al. (2013), Zajacz et al. (2015), Zajacz (2019), we can distinguish a small decrease in S solubility with decreasing pressure; although it could be considered at stable.

In the present work, Gaillard et al. (2013) attest in their work that T has a role on S solubility. We did not observe an increase of S solubility with increasing T in our experiments. However, the temperature range was only varying between 1400 to 1500 °C. When looking at the Fig.III.7F, representing all the data from the model, we can see a trend of an increasing S dissolved in the melt with increasing temperature, which seems in accordance with the work of Gaillard et al. (2013).

121
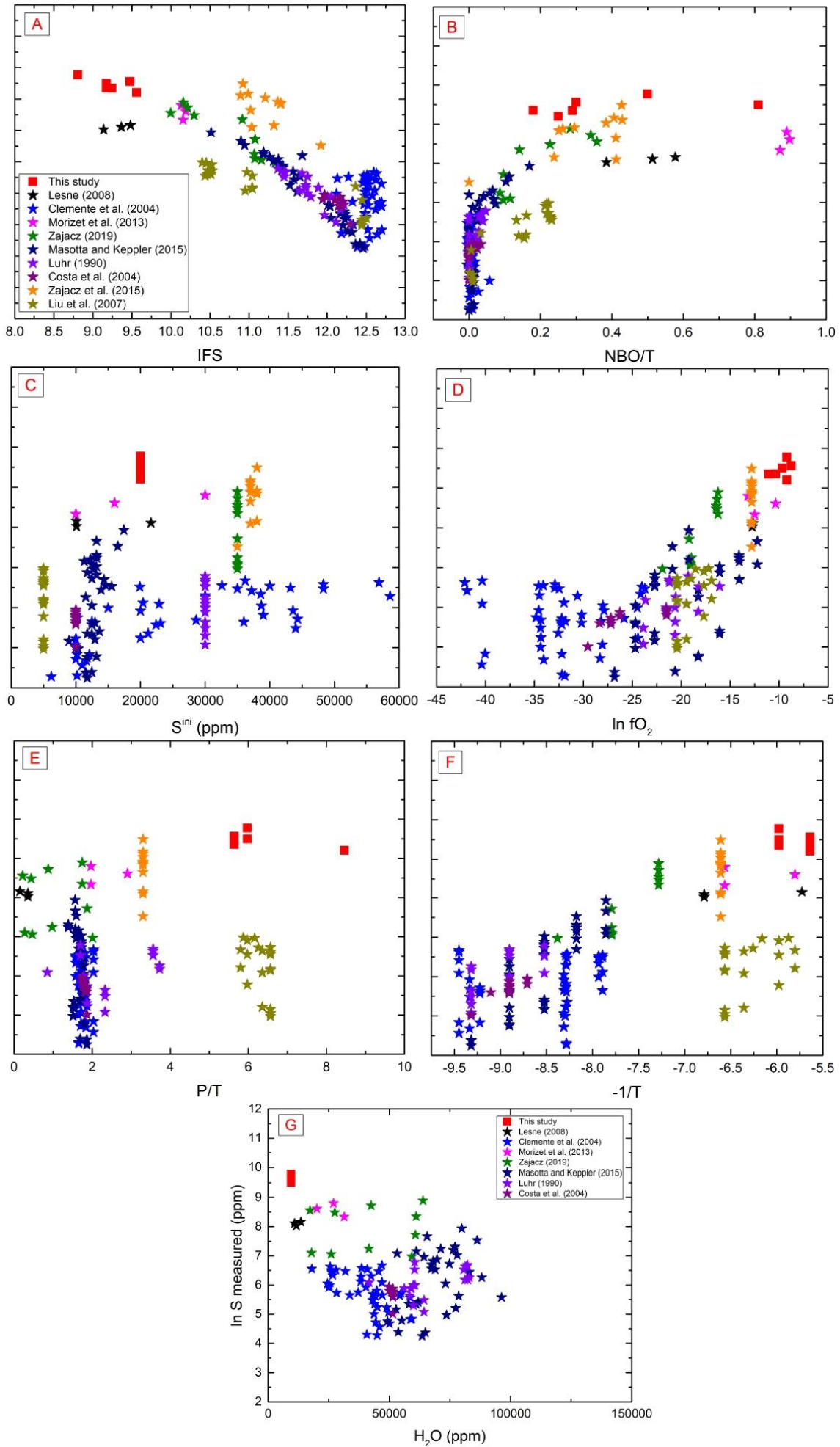
Fig.III.7: Presentation of the different parameter impact used in the model of S solubility: A) IFS; B) NBO/T; C) Initial S content (ln S_{ini}); D) Oxygen fugacity ($lnfO_2$); E) Pressure ; F) Temperature (in Kelvin); G) H_2O content (ppm).

Finally, in Fig.III.7G, we can see the effect of H_2O on the solubility of S. The results show that the addition of H_2O tends to decrease the S solubility in the melt. We can see that the composition of Masotta and Keppler, which are the most hydrous (~100 000 ppm H_2O), presents a ln S = 5.5 for almost 10 wt % H_2O for the less hydrous glasses (< 10 000 ppm); but their experiments do not show a specific trend. On the contrary, the work of Clemente et al. (2004) seems to present an increase in the S dissolved in the melt with the decrease of H_2O content. Although the trend is not clear, we can postulate that the S is impacted by the H_2O present in the system regarding the Fig.III.7G, but the chemical composition may be playing a role.

Consequently, according to the Fig.III.7 and the previous investigations on S behavior in silicate melt, we have developed a model based on thermodynamically laws to get a semi-empirical model considering T, P, S_{ini}, H_2O, fO_2, the IFS and the NBO/T.

For a given P and T, the relationship between S in the silicate melt and the S in the fluid phase can be described as an equilibrium between the chemical potential (μ) of S in the melt and in the fluid phase:

$$(9)\ \mu_S^{P,T\ m} = \mu_S^{P,T\ fl}$$

With m for melt and fl for fluid. The equilibrium can be developed:

$$(10)\ \mu_S^{0,T\ m} + RT\ln(a_S^m) = \mu_S^{0,T\ fl} + RT\ln(a_S^{fl})$$

Where:

$$(11)\ a_S^m = X_S^m \times \gamma_S^m$$
$$(12)\ a_S^{fl} = P \times \varphi_S^{fl} \times X_S^{fl}$$
$$(13)\ a_S^{fl} = \frac{f_S^{P,T\ fl}}{f_S^{1,T\ fl}}$$

Where a_S^m and a_S^{fl} the activity of S in the melt and the fluid phase, respectively. With X_S^m γ_S^m, the molar fraction and coefficient activity of S in the melt, and φ_S^{fl} X_S^{fl} the activity coefficient and molar fraction of S in the fluid phase. Then:

$$(14)\ \mu_S^{0,T\ m} + RT\ln(X_S^m) + RT\ln(\gamma_S^m) = \mu_S^{0,T\ fl} + RT\ln(\frac{f_S^{P,T\ fl}}{f_S^{1,T\ fl}})$$

X_S^m corresponds to the molar fraction of S in the melt, γ_S^m is the activity coefficient of S and f the fugacity of S in the fluid phase.

We know that:

$$(15)\ \mu_S^{0,T\ m} - \mu_S^{0,T\ fl} = \Delta G$$

The variation of the two chemical potentials corresponds to the Gibbs energy. This energy represents the transformation of S from the fluid phase to the melt phase. This energy depends on the variation of three parameters:

(16) $\Delta G = \Delta H + T\Delta S + \int P\Delta V$

Where H represents the enthalpy, S the entropy and V the partial volume.

Thus, if we incorportate the equations 15 and 16 into the 14:

(17) $\mu_S^{0,T\,m} - \mu_S^{0,T\,fl} + RT\ln(X_S^m) = RT\ln(\frac{f_S^{P,T\,fl}}{f_S^{1,T\,fl}}) - RT\ln(\gamma_S^m)$

(18) $RT\ln(X_S^m) = RT\ln(\frac{f_S^{P,T\,fl}}{f_S^{1,T\,fl}}) - RT\ln(\gamma_S^m) - (\Delta H + T\Delta S + \int P\Delta V)$

(19) $\ln(X_S^m) = \ln(\frac{f_S^{P,T\,fl}}{f_S^{1,T\,fl}}) - \ln(\gamma_S^m) - \frac{\Delta H}{RT} - \frac{\Delta S}{R} - \int \frac{P\Delta V}{RT}$

To simplify the thermodynamical model, we have made some approximations to obtain a semi-empirical model, such as:

(20) $\frac{f_S^{P,T\,fl}}{f_S^{1,T\,fl}} = f_{S_2}^{fl}$

(21) $\gamma_S^m = IFS$

(22) $\frac{\Delta H}{RT} = \frac{H}{T}$

(23) $\int \frac{P\Delta V}{RT} = \frac{P}{T}$

(24) $\frac{\Delta S}{R} = constant$

Coupling the approximations in eq. (20) to (24) into the equation (19), we obtain:

(25) $\ln X_S^m \propto \ln(f_{S_2}) - \ln(IFS) - \frac{H}{T} - \frac{P}{T} - cst$

From these demonstrations, a semi-empirical model has been proposed following the trends observed in Fig.III.7, and adding the initial S and H_2O content:

(26) $\ln S\,(ppm) = -\frac{a}{T} + b \times \frac{P}{T} + c \times \ln fO_2 + d \times (\ln fO_2)^2 + e \times \ln S^{ini} + f \times IFS +$
$$g \times IFS^2 + h \times \ln(1 + \frac{NBO}{T}) + i \times H_2O$$

With T in K, P in bars, S_{ini} (i.e., initial content of S) and H_2O in ppm.
Parameters a to h are constants determined by the model using DROITEREG matrix. They are listed in the Table III.3 below.

a	0.62439
b	-0.02662
c	0.19612
d	0.00386
e	0.81464
f	1.69623
g	-0.10436
h	-0.02974
i	8.28651×10^{-6}

Table III.3: Parameters obtained for the solubility model of S in equation (26). The R^2 obtained is at 0.90.

The results from equation 26 on our 156 data are exposed in the following section.

III.5.3. Applications and limitations of the model
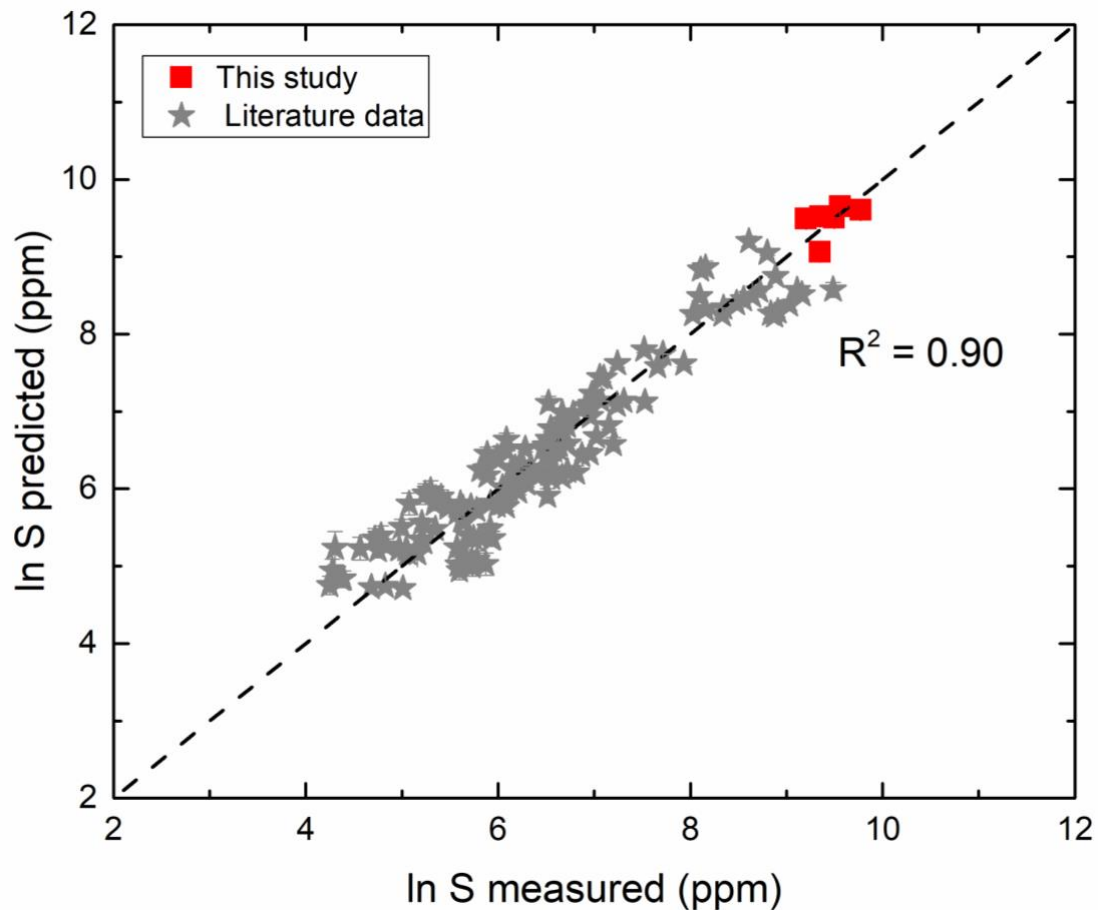
Fig.III.8 :S measured in samples versus the S calculated according to the model equation (26). Data from the literature (see text for references) are represented in grey stars. Red squares are S saturated data obtained in this study. The R^2 represents the linear regression coefficient defining the quality of the model. The black dotted line corresponds to 1:1 line.

The chemical composition in this proposed model include rhyolites, dacites, basalts, Fe-rich basalts and haplo-basalt. From eq. (26), we have quantified the impact of each factor on the new solubility model. The chemical composition parameter, IFS, impacts at ~70 % the S solubility, followed by the initial S contet ~16 %. The oxygen fugacity will affect the S solubility up to 13 % according to the model. Then the H_2O content is at 1 % impact. The rest is attributed to P, T and NBO/T.

In the Fig.III.8., we have exposed the ln(S) predicted by the model (eq. 26) in the x-axis versus the ln(S) measured in various samples. The model well predicts the data considering the wide variety of samples taken into account (i.e., fO_2, H_2O bearing glasses, melt composition, P, T). The data are less constrained for the bottom and top end of the graph, for extremely low and to high S content.

The model predicts with accuracy the solubility of S up to 2 wt %. It could be improved with glasses with higher S content dissolved. Morizet et al. (subm.) have determined than more than 2 wt % can be dissolved in a haplo-kimberlitic composition, but saturation was not reached. This implies that kimberlites could dissolved higher S content. Saturation data on this Si-poor composition could be implemented and improved the present model to reproduce higher S solubility (> 3 wt%).

On the other hand, the model simulates the data with accuracy even at very low S content (70 ppm). Hence, we could attest that the S solubility model established here reproduces S measured in samples between 0 – 20 000 ppm S (0 – 2 wt % S).

Even though we have created a new model presenting the S solubility in a wide range of chemical composition (from basalt to rhyolite), fO_2 and various P, T, and H_2O content, the model presents some limitations. The recovered equation to determined S solubility needs the knowing of the initial S content in the melt source. For natural magmas, this information is sometimes lacking. Nonetheless, the model could be use in at the reverse for natural applications. Indeed, in that case, the recovered natural volcanic glass will present the final S recorded and will maybe contains vitreous inclusions trapping the S dissolved at depth prior degassing. With this value, the initial S present in the magmatic source can be obtained with equation (26).

On the other hand, with the knowing of the partial melting and the S presents in the terrestrial crust/mantle, we can find the S available at depth. For Mars, the S at depth in the core and mantle from cosmochemical constrains and geodetic data (Wänke and Dreibus 1997; Rivoldini et al. 2011) have been determined at 14 -18 wt % S and ~2000 ppm S, respectively; even though Gaillard and Scaillet (2009) suggested this latter value as a upper limit. According to Gaillard and Scaillet (2009), with 10 to 20 % partial melting, 0.35 to 1.8 wt % S can be expected in the primary mantle martian basalt at depth. Then, the solubility of S according to this S initial available at depth, fO_2, H_2O content, P, T and melt composition can be calculated for Fe-rich melts such as martian basalts.

III.5.3. Implications for Mars

The new solubility data obtained in this study at high pressures show that the S in Fe-rich melt (from 9 to 23 wt % FeO_{tot}) can exceed 1 wt %. Righter et al. (2009) have proposed an upper

limit in primary martian basalt close to Shergottites composition, to be at 4000 ppm (i.e., 0.4 wt % S) at sulfide saturation. Gaillard and Scaillet (2009) proposed from modelling data a range of 4000 - 7000 ppm for martian basalts at 1300 - 1400 °C. These values could be in accordance with ours since we performed our experiments at 1500°C. Indeed, referring to Gaillard and Scaillet (2009) models, at 1500 °C the S dissolution increases up to 12000 ppm at 1 GPa (i.e., 1.2 wt % S). However, in our results we did not observe an increase in S solubility with increasing T. For instance, when looking at the Table III.1, we can reasonably compare GCS_0-2S-1.5G and GCS_0-2S-2G since the P does not affect the S solubility (Fig.III.1): ~1 wt % S dissolved at 1500°C, for 1.1 at 1400°C, respectively.

The fO_2 experimented in our work is different from Righter et al. (2008) and Gaillard and Scaillet (2009) studies. Indeed, our experiments were performed with no fO_2 control. The study of Kägi et al. (2005) proposed a fO_2 buffering of the piston-cylinder at QFM+1. We did not calculate the fO_2 from the Fe^{2+}/Fe^{3+} ratio obtained by wet chemistry due to the difficulty to obtain accurate fO_2 with actual calibration. Indeed, Righter et al. (2012) demonstrated in their study that the fO_2 calibration method proposed by Kress and Carmichael (1991) cannot applied on Fe-rich compositions. Nonetheless, we have seen from wet chemistry measurement that GCS_0 experiments were strongly reduced with respect to Fe compared to GCS samples. Previously, we have postulated that GCS samples were controlled by the buffering of the piston-cylinder, and hence could have recorded a fO_2 at QFM+1. Due to the strong Fe^{2+} abundance in GCS_0 experiments, we can reasonably assume that the fO_2 is below QFM+1.

The fO_2 in martian interiors is still debated. While there is quite an agreement on the primitive martian mantle redox state controlled by the Iron-Wüstite buffer (i.e., IW; Wadwha 2008), some suggested more oxidized layers, notably for the crust that could be oxidized up to the QFM buffer (Herd et al. 2002; Herd 2008; Schmidt et al. 2013). The range of fO_2 experimented in our study could be down to the QFM buffer with GCS_0 samples. Hence, the results of S solubility obtained in this study could be applied for Mars. We, therefore, suggest a maximum of S solubility in Fe-rich melt at ~1 wt % S. Then, we can argue with the upper limit of S solubility in Fe-rich melt proposed by Gaillard and Scaillet (2009) and extent the range of S in martian basaltic melt between 4000 - 10000 ppm (i.e., 0.4 - 1.0 wt % S).

III.6. Conclusion and perspectives

In this study, we have performed Fe-rich glasses at S saturation at high pressures (0.5 - 2 GPa). Two experiments were made: with S^{6+} and S^0 as started material. We have found that the maximum of solubility in a Fe-rich melt is at 1.4 wt % S dissolved as S^{6+}, in the initially oxidized composition. For initial reduced samples (containing S^0), the maximum of solubility is at 1.3 wt %. At the end of the experiment all the S^0 has been oxidized into S^{6+} as revealed by both Raman and XPS spectroscopies. Fe-S species has been maybe identified by XPS, but also in Raman spectroscopy at low wavenumbers, although the signal is not predominant and may be not present.

The configuration of Bridging and Non Bridging Oxygen in the Fe-rich glasses observed with XPS suggests a strongly polymerized structure whereas theoretical calculations proposed the opposite for reduced initial composition (i.e., GCS_0). The role of Fe between network modifier and network former seems to play a role in these compositions. Formation of FeS species could

be at the origin of the polymerization for GCS_0 glasses. Further investigation of the Fe nearest neighbor in these atypical S-rich melts is needed.

From solubility data obtained on Fe-rich glasses ($9 < FeO_{tot}$ wt % < 24) and a compilation of S-saturated experiments of the literature, a model of S solubility has been proposed. This new model is based on both the Ionic Field Strength and NBO/T parameters. The IFS will represent the presence of all the cations present in the melt (including volatile species) and the NBO/T will define the degree of polymerization of the melt (anhydrous basis). The model is also dependent on the H_2O content, fO_2, S initial (ppm), P (bars), T (K). With 156 data, this model predicts S solubility from basaltic to rhyolitic melt composition and for various oxygen fugacities (NNO $-$ 2.3 to $+$ 0.6). Finally, this S solubility model can apply for both terrestrial and extraterrestrial melt composition, notably to Mars.

The solubility of S observed in this study in Fe-rich melt has crucial impact for the understanding of volatile degassing in the primitive time of Mars. We have estimated more that 1 wt % S can be present in a martian basaltic melt at depth. This new data would increase the amount of S degassed, calculated by previous study. Gaillard and Scaillet (2009) have demonstrated that the maximum of S degassed for martian basalt is at oxidized conditions and for hydrous melts (0.4 wt % H_2O, QFM $-$ 0.5). Our experiment obtained with hydrous S-rich glasses with S_0 as starting material could represent such case. Considering the solubility of S in this experiment at 1.3 wt %, the amount of S degassed could be far above the 0.7 wt % S determined by Gaillard and Scaillet (2009). Further investigation on degassing models considering these new values are needed to better constrain the volatile degassing to the primary atmosphere of Mars and justify the possible warm and dense atmosphere, which has allowed liquid water at the surface.

With this new update of S solubility in Fe-rich melts, we have new insights on the volatile budget of S at depth. From the previous section, we have also observed that the H_2O dissolution in such melts seems lower than for terrestrial basalt at high-pressure (see Chapter II); although no H_2O-saturated experiment could have been performed. The high S solubility in these Fe-rich melt compositions could compensate the low H_2O dissolved (referring to the Chapter II) and degassed into the atmosphere of Mars. Once degassed, the S as SO_2, H_2S and S_2 are strong contributors to a greenhouse effect which will increase surface temperatures above the freezing point of water or brines (Halevy et al. 2007; Hirschmann and Withers 2008; Johnson et al. 2008, 2009; Mischna et al. 2013). The involvement of water vapor feedback would have probably increased surface temperature in addition with the S greenhouse effect to maintain liquid water at the surface according to Johnson et al. (2008). SO_2 would be the predominant gas to persist in the atmosphere due to its longer lifetime. However, Gaillard et al. (2013) have concluded that in reduced conditions that would have prevailed during the Noachian, H_2S and S_2 were the main S species to degas in the atmosphere, with moderately low SO_2 content. On the other hand, Kerber et al. (2015) have demonstrated that S degassing could not result in a greenhouse effect but on the contrary, to a cooling phenomenon, with locally warming surface when degassing of CO_2. Hence, the question of the potential S effect on the climate is still unclear.

In addition, not all the S will be degassed during the magma ascent and a significant amount of S can be present within igneous rocks at the surface. The emitted S into the atmosphere could also fall back on Mars surface through photochemical processes into S_8 species, sulfate aerosols

or through SO_2 rainout (Johnson et al. 2009). Then, through surficial weathering, the S can be transported and transformed into sulfate deposits.

With our experimental study, we have estimated a maximum of S dissolved in the Fe-rich melt at depth, which helps to establish a S budget on Mars. To constrain the total S budget on Mars and quantify the amount of S emitted in the past atmosphere, the quantification of S in the martian surface is necessary to combined with our experimental work. This is the aim of the last chapter of this manuscript. In the following study, we will explain the Raman calibration established on binary and ternary mixtures with sulfates. These calibrations will permit to quantify S below 5 wt %, which was not possible with the current ChemCam instrument (Wiens et al. 2012). Then, the proposed Raman calibration of sulfate mixtures has a strong interest for the S quantification with the SuperCam instrument onboard the future 2020 Mars mission.

Chapter IV: Quantitative Raman calibration of sulfate-bearing polymineralic mixtures: a S quantification in sedimentary rocks on Mars surface

IV.1. Abstract

The NASA 2020 Mars mission is a Curiosity-type rover aiming to improve the knowledge of the geologic and climatic evolution of Mars and collect rock samples for future return to Earth. The new rover presents a payload of seven instruments including the SuperCam instrument which is constituted of four tools including a Raman spectrometer. This Raman device will be non-destructive and will analyze the surface remotely in order to determine the mineralogy of rocks and, by extent, detect and quantify major elements such as sulfur. Sulfur has been detected under sulfate forms (Ca,Mg,Fe-sulfates) in sedimentary rocks. This element is difficult to quantify using the laser ablation tool of the ChemCam instrument onboard the Curiosity rover. We propose a Raman calibration to constrain the sulfur abundance in multi-minerallic mixtures. We acquired Raman signatures on binary and ternary mechanical mixtures containing Ca and Mg sulfates, mixed with natural silicate minerals: olivine, clinopyroxene, orthopyroxene and plagioclase; and supposed to be relevant of basaltic-sedimentary rocks at the surface of Mars. Specific processing of Raman spectra extracted from our mixtures using Voigt function allows us to recover the initial proportions of our preparations on Ca and Mg sulfates. From these simulations, calibration equations have been provided allowing us to determine sulfate proportions ($CaSO_4$ and $MgSO_4$) in a mixture with basaltic minerals. With the presented calibration, S can be quantified at a lower limit of 0.7 wt % in martian soil.

IV.2. Introduction

The martian alteration processes history can be decoupled in three parts (Bibring et al. 2006). From its early formation and to the late Noachian (4.5 to 3.7 Ga), the surface of Mars is dominated by phyllosilicates, which defines the phyllosian era. The theiikian epoch followed the phyllosian with the large formation of sulfates during the Hesperian (i.e., 3.7 - 3.2 Ga). From late Hesperian to the present days (i.e., Amazonian > 3.2 Ga), the last part of alteration processes of Mars is dominated by anhydrous ferric oxides representing the siderikian epoch.

The first two alteration products undeniably require liquid water to form; whereas ferric oxides are formed without, or with transient liquid water (Gooding 1978; Bibring et al. 2006). The phyllosian era is supposed to be dominated by alkali water compared to the theiikian period that is more likely to have required acidic aqueous environment to form sulfates.

The high abundances of sulfates detected at the surface of Mars (5 - 10 %; McSween et al. 2010), indicate that the S has played a major role in Mars history. In the Fig.IV.1, the distribution of sulfates along with phyllosilicate minerals are reported, according to compiled data from Ehlmann et al. (2011) and Carter et al. (2013).
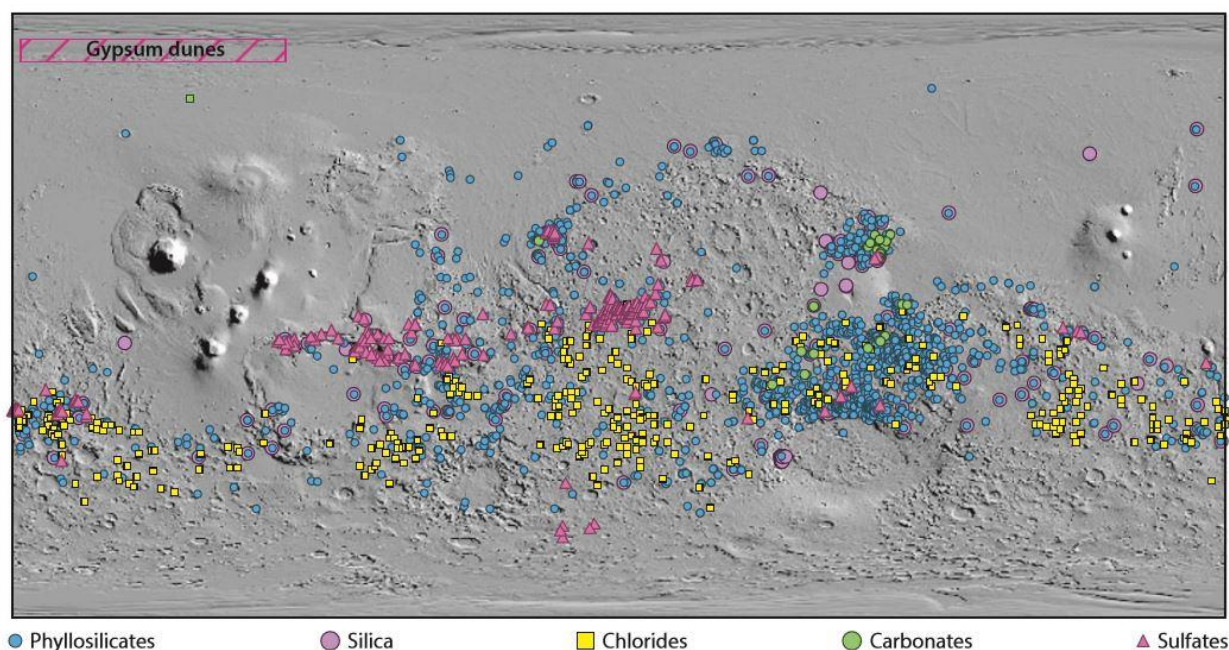
Fig.IV.1 : Map of the global distribution of hydrated minerals on Mars; after Elhman and Edwards (2014).

Various sulfate deposits have been reported on the surface of Mars and are gathered into 5 distinctive groups (Clark et al. 2005; McLennan et al. 2005; Squyres and Knoll 2005; Wang et al. 2006; Lane et al. 2008): Hesperian Layered Sulfates, Interior Layered Deposits (ILDs), Polar deposits, Intracrater sediments, Global dust and regolith. Another sulfate group has been proposed as secondary vein minerals within silicate bedrock on the rim of Endurance Crater (Squyres et al. 2012, Nachon et al. 2014). These various sulfates content in the surface of Mars must result in abundant volatile degassing during martian history. Indeed, either sulfates were formed during weathering of S-bearing igneous rocks, either by transformation of SO_2 into H_2SO_4 in the atmosphere, which then will precipitate into sulfates.

One of the main objectives of both orbital and landed Mars missions is the mineralogical characterization of the igneous and sedimentary rocks in order to constrain past geological processes such as the early volcanism and aqueous alteration. So far, many igneous rocks have been detected at the surface of Mars and basaltic rocks represent the most abundant part (e.g., Bandfield et al. 2000; McSween et al. 2009; Taylor and McLennan 2009; Ody 2012; Baratoux et al. 2013; Sautter et al. 2016; Cousin et al. 2017). Although the Curiosity rover and the orbital spectrometer CRISM have recently discovered more felsic and alkali-rich rocks including trachyte, andesite, diorite and putative granitoïds (Wray et al. 2010; Stolper et al. 2013; Sautter et al. 2015; Mangold et al. 2016). These magmatic rocks have been altered into various minerals such as clays (various smectites, kaolinite, chlorite), sulfates (Ca-, Fe-, Mg-sulfates), which are often detected in sediment layers overlying the igneous bedrock or in crustal outcrops exhumed by impact craters (e.g., Squyres et al. 2004; Arvidson et al. 2005; Poulet et al. 2005; Gendrin et al. 2005; Elhmann et al. 2013, Carter et al. 2013).

The Curiosity rover currently analyzes rocks and soils on Mars using Laser Induced Breakdown Spectroscopy (LIBS) (Maurice et al. 2012; Wiens et al. 2012; Meslin et al. 2013; Maurice et al. 2017; Cousin et al. 2017; Mangold et al. 2017). The LIBS equipment enables the detection and

quantification of all major elements (e.g., Si, Al) and the detection of volatiles and halogens (C-H-O-N-P-S-F-Cl). However, the detection of these elements is difficult with this method because of the high excitation energies, their peak positions near the instrument limit and the coupling of different major elements rays (e.g. Sallé et al. 2004, Clegg et al. 2007). It results in variation of the detection levels and a lack of quantification for some of them. In particular, the detection limit for S is between 5 to 10 wt% S (Wiens et al. 2012). Quantitative determination of S is of prime interest, as this element is known to be fundamental for Mars evolution (King and McLennan 2010).

In the future Mars 2020 mission, the SuperCam analytical equipment will include Raman and IR spectrometers in addition to the LIBS instrument similar to ChemCam instrument onboard Curiosity (Fouchet et al. 2016; Wiens et al. 2016, Ollila et al. 2017). Relevant interpretations of Raman spectra will require the acquisition of laboratory data under similar analytical conditions of the Raman spectrometer onboard. Although Raman spectroscopy is nominally non-quantitative with relevant calibration, it can be used for quantifying S at low concentrations (thousands of ppm) owing to the high Raman activity of S-bearing molecular groups (Morizet et al. 2017).

Previous studies have focused on the quantification of volatile species (H_2O, CO_2 and SO_4^{2-}) in silicate glasses with application to Earth volcanism (Zajacz et al. 2005; Mercier et al. 2009; Le Losq et al. 2012; Morizet et al. 2013, 2017). However, up to now, the quantification of individual mineral species in multi-minerallic mechanical mixtures have been merely addressed using Raman spectroscopy (Kontoyannis et al. 1997; Jehlicka et al. 2009; Noguchi et al. 2009; Kriskova et al. 2013). Jehlicka et al. (2009) have shown, the possibility to quantify multi-component mixtures with a portable micro-Raman spectrometer. In Kriskova et al. (2013) and Noguchi et al. (2009) only multi-minerallic mixtures with carbonates have been studied. Kontoyannis et al. (1997) have established a calibration on carbonates mixed with gypsum using Raman spectroscopy, but it is not applied on mineralogical mixtures representative of Mars mineralogy.

In the present work, we propose a calibration for quantifying the sulfate content (thereby also the elemental sulfur content) in multi-minerallic mixtures. This calibration aims to be subsequently applied on the S quantification under its sulfate form on the surface of Mars with the Raman spectrometer of SuperCam. Several mixtures of sulfates (Ca-sulfate, Mg-sulfate) with silicate minerals (i.e., pyroxenes, olivine, and plagioclase) were prepared in order to reproduce sulfate-bearing martian-like sedimentary rocks. These mixtures were analyzed by Raman spectroscopy. The equations derived from calibration curves are then used to quantify sulfates in these mixtures. Finally, we discuss the potential of this method to S quantification carried by sulfates in the martian soil and rocks.

IV.3. Sample preparation and analytical methods
IV.3.1 Multi-minerallic mixtures preparation

Multi-minerallic mixtures were prepared from hydrated Ca-sulfate ($CaSO_4.2H_2O$) and Mg-sulfate ($MgSO_4.nH_2O$) synthetic powders and silicate minerals selected from natural rocks. Pyroxenes and olivine were extracted from a xenolith collected at the maar of Borée (France) and plagioclase from a norite of Stillwater (USA). Chemical compositions of minerals selected

for this study are reported in Table IV.1. The chosen olivine is Mg-rich in composition (forsterite, $Si_{1.00} Fe_{0.18} Mg_{1.78} Na_{0.01} O_4$). Pyroxenes have compositions close to enstatite ($Si_{1.85} Al_{0.16} Fe_{0.16} Mg_{1.62} Ca_{0.02} Na_{0.02} O_6$) and augite endmembers ($Si_{1.78} Al_{0.23} Fe_{0.09} Mg_{0.95} Ca_{0.57} Na_{0.11} O_6$). The plagioclase from this study is Ca-rich and has a composition close to the anorthite endmember ($Si_{2.21} Al_{1.76} Fe_{0.01} Mg_{0.01} Ca_{0.85} Na_{0.16} O_8$). The natural silicate minerals were crushed in a steel-mortar with pestle and crushed again in an agate mortar. Ethanol was added during crushing to clean the samples.

Mineral	Origin	Chemical formula
Olivine	Forsterite from Maar de Borée (France)	$Si_{1.00} Fe_{0.18} Mg_{1.78} Na_{0.01} O_4$
Clinopyroxene	Augite from Maar de Borée (France)	$Si_{1.78} Al_{0.23} Fe_{0.09} Mg_{0.95} Ca_{0.57} Na_{0.11} O_6$
Orthopyroxene	Enstatite from Maar de Borée (France)	$Si_{1.85} Al_{0.16} Fe_{0.16} Mg_{1.62} Ca_{0.02} Na_{0.02} O_6$
Plagioclase	Anorthite from a diorite of StillWater (USA)	$Si_{2.21} Al_{1.76} Fe_{0.01} Mg_{0.01} Ca_{0.85} Na_{0.16} O_8$
Gypsum	Synthetic calcium sulfate from MERCK (Germany)	$CaSO_4 . (2H_2O)$
Mg-sulfate	Synthetic magnesium sulfate hydrated from LABOSI (France)	$MgSO_4 . (nH_2O)$

Table IV.1: Origins and chemical compositions of basaltic minerals (olivine, pyroxenes and plagioclase, determined by Scanning Electron Microscopy (SEM) analysis) and sulfates used in this study.

Mixtures between silicate minerals and sulfates were prepared and mixed together. The resulting powder was not sieved because grain size does not exceed 50 µm with this grinding procedure (see Fig.IV.2A below). Several samples with various sulfate proportions were prepared: WF_{gypsum} = 0.20, 0.10, 0.05, 0.03, 0.01 and $WF_{mg-sulfate}$= 0.20, 0.10, 0.05 and 0.03; where WF represents the Weight Fraction of sulfates. Ternary mixtures were prepared with Ca-sulfate, clinopyroxene and olivine. Gypsum, clinopyroxene and olivine concentrations in mixtures were respectively: WF_{gypsum} = 0.20, 0.10 and 0.05, $WF_{clinopyroxene}$ = 0.40, 0.40 and 0.45, $WF_{olivine}$ = 0.40, 0.50 and 0.50. The investigated sulfate concentrations are consistent with the abundances of these minerals as locally estimated in evaporites at Meridiani Planum (McLennan et al. 2006) or in fluvio-lacustrine sedimentary rocks at Gale crater (Vaniman et al. 2017).

We also prepared ternary mixtures in order to reproduce in a more realistic system to represent the martian surface mineralogy: sulfates mixed with silicate minerals, resulting from basalt

weathering (Carter et al. 2013; Forni et al. 2015; Cousin et al. 2017; Mangold et al. 2017). The resulting powders were then pressed into pellets, with an example given in Fig.IV.2A. Pressures used were between 5,000 and 9,000 kg/cm2 to create pellets with diameters of 7 to 10 mm, respectively.

No mixture with basaltic glasses were made due to the difficulty to establish a Raman calibration on a glass component mixed with a crystal. This difficulty is mainly caused by the mixing of two different kind of materials: a glass with crystals. Indeed, crystals will show intense peaks compared to a glass signature. However, further work could be done on this kind of mixtures to better constrain the S abundance of Mars.

IV.3.2. Raman spectroscopy

Raman spectra for each pellet were acquired on a Jobin-Yvon Labram HR800 spectrometer equipped with a solid state laser diode operating at 532 nm. A 20X Olympus objective was used. A 785 nm solid state laser has also been used on one sample (GPG80, plagioclase-gypsum mixture with $WF_{gypsum} = 0.20$) to circumvent the fluorescence. Spectra are acquired with a 300 grooves/mm grating with a 3 cm-1 spectral resolution. The output power of the laser was set to 74 mW for Ca-sulfate mixtures and 50 mW for Mg-sulfates. For binary mixtures, we did not use the confocal mode (with a hole calibrated around 50 µm) and instead, the hole was fixed at 200 µm. However, ternary mixtures were analyzed in a confocal mode due to fluorescence problems (Panzcer et al. 2012) in the non-confocal configuration.

The acquisition time varied from 3 to 10 s and 3 repetitive scans were made on each point. Background substraction for each spectrum has been applied following the procedure of Tarcea and Popp (2012): a fit of polylines (i.e., multiple lines added to create a baseline under the spectrum) was made for each spectrum to perform a baseline correction, in order to measure areas and intensities for each peak. Peak intensity and area were determined on normalized spectra, i.e., spectra acquired at the same acquisition time length (10 or 15 s). Details of the analytical conditions are reported in the annex section (Table IV.A1).

A large mapping of 5 by 5 mm (Fig.IV.2B) was conducted on each pellet with a spot size of about 1.6 µm. Each analysis was performed every 150 µm. This mapping procedure results in 1024 spectra representing the mixture analyzed. Since grain size did not exceed 50 µm, possible coupling of the same crystal analysis is expected. This phenomenon would have occurred for every crystal since we suppose the mixture homogeneous in grain size (Fig.IV.2A). Then, an average of these spectra, that will consider the previous artefact, is computed to obtain a single Raman spectrum representative of the analyzed mixture (Fig.IV.2C).
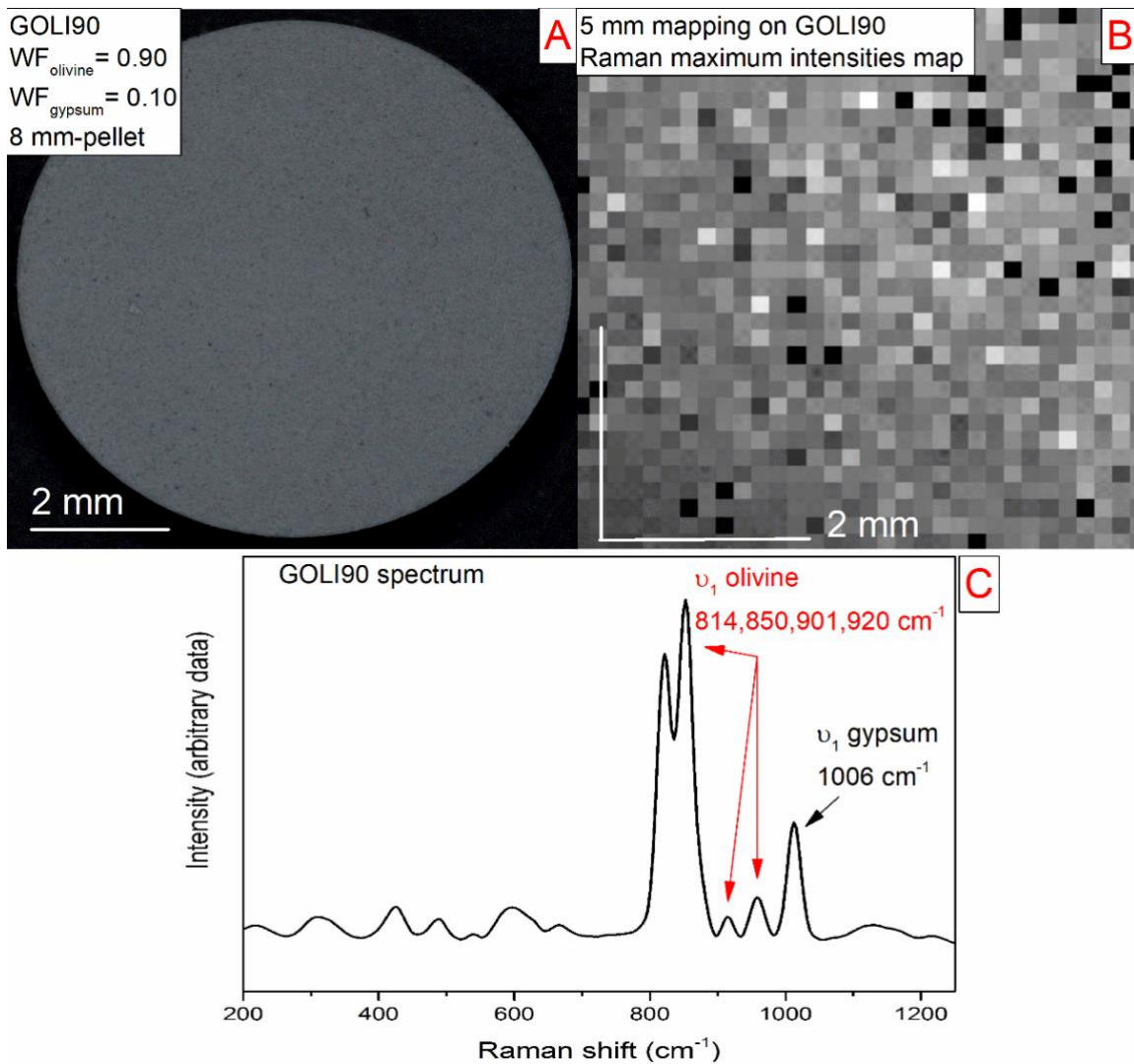
Fig.IV.2: A) Pellet of a 90/10 mixture of olivine (weight fraction WFolivine = 0.90) and gypsum (WFgypsum = 0.10) named GOLI90; B) 5 mm mapping of spectrum intensities acquired by Raman spectroscopy showing the homogeneity of GOLI90; C) The average spectrum issued from the 5 mm mapping of GOLI90 with ν_1 peaks (symmetric stretching mode of SiO_4 and SO_4 molecules) of olivine and gypsum reported.

The polarization effect was also tested on pure minerals Raman spectra. We have observed that the spectrum intensity is modified when acquisition angle on the crystal is changed, which is consistent with the results of Bremard et al. (1986) and Rull (2012). Nevertheless, we assumed that the polarization effect is averaged out by the large mapping procedure adopted and considering that crystals in the pellet have all possible crystallographic orientations from a statistical point of view.

The Raman spectrum of each individual mineral used in this study is reported in Fig.IV.3. The gypsum Raman pure spectrum (Fig.IV.3A) exhibits several peaks with low intensities in the 400-700 cm$_{-1}$ region corresponding to the symmetric (400-500 cm$_{-1}$) and antisymmetric (600-700 cm$_{-1}$) bending vibrations of SO$_4$ molecules (v_2 and v_4). The strong peak at 1006 cm$_{-1}$ corresponds to the symmetric stretching vibration (or v_1) of S-O bonds in SO$_4$ molecular groups (Knittle et al. 2001; Buzgar et al. 2009; Bishop et al. 2014). Peaks observed in the highest frequency region (> 1100 cm$_{-1}$) are attributed to antisymmetric stretch vibrations (v_3) of SO$_4$ and have a weak Raman activity.

Fig.IV.3: Multi-minerallic pure Raman spectrum with their acquisition time for A : olivine ; B: Mg-sulfate; C: gypsum; D: plagioclase; E: clinopyroxene; and F: orthopyroxene. Significant peaks for each mineral have been reported in graphs. For peak assignments see Table IV.2.

A Olivine pure spectrum
Acquisition time : 10 s

Si-O stretching (υ_1)

810
850
910 950

D Plagioclase pure spectrum
Acquisition time : 10 s

500 : Al-O or Si-O stretching (υ_1)

B Mg-sulfate pure spectrum
Acquisition time : 15 s

Stretching SO$_4$ (υ_1)
1040

Asymmetric bending SO$_4$
620

Asymmetric stretch SO$_4$
1110

E Clinopyroxene pure spectrum
Acquisition time : 15 s

666 : Si-O bending

1006 : Si-O stretching (υ_1)

250-410 : Cations stretching (Ca,Mg,Al)

C Gypsum pure spectrum
Acquisition time : 3 s

Stretching SO$_4$ (υ_1) : 1006

Symmetric bending of SO$_4$

415 490

antisymmetric stretch SO$_4$: 1133

F Orthopyroxene pure spectrum
Acquisition time : 15 s

678 : Si-O stretching of bridging O

1006 : Si-O stretching (υ_1)

342: Mg-O stretching

Raman shift (cm^{-1})

Raman shift (cm^{-1})

136

Similar to gypsum, the principal symmetric ν_1 vibration of Mg-sulfate is identified in Fig.IV.3B around 1040 cm$_{-1}$ (Buzgar et al. 2009). Antisymmetric bending and stretching of SO$_4$ molecules are observed at 620 and 1110 cm$_{-1}$, respectively.

The Raman spectrum of olivine (Fig.IV.3C) shows two strong peaks above 800 cm$_{-1}$, followed by two less intense peaks above 900 cm$_{-1}$, which are attributed to the symmetric stretch of the Si-O bonds of SiO$_4$ tetrahedrons (Chopelas 1991; Kolesov and Tanskaya 1996; Kolesov and Geiger 2004; Kuebler et al. 2006; McKeown et al 2010).

Plagioclase Raman spectrum shown in Fig.IV.3D exhibits a strong peak around 500 cm$_{-1}$ attributed to the ν_1 of Al$_2$O$_3$ or SiO$_4$ tetrahedrons in the tectosilicate structure (Sharma et al. 1983; Freeman et al. 2008). Peaks identified at higher wavenumbers correspond to the ν_3 vibrations for these tetrahedrons.

Pyroxenes spectra shown in Fig.IV.3E and Fig.IV.3F are similar in the high frequency region (> 600 cm$_{-1}$) where bending and stretching vibrations of SiO$_4$ tetrahedrons are observed, for signatures ~660 and 1006 cm$_{-1}$ respectively. At low frequency, in the 200 - 400 cm$_{-1}$ region, it is possible to discriminate clinopyroxene from orthopyroxene spectrum, which does not present the same peak intensities. In this region, vibrations related to Fe, Ca and Mg molecular environments are responsible for the observed peaks (Sharma et al. 1983; Huang et al. 2000; Wang et al. 2001; Prencipe et al. 2011). Specific peak assignments for each mineral in this study are described in Table IV.2.

Raman shift (cm^{-1})	Mode assignments
Orthopyroxene [1], [2], [3], [4]	
225-325	Fe-O octahedron
375-490	Mg-O octahedron
650-750	Si-O ν_{3c}
800-1100	Si-O ν_{1a}
Clinopyroxene [1], [2],[3], [4]	
230 and 327	M-O* stretching
255 and 360	Ca-O stretching
393	Mg-O stretch
665	Si-O-Si ν_{2b}
1010	Si-O ν_1
Olivine [5], [6], [7], [8]	
820	Si-O ν_1
850	Si-O ν_1
914	Si-O ν_3
950	Si-O ν_3
Plagioclase [9] and [3]	
200-400	Lattice modes
420-503	Al-O or Si-O ν_1
900-1000	Si-O-Al ν_3
> 1000	Si-O-Si ν_3
Gypsum [10], [11], [12]	
400-500	SO_4 ν_2
600-700	SO_4 ν_{4d}
1006	SO_4 ν_1
>1100	SO_4 ν_3
Mg-sulfate [11]	
400 - 600	SO_4 ν_2
620	SO_4 ν_4
1040	SO_4 ν_1
1050 – 1150	SO_4 ν_3

Notes:

a ν_1: Symmetric stretch

b ν_2: symmetric bending

c ν_3: antisymmetric stretch

d ν_4: antisymmetric bending

* With M referring as different metal cations present in the chemical structure of the mineral (Buzgar et al. 2009)

Table IV.2: Specific peak assignments for each mineral used in this study. Principal peaks observed in spectra are described according to [1]: Huang et al. (2000), [2]: Prencipe et al. (2011), [3]: Sharma and al. (1983), [4]: Wang et al. (2001) [5]: Chopelas (1991), [6]: Kolesov and Tanskaya (1996), [7]: Kolesov and Geiger (2004), [8]: McKeown et al. (2010), [9]: Freeman et al. (2008) [10]: Bishop et al. (2014), [11]: Buzgar et al. (2009) and [12]: Knittle et al. (2001).

The new rover send for the 2020 Mars mission will use a laser-pulsed Raman spectrometer with a 532 nm solid-state laser (Olila et al. 2012, Wiens et al. 2016). The rover will target rocks and soil from several meters away and with a resolution of ~10 cm_{-1} (Wiens et al. 2016).

Knowing those conditions, we performed several tests to analyze the pellets. A map size of 5 by 5 mm was necessary to reproduce in an adequate way the mineral mixtures. Using 2 by 2 or 3 by 3 mm map size was not sufficient to retrieve the initial mineral proportions in the mixture. Furthermore, the 5 by 5 mm size map is also consistent with the analytical conditions for the 2020 rover, which will have a large analytical area. The adopted laboratory analytical conditions (i.e., focus 20X, 300 grooves/mm grating and non-confocal mode) were optimized to obtained spectra that could be compared with Raman spectra acquired by SuperCam.

IV.4. Calibration tests

Several tests were performed to establish the Raman calibration. Three of them will be exposed here, with the last test corresponding to the valid calibration used in this study.

IV.4.1. Calibration with Solveur

The first test ran out was using the Excel tool: Solveur. This method was chosen according to the method of Di Genova et al. (2016) which calibrates Raman spectrum with a Rp parameter to estimate the $Fe_{2+}/\sum Fe$ ratio in Fe-rich basaltic glasses. Following this method, we calculated a Rp parameter, corresponding to the ratio of each species in the mixture according to the following equation:

$$(1)\ Y_{calc} = Y_{sulfate} \times \left(1 - R_p\right) + Y_{mineral} \times R_p$$

With Y, the Raman intensity of the sulfate in the mixture (either Ca, or Mg sulfate; $Y_{sulfate}$) or the mineral mixed with (clinopyroxene, orthopyroxene, olivine or plagioclase; $Y_{mineral}$), and Y_{calc} the calculated intensity of the mixture. To create our calibration, we have implemented the pure spectrum of each component of the mixture, for instance a Raman spectrum of clinopyroxene and gypsum, for the 200 – 3500 cm_{-1} area. The Rp parameter also considers the acquired Raman spectrum of the mixture. Using the two endmembers spectra and the mixtures, the parameter Rp can be calculated. Then, calculated Y_{calc} spectrum will be calculated according to Rp as presented in equation (1).

The results of this method are reported in the Fig.IV.4 for mixtures presenting 0.05 Weight Fraction of gypsum (i.e. $CaSO_4$). In Fig.IV.4A, the mixture of clinopyroxene and gypsum is exhibited. From the Solveur method, 0.01 WFgypsum is calculated where 0.05 is initially presents in the mixture (report to Table IV.3 for initial mixture proportion). For plagioclase mixture, the Solveur also underestimates the gypsum content with 0.03 in Fig.IV.4D. In Fig.IV.4C, in orthopyroxene mixture, the Solveur overestimates greatly the gypsum content with 0.16 against 0.05 Weight Fraction. Finally, the only mixture well reproduced by this method is the mixture with olivine, with 0.05 WFgypsum calculated (Fig.IV.4B).
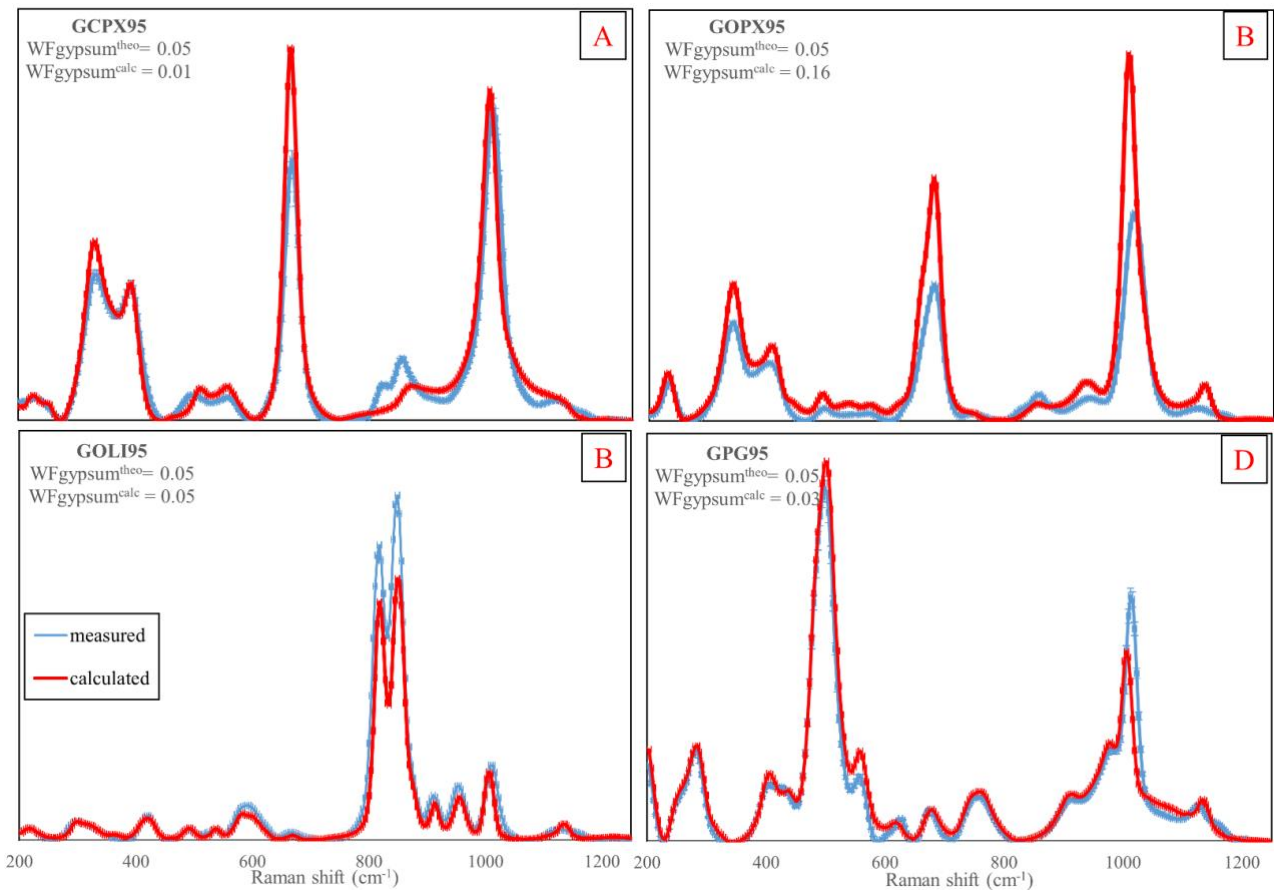
Fig.IV.4 :Solver simulations for mixtures presenting 0.05 Weight Fraction (WF) of gypsum (CaSO4). A) simulation of clinopyroxene mixture Raman spectrum; B) orthopyroxene mixture simulation; C) olivine with gypsum; D) plagioclase. The blue spectrum represents the acquired Raman spectra against the simulated in red.

Referring to the calibration exposed in the Fig.IV.4, we can see that the results could be good for some mixtures within error (e.g., olivine and plagioclase). However, we can see that the calculated Raman spectrum shows strong discrepancies compared with the measured one, even if a good sulfate estimation is made. For instance, in Fig.IV.4B with olivine and gypsum mixture, we can see that the $200 - 600$ cm-1 area is well reproduced, as well as the $900 - 1200$ cm-1. But when looking at the olivine doublet between 800 and 900 cm-1, we can see that the calculated intensity is strongly below the measured spectrum. The difference is even more important for the mixture with orthopyroxene in Fig.IV.4C for the 670 and 1006 cm-1 peaks. Hence, considering these differences, we could not consider that the model was accurate.

IV.4.2. Calibration with simulation of the entire Raman spectrum

Then, we chose to perform simulation on each individual spectrum (pure spectrum of the mineral) and used each peak to simulate the mixture spectrum. For this method, we used the Origin© software with Voigt deconvolutions (a mixture of Gaussian and Lorentzian contribution). Examples of simulation for 0.10 WFgypsum are reported in the Fig.IV.5.
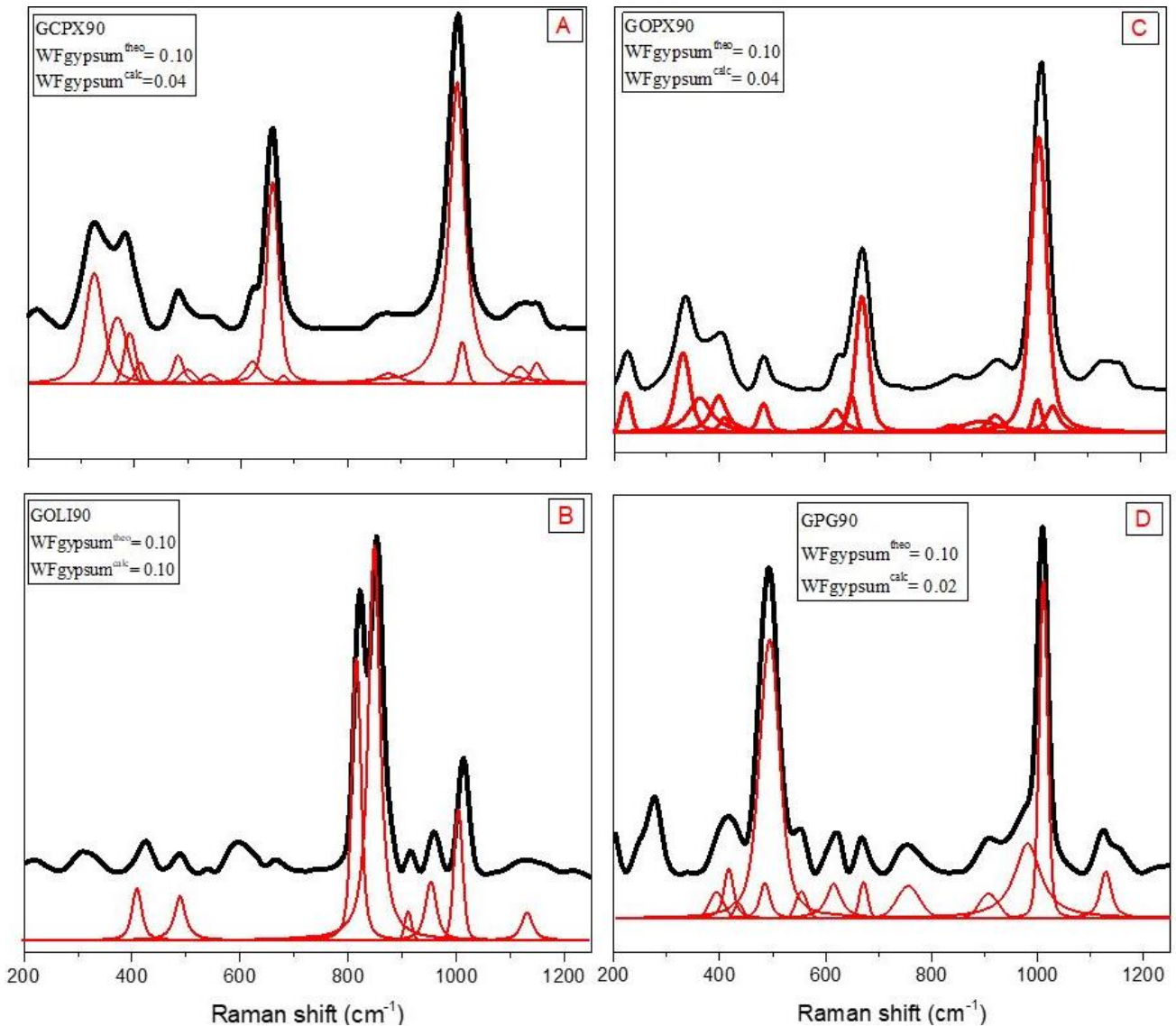
Fig.IV.5: Voigt deconvolutions of Raman spectra mixtures with WFgypsum = 0.10 for: A) clinopyroxene; B) olivine; C) orthopyroxene; D) plagioclase.

From the Fig.IV.5, we can see that the only simulation that estimates correctly the gypsum content is, again, for the olivine mixture in Fig.IV.5B. For pyroxene mixtures in Fig.IV.5A and Fig.IV.5C, the WFgypsum calculated = 0.04, whereas with the plagioclase it is only 0.02, for 0.10 initially added.

These results were then, not accurate enough to use as calibration. These discrepancies could result in the entire spectrum simulation. Indeed, as presented in the Fig.IV.2 and reported in Table IV.2, some mineral exhibits vibrations in the same region. Indeed, pyroxenes possess a strong peak at 1006 cm$_{-1}$, where the SO$_4$ species are vibrating in gypsum. Hence, the deconvolution of this peak in mixtures of pyroxenes are flawed. Since, we do not know the contribution of each mineral in this peak, the simulation can either underestimates or overestimates the gypsum contribution. In Fig.IV.5, it seems more likely that the deconvolution underestimates the gypsum content because the pyroxene 1006 cm$_{-1}$ peak contribution is overestimated. The same observation applied for the plagioclase mixture, since it also shares vibrations with gypsum around 1000 cm$_{-1}$ (see Fig.IV.2).

Finally, the olivine is the only mixture that is well reproduced by the model. This is due to the specific vibrations of olivine that do not overlap those of gypsum's, hence its contribution can be well calculated.

Considering the results of the subsequent tests, we had to find another method to quantify the sulfate into our mixtures. For this, we had to find specific peaks to simulate, instead of simulation of the entire Raman spectrum. The following method is the one that has been published in Mineralogical Magazine.

IV.4.3. The valid calibration method

The calibration method in the present study is similar to that used by Kontoyannis et al. (1997), Noguchi et al. (2009) and Kristova et al. (2013). Our method is based on the spectral deconvolution of the investigated pure minerals Raman spectrum presented in the previous section. For instance, to establish a calibration on a gypsum-olivine mixture, pure spectrum of gypsum and olivine are treated individually. The spectrum treatment consists in extracting peak information using subsequent deconvolution. Since we are analyzing crystallized species, we expect the Raman signature to have a pure Lorentzian shape; however, a contribution of a Gaussian component in addition to the Lorentzian signal has been observed. This would likely be caused by intrinsic crystal defaults. Therefore, we used a Voigt simulation (i.e., a mix of Gaussian and Lorentzian deconvolution) which provides better simulations of our spectra. The simulation equation of a Voigt deconvolution is given below (Eq.2):

$$(2)\ y = y_0 + A\ \frac{2\ln 2}{\pi^{\frac{3}{2}}} \times \frac{W_L}{W_G^2} \times \int_{-\infty}^{\infty} \frac{e^{-t^2}}{\left(\sqrt{\ln 2} \times \frac{W_L}{W_G}\right)^2 + (\sqrt{4\ln 2} \times \frac{x - x_c}{W_G} - t)^2}\ dt$$

Where y_0 and y are the intensity after a baseline correction of the spectrum and the intensity for the peak simulated, respectively. The parameter A represents the simulated area and W_G et W_L are respectively the Gaussian and Lorentzian widths for a given peak. The x parameter is the position in cm$_{-1}$; where x is the Raman shift and x_c is the derived peak position simulated in cm$_{-1}$. Finally, in Eq. 2, t is the time component. Since the Raman spectra are not time-dependent, t is set to 0. We reported in the Table IV.A1 (annex section) all peaks simulated for mineral pure spectrum, with their specifics parameters (width, position, area). For clarity, simulations of silicate and sulfate minerals pure spectrum are only shown in the annex section of this chapter (Fig.IV.A1).

Due to the strong overlapping between the different spectral lines in the recovered average Raman spectrum for each pellet, it was not possible to perform the simulation of all the identified peaks for pure spectrum of minerals reported in Table IV.2, as stated in the previous section. Hence, for each species, we have selected peaks that are distinct in their position and are indicated in Table IV.3.

The protocol to simulate Raman peaks is fully described in previous studies and is routinely used for the quantification of volatiles species in silicate glasses (e.g., Mysen and Virgo 1980a, b; Mercier et al. 2009; Morizet et al. 2013, 2017). First, we have fixed the peak position and widths (Gaussian and Lorentzian), leaving only the peak area optimized. Position is then optimized as we observed slight variations in the peak position in our mixture spectrum compared to the position derived from the acquired pure spectrum. These variations could be due to the dependence of the Raman signature on crystal orientation or unaccounted chemical heterogeneity. Gaussian and Lorentzian widths are also optimized to better adjust our simulations. This procedure is repeated several times until the chi-square (χ_2 parameter representing the robustness of the fit) is the lowest possible and the residual are small (see Fig.IV.3).

With parameters extracted from simulations, we were able to calculate the mixing proportion presents in the analyzed pellet. We determined a ratio R between the simulated area for the peak of the mixed spectrum and that of the pure spectrum such as:

$$(3)\ R = \frac{A_{mixture}}{A_{pure}}$$

In Eq.3, A represents the area determined with a Voigt simulation for a same peak for the mixture ($A_{mixture}$) and the pure Raman spectrum (A_{pure}). This method differs from previous Raman calibration studies of Kontoyannis et al. (1997) and Kriskova et al. (2013) where peak intensities were chosen instead of areas. Since we observed several variations in intensity and peak positions between pure spectrum and the average spectrum of the mixture, we consider that peak areas averaged out every possible variation between acquisitions with the 300 grooves/mm grating. The ratios are then normalized to obtain the result in weight fraction (WF). This proportion is then assimilated to a coefficient "a":

$$(4)\ a = \frac{\Sigma A_{gypsum}}{\Sigma A_{mineral}}$$

With A being peak areas for gypsum (A_{gypsum}) and for mineral in the mixture ($A_{mineral}$). In case of the ternary mixtures with more than 2 peaks simulated for one mineral, $A_{mineral}$ is entirely summed in the denominator. Examples of mineral pure spectrum and mixture deconvolutions are provided in the Annex section (Fig.IV.A2).

IV.5. Results
IV.5.1. Binary and ternary mixtures with Ca-sulfate

A typical example of the spectral treatment is presented in Fig.IV.6. In Fig.IV.6A, Raman spectra collected represent olivine and gypsum mixtures with: WF_{gypsum} = 0.2, 0.1, 0.05 and 0.01. The Raman spectra obtained for the mixtures with other minerals (pyroxenes and plagioclase) are reported in the annex (Fig.IV.A2). In Fig.IV.6A, it can be observed that the peak intensity for ν_1 gypsum at 1006 cm-1 increases with increasing the proportion of gypsum

in the mixture. For instance, in GOLI80 $WF_{gypsum} = 0.20$ (see Table IV.3 for theoretical WF of each mixture), the 1006 cm-1 symmetric stretch peak is more intense as compared to the one in GOLI90 ($WF_{gypsum} = 0.10$). For these two mixtures, the measured intensity in the SO_4 vibrations peak is twice for GOLI80 as compared to the one in GOLI90 which appears to be consistent with the prepared compositions (Table IV.3). Although the gypsum content in the GOLI99 mixture is extremely low ($WF_{gypsum} = 0.01$), the peak at 1006 cm-1 is still detected because of the strong Raman activity of symmetric stretch of the S-O bonds in SO_4 molecular groups in gypsum (see Fig.IV.6A).

We chose to simulate three different peaks in the 890-1100 cm-1 region and located at 914, 958 for olivine and 1006 cm-1 for gypsum (Fig.IV.6). For olivine mixtures, relevant results were obtained when considering two Raman peaks identified in Table IV.2: 914 cm-1 for olivine and 1006 cm-1 for gypsum. In order to avoid contribution of the 1006 cm-1 gypsum peak over the 950 cm-1 of olivine (see on Fig.IV.6E-H), we have simulated the olivine peak at 914 cm-1 for our simulations. The robustness of our simulations is asserted by the small residual observed in Fig.IV.6E-H. For a theoretical proportion mixture of 0.80 and 0.20 weight fraction of olivine and gypsum respectively (FigIV.6D), the calculated proportions (from Eq. 3 and 4) are 0.79 (0.08, error relative to simulations) for olivine and 0.21 (0.01) for gypsum (Fig.IV.6H). With lower Ca-sulfate proportion, we obtain consistent results in between the measured and theoretical mixtures. For initial proportions at 0.90 and 0.10, we calculate 0.91 (0.01) for olivine and 0.09 (0) for gypsum (Fig.IV.6C and 6G). The same applies with the 0.01 and 0.05 mixtures of gypsum where 0.01 (0.01) and 0.06 (0) weight fraction of gypsum is calculated respectively, as shown in Fig.IV.6A-B and Fig.IV.6E-F.

A

GOLI99
WF$_{olivine}$ = 0.99
WF$_{gypsum}$ = 0.01

E

GOLI99 theoretical :
WF$_{gypsum}$ = 0.01
Calculated :
WF$_{gypsum}$ = 0.01

B

GOLI95
WF$_{olivine}$ = 0.95
WF$_{gypsum}$ = 0.05

F

GOLI95 theoretical :
WF$_{gypsum}$ = 0.05
Calculated :
WF$_{gypsum}$ = 0.06

C

GOLI90
WF$_{olivine}$ = 0.90
WF$_{gypsum}$ = 0.10

G

GOLI90 theoretical :
WF$_{gypsum}$ = 0.10
Calculated :
WF$_{gypsum}$ = 0.09

D

GOLI80
WF$_{olivine}$ = 0.80
WF$_{gypsum}$ = 0.20

υ_1 olivine
(804, 850, 910, 930 cm^{-1})

υ_1 gypsum (1006 cm^{-1})
intensity variations

H

GOLI80 theoretical :
WF$_{gypsum}$ = 0.20
Calculated:
WF$_{gypsum}$ = 0.21

GOLI80 spectrum
cumulative peaks fitted
peaks fitted
υ_1 olivine (903, 948 cm^{-1}) υ_1 gypsum (1006 cm^{-1})
residuals

Raman shift (cm^{-1})

Raman shift (cm^{-1})

Fig.IV.6: Global spectra for every mixtures of olivine with gypsum in different proportions: A) WFolivine = 0.99; B) WFolivine = 0.95; C) WFolivine = 0.90; D) WFolivine = 0.80; with their main peaks reported. Variations of gypsum υ_1 (symmetric stretch of SO_4) peak intensity are shown in red arrows. Zoom (890-1100 cm_{-1} area) of spectra acquired by Raman spectroscopy after mapping, from different mixtures of olivine with gypsum in several proportions: E) WFgypsum = 0.01; F) WFgypsum = 0.05; G) WFgypsum = 0.10; H) WFgypsum = 0.20. Spectra are correlated with peak simulations: blue for olivine peaks and green for gypsum. Red curves are cumulative peaks and black dotted lines are residuals from simulations. Weight fractions are calculated with peak simulations and reported in boxes in each graph and in Table IV.3.

On the Fig.IV.7 is showed the calculated coefficients from simulated areas in each mixture (see Eq.4) as a function of the theoretical $CaSO_4$ content. The results are represented for the different mixtures with basaltic minerals: plagioclase-gypsum mixture in Fig.IV.7A, orthopyroxene-gypsum in Fig.IV.7B, clinopyroxene and olivine-gypsum in Fig.IV.7C and 7D, respectively. Results from simulations are reported in Table IV.3. In Fig.IV.7, we can observe that the best calibration (based on the linear regression coefficient R_2 which defines the quality of the linear regression on experimental data) is obtained for olivine-gypsum simulations comparing to the calibration with other silicate minerals. Simulations (Fig.IV.7A to 7C) show good R_2 with 0.95, 0.94 and 0.96 for plagioclase, orthopyroxene and clinopyroxene, respectively.

The plagioclase-mixture with 0.20 weight fraction of gypsum (i.e., GPG80, see Table IV.3) has been calibrated using different peaks because of the use of the 785 nm laser for our analysis. Consequently, this point is not reported in Fig.IV.7A.

Fig.IV.7: Calibration coefficients calculated from simulated areas of gypsum and mineral mixed versus the weight fraction (WF) of gypsum theoretical. Black square are samples simulated with their relative errors. Red lines correspond to calibration lines extrapolated from calibration coefficients depending on theoretical weight fraction of gypsum. Calibration lines established on four binary mixtures of: A) plagioclase; B) orthopyroxene; C) clinopyroxene; D) olivine; with gypsum in different proportions (WFgypsum = 0.20, 0.10, 0.05, 0.03, 0.01). Equations and linear regression coefficient (R_2) of each calibration lines are reported in boxes in each graph.

We adopted the same procedure as for binary mixtures for ternary mixtures. The retained peak positions for our simulations are reported in Table IV.3. We considered the 300-390 cm_{-1} clinopyroxene peak areas, representative of Ca-O stretching vibrations, since they are isolated from the contribution of olivine and gypsum peaks in the Raman spectrum. For olivine, we consider the 947 cm_{-1}, one of SiO_4 symmetric stretching vibration signatures, and 485 cm_{-1} for gypsum which represents the bending of SO_4 molecules. Those peaks were selected because they were the most separated from each other.

Sample name	WF theoretical	WF calculated	a
		Olivine – Gypsum	
		Peak simulated : 914 and 1006 cm^{-1}	
		Calibration equation: a = 81.36 x WF$_{sulfate\ theoretical}$	
GOLI80	0.80 - 0.20	0.79 (0.08) – 0.21 (0.01)	17.21(3.20)
GOLI90	0.90 – 0.10	0.91 (0.01) – 0.09 (0)	6.55 (0.36)
GOLI95	0.95 – 0.05	0.94 (0.01) – 0.06 (0)	4.04 (0.22)
GOLI97	0.97 – 0.03	0.97 (0.02) – 0.03 (0.04)	1.87 (0.88)
GOLI99	0.99 – 0.01	0.99 (0) – 0.01 (0)	0.76 (0.08)
		Orthopyroxene - Gypsum	
		Peak simulated : 230 and 491 cm^{-1}	
		Calibration equation: a = 8.23 x WF$_{sulfate\ theoretical}$	
GOPX80	0.80 – 0.20	0.85 (0.04) – 0.15 (0.03)	1.52 (0.01)
GOPX90	0.90 – 0.10	0.89 (0.03) – 0.11 (0.04)	0.99 (0.12)
GOPX95	0.95 – 0.05	0.94 (0.02) – 0.06 (0.05)	0.51 (0.01)
GOPX97	0.97 – 0.03	0.96 (0.01) – 0.04 (0.08)	0.34 (0.35)
GOPX99	0.99 – 0.01	0.98 (0.01) – 0.02 (0.05)	0.19 (0.23)
		Clinopyroxene – Gypsum	
		Peak simulated : 362 and 412 cm^{-1}	
		Calibration equation: a = 1.93 x WF$_{sulfate\ theoretical}$	
GCPX80	0.80 – 0.20	0.82 (0.02) – 0.18 (0.02)	0.40 (0.49)
GCPX90	0.90 – 0.10	0.92 (0.01) – 0.08 (0.03)	0.15 (0.69)
GCPX95	0.95 – 0.05	0.93 (0) – 0.07 (0.01)	0.13 (0.38)
GCPX97	0.97 – 0.03	0.96 (0.01) – 0.04 (0.06)	0.07 (0.54)
GCPX99	0.99 – 0.01	0.99 (0) – 0.01 (0)	0.02 (0.42)
		Plagioclase - Gypsum	
		Peak simulated : 504 and 1006 cm^{-1}	
		Calibration equation: a = 59.83 x WF$_{sulfate\ theoretical}$	
GPG80	0.80 – 0.20	0.83 (0.01) – 0.17 (0.01)	1.19 (0.02)
GPG90	0.90 – 0.10	0.90 (0.03) – 0.10 (0.01)	6.24 (0.89)
GPG95	0.95 – 0.05	0.95 (0.01) – 0.05 (0)	2.75 (0.10)
GPG97	0.97 – 0.03	0.98 (0.01) – 0.02 (0.01)	1.17 (0.04)
GPG99	0.99 – 0.01	0.98 (0) – 0.02 (0)	1.15 (0.01)
		Olivine – Clinopyroxene - Gypsum	
		Peak simulated : 947 - 310/328/359/384 - 485	
		Calibration equation: a = 1.71 × W$_{sulfate\ theoretical}$	
GOLCX90	0.50 – 0.40 – 0.10	0.49 (0.16) – 0.35 (0.06) – 0.05 (0.03)	0.15 (0.03)
GOLCX95	0.50 – 0.45 – 0.05	0.39 (0.17) – 0.44 (0.07) – 0.03 (0.03)	0.07 (0.02)
		Olivine - Mg-sulfate	
		Peak simulated : 950 and 1040 cm^{-1}	
		Calibration equation: a= 5.26 x WF$_{sulfate\ theoretical}$	
MgOLI80	0.80 - 0.20	0.84 (0.05) - 0.16 (0.09)	0.90 (0.19)
MgOLI90	0.90 - 0.10	0.86 (0.02) - 0.14 (0.03)	0.81 (0.03)
MgOLI95	0.95 - 0.05	0.94 (0.03) - 0.06 (0.19)	0.30 (0.59)
MgOLI97	0.97 - 0.03	0.95 (0.02) – 0.05 (0.20)	0.23 (0.63)
		Orthopyroxene - Mg-sulfate	
		Peak simulated: 330/370/400 - 1040 cm^{-1}	
		Calibration equation: a = 2.19 x WF$_{sulfate\ theoretical}$	
MgOPX80	0.80 - 0.20	0.82 (0.02) - 0.18 (0.02)	0.43 (0.02)
MgOPX90	0.90 - 0.10	0.89 (0.01) - 0.11 (0.02)	0.25 (0)
MgOPX95	0.95 - 0.05	0.90 (0.01) - 0.10 (0.02)	0.20 (0)
MgOPX97	0.97 – 0.03	0.96 (0) – 0.04 (0.01)	0.08 (0)

	Clinopyroxene - Mg-sulfate		
	Peak simulated: 666/1006 and 1040 cm_{-1}		
	Calibration equation: a = 1.05 x $WF_{sulfate\ theoretical}$		
MgCPX80	0.80 - 0.20	0.82 (0) – 0.18 (0.04)	0.19 (0.01)
MgCPX90	0.90 - 0.10	0.87 (0) – 0.13 (0.03)	0.14 (0.01)
MgCPX95	0.95 - 0.05	0.94 (0) – 0.06 (0.04)	0.06 (0.01)
MgCPX97	0.97 – 0.03	0.96 (0) – 0.04 (0.03)	0.03 (0.01)
	Plagioclase - Mg-sulfate		
	Peak simulated: 750 and 1113 cm_{-1}		
	Calibration equation: a = 2.88 x $WF_{sulfate\ theoretical}$		
MgPG80	0.80 - 0.20	0.86 (0.04) – 0.14 (0.09)	0.51 (0.15)
MgPG90	0.90 - 0.10	0.91 (0.03) – 0.09 (0.12)	0.33 (0.21)
MgPG95	0.95 - 0.05	0.93 (0.01) – 0.07 (0.07)	0.23 (0.11)
MgPG97	0.97 – 0.03	0.93 (0.02) – 0.07 (0.06)	0.22 (0.10)

Table IV.3: Samples created in this study for binary and ternary mixtures with sulfates (Ca and Mg) and basaltic minerals (i.e olivine, orthopyroxene, clinopyroxene and plagioclase). Peak simulated in each mixture are reported, followed by the calibration equation resulting from calibrations. Weight fractions (WF) theoretical, WF calculated and coefficients (a) are reported for each mixture. Errors relative to calculations are reported next to the WF calculated and coefficients.

Simulation results and derived coefficients are reported in Table IV.3. We established a calibration expressed with the coefficient calculated (Eq.4) from areas simulated for each mineral according to the initial weight fraction of gypsum, indicated in Fig.IV.8. In the Fig.IV.8, we obtained a good calibration with R_2 = 0.99 on ternary mixtures.
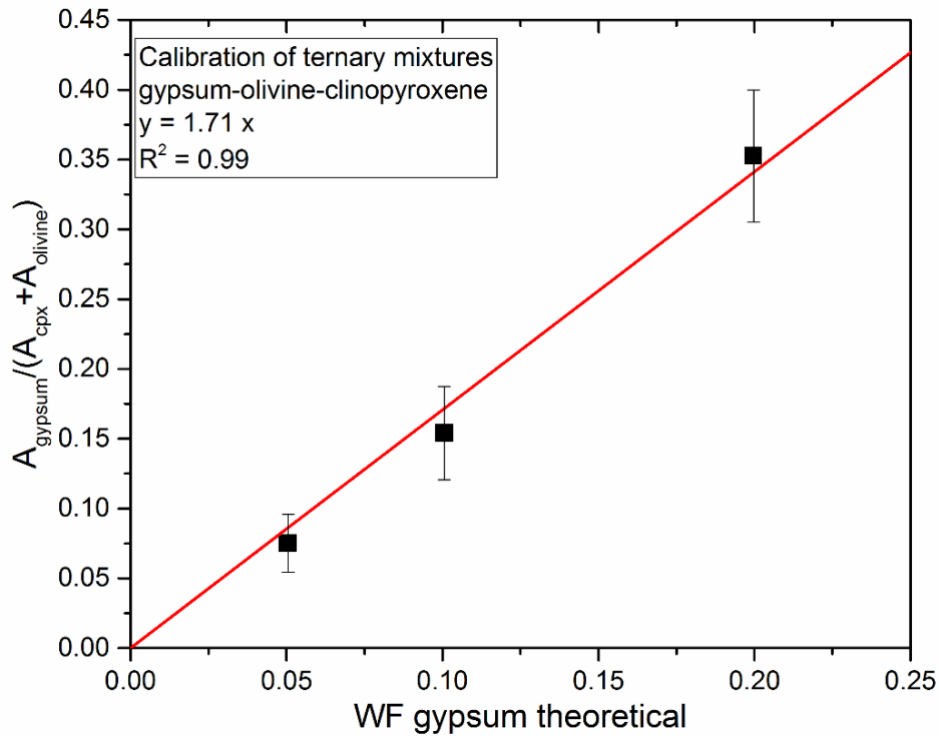
Fig.IV.8: Calibration line for ternary mixtures of gypsum (WFgypsum =0.2, 0.1, 0.05) with olivine (WFolivine = 0.40, 0.50, 0.50) and clinopyroxene (WFclinopyroxene = 0.40, 0.40, 0.45). Black squares are simulations results with their errors (black vertical lines). Red line is the calibration line calculated from simulation results. Equation and regression linear coefficient (R2) are specified in the graph box.

IV.5.2. Binary mixtures with Mg-sulfate

As for Ca-sulfate mixtures, we proceeded with the same method for pellets containing Mg-sulfate. We reported results from Mg-sulfate calibration on Fig.IV.9 where the same mixtures of natural silicate minerals of olivine, pyroxenes and plagioclase are represented. In Fig.IV.9A and 9C, pyroxenes calibrations with Mg-sulfate are showed. As we can see on these results, the R2 is fairly good (0.86 for orthopyroxene mixtures and 0.85 for clinopyroxene) and initial proportions of Mg-sulfate can be well estimated from our method. Plagioclase mixtures with Mg-sulfate is reported on Fig.IV.9B, where we obtained R2= 0.43 and show the less consistent results. Finally, olivine mixtures with initial proportions of Mg-sulfate (Fig.IV.9D) result in a R2= 0.69. All results of calculated mixtures proportions are reported in Table IV.3.
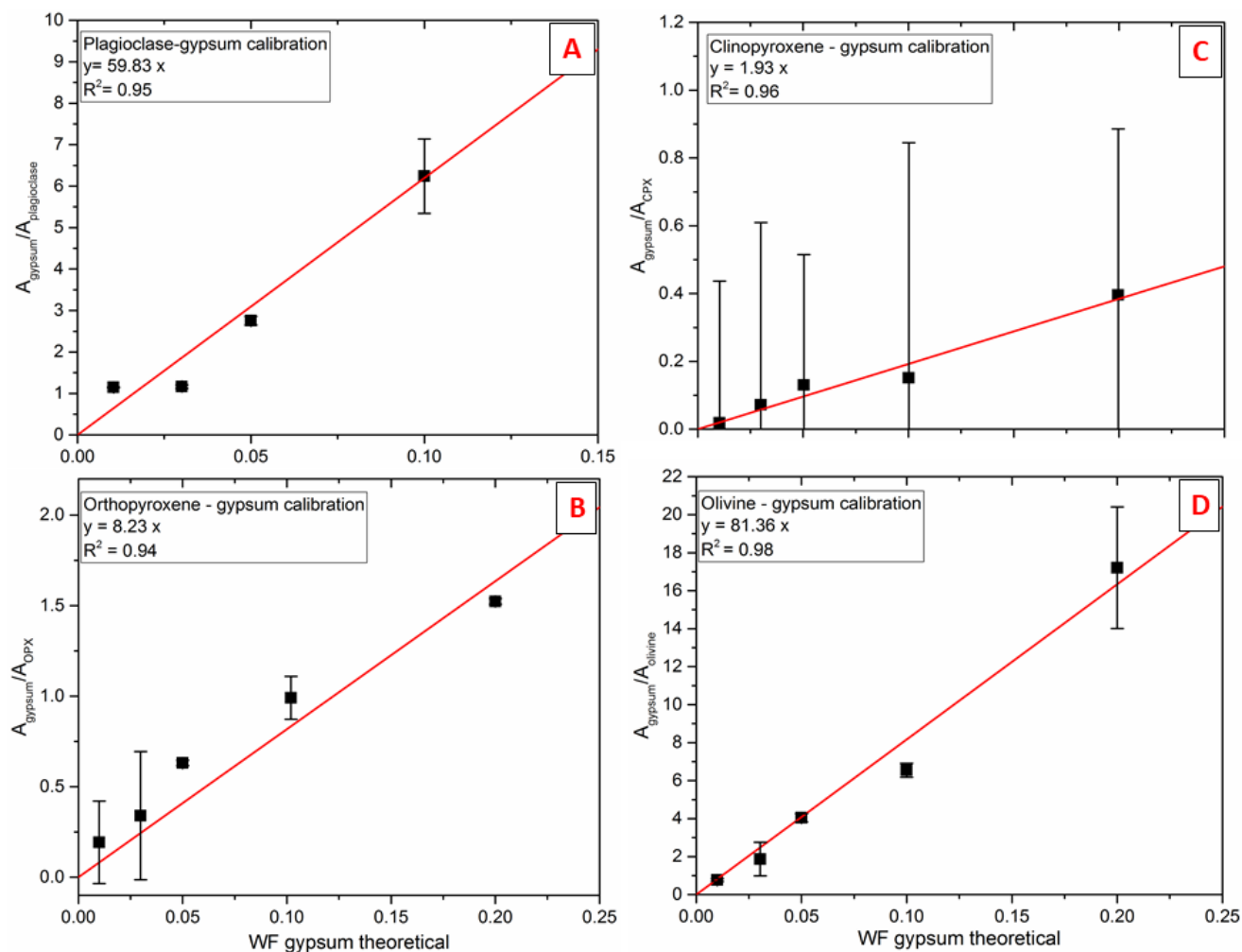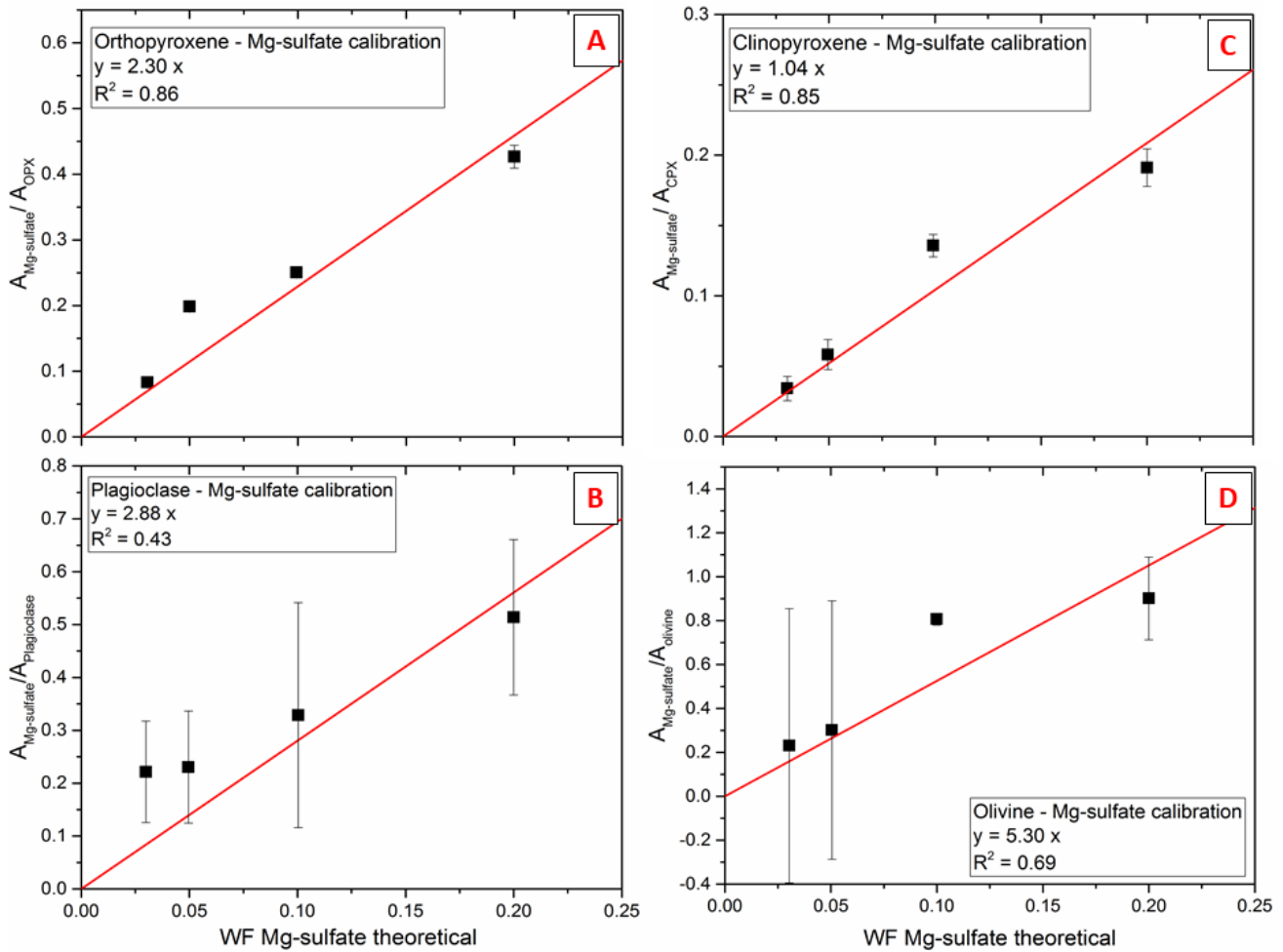
Fig.IV.9: Calibration coefficients calculated from simulated areas on Mg-sulfate and mineral mixed versus the theoretical weight fraction (WF) of the sulfate. Black squares are samples simulated with their relative errors. Red lines correspond to calibration lines extrapolated from calibration coefficients depending on theoretical weight fraction of Mg-sulfate. Calibration lines established on four binary mixtures: A) orthopyroxene; B) plagioclase; C) clinopyroxene; D) olivine; with Mg-sulfate in different proportions (WFgypsum = 0.20, 0.10, 0.05 and 0.03). Equations and linear regression coefficients (R2) of each calibration lines are reported in boxes for every graph.

IV.6. Discussion

Binary and ternary mixtures with sulfates were calibrated with several proportions of sulfate tested. In this section, we discuss the limit of our calibration method and its application to the martian context.

IV.6.1. Detection limit of sulfur

In Fig.IV.7 we have reported results from gypsum binary mixtures. We reported error bars extracted from peak areas simulations. From Fig.IV.7B and 7C, corresponding to pyroxene-bearing mixtures, samples with 0.03 and 0.01 weight fractions of gypsum present a significant vertical error. Some selected peaks for the calibration do not exhibit a high Raman activity but

we had to select those peaks, caused by the necessity to choose individual peaks for our simulations. In simulation results shown in Table IV.3, we can see that we have still a good agreement in between the calculated proportions and the initial proportions within the mixtures. Considering that some of molecule vibrations are less Raman active relative to Raman spectroscopy, we consider that our method of calibration is reliable until $WF_{sulfate}= 0.03$ weight fraction in a mechanical mixture.

Knowing this detection limit of our calibration, we can extrapolate this method to martian rocks. With the proposed method and the calibration equations, S could be determined at the surface of Mars for a sedimentary rock containing S until approximately $WF_S = 0.007$ weight fraction (i.e., 7 000 ppm). Below this content, our calibration can still be applied, but the errors will be higher, and results might not be reliable.

IV.6.2. Application of the calibration to the determination of sulfur on the martian surface

Results provided by the calibration are specified in Fig.IV.10 for all mixtures created. On Fig.IV.10, we can see the good agreement of our calibration method. This plot showed us that the calculated proportions of gypsum are close to the theoretical proportions and all data points are aligned along the 1:1 line. Ternary mixtures with gypsum are also represented and are in good accordance. Mg-sulfate mixtures in Fig.IV.10 showed us that the calibration is also good and data points are aligned along the 1:1 line.
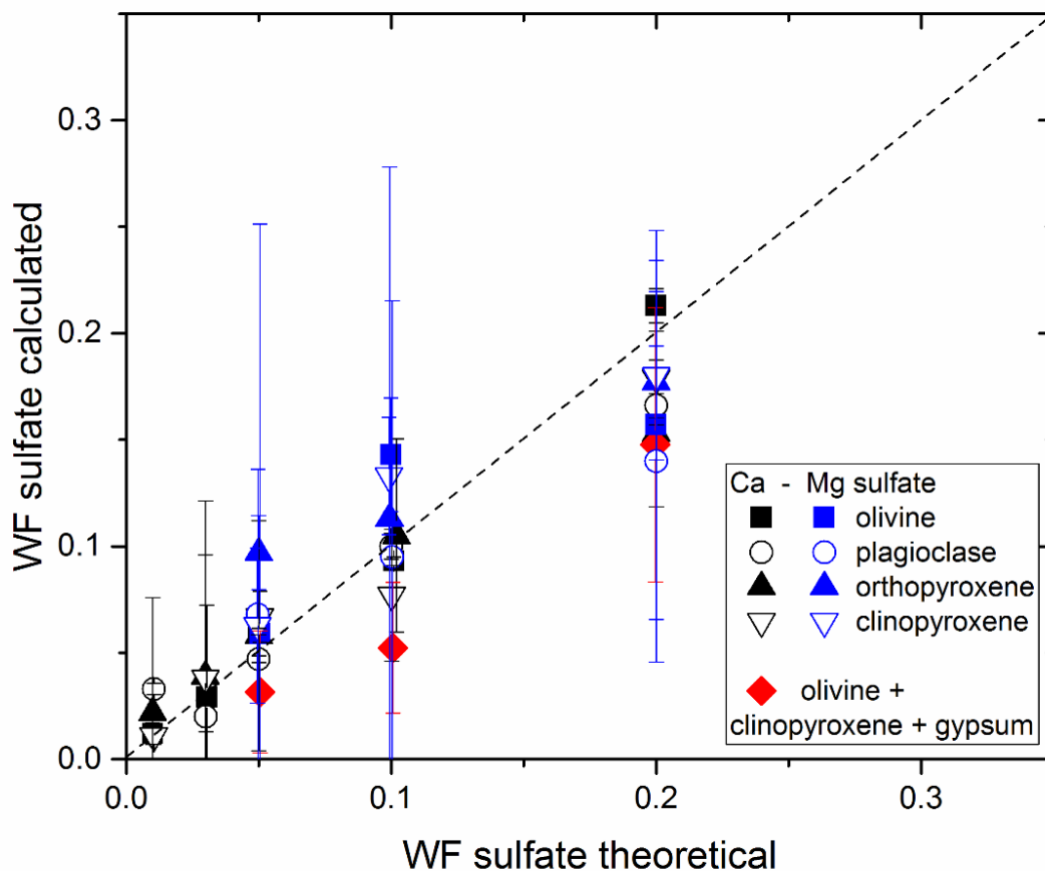
Fig.IV.10: Weight fractions calculated for sulfates (Ca and Mg-sulfate) depending on its theoretical weight fraction in each mixture of olivine, clinopyroxene, orthopyroxene and plagioclase. In black, gypsum binary samples are represented. Mg-sulfate mixtures are in blue. Red diamonds: ternary mixtures of gypsum.

We have reported on Table IV.3 all calibrations equations calculated from our calibration method on gypsum and Mg-sulfate mixtures.

As a result, we can determine the sulfate content in a mixture with olivine, pyroxenes and plagioclase in unknown proportions according to equations extracted from our simulations shown in Fig.IV.7, 8, 9 and 10. To apply our calibration method, the first step is to acquire a Raman spectrum on the Mars surface a mechanical solid mixture containing sulfate (Ca or Mg). After identification of the mineralogy presents, it is possible to perform the simulation on specific peaks according to the phases in the mixure (reported in Table IV.3). Then, a coefficient can be calculated (i.e., the "a" component in equations in Table IV.3) and reported in our calibration figures (i.e., Fig.IV.7,8,9 or 10) to determine the S content.

The established calibration method based on Raman spectroscopy will be of use for the future 2020 Mars mission to quantify S abundance when present as sulfates. For the application of the present calibration, the peak selections from Raman spectrum must be conducted with care. We suggest using only the peaks mentioned in the present work and reported in the Table IV.A1 (in annex section). However, this will be dependent on the resolution of the SuperCam Raman spectrometer and the quality of the acquired signal (Wiens et al. 2016). In the case of a low resolution, peaks with low intensities (for instance ν_3) will be difficult to constrain. However, other peaks mentioned in the Table IV.A1, such as ν_1 or ν_2 can be well defined by the future rover and calibration can still be applicable (referred with the Table IV.A1). Since our analyses were performed with a high-resolution Raman spectrometer, further analyses will be performed with a pulsed-Raman with distance from the sample similar to the one presupposed for SuperCam, in order to compare data and modify, if necessary, the calibration.

Furthermore, Mars mineralogy has been partly investigated using remote sensing and rover data, as well as martian meteorites, showing that pigeonite and augite are the two most common pyroxenes found in martian rocks (both are clinopyroxenes but with low Ca content for pigeonite; e.g., Lodders 1998, Agee et al. 2004; Mustard et al. 2005; Cousin et al. 2017; Morrison et al. 2017). Mg-rich olivine, orthopyroxene and plagioclase have also been detected in martian meteorites and at the surface of the planet (Agee et al. 2004; Mustard et al. 2005; Dehouck et al. 2014; Cousin et al. 2017; Morrison et al. 2017). Nonetheless, Fe-rich olivine can be expected in small amounts which only differs in spectral signature by the relative intensity between the double peak around 800-850 cm$_{-1}$. Since our calibration is not based on those peaks (see Table IV.3), the quantification of sulfate with fayalite is still be possible. Plagioclase such as anorthite may be the most common feldspar on Mars (Bish et al. 2013, Blake et al. 2013, Vaniman et al. 2014) although andesine has been observed as the predominant plagioclase at Gale crater by the Curiosity rover instruments (Sautter et al. 2016, Morrison et al. 2017). Consequently, the proposed calibration method can be useable for a mixture of sedimentary rocks containing sulfates and silicate minerals even if the minerals present does not have the same chemical composition within a solid solution as used in our study.

IV.7. Summary

In the present study, we have prepared pellets by mixing Ca and Mg sulfates with silicate minerals commonly found in basalt (olivine, pyroxenes and plagioclase) in order to investigate the Raman signature of multi-minerallic mechanical assemblages. The main objective was to establish a relevant calibration for the determination of S content at the surface of Mars with analytical conditions close to the future Raman spectrometer on SuperCam equipment for the 2020 spatial mission. Calibration equations were obtained for both binary and ternary mixtures of $CaSO_4$ with minerals for a range of gypsum of 0.01 to 0.20 weight fraction. Equations were also estimated from Mg-sulfate mixtures with initial proportion of 0.03 to 0.20 weight fraction. The protocol used in this study involves simulations of the resulting average Raman spectrum using a Voigt distribution on peaks attributed to each mineral. The simulation of the entire Raman spectrum is not simulated with an enough good accuracy and careful attention is necessary for peak identifications. The actual method could be applied to the quantitative characterization of the martian soil, which is recognized to present sedimentary rocks containing sulfates and silicate minerals obtained from bedrock erosion.

Given our equations extracted from calibrations on both Mg and Ca sulfates, we would be able to calculate a coefficient from a given Raman spectrum acquired on Mars and treated according to specific peak simulations. Coupling this coefficient with the proper calibration equation (i.e., when knowing the mineralogical characterization of the mixture analyzed) we can estimate the proportion of this sulfate in weight fraction. By extent, this calibration could be used to constraint part of the S content at the surface carried by sulfate mineral phases. We have estimated the detection limit of S at 7 000 ppm (i.e., 0.7 wt %) which is well below the current detection limit by the LIBS technique (i.e., 5 - 10 wt %; e.g., Wiens et al. 2012; Nachon et al. 2014, Anderson et al. 2017). Nevertheless, further calibrations are requested involving more complex mineral mixtures, including other sulfates (Fe-sulfate), sulfides, and mixtures with more than four compounds. Calibration using a martian basalt glass analogue in presence of sulfates could also be established to better constrain the S quantification on the surface of Mars.

IV.8. Perspectives

The Raman calibration presented in this study shows good results and seemed to be promising to help for sulfate quantification with the Mars 2020 rover. However, until the rover land on the planet, improvement of the current calibration could be done. At the end of this study, several perspectives have been considered.

For instance, to improve our method, some tests could be done. Indeed, the mixtures tested here were prepared and analyzed by the same person, hence the proportion of each mineral was known. We were able to determine if the calibration was accurate or not according to the already known proportion. To validate this study, it would be of interest to realize a mixture without knowing the proportions. Indeed, the scientist performing the Raman analyses and subsequent calculation to quantify the sulfate present in the mixture (according to our study), will not be aware of the mixture proportion. With this test, we would be able to determine if it can be applied on sulfate mixtures on Mars. In addition, more complex mixtures can be considered.

Here, we have managed to realize a Raman calibration with 3 minerals in addition to the sulfate. However, it is clear that this case is not entirely representing the sedimentary rocks containing sulfates at the surface of Mars. Although, we have started this study with mixture of a basaltic glass coupled to gypsum, but we did not succeed to obtain a good calibration. Additional work is needed to better constrain the sulfate Raman calibration.

The calibration established in this work is made on a solid-state laser Raman spectrometer, which is different from the future Raman onboard the SuperCam instrument. Indeed, the latter will be a pulsed Raman spectrometer (Wiens et al. 2016). It could be of interest to process to the same procedure used in this work, but with a pulsed-Raman. Also, it could be interesting to perform such acquisition in a martian atmosphere simulation. Indeed, the actual Raman acquisitions are made under terrestrial atmosphere. The martian atmosphere presents a different chemical composition than Earth (i.e., CO_2-rich), which induces variation in the Raman spectra. Performing these experiments will permit to identify the martian atmosphere contribution into the Raman spectra and compare it with those obtained in this study. With this, our current calibration could still be applied. In addition, some tests could be ran using the LIBS on our pellets and establish a new calibration. Currently, the LIBS cannot detect S below 5 wt % (Wiens et al. 2012). With these mixtures, the detection limit could be improved. Then, until the Mars 2020 rover arrives on Mars, the LIBS could perform accurate S quantification with the Curiosity Rover.

Finally, another way to improve our current calibration is to proceed with Multi-Component Analysis simulation. With the same method presented previously in the section IV.3 (calibration tests), it will consist in the implementation of two or three endmembers present in the mixture, and the acquired mixture spectrum. From this, the multi-component analysis calculates the contribution of each endmember to produce the mixture spectrum. We were not able to realize this work due to a lack of time, but it should be seriously considered as an improvement for this study.

In this manuscript, we have investigated the behaviors of various volatile species which are both H_2O and SO_4^{2-} in amorphous and crystallized materials. Their observation at depth and in the surface have proven that a lot of work is currently needed to better understand the volatile behavior on Mars. We will summarize those discoveries in the next section, as well as the future work to consider.

Conclusion and application

Summary of the findings from this thesis

Part of this study was based on an experimental work aiming at the understanding of volatile behaviors in Fe-rich melts. There is a lack of study on this topic due to the difficulty to quench Fe-rich melts. However, these experiments are needed to better constrain the magmatic system of Mars. With this, the understanding of volatile content and their contribution to the primitive atmosphere of Mars could be better understood.

The high-pressure experiments were performed with a piston-cylinder apparatus to realize Fe-rich glasses containing H_2O and S. These glasses were experimented at pressures representing a maximum of 200 km in deep, which corresponds to the suggested source for martian melts (Filiberto 2009). The sample characterizations have been fully addressed notably with spectroscopic instruments (Raman, FTIR, XPS), which indicate the volatile content, speciation and their interaction within the silicate melt. The spectroscopic investigations were combined with chemical composition analyses (SEM, EPMA, wet chemistry) and X-Ray diffraction was used for a specific case of crystallized samples (Chapter II, section II.3). The different instrument used to characterize our experiments have permitted to obtain new insights on the volatile behaviors in martian basaltic analogues. Mostly, this new study has permitted to develop a Raman database on Fe-rich glasses obtained at high pressure, or in mineral mixtures, and containing S and H_2O. This work could serve as a reference for the future 2020 Mars mission, in particular, as there will be a Raman spectrometer onboard the SuperCam instrument.

First, the H_2O behavior in Fe-rich glasses showed unexpected results.
On one hand, the glasses obtained with low H_2O content (< 3 wt %) in glasses with ($10 - 16$ wt % FeO_{tot}) presented new features discovered by Raman spectroscopy compared to terrestrial basalts at the same H_2O content. The Raman signatures of our martian analogues is different, with the bending vibration ($200 - 600$ cm$_{-1}$) much less intense than the stretching region ($800 - 1200$ cm$_{-1}$). More importantly, the Raman spectroscopy analyses have enabled the detection of Free OH species in our Fe-rich glasses at low H_2O content (~ 1 wt %). On the contrary, these species are only observed at high H_2O content in our terrestrial analogues (> 6 wt %). The formation of such species could affect the polymerization of the silicate network, hence the viscosity of the melt.

On the other hand, we have performed H_2O-rich experiments in the same chemical composition (i.e., Fe-rich, GC). With our experimental device, we were not able to quench such melt with > 3 wt % H_2O. Instead, a dendritic texture is observed, corresponding to a trachy-dacitic liquid coupled to pyroxene and amphibole crystals. Although no glass is obtained, these results are interesting and applied for martian melts. It could be of interest to establish experiment with controlled temperature drop to investigate the crystallization sequence in these Fe-H_2O-rich compositions.

Although no solubility results could have been obtained on Fe-rich glasses with H_2O, we could not dissolve more than 1 wt % H_2O in our glasses with our current experimental settings. This value is quite low compared to terrestrial basalts that can dissolve more than 6 wt % H_2O for the same pressure range.

While the H_2O results evoke a small amount of H_2O degassed into the primitive atmosphere of Mars (although the solubility was not reached), **we have investigated the S solubility in the same chemical composition (i.e., GC and CL: 15.5 and 23.5 wt % FeO_{ini}; respectively).** We performed experiments with S presents as $CaSO_4$ or S_0 at the beginning of the experiments. A

maximum of 1.4 wt % S is dissolved. No difference in S dissolved between S_0 and $CaSO_4$ experiments was found, due to a strong oxidation of the S_0, in exchange with Fe^{3+} into Fe^{2+}. With our new results, we have developed a new S solubility law at various fO_2 and in different melt compositions (from basalt to rhyolite). The model is parametrized with a new compositional parameter, the IFS, but depends also on the NBO/T. The law is established on 150 S-saturated experiments from the literature coupled to our 6 S-saturated Fe-rich glasses. The model developed reproduces the S solubility for both terrestrial and martian melt compositions. The highest S solubility value obtained in our study reconsider the maximum of S that could be dissolved in a martian melt.

The high S content dissolved in the martian melt could explain the large amount of sulfates detected at the surface of Mars. Then, a way to quantify the S in the sulfates has been developed. **With this method, the S can be detected down to 1 wt % in mixtures with sulfates (Ca or Mg) with the future Raman of the SuperCam instrument.** The coupling of the experimental investigation of S in martian melts to its quantification in sulfates at the surface of Mars, permits to better constrain the S budget of Mars.

Evolution of the S solubility during a martian melt ascent

Based on our two high-pressure experimental studies, we were able develop a model predicting the S evolution in a martian melt, combining our results on both H_2O and S behaviors in a martian melt.

To establish the model, the solubility law established in Chapter III for S has been used (i.e., eq. 26). We chose two different chemical compositions, with one that is supposed to represent the primitive parental melt of Shergottites (Dreibus and Wänke 1985), and a differentiated rock observed at the surface of Mars (Sautter et al. 2015). Hence, the calculated IFS for those two compositions are around 9 for the primitive composition, and 12 for the differentiated (see Fig.C.1). The NBO/T calculated, with Fe^{2+} as major species, is depolymerized for the composition of Dreibus and Wänke at 2.8 and strongly polymerized for the differentiated rock at 0.18. The compositions are detailed in the annex section (Table C.A1). The temperature was fixed at 1300 °C, according to Filiberto (2008) which details the temperature and depth of formation for such basaltic composition. The pressure has been calculated according to the martian depth (i.e., considering g = 3.711 m/s^2 and the density of the martian mantle at 2900 g/cm^3) and range from 2.5 to 0 GPa.
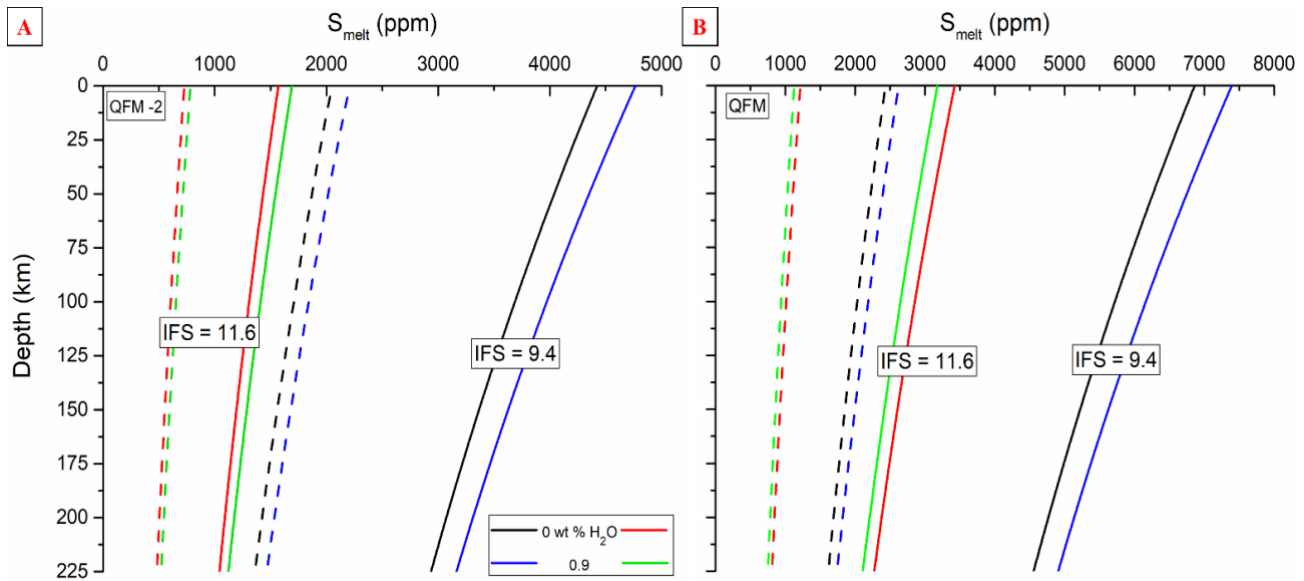
Fig.C.1 : S solubility evolution during the ascent, considering the S solubility law established in the Chapter III (see section III.5.2) for different conditions: A) at QFM -2; B) QFM. Dashed lines are for 0.7 wt % S in the source (i.e., S_{ini}) whereas bold lines are calculated for 1.8 wt % S_{ini} (according to Gaillard and Scailler 2009). The black and blue lines are referring to calculation on Dreibus and Wänke (1985) primitive composition at an IFS and NBO/T of 9.4 and 2.8 respectively. Red and green lines are for the differentiated rock reported in Sautter et al. (2015) with 11.6 and 0.18 for the calculated IFS and NBO/T, respectively.

According to Gaillard and Scaillet (2009), the basaltic source should contain between 0.7 to 1.8 wt % S. Hence, we have tested a model considering those two values as initial S content. The H_2O content tested, varied between 0 to 0.9 wt %. We have simulated the S in the melt for two redox conditions: QFM -2 and QFM.

The prediction of S in the martian melts is reported in Fig.C.1. In Fig.C.1A, the reduced condition model is represented. For the primitive composition at IFS = 9.4, we can see that the maximum S reached is ~4700 ppm in the melt at the surface with 0.9 wt % H_2O and 1.8 wt % S_{ini} available in the source. With 0.7 wt % S_{ini}, the maximum of S barely reaches 2500 ppm at the surface. The slope in S content in the melt is higher with 1.8 wt % S_{ini} present, compared to 0.7 wt % S_{ini}.

For the differentiated igneous rock at IFS = 11.6, the maximum of S dissolved in the melt is ~1700 ppm in a hydrous melt and S-rich source (i.e., 0.9 wt % H_2O and 1.8 wt % S_{ini}). In a low S content in the source (i.e., 0.7 wt %), less than 1000 ppm S reached the surface within the melt. This could be compared to terrestrial basalt values (Gaillard and Scaillet 2009) which can bring no more than 2000 ppm at the surface for such conditions (i.e., 1300 °C).

In Fig.C.1B, the oxidized condition model is represented. The same trend is observed: the primitive composition will bring almost 7500 ppm S once reaching the surface in presence of H_2O and with a S-rich source. On the contrary, a hydrous differentiated melt will only bring a maximum of 3500 ppm S.

Considering the Fig.C.1, values for the primitive composition (IFS = 9.4) with a S-poor source are close to the S-rich source for the differentiated melt (IFS = 11.6). The S-rich source (i.e., 1.8 wt % S_{ini}) with the IFS= 9.4 is more distant from the other values.

The results predicting the S evolution in a martian melt are different than the S solubility determined in Chapter III. Indeed, in our compositions GCS and GCS_0, the dissolution of S reached 1.7 and 1.3 wt % S, respectively, at 1 GPa. In the proposed model, we do not reach such values. Indeed, the model presented here considers parameters that are different from our experimental setting: 1) the chemical composition, 2) the temperature, 3) the oxygen fugacity, 4) the S in the source (i.e., S_{ini}). When ajusting the parameters close to our experimental conditions presented in Chapter III, the S in the melt at the surface reaches 1.2 wt %, which is close to our S results in GCS and GCS_0 experiments.

Hence, S will be more important in the martian melt with a low IFS and in a hydrous system, with also a high S content available in the source. The S dissolved will be increased with increasing the fO_2. These results are consistent with the degassing model of Gaillard et al. (2013) which determined that the maximum of S degassed will be considering oxidized conditions and 0.4 wt % H_2O in the melt.

The range of S dissolved in the melt seemed in accordance with the findings of Gaillard and Scaillet (2009); although the values are based on thermodynamical models. In more reduced conditions, such as IW +2 that is supposed to prevail in the primitive martian mantle, the S dissolved would be considerably lower than our current results. However, the melt will rise into various redox conditions and toward oxidized layers (i.e., the martian crust) up to QFM or higher (Herd et al. 2002; Herd 2008; Schmidt et al. 2013). Then, we can postulate that martian basalts could contain up to 6700 ppm S once they reached the surface. Then, the Raman spectra acquired in our study on various S content in different Fe-rich composition can serve as a reference. From a qualitative point of view, they can be compared to approximate the S content present or determined their redox conditions, since we have spanned S values from 3000 to 17 000 ppm S and probably experimented between QFM and QFM+1. Then, we can quantify the S content in basaltic glasses with the calibration of Morizet et al. (2017). Since the melt will suffer oxidation during its ascent, we can expect to find S^{6+} species in the martian basaltic glasses.

Volatile budget

We have found that a lot of S can be brought to the surface through a martian basaltic melt. With our new solubility model, we can expect a maximum of S present in basaltic glasses at 6700 ppm, in the most hydrous and oxidized condition scenario. Hence, a first estimation of the S budget from the volcanism can be estimated, although calculation of the gas fraction emitted in the atmosphere needs to be combined to our results.

The S-rich basaltic glasses are then available to be weathered at the surface of Mars. The presence of large sulfates areas discovered at the surface could be coming from the weathering of such S-rich glasses, coupled to the S from the atmosphere emitted by volcanism. The Raman calibration established in our study permits the quantification of this element in various sulfate mixtures down to 1 wt % S (see Chapter IV).

Combining the quantification of S in basaltic glasses with Raman calibration already developed and the Raman calibration on sulfates, will permit to have a good estimate of the S content at the surface of Mars. The experimental work established here will also help to determine the amount of S that are in the source of basaltic melt when using the solubility law proposed in our study (Chapter III).

While our study made on S behavior in Fe-rich melts combined to the Raman calibration in sulfates allows a good knowledge of this volatile in the martian magmatic system, the H_2O behavior still need further investigation. Indeed, we have encountered difficulties to obtain a Fe-rich glass with high H_2O content (> 3 wt %), hence no solubility law could be obtained in our study (Chapter I & II). However, we realized that it is probable that martian basalt cannot

dissolved more than 1 wt % H_2O without crystallizing needle-like crystals. This value lie in the range of H_2O proposed (up to 2 wt %) to be present in martian basalts according to previous studies (Dann et al. 2001; Jones 2004; Nekvasil et al. 2007; Filiberto 2008; McCubbin et al. 2010a, 2012; Usui et al. 2012, 2015). This suggests that martian basalt will carry a small amount of H_2O to the surface and in the atmosphere, in comparison to S. We could expect less than 1 wt % of H_2O dissolved, and even less brought to the surface upon decompression.

Future work

With the results obtained in this study, several applications can be made with the SuperCam rover:

1) Sulfate quantification through the calibrations established in Chapter IV. The spectra obtained at the surface on sulfate-mixtures will be compared with the database obtained in our study. The closest Raman spectra from our database will be selected (according to the predominance of either olivine, pyroxenes or plagioclase and sulfate species) and used to apply the calibration.

2) Determination of igneous glass at the surface. The acquired Raman spectra of SuperCam can be compared with our Raman spectra on Fe-rich glasses in presence of either H_2O or S. Then, it can be used to decipher an igneous glass material from another amorphous silica component.

3) Fe redox speciation. The analogues established in our study represent different Fe redox states. Then, using these spectra can help to understand the redox recorded by the igneous glasses.

4) Presence of Free OH. If the feature at 670 and 3660 cm^{-1} are observed in the igneous glass Raman spectra, then it can inform on the amount of H_2O carried by the martian melt through the surface.

5) S quantification in glass material. The use of the calibration already established by Morizet et al. (2017) using Raman spectroscopy has proven to be accurate even on Fe-rich glasses.

Except to the first application mentioned above, the others imply the presence of igneous glass. Even if amorphous materials have been detected at the surface (Bish et al. 2013, 2014; Dehouck et al. 2014; Rampe et al. 2014), their origin is still unclear. We have to consider that there is a possibility to find only crystallized basaltic rocks. In that case, our results presented in Chapter II on H_2O-Fe-rich basaltic composition can be used.

Nonetheless, the current work established here for three years has permitted to obtain crucial knowledge on the behavior of both H_2O and S in analogues to martian rocks. The next steps of this study are multiple. Only two volatile behaviors in martian basalt analogues have been investigated 1) due to the unexpected difficulty to perform high pressure experiments, and 2) due to a lack of experimental work considering the martian magmatic system in presence of volatiles. However, the S and H_2O are not the only volatiles detected on Mars. Indeed, the currently atmosphere of Mars is CO_2-rich, which indicates that this volatile has also played a role; although experimental studies have determined that a small amount of CO_2 is expected in martian basalts (i.e., 2400 ppm at IW +1; Stanley et al. 2011, 2012, 2014).

Among the other volatiles detected at the surface of Mars or within martian meteorites, we can find Cl and F (Keller et al. 2007; Taylor et al. 2010; Usui et al. 2012; Agee et al. 2013; Forni et al. 2015; McCubbin et al. 2016). Actually, the Cl has been detected in high content at the surface of Mars from 1.5 to 7 wt % Cl (Filiberto et al. 2018). Thus, an experimental study on the same chemical composition established in this thesis (i.e., GC with 15.5 wt % FeO_{ini}), containing Cl can be interesting to perform. The first experiments should be only Cl-rich, without another volatile species present. Indeed, the Cl detection by Raman spectroscopy in glasses is still not well constrain. It will be interesting to identify Cl-species in Fe-bearing glasses, quantify it and

perhaps develop a quantification method by Raman spectroscopy. Combined to these experiments, the addition of S and H_2O is needed to observe the impact on each volatile at pressure. In extent, the same work can be performed with F-bearing experiments.

Although the experiments considered will take time, a degassing model combining H_2O and S can be realized meanwhile. Indeed, these two volatiles are thought to be the more abundant into the martian melts, in the light of our recent results, with 1 wt % dissolved for both H_2O and S. By the arrival of the 2020 Mars rover, some of these perspectives can be achieved and Raman spectra can be obtained to serve also as a database. The latter can be fed with additional work on Raman calibration with mixtures corresponding to the sedimentary rocks at the surface of Mars. It could be developed on other sulfate species (i.e., Fe-sulfate), with more complex mixtures (> 3 components), or to calibrate other volatile-bearing minerals containing Cl, F or even P (such as apatite or chloride) that are less constrained by Raman spectroscopy.

The Raman database could be also filled with experimental investigation on martian basalt analogues containing volatiles. Either way, there is currently a lack of experimental study using atypical composition such as martian rocks. The available wide variety of analytical instruments to characterize such experiments, notably the Raman spectroscopy for the future martian mission, will permit to develop many interesting researches for the future years to come.

References

Agee, C.B., Draper, D.S. (2004): Experimental constraints on the origin of Martian meteorites and the composition of the Martian mantle. Earth Planet Science Letters, 224, 415-429.

Alexander, C.M.O.D, Bowden, R., Fogel, M.L., Howard, K.T., Herd, C.D.K., Nittler, L.R. (2012): The provenances of asteroids, and their contributions to the volatile inventories of the terrestrial planets. Science, 337, 721 - 723.

Anderson, D.E., Ehlmann, B.L., Forni, O., Clegg, S.M., Cousin, A., Thomas, N.H., Lasue, J., Delapp, D.M., McInroy, R.E., Gasnault, O., Dyar, M.D., Schröder, S., Maurice, S., and Wiens, W.C. (2017): Characterization of LIBS estimation lines for the identification of chlorides, carbonates, and sulfates in salt/basalt mixtures for the application to MSL ChemCam data. Journal of Geophysical Research: Planets, 122, 744 – 770.

Aoki, S., Nakagawa, H., Sagawa, H, Giuranna, M., Sindoni, G., Aronica, A. et al. (2015): Seasonal variation of the HDO/H_2O ratio in the atmosphere of Mars at the middle of northern spring and beginning of northern summer. Icarus, 260, 7 - 22.

Ardia, P., Hirschmann, M.M, Withers, A.C., Stanley, B.D (2013): Solubility of CH_4 in a synthetic basaltic melt, with applications to atmosphere-magma ocean-core partitioning of volatiles and to the evolution of the Martian atmosphere. Geochimica et Cosmochimica Acta, 114, 52 – 71.

Armstrong, L.S., Hirschmann, M.M, Stanley, B.D., Falksen, E.G., Jacobsen, S.D. (2015): Speciation and solubility of reduced C-O-H-N volatiles in mafic melts: Implications for volcanism, atmospheric evolution, and deep volatile cycles in the terrestrial planets. Geochimica et Cosmochimica Acta, 171, 283 – 302.

Arvidson, R.E., Poulet, F., Bibring, J.-P., Wolff, M., Gendrin, A., Morris, R.V., Freeman, J.J., Langevin, Y., Mangold, N., Bellucci, G. (2005): Spectral reflectance and morphologic correlations in Eastern Terra Meridiani, Mars. Science, 307, 1591-1594.

Baker, D.R., Moretti, R. (2011): Modeling the solubility of sulfur in magmas: A 50-year old geochemical challenge. Reviews in Mineralogy & Geochemistry, DOI: 10.2138/rmg.2011.73.7.

Balta, J.B., McSween Jr, H.Y. (2013): Water and the composition of Martian magmas. Geology, 41, 1115 – 1118.

Bandfield, J.L., Hamilton, V.E., Christensen, P.R. (2000): A global view of Martian surface composition from MGS-TES. Science, 287, 1626-1630.

Baratoux, D., Pinet, P., Toplis, M.J., Mangold, N., Greeley, R., Baptista, A.R. (2009): Shape, rheology and emplacement times of small martian shield volcanoes. Journal of Volcanology and Geothermal Research, 185, 47 – 68.

Baratoux, D., Toplis, M.J., Monnereau, M., Sautter, V. (2013): The petrogical expression of early Mars volcanism. Journal of Geophysical Research: Planets, 118, 59-64.

Beermann, O., Botcharnikov, R.E., Holtz, F., Diedrich, O., Nowak, M. (2011): Temperature dependence of sulfide and sulfate solubility in olivine-saturated basaltic magmas. Geochimica et Cosmochimica Acta, doi:10.1016/j.gca.2011.09.024.

Behrens, H., Roux, J., Neuville, D. R., & Siemann, M. (2006): Quantification of dissolved H_2O in silicate glasses using confocal microRaman spectroscopy. Chemical Geology, 229, 96–112.

Behrens, H., Misiti, V., Freda, C., Vetere, F., Botcharnikov, R.E., Scarlato, P. (2009): Solubility of H_2O and CO_2 in ultrapotassic melts at 1200 and 1250°C and pressure from 50 to 500 MPa. American Mineralogist, 94, 105 – 120.

Bény, C., Guilhaumou, N., Touray, J.-C. (1982): Native-sulphur-bearing fluid inclusions in the CO_2-H_2S-H_2O-S system – microthermometry and Raman microprobe (mole) analysis – thermochemical interpretations. Chemical Geology, 37, 113 – 127.
Bertka, C.M., Fei, Y. (1997): Mineralogy of the Martian interior up to core-mantle boundary pressures. Journal of Geophysical Research: Solid Earth, 102.

Bish, D.L., et al. (2013): X-ray diffraction results from Mars Science Laboratory: Mineralogy of Rocknest at Gale Crater. Science. 341, 3153.

Bish, D. et al. (2014): The first X-ray diffraction measurements on Mars. International Union of Crystallography, 1, 514 – 522.

Bishop, J.L., Lane, M/D/, Dyar, M.D., King, S.J., Brown, A.J., Swayze, G. (2014): Spectral properties of Ca-sulfates: Gypsum, Bassanite and Anhydrite. American Mineralogist, 99, 2105 – 2115.

Black, L., Breen, C., Yarwood, J., Garbev, K., Stemmermann, P., Gasharova, B. (2007): Structural features of C-S-H(I) and it carbonation in air – a Raman spectroscopic study. Part II: Carbonated phases. Journal of the Amercian Ceramic Society, 90, 908 – 917.

Blake, D.F., et al. (2013): Curiosity at Gale crater, Mars: Characterization and analysis of the Rocknest sand shadow. Science, 341, 6153.

Bouvier, A., Blichert-Toft, J., Vervoort, J.D., Albarède, F. (2005): The age of the SNC meteorites and the antiquity of the Martian surface. Earth and Planetary Science Letters, 240, 221 – 233.

Bouvier, A., Blichert-Toft, J., Albarède, F. (2009): Martian meteorite chronology and the evolution of the interior of Mars. Earth and Planetary Science letters, 280, 285 – 295.

Botcharnikov, R.E., Koepke, J., McCammon, C., Wilke, M. (2005): The effect of water activity on the oxidation and structural state of Fe in a ferro-basaltic melt. Geochimica et Cosmochimica Acta, 69, 5071-5085.

Borg, L., Drake, M.J. (2005): A review of meteorite evidence for the timing of magmatism and of surface or near-surface liquid water on Mars. Journal of Geophysical Research, 110.

Bremard, C., Dhamelincourt, P., Laureyns, J., Turrell, G. (1986): Polarization measurements in micro-Raman and microfluorescence spectrometries. Journal of Molecular Structure, 142, 13-16.

Brey, G., & Green, D. H. (1976). Solubility of CO_2 in Olivine Melilitite at High Pressures and Role of CO_2 in the Earth's Upper Mantle. Contributions to Mineralogy and Petrology, 55, 217–230.

Brey, G.P, Kogarko, L.N, Ryadchikov, I. (1991). Carbon dioxide in kimberlitic melts. Journal of Mineralogy and Geochemistry, 4, 159 – 168.

Bribing, J.-P., Langevin, Y., Mustard, J.F., Poulet, F., Arvidson, R., Gendrin, A., Gondet, B., Mangold, N., Pinet, P., Forget, F. and the OMEGA team (2006): Global mineralogical and aqueous Mars history derived from OMEGA/Mars Express Data. Science, 312, 400 – 403.

Bridges, J.C., Grady, M.M. (2000): Evaporite mineral assemblages in the nakhlite (martian) meteorites. Earth and Planetary Science Letters, 176, 267 - 279.

Brooker, R.A. (1998): The effect of CO_2 saturation on immiscibility between silicate and carbonate liquids: an experimental study. Journal of Petrology, 39, 1905 – 1915.

Brooker, R. A., Kohn, S. C., Holloway, J. R., & Mcmillan, P. F. (2001): Structural controls on the solubility of CO_2 in silicate melts Part I : bulk solubility data. Chemical Geology, 174, 225–239.

Brugier, Y.-.A., Alletti, M., Pichavant, M. (2015): Fe pre-enrichment: A new method to counteract iron loss in experiments on basaltic melts. American Mineralogy; 100, 2106 – 2111.

Burgess K.D., Musselwhite, D.S., Treiman, A.H. (2006): Experimental petrology of olivine-phyric Shergottite NWA 1068: Toward defining a parental melt. Lunar and Planetary Science XXXVII.

Burke, E.A.J. (2001): Raman microspectrometry of fluid inclusions. Lithos, 55, 139 – 158.

Buzgar, N., Buzatu, A., Sanislav, I.V. (2009): The Raman study on certain sulfates. Analele Ştiinţifice ale Universităţii „AL. I. Cuza" Iaşi, seria Geologie, 55(1), 5–23.

Carr, M.H. (1973): Volcanism on Mars. Journal of Geophysical Research: Solid Earth, 78, 4049 – 4062.

Carr, M.H. (1983): Stability of streams and lakes on Mars. Icarus, 56, 476 – 495.

Carr, M.H. (1989): Recharge of the early atmosphere of Mars by impact-induced release of CO_2. Icarus, 79, 311-327.

Carter, J., Poulet, F., Bibring, J-P., Mangold, N., Murchie, S. (2013): Hydrous minerals on Mars as seen by the CRISM and OMEGA imaging spectrometers: Updated global view. Journal of Geophysical Research, https://doi.org/10.1029/2012JE004145.
Carter, J., Loizeau, D., Mangold, N., Poulet, F., Bibring, J-P. (2015): Widespread surface weathering on early Mars: A case for a warmer and wetter climate. Icarus, DOI:10.1016/j.icarus.2014.11.011.
Chassefière, E., Leblanc, F. (2004): Mars atmospheric escape and evolution; interaction with the solar wind. Planetary and Space Science, 52, 1039 – 1058.
Chevrel, O.M., Giordano, D., Potuzak, M., Courtial, P., Dingwell, D.B. (2013): Physical properties of $CaAl_2Si_2O_8$-$CaMgSi_2O_6$-FeO-Fe_2O_3 melts: analogues for extra-terrestrial basalt. Chemical Geology, 346, 93 – 105.
Chevrel, M.O., Baratoux, D., Hess, K.-U., Dingwell, D.B. (2014): Viscous flow behavior of tholeiitic and alkaline Fe-rich martian basalts. Geochimica et Cosmochimica Acta, 124, 348 – 365.

Chopelas, A. (1991): Single crystal Raman spectra of forsterite, fayalite, and monticellite. American Mineralogist, 76, 1101-1109.

Clark, B.C., Baird, A.K., Rose Jr, H.J., Toulmin, P., Christian, R.P., Kelliher, W.C., Castro, A.J., Rowe, C.D., Keil, K., Huss, G.R. (1997): The Viking X ray fluorescence experiment: analytical methods and early results. Journal of Geophysical Research, 82, 4577 - 4594.

Clark, B.C. (1993): Geochemical components in martian soil. Geochimica and Cosmochimica Acta, 57, 4575 - 4581.

Clark, B.C., Morris, R.V. (2005): Chemistry and mineralogy of outcrops at Meridiani Planum. Earth and Planetary Science Letters, 240, 73 - 94.

Clemente B., Scaillet B., Pichavant M. (2004): The solubility of sulphur in hydrous rhyolitic melts. Journal of Petrology, doi:10.1093/petrology/egh052.

Cochain, B., Neuville, D.R., Henderson, G.S., McCammon, C.A., Pinet, O., Richet, P. (2012): Effects of the iron content and redox state on the structure of sodium borosilicate glasses: A

Raman, Mössbauer and Born K-edge XANES spectroscopy study. Journal of the American Ceramic Society, 95, 962 – 971.

Colomban, P. (2013): Proton and protonic species: The hidden face of solid state chemistry. How to measure H-content in materials ? Fuel Cells, 13, 6 – 18.

Corridoni, T., Sodo, A., Bruni, F., Ricci, M.A., Nardone, M. (2007): Probing water dynamics with OH-. Chemical Physics, 336, 183-187.

Cousin, A., Sautter, V., Payré, V., Forni, O., Mangold, N., Gasnault, O., Le Deit, L., Johnson, J., Maurice, S., Salvatore, M., Wiens, R.C., Gasda, P., Rapin, W. (2017): Classification of igneous rocks analyzed by ChemCam at Gale Crater, Mars. Icarus, 288, 265-283.

Craddock, R.A., Greeley, R. (2009): Minimum estimates of the amount and timing of gases released into the martian atmosphere from volcanic eruptions. Icarus, 204, 512 – 526.

Culka, A., Kosek, F., Drahota, P., Jehlicka, J. (2014): Use of miniaturized Raman spectrometer for detection of sulfates of different hydration states – Significance for Mars studies. Icarus, 243, 440-453.

Dalou, C., LeLosq, C., Mysen, B.O., Cody, G.D. (2015): Solubility and solution mechanisms of chlorine and fluorine in aluminosilicate melts at high pressure and high temperature. American Mineralogist, 100, 2272 – 2283.

Dalton, H.A., Musselwhite, D.S., Kiefer, W., Treiman, A.H. (2005): Experimental petrology of the basaltic Shergottite Yamato 980459: Implications for the thermal structure of the martian mantle. Lunar and Planetary Science XXXVI.

Daniel, I. and Edwards, H.G.M. (2012): Raman spectroscopy in biogeology and astrobiology. EMU Notes in Mineralogy, 12, 389-412.

Dann, J.C., Holzheid, A.H., Grove, T.L., McSween Jr, H.Y. (2001): Phase equilibria of the Shergotty meteorite: Constraints on pre-eruptive water contents of martian magmas and fractional crystallization under hydrous conditions. Meteoritics & Planetary Science, 36, 793 – 806.

De Faria, D.L.A., Venâncio Silva, S., de Oliveira, M.T. (1997): Raman Microspectroscopy of some iron oxides and oxyhydroxides. Journal of Raman spectroscopy, 28, 873 – 878.

Dehouck, E., McLennan, S.M., Meslin, P.-Y., Cousin, A. (2014): Constraints on abundance, composition, and nature of X-ray amorphous components of soils and rocks at Gale crater, Mars. Journal of Geophysical Research: Planets, 119, 2640-2657.

Delhaye, M., and Dhamelincourt, P. (1975): Raman microprobe and microscope with laser excitation. Journal of Raman spectroscopy, 3, 33-43.

Della-Pasqua, F.N., Varne, R. (1997): Primitive ankaramitic magmas in volcanic arcs: a melt-inclusion approach. Oceanic Literature Review, 44.

Di Genova, D., Hess, K-U., Chevrel, M. O., Dingwell, D.B. (2016): Models for the estimation of the Fe_{3+}/Fe_{tot} ratio in terrestrial and extraterrestrial alkali- and iron-rich silicate glasses using Raman spectroscopy. American Mineralogist, 101, 943-952.

Di Genova, D., Sicola, S., Romano, C., Vona, A., Fanara, S., Spina, L. (2017): Effect of iron and nanolites on Raman spectra of volcanic glasses: A reassessment of existing strategies to estimate the water content. Chemical Geology, 475, 76-86.

Ding, S., Dasgupta, R., Tsuno, K. (2014): Sulfur concentration of martian basalts at sulfide saturation at high pressures and temperature – implications for deep sulfur cycle on Mars. Geochimica et Cosmochimica Acta, 131, 227 – 246.

Ding, S., Dasgupta, R., Lee, C-T. A., Wadhwa, M. (2015): New bulk sulfur measurements of Martian meteorites and modeling the fate of sulfur during melting and crystallization – implications for sulfur transfer form Martian mantle to crust-atmosphere system. Earth and Planetary Science Letters, 409, 157 – 167.

Dixon, J. E., & Stolper, E. M. (1995): An experimental study of water and carbon dioxide solubilities in mid-ocean ridge basaltic liquids. Part II. Journal of Petrology, 36, 1633–1646.

Dostal, J., Dupuy, C., Carron, J.P., Le Guen de Kerneizon, M., Maury, R.C. (1983): Partition coefficients of trace elements: Apllication to volcanic rocks of St. Vincent, West Indies. Geochimica et Cosmochimica Acta, 47, 525 – 533.

Dreibus, G. and Wänke, H. (1985): Mars, a volatile-rich planet. Meteoritics, 20, 367-381.

Dreibus, G., and Wänke, H. (1987): Volatiles on Earth and Mars: a comparison. Icarus, 71, 225 – 240.

Dreibus, G., Jagoutz, E., Wänke, H. (1995): Water in the Earth's mantle. Sixth International Kimberlite Conference: Extended Abstracts, 141 – 142.

Dreibus, G. and Palme, H. (1996): Cosmochemical constraints on the sulfur content in the Earth's core. Geochimica et Cosmochimica Acta, https://doi.org/10.1016/0016-7037(96)00028-2.

Dubessy, J., Caumon, M.-C., Rull, F., and Sharma, S. (2012): Instrumentation in Raman spectroscopy: elementary theory and practice. EMU Notes in Mineralogy, 12, 83-172.

Ebel, D.S. (2011): Sulfur in extraterrestrial bodies and the deep Earth. Reviews in Mineralogy & Geochemistry, 73, 315 - 336.

Elhmann, B.L., Mustard, J.F., Fassett, C.I., Schon, S.C., Head III, J.W., Des Marais, D.J., Grant, J.A., Murchie, S.L. (2008): Clay minerals in delta depostits and organic preservation potential on Mars. Nature Geosciences, 1, 355 – 358.

Elhmann, B.L., Edwards, C.S. (2014): Mineralogy of the Martian surface. Annual Review of Earth and Planetary Sciences, 42, 291 – 315.

Elkins-Tanton, L.T. (2008): Linked magma ocean solidification and atmospheric growth for Earth and Mars. Earth and Planetary Science Letters, 271, 181 – 191.

Everall, N.J. (2008): Confocal Raman microscopy: performance, pitfalls, and best practice. Applied Spectroscopy, 63, 245A -262 A.

Fassett, C.I., Head III, J.W. (2005): Fluvial sedimentary deposits on Mars: ancient deltas in a crater lake in the Nili Fossae region. Geophysical Research Letters, 32, L14201.

Filiberto, J. (2008): Experimental constraints on the parental liquid of the Chassigny meteorite: A possible link between the Chassigny meteorite and a Martian Gusev basalt. Geochimica et Cosmochimica Acta, 72, 690-701.

Filiberto, J., Treiman, A.H. (2009): The effect of chlorine on the liquidus of basalt: First results and implications for basalt genesis on Mars and Earth. Chemical Geology, 263, 60 – 68.

Filiberto, J., Baratoux, D., Beaty, D., Breuer, D., Farcy, B.J., Grott, M., Jones, J.H., Kiefer, W.S., Mane, P., McCubbin, F.M., Schwenzer, S.P. (2016): A review of volatiles in the Martian interior. Meteoritics & Planetary Sciences, 1-24.

Filiberto, J., Schwenzer, S.P.: Introduction to volatiles in the Martian Crust. Volatiles in the Martian Crust, Elsevier. 2019.

Filiberto, J., McCubbin, F.M., Taylor, G.J.: Volatiles in Martian Magmas and the interior: inputs of volatiles into the crust and atmosphere. Volatiles in the Martian Crust, Elsevier. 2019.

Fincham, C.J., Richardson, F.D. (1954): The behavior of sulfur in silicate and aluminate melts. Proceding in Royal Society London, 223A, 40 – 61.

Forni, O., Gaft, M., Toplis, M.J., Clegg, S.M., Maurice, S., Wiens, R.C., Mangold, N., Gasnault, O., Sautter, V., Le Mouélic, S., Meslin, P.-Y., Nachon, M., McInroy, R.E., Ollila, A.M., Cousin, A., Bridges, J.C., Lanza, N.L., Dyar, M.D. (2015): First detection of fluorine on Mars: Implications for Gale Crater's geochemistry. Geophysical Research Letters, 42, 1020-1028.

Fouchet, T., et al. (2016): The SuperCam Remote Sensig Suite for MARS 2020: Nested and Co-Aligned LIBS, Raman, and VISIR Spectroscopies, and color micro-imaging. American Astronimical Society.

Frantz, J.D., Mysen, B.O. (1995): Raman spectra and structure of BaO-SiO$_2$ SrO-SiO$_2$ and CaO-SiO$_2$ melts to 1600°C. Chemical Geology, 121, 155 – 176.

Frantz, H.B., King, P.L., Gaillard, F.: Sulfur on Mars from the atmosphere to the core. Volatile in the Martian Crust, Elsevier. 2019.

Freeman, J.J., Wang, A., Kuebler, K.E., Jolliff, D.L., Haskin, L.A. (2008): Characterization of natural feldspars by Raman spectroscopy for future planetary exploration. The Canadia Mineralogist, 46, 1477-1500.

Freund, F., Wengeler, H., Kathrein, H., Knobel, R., Oberheuser, G., Maiti, G.C., Reil, D., Knipping, U., Kötz, J. (1982): Hydrogen and carbon derived from dissolved H$_2$O and CO$_2$ in minerals and melts. Bulletin de Minéralogie, 106, 185 – 200.

Gaillard, F. and Scaillet, B. (2009): The sulfur content of volcanic gases on Mars. Earth and Planetary Science Letters, 279, 34 – 43.

Gaillard, F., Michalski, J., Berger, G., McLennan, S.M., Scaillet, B. (2013): Geochemical reservoirs and timing of sulfur cycling on Mars. Space Science Review, 174, 251 - 300.

Gellert, R., Rieder, R., Brückner, J., Clark, B.C., Dreibus, G., Klingelhöfer, G., Lugmair, G., Ming, D.W., Wänke, H., Yen, A., Zipfel, J., Squyres, S.W. (2006): Alpha Particle X-Ray spectrometer (APXS): Results from Gusev crater and calibration report. Journal of Geophysical Research, 111, E02S05.

Gellert, R., Clark III, B.C., and the MSL and MER Science Teams (2015): In Situ compositional measurements of rocks and soils with the Alpha Particle X-Ray Spectrometer on NASA's Mars rovers. Elements, 11, 39 – 44.

Gendrin, A., Mangold, N., Bibring, J.P., Langevin, Y., Gondet, B., Poulet, F., Bonello, G., Quantin, C., Mustard, J., Arvidson, R., LeMouélic, S. (2005): Sulfates in Martian layered Terrains: the OMEGA/Mars express view. Science, 307, 1587-1591.

Govindaraju, K. (1994): 1994 Compilation of working values and sample description for 383 geostandards. Geostandards Newsletter, 18, 1 – 158.

Goudge, T.A., Mustard, J.F., Head, J.W., Fassett, C.I., Wiseman, S.M. (2015): Assessing the mineralogy of the watershed and fan deposits of the Jezero crater paleolake system, Mars. Journal of Geophysical Research: Planets, 120, 775 – 808.

Goudge, T.A., Milliken, R.E., Head III, J.W., Mustard, J.F., Fassett, C.I. (2017): Sedimentalogical evidence for a deltaic origin of the western fan deposit in Jezero crater, Mars and implications for future exploration. Earth and Planetary Science Letters, 458, 357 – 365.

Greeley, R., Foing, B.H., McSween Jr., H.Y., Neukum, G., Pinet, P., van Kan, M., Werner, S.C., Williams, D.A., Zegers, T.E. (2005): Fluid lava flows in Gusev crater, Mars. Journal of Geophysical Research, 110, 1 – 6.

Green, T.H, Ringwood, A.E., Major, A. (1966): Journal of Geophysical Research, 71, 3589 – 3594.

Greenwood, J.P., Itoh, S., Sakamoto, N., Vicenzi, E., Yurimoto, H. (2008): Hydrogen isotope evidence for loss of water from Mars through time. Geophysical Research Letters, 35, L05203.

Gross, S.H., McGovern, W.E., Rasool, S.I. (1966): Mars: Upper Atmosphere. Science, 151, 1216-1221.

Gross, J., Filiberto, J., Bell, A.S. (2013): Water in the martian interior: Evidence for terrestrial MORB mantle-like volatile content from hydroxyl-rich apatite in olivine-phyric shergottite NWA 6234. Earth and Planetary Science Letters, 369 – 370, 120 – 128.

Grott, M., Morschhauser, A., Breuer, D., Hauber, E. (2011): Volcanic outgassing of CO_2 and H_2O on Mars. Earth and Planetary Science Letters, doi:10.1016/j.epsl.2011.06.014.

Grott, M., Baratoux, D., Hauber, E., Sautter, V., Mustard, J., Gasnault, O., Ruff, S.W., Karato, S.-I., Debaille, V., Knapmeyer, M., Sohl, F., Van Hoolst, T., Breuer, D., Morschhauser, A., Toplis, M.J. (2013): Long-term evolution of the martian crust-mantle system. Space Science Reviews, 174, 49 – 111.

Halevy, I., Zuber, M.T., Schrag, D.P. (2007): A sulfur dioxide climate feedback on early Mars. Science, 318, 190 3- 1907.

Halevy, I., Head, J.W.I. (2014): Episodic warming of early Mars by punctuated volcanism. Nature Geosciences, 7, 865 – 868.

Halliday, A.N., Wänke, H., Birck, J.-L., Clayton, R.N. (2001): The accretion, composition and early differenciation of Mars. Space Science Reviews, 96, 197 – 230.

Hallis, L.J., Taylor, G.J., Nagashima, Huss, G.R. (2012): Magmatic water in the martian meteorite Nakhla. Earth and Planetary Science Letters, 359 – 360, 84 – 92.

Haughton, D.R., Roeder, P.L., Skinner, B.J. (1974): Solubility of sulfur in mafic magmas. Economic Geology, 69, 451 – 467.
Head III, J.W., Krevlavsky, M.A., Pratt, S. (2002): Northern lowlands of Mars: evidence for widespread volcanic flooding and tectonic deformation in the Hesperian period. Journal of Geophysical Research: Planters, 107, E15003.

Heide, K. and Schmidt, C.M. (2003): Volatiles in vitreous basaltic rims, HSDP 2, big island, Hawaii. Journal of Non-Crystalline Solids, 323, 97 – 103.

Herd, C.D.K., Borg, L.E., Jones, J.H., Papike, J.J. (2002): Oxygen fugacity and geochemical variations in the martian basalts: Implications for martian basalt petrogenesis and the oxidation state of the upper mantle of Mars. Geochimica et Cosmochimica Acta, 66, 2025 – 2036.

Herd, C.D.K. (2008): Basalts as probes of planetary interior redox state. Reviews in Mineralogy & Geochemistry, 68, 527-553.

Hewins, H., Zanda, B., Humayun, M., Nemchin, A., Lorand, J.-P., Pont, S., Deldicque, D., Bellucci, J.J., Beck, P., Leroux, H., Marinova, M., Remusat, L., Göpel, C., Lewin, E., Grange, M., Kenndy, A., Whitehouse, M.J. (2016): Regolith Northwes Africa 7533: Mineralogy and petrology with implications for early Mars. Meteoritics & Planetary Science, 52, 89-124.

Hicks, L.J., Bridges, J.C., Gurman, S.J. (2014): Ferric saponite and serpentine in the nakhlite martian meteorites. Geochimica et Cosmochimica Acta, 136, 194 - 210.

Hiesinger, H., Head III, J.W., Neukum, G. (2007): Young lava flow on the eastern flank of Ascraeus Mons: Rheological properties derived from High Resolution Stereo Camera (HRSC) images and Mars Orbiter Laser Altimeter (MOLA) data. Journal of Geophysical Research, 112, 1 – 24.

Hirschmann, M.M., Withers, A.C. (2008): Ventilation of CO_2 from a reduced mantle and consequences for the early Martian greenhouse. Earth and Planetary Science Letters, 270, 147 - 155.

Hirschmann, M.M., Withers, A.C., Ardia, P., Foley, N.T. (2012): Solubility of molecular hydrogen in silicate melts and consequences for volatile evolution of terrestrial planets. Earth and Planetary Science Letters, 345-348, 38-48.

Hoehse, M., Mory, D., Florek, S., Weritz, F., Gornushkin, I., Panne, U. (2009): A combined laser-induced breakdown and Raman spectroscopy Echelle systemn for elemental and molecular microanalysis. Spectrochimica Acta Part B: Atomic Spectroscopy, 64, 1219-1227.

Hou, T., Charlier, B., Holtz, F., Veksler, I., Zhang, Z., Thomas, R., Namur, O. (2018): Immiscible hydrous Fe-Ca-P melt and the origin of iron oxide-apatite ore depostits. Nature Communications, 9, 1-8.

Huang, E., Chen, C.H., Huang, T., Lin, E.H., and XU, J.-A. (2000): Raman spectroscopic characteristics of Mg-Fe-Ca pyroxenes. American Mineralogist, 85, 473-479.

Iacono-Marziano, G., Morizet, Y., Le Trong, E., & Gaillard, F. (2012): New experimental data and semi-empirical parameterization of H_2O-CO_2 solubility in mafic melts. Geochimica et Cosmochimica Acta, 97, 1–23.

Jakobsson, S. (1997): Solubility of water and carbon dioxide in an icelandite at 1400°C and 10 kilobars. Contributions to Mineralogy and Petrology, 127, 129–135.

Jackson, W.E., Farges, F., Yeager, M., Mabrouk, P.A., Rossano, S., Waychunas, G.A., Solomon, E.I., Brown Jr, G.E. (2005): Multi-spectroscopic study of Fe(II) in silicate glasses: Implications for the coordination environment of Fe(II) in silicate melts. Geochimica et Cosmochimica Acta, 69, 4315-4332.

Jaeger, W/L., Keszthelyi, L.P., McEwen, A.S., Dundas, C.M., Russel, R.S. (2007): Athabasca Valles, Mars: a lava-draped channel system. Science, 317, 1709.

Jégo, S. and Pichavant, M. (2012): Gold solubility in arc magmas: Experimental determination of the effect of sulfur at 1000 °C and 0.4 GPa. Geochimica et Cosmochimica Acta, 84, 560 – 592.

Jehlicka, J., Vitek, P., Edwards, H.G.M., Heagraves, M., Capoun, T. (2009): Application of portable Raman instruments for fast and non-destructive detection of minerals on outcrops. Spectrochimica Acta Part A: Molecular and Biomolecular Spectroscopy, 73, 410-419.

Johnson, J.R., Mischna, M.A., Grove, T.L., Zuber, M.T. (2008): Sulfur-induced greehouse warming on early Mars. Journal of Geophysical Research, 113, E08005.
Johnson, S.S., Pavlov, A.A., Mischna, M.A. (2009): Fate of SO_2 in the ancient Martian atmosphere: implications for transient greenhouse warming. Journal of Geophysical Research, 114, E11011.

Jugo, J., Luth, R.W., Richards, J.P. (2005a): An experimental study of the sulfur content in basaltic melts saturated with immiscible sulfide liquidus at 1300°C and 1.0 GPa. Journal of Petrology, 46, 783 – 798.

Jugo, P.J., Luth, R.W., Richards, J.P. (2005b): Experimental data on the speciation of sulfur as a function of oxygen fugacity in basaltic melts. Geochimica et Cosmochimica Acta, doi:10.1016/j.gca.2004.07.011.

Jugo, P.J., Wilke, M., Botcharnikov, R.E. (2010): Sulfur K-edge XANES analysis of natural and synthetic basaltic glasses: implications for S speciation and S content as a function of oxygen fugacity. Geochimica and Cosmochimica Acta, 74, 5926 - 5938.

Kägi, R., Müntener, O., Ulmer, P., Ottolini, L. (2005): Piston-cylinder experiments of H_2O undersaturated Fe-bearing systems: An experimental setup approaching fO_2 conditions of natural calc-alkaline magmas. American Mineralogist, 90, 708 – 717.

Kamenetsky, V., Clocchiatti, R. (1996): Primitive magmatism of Mt. Etna: insights from mineralogy and melt inclusions. Earth and Planetary Science Letters, 142, 553 – 572.

Kavner, A., and Jeanloz, R. (1998): High-pressure melting curve of platinum. Journal of applied physics, 83, 7553 – 7559.

Keppler, H. (2003): Water solubility in carbonatite melts. American Mineralogist, 88, 1822-1824.

Kerber, L., Forget, F., Wordsworth, R. (2015): Sulfur in the early Martian atmosphere revisited: experiments with a 3-D global climate model. Icarus, 261, 133 – 148.

Kessel, R., Ulmer, P., Pettke, T., Schmidt, M.W., Thompson, A.B. (2005): The water-basalt system at 4 to 6 gPa: phase relations and second critical endpoint in a K-free eclogite at 700 to 1400 °C. Earth and Planetary Science Letters, 237, 873 – 892.

King, P.L., Lescinsky, D.T., Nesbitt, H.W. (2004): The composition and evolution of primordial solutions on Mars, with application to other planetary bodies. Geochimica et Cosmochimica Acta, 68, 4993 – 5008.

King, P.L. and McLennan, S.M. (2010): Sulfur on Mars. Elements, 6, 107-112.

Klimm, K. and Botcharnikov, R.E. (2010): The determination of sulfate and sulfide species in hydrous silicate glasses using Raman spectroscopy. American Mineralogist, 95, 1574 – 1579.

Klimm K., Kohn S.C., O'Dell L.A., Botcharnikov R.E., Smith M.E. (2012a): The dissolution mechanism of Sulphur in hydrous silicate melts. I: Assessments of analytical techniques in determining the Sulphur speciation in iron-free to iron-poor glasses. Chemical Geology, doi:10.1016/j.chemgeo.2012.04.027.

Klimm, K., Kohn, S.C., Botcharnikov, R.E. (2012b): The dissolution mechanism of sulphur in hydrous silicate melts. II: Solubility and speciation of Sulphur in hydrous silicate melts as a function of fO_2. Chemical Geology, doi:10.1016/j.chemgeo.2012.04.028.

Knittle, E., Pillips, W., Williams, Q. (2001): An infrared and Raman spectroscopic study of gypsum at high pressures. Physics Chemistry Mineral, 28, 630 – 640.

Kolesov, B.A., and Tanskaya, J.V. (1996): Raman spectra and cation distribution in the lattice of olivines. Materials Research Bulletin, 31, 1035-1044.

Kolesov, B.A., and Geiger, C.A. (2004): A Raman spectroscopic study of Fe-Mg olivines. Physics and Chemistry Minerals, 31, 142-154.

Kontoyannis, C.G., Orkoula, M.G., Koutsoukos, P.G. (1997): Quantitative Analyses of Sulfates Calcium Carbonates using Raman Spectroscopy and X-ray Powder Diffraction. Analyst, 122, 33-38.

Kress, V.C. and Carmichael, I.S.E. (1991): The compressibililty of silicate liquids containing Fe_2O_3 and the effect of composition, temperature, oxygen fugacity and pressure on their redox states. Contributions to Mineralogy and Petrology, 108, 82 – 92.

Kristova, P., Hopkinson, L., Rutt, K., Hunter, H., Cressey, G. (2013): Quantitative analyses of powdered multi-minerallic carbonate aggregates using a portable Raman spectrometer. American Mineralogist, 98, 401- 409.

Kuebler, K.E., Jolliff, B.L., Wang, A., Haskin, L.A. (2006): Extractif olivine (Fo-Fa) compositions from Raman spectral peak positions. Geochimica et Cosmichimica Acta, 70, 6201-6222.

Kushiro, I. (1976): Changes in viscosity and structure of melt of $NaAlSi_2O_6$ composition at high pressures. Journal of Geophysical Research, 81, 6347 – 6350.

Laajalehto, K., Kartio, I., Nowak, P. (1994): XPS study of clean metal sulfide surfaces. Applied Surface Science, 81, 11 - 15.

Lammer, H., Chassefière, E., Karatekin, O., Morschhauser, A., Niles, P.B., Mousis, O., Odert, P., Möstl, U.V., Breuer, D., Dehant, V., Grott, M., Gröller, H., Hauber, E., Pham, L.B.S. (2013): Outgassing history and escape of the Martian atmosphere and water inventory. Space Science Review, 174, 113 – 154.

Lammer, H., Zerkle, A.L., Gebauer, S., Tosi, N., Noack, L., Scherf, M., Pilat-Lohinger, E., Güdel, M., Grenfell, J.L., Godolt, M., Nikolaou, A. (2018): Origin and evolution of the atmosphere of early Venus, Earth and Mars. The astronomy and Astrophysics Review, 26:2.

Lane, M.D., Bishop, J.L., Dyar, M.D., King, P.L., Parente, M., Hyde, B.C. (2008): Mineralogy of the Paso Robles soils on Mars. American Mineralogy, 93, 728 - 739.

Langevin, Y., Poulet, F., Bibring J.P., Gondet, B. (2005): Sulfates in the North polar region of mars detected by OMEGA/Mars express. Science, 307, 1584 - 1586.

Langlais, B., Purucker, M.E., Mandea, M. (2004): Crustal magnetic field of Mars. Journal of Geophysical Researh: Planets. 109, E02008.

Lapen, T.J., Righter, M., Brandon, A.D., Debaille, V., Beard, B.L., Shafer, J.T., Peslier, A.H. (2010): A younger age for ALH84001 and its geochemical link to Shergottite sources in Mars. Science, 328, 347 – 351.

Larre, C., Morizet, Y., Guillot-Deudon, C., Baron, F., Mangold, N. (2018): Quantitative Raman calibration of sulfate-bearing polymineralic mixtures: a S quantification in sedimentary rocks on Mars. Mineralogical Magazine, 1-38.

Le Deit, L., Le Mouélic, S., Bourgeois, O., Combe, J.-P., Mège, Sotin, C., Gendrin, A., Hauber, E., Mangold, N., Bribing J.-P. (2008): Ferric oxides in East Candor Chasma, Valles Marineris (Mars) inferred from analysis of OMEGA/Mars Express data : Identification and geological interpretation. Journal of Geophysical Research, 113, 1 – 18.

Le Losq, C., Neuville, D.R., Moretti, R., Roux, J. (2012): Determination of water content in silicate glasses using Raman spectrometry : Implications for the study of explosive volcanism. American Mineralogist, 97, 779 – 790.

Lesne, P. (2008): Etude expérimentale de la solubilité des volatils C-H-O-S dans les basaltes alcalins italiens. Simulations numériques du dégazage chimique : application à l'Etna. PhD thesis.

Liu, Y., Samaha, N-T., Baker, D.R. (2007): Sulfur concentration at sulfide saturation (SCSS) in magmatic silicate melts. Geochimica et Cosmochimica Acta, 71, 1783 - 1799.

Lodders, K., Palme, H., Gail, H.-P. (2009): Abundances of the elements in the solar system. In Landolt-Börnstein, New Series, VI/4B, 560 - 630.

Lorand, J.-P., Chevrier, V., Sautter, V. (2005): Sulfide mineralogy and redox conditions in some shergottites. Meteoritics & Planetary Science, 40.

Lorand, J.-P., Pont, S., Chevrier, V., Luguet, A., Zanda, B., Hewins, R. (2018): Petrogenesis of martian sulfides in the Chassigny meteorite. American Mineralogist, 103, 872 – 885.

Lundin, R., et al. (2004): Solar wind-induced atmospheric erosion at Mars: First results from ASPERA-3 on Mars Express. Science, 305.

Mandeville, C., Webster, J.D., Rutherford, M.J., Taylor, B.E., Timbal, A., Faure, K. (2002): Determination of molar absorptivities for infrared absorption bands of H_2O in andesitic glasses. American Mineralogist, 87, 813 – 821.

Mangold, N., Baratoux, D., Witasse, O., Encrenaz, T., Sotin, C. (2016): Mars: a small terrestrial planet. Astronomy and Astrophysics Review, 24:15.

Mangold, N., and others (2017): Classification scheme for sedimentary and igneous rocks in Gale crater, Mars. Icarus, 284, 1-17.

Marinova, M.M., Aharonson, O., Asphaug, E. (2008) : Mega-impact formation of the Mars hemispheric dichotomy. Nature, 453, 1216 – 1219.

Maurice, S., Wiens, R.C., Saccoccio, M., Barraclough, B., Gasnault, O., and 65 more authors (2012): The ChemCam Instrument Suite on the Mars Science Laboratory (MSL) Rover: Science objectives and Mast Unit Description. Space Science Reviews,170, 167-227.

Maurice, S., Cleff, S.M., Wiens, R.C., Gasnault, O., Rapin, W., Forni, O., Cousin, A., Sautter, V., Mangold, N., Le Deit, L., Nachon, et al. (2016): ChemCam activities and discoveries during the nominal mission of Mars Science Laboratory in Gale crater, Mars. Journal of Analytical Atomic Spectrometry, 31, 863-889.

Mavrogenes, J.A., and O'Neill, H. St.C. (1999): The relative effects of pressure, temperature and oxygen fugacity on the solubility of sulfide in mafic magmas. Geochimica et Cosmochimica Acta, 63, 1173 – 1180.

McCubbin, F.M., Smirnov, A., Nekvasil, H., Wang, J., Hauri, E., Lindsley, D.H. (2010): Hydrous magmatism on Mars: A source of water for the surface and subsurface during the Amazonian. Earth and Planetary Science Letters, 292, 132 – 138.

McCubbin, F. M., Hauri, E. H., Elardo, S. M., Vander Kaaden, K. E., Wang, J., & Shearer, C. K. (2012): Hydrous melting of the martian mantle produced both depleted and enriched shergottites. Geology, 40, 683–686.

McCubbin, F.M., Boyce, J.W., Srinivasan, P., Santos, A.R., Elardo, S.M., Filiberto, J., Steele, A., Shearer, C.K. (2016): Heterogeneous distribution of H_2O in the Martian interior: Implications for the abundance of H_2O in depleted and enriched mantle sources. Meteoritics & Planetary Science, 51, 2036 – 2060.

McDade, P., Wood, B.J., Van Westrenen, W., Brooker, R.A., Gudmundsson,G., Soulard, H., Najorka, J., Blundy, J. (2002): Pressure corrections for a selection of piston-cylinder cell assemblies. Mineralogical Magazine, 66, 1021 – 1028.

McGill, G.E., Dimitriou, A.M. (1990): Origin of the Martian global dichotomy by crustal thinning in the Late Noachian or Early Hesperian. Journal of Geophysical Research: Solid Earth, 95.

McKeown, D.A., Bell, M.I., and Caracas, R. (2010): Theoretical determination of the Raman spectra of single-crystal forsterite (Mg_2SiO_4). American Mineralogist, 95, 980-986.

McLennan, S.M., Bell, J.F., et al. (2005): Provenance and diagenesis of the evaporite-bearing Burns formation, Meridiani Planum, Mars. Earth and Planetary Science Letters, 240, 95 - 121.

McMillan, P. and Piriou, B. (1982): The structures and vibrational spectra of crystals and glasses in the silica-alumina system. Journal of Non-Crystalline Solids, 53, 279-298.

McMillan, P. (1984): Structural studies of silicate glasses and melts: applications and limitations of Raman spectroscopy. American Mineralogist, 69, 622-644.

McSween Jr, H.Y. (1985): SNC Meteorites: Clues to martian petrologic evolution. Reviews of Geophysics, 23, 391 – 416.

McSween, H.Y., Grove, T.L., Lentz, R.C.F., Dann, J.C., Holzheid, A.H., Riciputi, L.R., Ryan, J.G. (2001): Geochemical evidence for magmatic water within Mars from pyroxenes in the Shergotty meteorite. Nature, 409, 487 – 490.

McSween, H.Y., Taylor, G.J., Wyatt, M.B. (2009): Elemental Composition of the Martian Crust. Science, 324, 736-739.

Médard, E., Grove, T. L. (2006): Early hydrous melting and degassing of the Martian interior. Journal of Geophysical Research: Planets, 111, E11003.

Mekki, A., Holland, D., McConville, C.F., Salim, M. (1996) : An XPS study of iron sodium silicate glass surfaces. Journal of Non-Cyrstalline Solids, 208, 267 – 276.

Mercier, M., Di Muro, A., Giordano, D., Métrich, N., Lesne, P., Pichavant, M., Scaillet, B., Clocchiatti, R., Montagnac, G. (2009): Influence of glass polymerization and oxidation on micro-Raman water analysis in alumino-silicate glasses. Geochimica et Cosmochimica Acta, 73, 197-217.

Meslin, P.-Y., Gasnault, O., Forni, O., Schröder, S., Cousin, A., and 55 more authors and the MSL Science Team (2013): Soil Diversity and Hydration as Observed by ChemCam at Gale Crater, Mars. Science, 341.

Micoulaut, M., Malki, M., Simon, P., Canizares, A. (2005): On the rigid to floppy transitions in calcium silicate glasses from Raman scattering and cluster constraint analysis. Philosophical Magazine, 85, 3357 – 3378.

Mischna, M.A., Baker, V., Milliken, R., Richardson, M., Lee, C. (2013): Effects of obliquity and water vapor/trace gas greenhouses in the early Martian climate. Journal of Geophysical Research: Planets. 118, 560 - 576.

Monders, A.G., Médard, E., Grove, T.L. (2007): Phase equilibrium investigations of the Adirondack class basalts from the Gusev plains, Gusev crater, Mars. Meteoritics & Planetary Science, 42, 131 – 148.

Moore, G., Vennemann, T., Carmichael, I.S.E. (1995): Solubility of water in magmas to 2 kbars. Geology, 23, 1099 – 1102.

Moretti, R., Ottonello, G. (2003): Polymerization and disproportionation of iron and sulfur in silicate melts: insights from an optical basicity-based approach. Journal of Non-Crystalline Solids, 323, 111 – 119.

Morgan, J.W., Anders, E. (1979): Chemical composition of Mars. Geochimica et Cosmochimica Acta, 43, 1601 – 1610.

Morizet, Y., Brooker, R.A, Kohn, S.C. (2002): CO_2 in haplo-phonolite melt: Solubility, speciation and carbonate complexation. Geochimica et Cosmochimica Acta, 66, 1809-1820.

Morizet, Y., Paris, M., Gaillard, F., Scaillet, B. (2010): C-O-H fluid solubility in haplobasalt under reducing conditions: An experimental study. Chemical Geology, 279, 1-16.

Morizet, Y., Brooker, R.A., Iacono-Marziano, G., Kjarsgaard, B.A. (2013a): Quantification of dissolved CO_2 in silicate glasses using micro-Raman spectroscopy. American Mineralogist, 98, 1788-1802.

Morizet, Y., Paris, M., Di Carlo, I., Scaillet, B. (2013b): Effect of Sulphur on the structure of silicate melts under oxidizing conditions. Chemical Geology, 358, 131-147.

Morizet, Y., Gennaro, E., Jego, S., Zajacz, Z., Iacono-Marziano, G., Pichavant, M., Di Carlo, I., Ferraina, C., Lesne, P. (2017a): A Raman calibration for the quantification of SO_4^{2-} groups dissolved in silicate glasses: Application to natural melt inclusions. American Mineralogist, 102, 2065-2076.

Morizet, Y., Florian, P., Paris, M., Gaillard, F. (2017b): O^{17} NMR evidence of free ionic clusters $M_{n+} CO_3^{2-}$ in silicate glasses: Precursors for carbonate-silicate liquids immiscibility. Am. Min. ; 102, 1561 – 1564.

Morris, R.V. et al. (2004): Mineralogy at Gusev Crater from the Mössbauer Spectrometer on the Spirit Rover. Science, 305, 833 – 836.

Morrison, S.M. (2018): Crystal chemistry of martian minerals from Bradbury Landing through Naukluft Plateau, Gale Crater, Mars. American Mineralogist, 103, 857 - 871.

Mottl, M.J., Glazer, B.T., Kaiser, R.I., Meech, K.J. (2007): Water and astrobiology. Chemie der Erde Geochemistry, 67, 253 – 282.

Moussallam, Y., Morizet, Y., Massuyeau, M., Laumonier, M., Gaillard, F. (2014): CO_2 solubility in kimberlite melts. Chemical Geology, 418, 198 – 205.

Moussallam, Y., Morizet, Y., Gaillard, F. (2016). Unconventional H_2O-CO_2 solubility in kimberlite defines the depth of pipe root zone. Earth and Planetary Science Letters, 447, 151 – 160.

Musselwhite, D.S., Dalton, H.A., Kiefer, W.S., Treiman, A.H. (2006): Experimental petrology of the basaltic shergottite Yamato-980459: implications for the thermal structure of the Martian mantle. Meteoritics and Planetary Science, 41, 1271 – 1290.

Mustard, J.F., Poulet, F., Bibring, J.P., Langevin, Y., Gondet, B., Mangold, N., Bellucci, G., Altieri, F. (2005): Olivine and pyroxene diversity in the crust of Mars. Science, 307, 1594-1597.

Mustard, J.F., et al. (2008) Hydrated silicate minerals on Mars observed by the Mars Reconnaissance Orbiter CRISM instrument. Nature, 454, 305 – 309.

Mysen, B.O., Seifert, F., Virgo, D. (1980): Structure and redox equilibria of iron-bearing silicate melts. American Mineralogist, 65, 867-884.

Mysen, B.O., and Popp, R.K. (1980): Solubility of sulfur in $CaMgSiO_6$ and $NaAlSi_3O_8$ melts at high pressure and temperature with controlled fO_2 and fS_2. American Journal of Science, 280, 78 – 92.

Mysen, B.O., and Virgo, D. (1980a): Solubility mechanisms of carbon dioxide in silicate melts: a Raman spectroscopic study. American Mineralogist, 65, 885-899.

Mysen, B.O., and Virgo, D. (1980b): The solubility behavior of CO_2 in melts on the join $NaAlSi_3O_8$-$CaAl_2SiO_8$-CO_2 at high pressures and temperatures: A Raman spectroscopic study. American Mineralogist, 65, 1166-1175.

Mysen, B.O., Virgo, D., Seifert, F.A. (1982): The structure of silicate melts: implications for chemical and physical properties of natural magma. Reviews of Geophysics and Space Physics, 20, 353 – 383.

Mysen, B.O. and Virgo, D. (1986): Volatiles in silicate melts at high pressure and temperature: interaction between OH groups and Si_{4+}, Al_{3+}, Ca_{2+}, Na_+ and H_+. Chemical Geology, 57, 303-331.

Mysen B.O. (1991): Relations between Structure, Redox, Equilibria of Iron, and Properties of Magmatic Liquids. Advances in Physical Geochemistry, 9, 41-98.

Mysen, B.O., Frantz, J.D. (1994): Structure of silicate melts at high temperature: In-situ measurements in the system BaO-SiO_2 to 1669 °C. American Mineralogist, 78, 699 – 709.

Mysen, B.O. and Cody, G.D. (2005): Solution mechanisms of H_2O in depolymerized peralkaline melts. Geochimica et Cosmochimica Acta, 69, 5557 – 5566.

Mysen, B.O., Fogel, M.L., Morrill, P.L., Cody, G.D. (2009): Solution behavior of reduced C-O-H volatiles in silicate melts at high pressure and temperature. Geochimica et Cosmochimica Acta, 73, 1696-1710.

Mysen, B.O. (2014): Water-melt interaction in hydrous magmatic systems at high temperature and pressure. Progress in Earth and Planetary Science, 1 – 4.

Nachon, M., et al. (2014) : Calcium sulfate veins characterized by ChemCam/Curiosity at Gale crater, Mars. Journal of Geophysical Research : Planets, 119, 1991 – 2016.

Nachon, M. (2016) : Chimie de la surface de Mars dans le cratère Gale par l'analyse de données élémentaires de ChemCam sur Curiosity couplée à des simulations en laboratoire. PhD thesis.

Nachon, M., Mangold, N., Forni, O., Kah, L.C., Cousin, A., Wiens, R.C., Anderson, R., Blaney, D., Blank, J.G., Calef, F., Clegg, S.M., Fabre, C., Fisk, M.R., Gasnault, O., Grotzinger, J.P., Kronyak, R., Lanza, N.L., Lasue, J., Le Deit, L., LeMouélic, S., Maurice, S., Meslin, P.-Y., Oelher, D.Z., Payré, V., Rapin, W., Schröder, S., Stack, K., Sumner, D. (2017): Chemistry of diagnetic features analyzed by ChemCam at Pahrump Hill, Gale crater, Mars. Icarus, 281, 131-136.

Namur, O., Charlier, B., Holtz, F., Cartier, C. (2016): Sulfur solubility in reduced mafic silicate melts: implications for the speciation and distribution of sulfur on Mercury. Earth and Planetary Science Letters, http://dx.doi.org/10.1016/j.epsl.2016.05.024.

Nekvasil, H., McCubbin, F.M., Harrington, A., Elardo, S., Lindsley, D.H. (2009): Linking the Chassigny meteorite and the Martian surface rock Backstay: Insights into igneous crustal differenciation processes on Mars. Meteorit. Planet. Sci.; 44, 853 – 869.

Nesbitt, H.W., Muir, I.J., Pratt, A.R. (1995): Oxidation of arsenopyrite by air and air-saturated, distilled water, and implications for mechanism of oxidation. Geochimica et Cosmochimica Acta, 59, 1773 – 1786.

Nesbitt, H.W., Bancroft, G.M., Henderson, G.S., Ho, R., Dalby, K.N., Huang, Y., Yan, Z. (2011): Bridging, non-bridging and free (O_{2-}) oxygen in Na_2O-SiO_2 glasses: An X-ray Photoelectron Spectroscopic (XPS) and Nuclear Magnetic Resonance (NMR) study. Journal of Non-Crystalline Solids, 357, 170 – 180.

Nesbitt, H.W., Bandcroft, G.M. (2014): High resolution core - and valence-level XPS studies of the properties (structural, chemical and bonding) of silicate minerals and glasses. Reviews in Mineralogy & Geochemistry, 78, 271 – 329.

Neukum, G., et al. (2004): Recent and episodic volcanic and glacial activity on Mars revealed by the High Resolution Stereo Camera. Nature, 432, 971 – 979.

Newman, S. and Lowenstern, J.B. (2001): VolatileCalc: a silicate melt-H_2O-CO_2 solution model written in Visual Basic for excel. Computers & Geosciences, 28, 597 – 604.

Niles, P.B., Catling, D.C., Berger, G., Chassefière, E., Ehlmann, B.L., Michalski, J.R., et al. (2013): Geochemistry of carbonates on Mars: implications for climate history and nature of aqueous environments. Space Science Review, 174, 301 - 318.

Nilsson, K., Peach, C.L. (1993): Sulfur speciation, oxidation state, and sulfur concentration in backarc magmas. Geochimica et Cosmochimica Acta, 57, 3807 – 3813.

Nimmo, F., Hart, S.D., Korycansky, D.G., Agnor, C.B. (2008): Implications of an impact origin for the martian hemispheric dichotomy. Nature, 453, 1220 – 1223.

Noguchi, N., Shinoda, K., and Masuda, K. (2009): Quantitative analysis of binary mineral mixtures using Raman microspectroscopy: Calibration curves for silica and calcium carbonate minerals and application to an opaline silica nodule of volcanic origin. Journal of Mineralogical and Petrological Sciences, 104, 253-262.

Nyquist, L.E., Bogard, D.D., Shih, C.-Y., Greshake, A., Stöffler, D., Eugster, O. (2001): Ages and geologic histories of Martian meteorites. In: R. Kallenbach, R., Geiss, J., Hartmann, W.K.

(eds) Chronology and Evolution of Mars. Space Science Series of ISSI, vol 12. Springer, Dordrecht.

Ody, A. (2012): Dépouillement et interprétation des données spatiales d'imagerie hyperspectrale de Mars (OMEGA/MEx): Evolution volcanique de la surface de Mars. PhD thesis.

Ohlhorst, S., Behrens, H., Holtz, F. (2001): Compositional dependence of molar absorptivities of near-infrared OH- and H_2O bands in rhyolitic to basaltic glasses. Chem. Geol. ; 174, 5 – 20.

Okamoto, H. and Massalski, T.B. (1985): The Au-Pd (Gold-Palladium) system. Bulletin of Allow Phase Diagrams, 6, 229 – 235.

Ollila, A.M., Wiens, R.C., Perez, R., Nelson, A., Bodine, M., Maurice, S., Sharma, S., Gasda, P., Reess, J.-M., Fouchet, T., Cloutis, E., Johnson, J., Bender, S., Montmessin, F., Bernardi, P., Frydenvang, J., Mccabe, K., Cais, P. (2017): Preliminary Evaluation of the Mars 2020 Rover's SuperCam Development Unit: Co-Aligned Chemical and Mineralogical Analyses. Lunar and Planetary Science XLVIII.

Owen, T., Biemann, K., Rushneck, D.R., Biller, J.E., Howarth, D.W., Lafleur, A.L. (1977): The composition of the atmosphere at the surface of Mars. Journal of Geophysical Research, 82, 4635 – 4639.

Panzner, G. and Egert, B. (1984): The bonding state of sulfur segregated to α-iron surfaces and on iron sulfide surfaces studies by XPS, AES and ELS. Surface Science, 144, 651 - 664.

Panczer, G., De Ligny, D., Mendoza, C., Gaft, M., Seydoux-Guillaume, A.-M., and Wang, X. (2012): Raman and fluorescence. EMU Notes in Mineralogy, 12, 1-22.

Papale, P. (1997): Modeling of the solubility of a one-component H_2O or CO_2 fluid in silicate liquids. Contributions to Mineralogical Petrology, 126, 237 – 251.

Papale, P. (1999): Modeling of the solubility of a two-component H_2O + CO_2 fluid in silicate liquids. American Mineralogist, 84, 477 – 492.

Pepin, R.O. (1994): Evolution of the Martian atmosphere. Icarus, 111, 289 – 304.

Perez, R., Parès, L.P., Newell, R., Robinson, S. (2017): The SuperCam instrument on the NASA Mars 2020 mission: optical design and performance. International Conference on Space Optics – ISCO, Proceedings, 10562.

Phillips, R.J., Zuber, M.T., Solomon, S.C., Golombek, M.P., Jakosky, B.M., Banerdt, W.B., Smith, D.E., Williams, R.M.E., Hynek, B.M., Aharonson, O., Hauck II, S.A. (2001): Ancient geodynamics and global-scale hydrology on Mars. Science, 291, 2587 – 2591.

Plescia, J. (1990): Recent floods lavas in the Elysium regions of Mars. Icarus, 88, 465 – 490.

Pichavant, M., Di Carlo, I., Rotolo, S.G., Scaillet, B., Burgisser, A., Le Gall, N., Martel, C. (2013): Generation of CO_2-rich melts during basalt magma ascent and degassing. Contributions to Mineralogy and Petrology, 166, 545 – 561.

Pollack, J.B., Kasting, J.F., Richardson, S.M., Poliakoff, K (1987): The case for a warm, wet climate on early Mars. Icarus, 71, 203 – 224.

Pratt, A.R. and Nesbitt, H.W. (2000): Core level electron binding energies of realgar (As_4S_4). American Mineralogist, 85, 619 - 622.

Prencipe, M., Mantovani, L., Tribaudino, M., Bersani, D., Lottici, P.P. (2011): The Raman spectrum of diopside: a comparison between ab initio calculated and experimentally measured frequencies. European Journal of Mineralogy, 24, 457-464.

Rampe, E.B., et al. (2014): Amorphous phases on the surface of Mars. Eighth International Conference on Mars, 1239.

Reynard, B., Montagnac, G., and Cardon, H. (2012): Raman spectroscopy at high pressure and temperature for the study of the Earth's mantle and planetary minerals. EMU Notes in Mineralogy, 12, 365-388.

Righter, K., Pando, K., Danielson, L.R. (2009): Experimental evidence for sulfur-rich martian magmas: Implications for volcanism and surficial sulfur sources. Earth and Planetary Science Letters, 288, 235-243.

Righter, K., Danielson, L.R., Pando, K., Morris, R.V., Graff T.G., Agresti D.G., Martin, A.M., Sutton S.R., Newville M., Lanzirotti A. (2012): Redox systematics of martian magmas with implications for magnetite stability. American Mineralogist, https://doi.org/10.2138/am.2013.4251.

Rivoldini, A., Hoolst, T.V., Verhoeven, O., Mocquet, A., Dehant, V. (2011): Geodesy constraints on the interior structure and composition of Mars. Icarus, https://doi.org/10.1016/j.icarus.2011.03.024.

Rosenqvist, T. (1951): A thermodynamic study of the reaction $CaS + H_2O = CaO + H_2S$ and the desulphurization of liquid metals with lime. Journal of Metals, 3, 535 - 540.

Rossano, S. and Mysen, B. (2012): Raman spectroscopy of Silicate Glasses and Melts. EMU Notes in Mineralogy, 12, 319-364.

Rull, F. (2012): The Raman Effect and the vibrational dynamics of molecules and crystalline solids. EMU Notes in Mineralogy, 12, 1-60.

Saal, A.E., Hauri, E.H., Van Orman, J.A., Rutherford, M.J. (2013): Hydrogen isotopes in lunar volcanic glasses and melt inclusions reveal a carbonaceous chondrite heritage. Science, 340, 1317 – 1320.

Salvatore, M.R., Mustard, J.F., Wyatt, M.B., Murchie, S.L. (2010): Definitive evidence of Hesperian basalt in Acidalia and Chryse planitiae. Journal of Geophysical Research: Planets, 115.

Sasaki, Y., Mohri, M., Suyama, K., Ishii, K. (2000): The effect of Fe_{3+} ions on the anionic structure of iron-bearing sodium silicate melts. ISIJ International, 40, 1181-1187.

Sautter, V. and others (2015): In situ evidence for continental crust on early Mars. Nature Geosciences, 8, 605-609.

Sautter, V. and others (2016): Magmatic complexity on early Mars as seen through a combination of orbital, in-situ and meteorite data. Lithos, 254-255, 36-52.

Schiavi, F., Bolfan-Casanova, N., Withers, A.C., Médard, E., Laumonier, M., Laporte, D., Flaherty, T., Gomez-Ulla, A. (2018): Water quantification in silicate glasses by Raman spectroscopy: Correcting for the effects of confocality, density and ferric iron. Chemical Geology, 483, 312 – 331.

Schilling, F., Wunder, B. (2004): Temperature distribution in piston-cylinder assemblies: Numerical simulations and laboratory experiments. European Journal of Mineralogy, 16, 7 – 14.

Schmidt, B.C., Holtz, F.M., Bény, J.-M. (1998): Incorporation of H_2 in vitreous silica, qualitative and quantitative determination from Raman and infrared spectroscopy. Journal of Non-Crystalline Solids, 240, 91 – 103.

Schmidt, M.E., Schrader, C.M., McCoy, T.J., The primary fO_2 of basalts examined by the Spirit rover in Gusev Crater, Mars (2013): Evidence for multiple redox states in the martian interior. Earth Planet. Sci. Lett. , 384, 198 – 208.

Schuessler J.A., Botcharnikov R.E., Behrens H., Misiti V. and Freda C. (2008): Oxidation state of iron in hydrous phono-tephritic melts. American Mineralogist, 93, 1493-1504.

Seah, M.P., Gilmore, I.S., Spencer, S.J. (1998): XPS: binding energy calibration of electron spectrometers 4-assessment of effects for different x-ray sources, analyser resolutions, angles of emission and overall uncertainties. Surface and Interface Analysis, https://doi.org/10.1002/.

Sharma, S.K., Simons, B., and Yoder Jr, H.S. (1983): Raman study of anorthite, calcium Tschermak's pyroxene, and gehlnite in crystalline and glassy states. American Mineralogist, 68, 11-12.

Shi, P., Saxena, S.K. (1992): Thermodynamic modelling of the C-H-O-S fluid system. American Mineralogist, 77, 1038 – 1049.

Shishkina, T. A., Botcharnikov, R. E., Holtz, F., Almeev, R. R., Jazwa, A. M., & Jakubiak, A. A. (2014): Compositional and pressure effects on the solubility of H_2O and CO_2 in mafic melts. Chemical Geology, 388, 112–129.

Siegbahn, K. (1982): Electron spectroscopy for atmos, molecules, and condensed matter. Reviews of Modern Physics, 54, 709 – 728.

Simon, A.C., Ripley, R.M. (2011): The role of magmatic sulfur in the formation of ore deposits. Reviews in Mineralogy and Geochemistry, 73, 513 - 578.

Spilliaert, N., Métrich, N., Allard, P. (2006): S-Cl-F degassing pattern of water-rich alkali basalt: Modelling and relationship with eruption styles on Mount Etna volcano. Earth and Planetary Science Letters, 248, 772 – 786.

Squyres, S.W., Grotzinger, J.P., Arvidson, R.E., Bell III, J.F., Calvin, W., Christensen, P.R. et al. (2004a): In Situ evidence for an ancient aqueous environment at Meridiani Planum, Mars. Science, 306, 1709-1714.

Squyres, S.W., Arvidson, R.E., Bell III, J.F., Brückner, J., Cabol, N.A., Calvin, W., Carr, M.H., Christensen, P.R. et al. (2004b): The Opportunity Rovers's Athena Science investigation at Meridiani Planum, Mars. Science, 303, 1698-1703.

Squyres, S.W., Knoll, A.H. (2005): Sedimentary rocks at Meridiani Planum: Origin, diagenesis and implications for life on Mars. Earth Planetary Science Letters, 240, 1-10.

Squyres, S.W., Arvidson, R.E., et al. (2012): Ancient impact and aqueous processes at Endeavour crater, Mars. Science, 336, 570 - 576.

Stanley, B.D., Hirschmann, M.M., Withers, A.C. (2011): CO_2 solubility in Martian basalts and Martian atmospheric evolution. Geochimica et Cosmochimica Acta, 75, 5987 – 6003.

Stanley, B.D., Schaub, D.R., Hirschmann, M.M (2012): CO_2 solubility in primitive martian basalts similar to Yamato 980459, the effect of composition on CO_2 solubility of basalts, and the evolution of the martian atmosphere. American Mineralogist, 97, 1841 – 1848.

Stanley, B.D., Hirschmann, M.M., Withers, A.C. (2014): Solubility of C-O-H volatiles in graphite-saturated martian basalts. Geochimica et Cosmochimica Acta, 129, 545 – 76.

Stolper, E. (1982): Water in silicate glasses: An infrared spectroscopic study. Contrib. Mineral. Petrol. ; 81, 1 – 17.

Stolper, E.M., and the MSL team (2013): The Petrochemistry of Jake_M: Martian Mugearite. Science, 341.

Tamic, N., Behrens, H., Holtz, F. (2001): The solubility of H_2O and CO_2 in rhyolitic melts in equilibrium with a mixed $CO_2 – H_2O$ fluid phase. Chemical Geology, 174, 333 – 347.

Tanaka, K.L., Robbins, S.J., Fortezzo, C.M., Skinner Jr., J.A., Hare, T.M. (2014): The digital geologic map of Mars: Chronostratigraphic ages, topographic and crater morphologic characteristics and updated resurfacing history. Planetary and Space Science, 95, 11 – 24.

Tarcea, N., and Popp, J. (2012): Raman data analysis. EMU Notes in Mineralogy, 12, 195-228.

Taylor, S.R., McLennan, S.M. (2009): Planetary Crusts. Cambridge, 378.

Tillman; J.E., Johnson, N.C., Guttorp, P., Percival, D.B. (1993): The Martian annual atmospheric pressure cycle: Years without great dust storms. Journal of Geophysical Research: Planets. 98, 10963 – 10971.

Tosca, N.J. and Knoll, A.H. (2009): Juvenile chemical sediments and the long-term persistence of water at the surface of Mars. Earth and Planetary Science Letters, 286, 379 – 386.

Trcera, N., Rossano, S., Tarrida, M. (2010): Structural study of Mg-bearing sodosilicate glasses by Raman spectroscopy. Journal of Raman spectroscopy, 42, 765 – 772.

Treiman, A.H., Gleason, J.D., Bogard, D.D. (2000): The SNC meteorites are from Mars. Planetary and Space Science, 48, 1213 – 1230.

Treiman, A.H. (2003): Chemical compositions of Martian basalts (shergotittes): some inferences on basalt formation, mantle metasomatism. Meteoritics, 20, 229 – 243.

Tribaudino, M., Mantovani, L., Bersani, D., and Lottici, P.P. (2012): Raman spectroscopy of $(Ca,Mg)MgSi_2O_6$ clinopyroxenes. American Mineralogist, 97, 1339-1347.

Udry, A., Gazel, E., McSween Jr., H.Y. (2018): Formation of evolved rocks at Gale Crater by crystal fractionation and implications for Mars crustal composition. Journal of Geophysical Research: Planets, 123, 1525 – 1540.

Usui, T.: Hydrogen reservoirs in Mars as revealed by martian meteorites. Volatiles in the Martian Crust, Elsevier. 2019.

Vaniman, D.T., Martinez, G.M., Rampe, E.B., Bristow, T.F., Blake, D.F., Yen, A.H., Ming, D.W., Rapin, W., Meslin, P.-Y., Morookian, J.M., Downs, R.T., Chipera, S.J., Morris, R.V., Morrison, S.M., Treiman, A.H., Achilles, C.N., Grotzinger, J.P., Hazen, R.M., Crisp, J.A. (2017): Calcium Sulfates At Gale Crater And Limitations On Gypsum Stability. 48th Lunar Planetary Science Conference.

Vaucher, J., Baratoux, D., Toplis, M.J., Pinet, P., Mangold, N., Kurita, K. (2009): The morphologies of volcanic landforms at Central Elysium Planitia: Evidence for recent and fluid lavas on Mars. Icarus, 200, 39 – 51.

Villanueva, G.L., Mumma, M.J., Novak, R.E., Kaüfl, H.U., Hartogh, P., Encrenaz, T., et al. (2015): Strong water isotopic anomalies in the Martian atmosphere: probing current and ancient reservoirs. Science, 348, 218 - 221.

Wadhwa, M. (2008): Redox conditions on small bodies, the Moon and Mars. Reviews in Mineralogy & Geochemistry, 68, 493-510.

Waff, H.S. (1977): The structural role of ferric iron in silicate melts. Canadian Mineralogist, 15, 198-199.

Wallace, P. and Carmichael, I.S.E. (1991): Sulfur in basaltic magmas. Geochimica et Cosmochimica Acta, 56, 1863 – 1874.

Wallace, P.J. (2003): From mantle to atmosphere: magma degassing, explosive eruptions, and volcanic volatile budgets. Developments in Volcanology, 5, 105 – 127.

Wallace, P.J. (2005): Volatiles in subduction zone magmas: concentrations and fluxes based on melt inclusion and volcanic gas data. Journal of Volcanology and Geothermal Research, 140, 217 – 240.

Wang, A., Kuebler, K.E., Haskin, L.A. (2003): Raman spectroscopy characterization of the feldspars – Implications for In situ surface mineral characterization in planetary exploration. Lunar and Planetary Science XXXIV.

Wang, A., (2006): Sulfate deposition in subsurface regolith in Gusev Crater, Mars. Journal of Geophysic Research: Planets, 111, E02S17.

Wänke, H. and Dreibus, G. (1997): Chemistry and accretion history of Mars. The Royal Society, https://doi.org/10.1098/rsta.1994.0132.

Weis, F.A., Bellucci, J.J., Skogby, H., Stalder, R., Nemchin, A.A., Whitehouse, M.J., Water content in the Martian mantle (2017): A Nakhla perspective. Geochim. Cosmochim. Acta., 212, 84 – 98.

Wendlandt, R.F. (1982): Sulfide saturation of basalt and andesite melts at high pressures and temperatures. American Mineralogy, 67, 877 – 885.

Wetzel, D.T., Rutherford, M.J., Jacobsen, S.D., Hauri, E.H., Saal, A.E. (2013): Degassing of reduced carbon from planetary basalts. Proceedings of the National Academy of Sciences of the United States of America, 20, 8010 – 8013.

Wiens, R.C., et al. (2012): The ChemCam instrument suite on the Mars Science Laboratory (MSL) Rover: Body unit and combined system tests. Space Science Review, DOI 10.1007/s11214-012-9902-4.

Wiens, R.C., Maurice, S., Rull, F. and the SuperCam Team (2016): SuperCam remonte sensing on the Mars 2020 rover: Science Goals and overview. 3rd International Workshop on Instrumentation for Planetary Missions.

Wiens, R.C., Maurice, S., Rull Perez, F. (2017): The SuperCam remote sensing instrument suite for the Mars 2020 rover mission: a preview. Spectroscopy.

Wilke, M., Klimm, K., Kohn, S.C. (2011): Spectroscopy studies on sulfur speciation in synthetic and natural glasses. Reviews in Mineralogy & Geochemistry, DOI: 10.2138/rmg.2011.73.3.

Williford, K.H., et al. (2018): The NASA Mars 2020 Rover mission and the search for extraterrestrial life. From Habitability to Life on Mars, 275 – 308.

Wilson, A.D. (1960): The micro-determination of Fe_{2+} in silicate minerals by a volumetric and a colorimetric method. Analyst, 85, 823 – 827.

Wray, J., Hansen, S.T., Dufek, J., Swayze, G.A., Murchie, S.L., Seelos, F.P., Skok, J.R., Irwin III, R.P., Ghiorso, M.S. (2013): Prolonged magmatic activity on Mars inferred from the detection of felsic rocks. Nature Geoscience, 6, 1013-1017.

Xue, X., and Kanzaki, M. (2004): Dissolution mechanisms of water in depolymerized silicate melts: Constraints from $_1H$ and $_{29}Si$ NMR spectroscopy and ab initio calculations. Geochimica et Cosmochimica Acta, 68, 5027 – 5057.

Zajacz, Z., Halter, W., Malfait, W.J., Bachmann, O., Bodnar, R.J., Hirschmann, M.M., Mandeville, C.W., Morizet, Y., Müntener, O., Ulmer, P., Webster, J.D. (2005): A composition-independent quantitative determination of the water content in silicate glasses and silicate melt inclusions by confocal Raman spectroscopy. Contrib. Mineral. Petrol., 150, 631-642.

Zajacz, Z. (2015): The effect of melt composition on the partitioning of oxidized sulfur between silicate melts and magmatic volatiles. Geochimica et Cosmochimica Acta, http://dx.doi.org/10.1016/j.gca.2015.01.036.

Zajacz, Z., Tsay, A. (2019): An accurate model to predict sulfur concentration at anhydrite saturation in silicate melts. Geochimica et Cosmochimica Acta, https://doi.org/10.1016/j.gca.2019.07.007.

Zhao, J., Zhou C., Li, M., Li, J., Li, G., Ma, D., Li, Z., Zou, D. (2017): Bottom-up synthesis of ultra-small molybdenum disulfide-polyvinylpyrrolidone nanosheets for imaging-guided tumor regression. Impact Journals, 8, 106707 - 106720.

Annex Section

T_0	1246.1474
v_0	7.2701221
p_1	94.321033
p_2	7.3899296
p_3	-0.15880987
p_4	0.012681877
q_1	0.10113834
q_2	-0.001614596
q_3	-4.10863e-06

Table I.A1: Parameters for B-type thermocouple calibration equation for temperatures between 700 to 1820°C

GC-H2O-4h
1 GPa
1600 °C
4h
2.6 wt % H_2O

G2   Mag = 450 X

CL-3H-6h
1 GPa
1600 °C
6h
2.9 wt % H_2O

G19   Mag = 170 X

GC-3H-6h
1 GPa
1600 °C
6h
2.4 wt % H_2O

G24   Mag = 370 X

PR-6Hb
1 GPa
1500 °C
1h
6.5 wt % H_2O

G20   Mag = 400 X

GC-3H-chiller
1 GPa
1600 °C
1h
2.6 wt % H_2O

G27   Mag = 700 X

GCD-3H-6h
1 GPa
1600 °C
6h
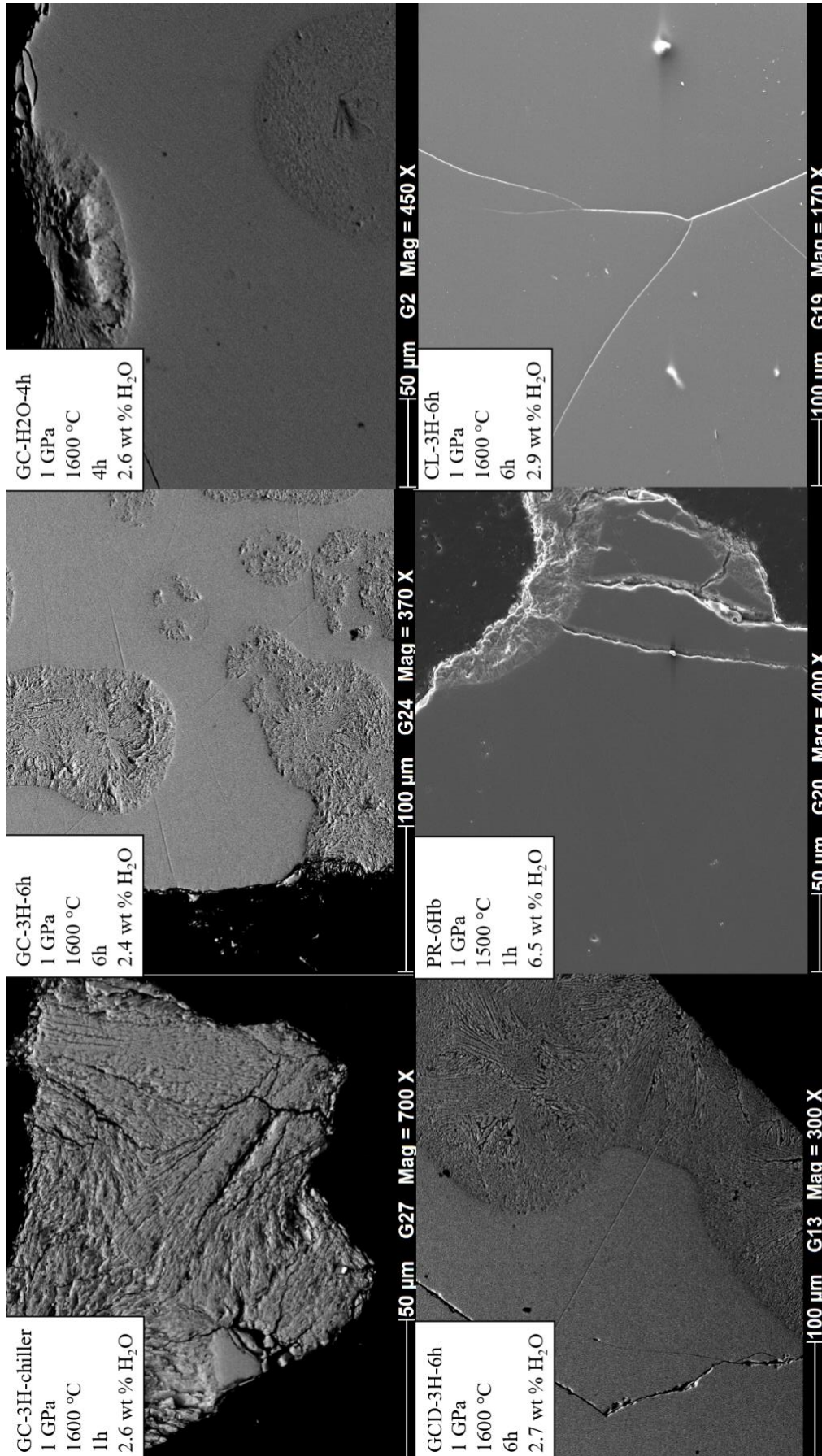2.7 wt % H_2O

G13   Mag = 300 X

190

Fig.II.A1: SEM images on various samples obtained in the Chapter II. Backscattered and secondary electron images are presented. Sample descriptions are reported in Table II.2.

	GC-H$_2$O-chiller	GC-H$_2$O-4h	GC-3H-6h	GC-1H-4h	GCD-3H-6h	GCD-3H-6h-1.5G	GCD-2H-0.5G	CL-3H-6h	PR-3H-6h	PR-6H-4h
m_c*	0.36216	0.3638	0.32327	0.35249	0.35369	0.35892	0.45074	0.35037	0.37726	0.34704
m_c+H$_2$O	0.36277	0.36447	0.32377	0.35275	0.35434	0.35971	0.45177	0.35102	0.37801	0.34824
m_c+H$_2$O+powder	0.38514	0.38701	0.34369	0.3774	0.37658	0.38454	0.50144	0.37209	0.40288	0.36892
cut	0.38463	0.36542		0.37193	0.3637	0.37587		0.36952	0.40288	0.34599
m_{total} (weld)	0.38461	0.36534	0.34367	0.37188	0.36365	0.37582	0.5014	0.36948	0.38693	0.34597
m_{total} (after experiment)	0.38559	0.36698	0.34584	0.37197	0.36609	0.40706	0.52981	0.37005	0.38717	0.34608
m_{degas}	0.38448	0.36583	0.34455	0.37042	0.36592	0.40671	0.52888	0.36875	0.38678	0.34596
Hiss	yes	?	?	yes	no	no	yes	?	no	no-
Macroscopic aspect	small crystals + vitreous phases	glass	glass	glass	glass	glass	glass	no apparent crystal phases	glass	glass

Table II.A1: Sample preparation prior experiment and weight measurements of capsule after experiments. Macroscopic descriptions of the sample after opening of the capsules (after high-pressure experiment) are also reported. * m_c: mass of the Pt capsule. Weight values are expressed in grams.

Table II.A2: Deconvolution results for each sample in the HF (800 – 1250 cm$_{-1}$) and H$_2$O region (3000 – 4000 cm$_{-1}$). For each deconvolution, the peak position is first described, the the FWHM (i.e., the Full Width at Half Maximum) and the area percentage (% area). The addition of D1 to D3 coupled to the Free OH peak represents the entire H$_2$O vibration

			GC-H2O-chiller	GC-H2O-4h	GC-3H-6h	GC-1H-4h	GCD-3H-6h	GCD-3H-6h-1.5G	GCD-2H-0.5G	CL-3H-6h	PR-3H-6h	PR-6H-4h	PR-6Hb
HF region	Q1	Position (cm-1)	884	887	874	886	877	882	875	882	879	885	905
		FWHM	80	81	82	78	78	82	77	84	84	79	70
		Area %	20	20	18	20	22	20	18	20	15	15	14
	Q2	Position (cm-1)	948	951	940	951	940	946	940	947	951	950	969
		FWHM	82	86	81	83	87	87	76	83	78	82	69
		Area %	33	32	32	32	33	32	34	34	26	28	31
	Q3	Position (cm-1)	1011	1014	1001	1012	1001	1009	999	1011	1007	1005	1020
		FWHM	82	88	90	82	94	87	81	83	74	77	66
		Area %	29	29	29	28	27	29	29	31	32	34	31
	Q4	Position (cm-1)	1079	1082	1073	1081	1072	1076	1065	1075	1077	1077	1078
		FWHM	86	91	90	83	90	90	79	84	72	83	63
		Area %	19	20	21	19	18	19	19	16	25	23	26
H2O region	D1	Position (cm-1)	3357	3252	3278	3380	3323	3374	3398	3477	3410	3278	3279
		FWHM	208	200	222	219	126	284	126	220	201	356	228
		Area %	16	23	16	28	40	20	18	28	42	24	19
	D2	Position (cm-1)	3473	3478	3391	3480	3446	3514	3558	3590	3573	3447	3459
		FWHM	146	220	109	129	122	160	137	130	149	176	184
		Area %	30	40	23	31	50	32	82	55	58	32	29
	D3	Position (cm-1)	3581	3590	3556	3596	3571	3606				3576	3586
		FWHM	130	130	179	116	133	130				141	148
		Area %	48	34	61	41	10	42				44	50
	Free OH	Position (cm-1)	3666	3672				3673		3661			3665
		FWHM	52	50				48		54			43
		Area %	6	3				7		17			2
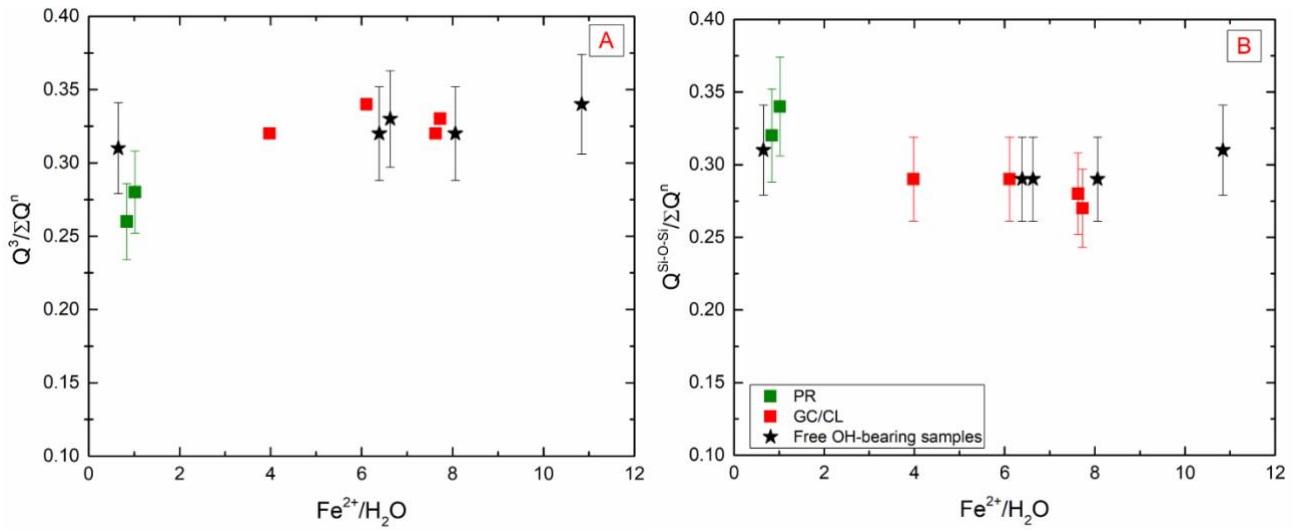
Fig.II.A2: Ratio of the Q_n species in function of the Fe_{2+} normalized by the H_2O content for PR glasses (i.e., Fe-poor) in green, GC/CL samples (Fe-rich synthetic glasses) in red, and the glasses presenting Free OH molecular groups in black stars: A) $Q_3/\sum Q_n$, B) $Q_{Si-O-Si}/\sum Q_n$. A relative error of 10 % on the deconvolution is applied.

GCS-2S-1G
1 GPa
1500 °C
2.0 wt % S

100 µm   G5   Mag = 270 X

GCS-2SH-1G
1 GPa
1400 °C
2.0 wt % S
2.0 wt % H_2O

200 µm   G21   Mag = 130 X

GCS-1S-1G
1 GPa
1500 °C
1.0 wt % S

500 µm   G11   Mag = 65 X

GCS°-2SH-1G
1 GPa
1400 °C
2.0 wt % S
2.0 wt % H_2O

500 µm   G13   Mag = 65 X

CLS-2S-1G
1 GPa
1500 °C
1.0 wt % S

100 µm   G2   Mag = 270 X

GCS°-2S-1G
1 GPa
1500 °C
2.0 wt % S

500 µm   G7   Mag = 65 X

CLS-1S-1G
1 GPa
1500 °C
1.0 wt % S

500 µm   G7   Mag = 65 X

GCS°-1S-1G
1 GPa
1500 °C
1.0 wt % S

200 µm   G9   Mag = 90 X

195

Fig.III.A1: SEM images on various samples obtained in the Chapter III. Backscattered and secondary electron images are presented. Sample references are described in Table III.1.

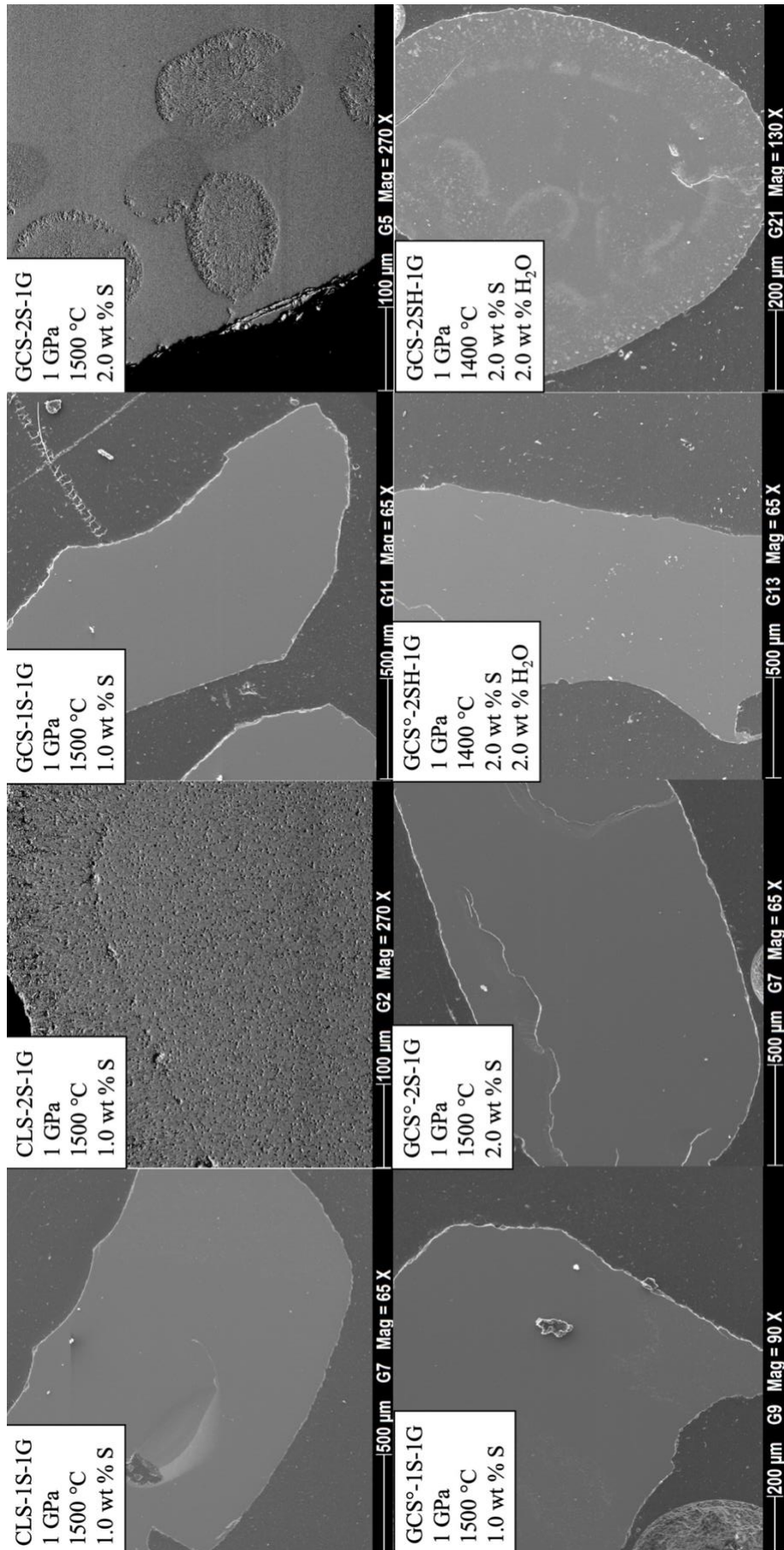|	GCS-4000S	GCS-4000-1G	GCS-1S-1G	GCS-1S-1,5G	GCS-1S-2G	GCS-2S-1G	GCS-2SH-1G *$_c$
m_c*	0,43583	1,09107	0,45911	0,41757	0,35127	0,39413	0.38655
m_c+H_2O							0.38725
m_c+ powder	0,48484	1,30183	0,51701	0,4626	0,38881	0,43233	0.41932
cut			0,50934	0,45341		0,41598	0.41046
m_{total} (weld)	0,48478	1,43455 (+Pt lid)	0,50927	0,4534	0,3888	0,41599	0.41048
m_{total} (after experiment)	0,49351	1,48872	0,53506	0,47467	0,39812	0,41661	0.41870
m_{degas}	0,4933	1,48722	0,53403	0,4727	0,39803	0,41661	0.41803
Hiss	no	yes	no	no	no	no	no
Macroscopic aspect	glass	glass	glass	glass	glass	dendritic crystals + glass	dendritic crystals + glass

	GCS°-1S-1G	GCS°-2S-1G	GCS°-1S-1,5G	GCS°-2S-1,5G	GCS°-2S-2G	GCS°-2SH-1G
m_c*	0.41065	0.3888	0.42419	0.37100	0.33776	0.36544
m_c+H_2O						0.36609
m_c+ powder	0.45933	0.43107	0.47429	0.40433	0.37310	0.39784
cut	0.45728	0.42718	0.45909	0.39914	0.36699	0.39335
m_{total} (weld)	0.45722	0.4271	0.45909	0.39914	0.36698	0.39335
m_{total} (after experiment)	0.45812	0.4168	0.45995	0.35610	0.36545	0.39011
m_{degas}	0.45805	0.41678	0.45993	0.35607	0.36528	0.39002
Hiss	no	no	no	no		no
Macroscopic aspect	glass	glass	glass	glass	glass	glass

	CLS-4000S	CLS-1S-1G	CLS-1S-1,5G	CLS-2S-1G
m_c*	0.41675	0.42248	0.42658	0.39743
m_c+ powder	0.46641	0.47553	0.47025	0.4409
cut	0.44834		0.45922	0.43202
m_{total} (weld)	0.44834	0.47542	0.45919	0.43191
m_{total} (after experiment)	0.47321	0.48526	0.48407	0.43517
m_{degas}	0.46418	0.48397	0.48323	0.43506
Hiss	no	no	no	no
Macroscopic aspect	crystallized	crystallized	crystallized	crystallized

Table III.A1: Sample preparation prior experiment and weight measurements of capsule after experiments for GCS, GCS$_0$ and CLS compositions. Macroscopic descriptions of the sample after opening of the capsules (after high-pressure experiment) are also reported. * m$_c$: mass of the Pt capsule. Weight values are expressed in grams.

Mineral	t_a (s)	H_b (μm)	Raman shift (cm^{-1})	A_c (%)	W_{Gd}	W_{Le}
Gypsum	10	200	412	9	12	15
			492	11	16	12
			574	4	~ 0	49
			616	7	19	15
			669	3	18	5
			1007	48	17	4
			1105	2	3	22
			1134	15	17	12
	15	200	412	9	12	14
			492	12	13	15
			576	4	~ 0	49
			616	6	25	2
			669	4	14	10
			1007	48	17	4
			1108	3	0.01	27
			1135	14	17	11
	15	50	412	11	33	~ 0
			485	22	15	16
			604	15	7	27
			621	6	16	~ 0
			663	6	17	5
			1007	9	16	6
			1122	23	~ 0	30
			1155	9	9	26
Olivine	15	200	818	28	17	4
			850	62	8	23
			914	3	11	6
			956	7	16	13
	15	50	809	24	23	0.7
			842	73	0.02	29
			901	0	10	~ 0
			948	3	19	~ 0

Orthopyroxene	15	200	231	3	22	~ 0
			339	13	24	15
			367	6	7	51
			400	8	~ 0	35
			439	0	31	~ 0
			652	4	20	~ 0
			678	23	23	11
			736	0	22	~ 0
			853	1	38	~ 0
			898	4	~ 0	89
			935	3	36	~ 0
			1007	28	26	15
			1036	6	0.1	28
			1098	1	63	~ 0
Mg-sulfate	10	200	213	9	20	20
			263	5	20	20
			432	12	~ 0	24
			496	12	12	26
			632	14	~ 0	27
			667	3	21	21
			983	5	28	28
			1043	31	16	8
			1113	9	15	19
			1215	1	19	8
	15	200	213	9	20	20
			263	5	20	20
			431	12	~ 0	23
			496	13	8.5	29
			632	13	~ 0	25
			665	2	15	15
			981	5	30	30
			1043	31	17	8
			1113	10	~ 0	29

Clinopyroxene	15	200	331	18	25	24
			371	6	40	~ 0
			396	5	25	~ 0
			517	2	37	~ 0
			558	2	32	~ 0
			666	24	20	12
			875	3	31	31
			934	5	54	82
			1006	32	~ 0	34
			1074	2	65	~ 0
			1119	1	35	~ 0
		50	314	10	36	6
			346	17	32	31
			382	8	33	~ 0
			504	1	32	~ 0
			539	2	45	~ 0
			657	20	23	13
			805	0	15	~ 0
			863	7	89	~ 0
			940	1	44	~ 0
			998	33	~ 0	41
			1047	1	4	44
			1103	0	41	~ 0
Plagioclase	10	200	252	2	22	0.1
			282	7	33	0.02
			402	3	31	~ 0
			435	1	19	0.001
			499	44	32	21
			559	4	25	0.2
			681	1	26	~ 0
			757	6	45	10
			910	3	43	~ 0
			975	15	0.3	60
			1028	11	70	89
			1096	2	88	~ 0

[a] acquisition time normalized used for calibration

[b] confocal mode during acquisition

[c] simulated peak areas in percentage

[d] Gaussian width simulated

[e] Lorentzian width simulated

Table IV.A1: Analytical conditions and characterizations of mineral pure spectrum used for the calibration.
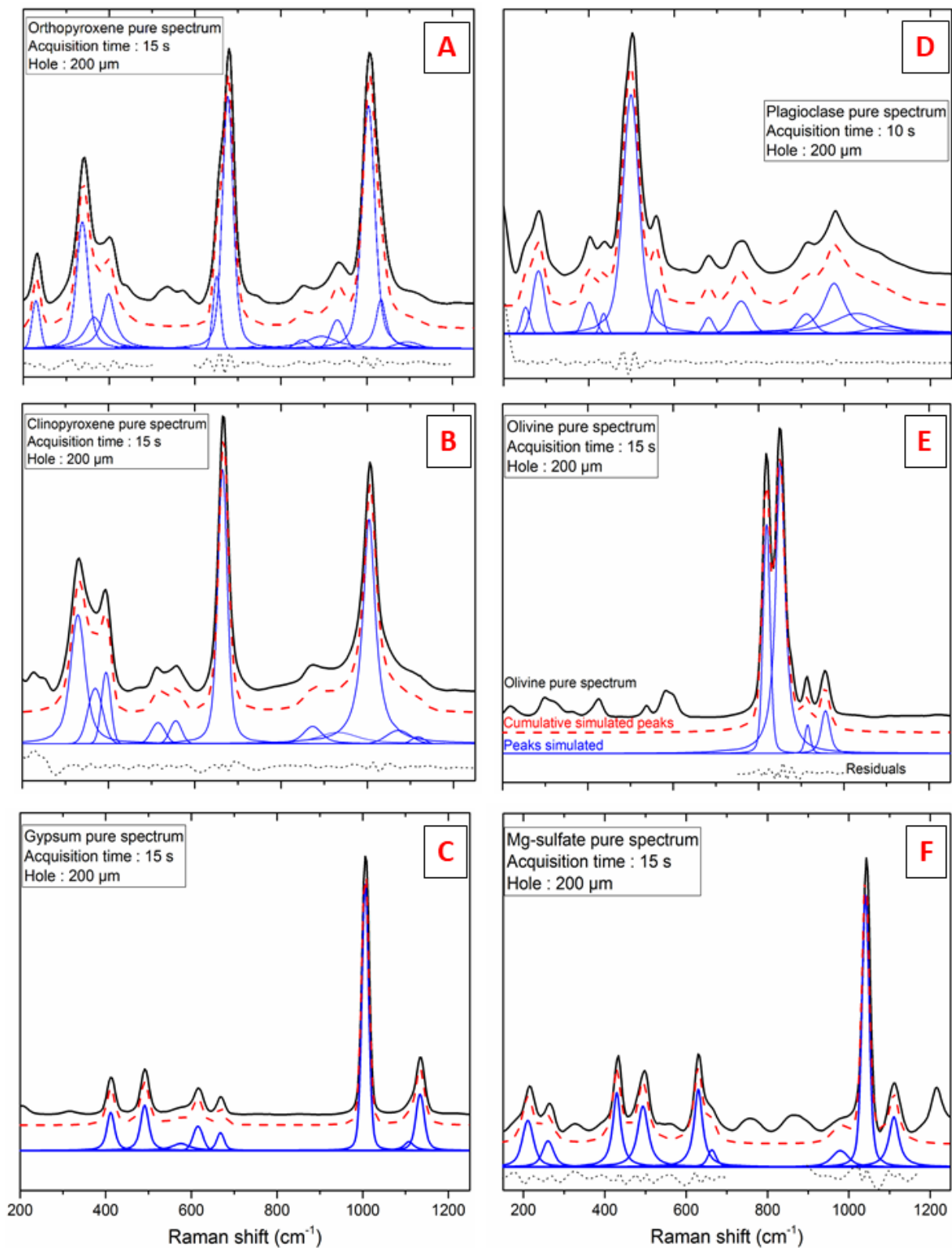
Fig.IV.A1: Deconvolution of minerals pure spectrum for A: orthopyroxene B: clinopyroxene; C: gypsum; D: plagioclase; E: olivine; and F: Mg-sulfate. With individual peaks simulated in blue, cumulative peaks simulated in red dashed lines and residuals in black dotted lines. Analytical parameters (acquisition time and confocal mode) are described for each spectrum.
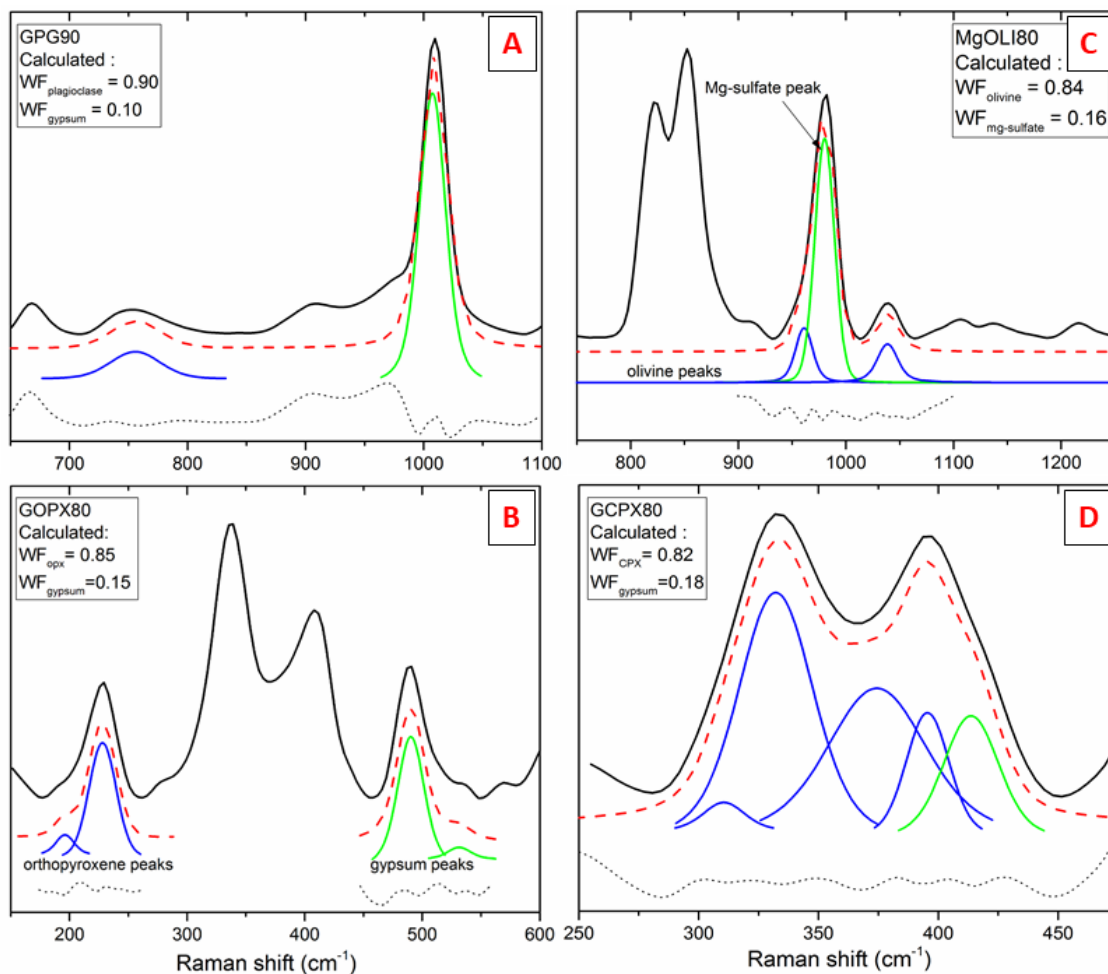
Fig.IV.A2: Peak simulations for the other different mixtures: A: plagioclase-gypsum mixture with theoretical proportions of 0.9 and 0.1; B: orthopyroxene-gypsum mixture with initial proportion of 0.8 and 0.2 respectively; C: olivine-Mgsulfate mixture (theoretical proportions: $WF_{olivine}=0.8$ and $WF_{Mg-sulfate}=0.2$); D: clinopyroxene-gypsum mixture of theoretical weight fraction of 0.90 and 0.10 respectively. Green peaks are attributed to sulfates vibrations (Ca or Mg) and blue ones for silicate minerals. Red dashed and blacks dotted lines are cumulative peaks simulated and residuals left after simulations. Weight fraction calculated by simulations for examples shows in this figure are reported in each graph. All results from simulations on the different mixtures are described in Table IV.3.

Titre : Comportements du S et H_2O dans le système magmatique martien : approche expérimentale et spectroscopique.

Mots clés : Mars, espèces volatiles, magmas, expérimentation haute pression, Mars 2020

Résumé : La compréhension de la planète Mars est essentielle pour contraindre l'évolution de notre Système Solaire, notamment celle de la Terre. La future mission spatiale Mars 2020 comportera un spectromètre Raman permettant de caractériser la minéralogie de surface sur Mars. A travers des calibrations préétablies, le budget des éléments volatils présents sur Mars peut être déterminé. Quantifier les volatils sur Mars permet de comprendre la formation de son atmosphère primitive ayant maintenue de l'eau liquide à la surface.

Ainsi, des analogues à des basaltes martiens ont été synthétisés sous pressions en présence d'H_2O et S. Les verres hydratés présentent des espèces hydroxyles à très faibles teneurs en H_2O, pouvant entraîner une polymérisation du magma martien.

Au contraire, de nouvelles valeurs de teneurs en S sont obtenues et réhaussent celles proposées dans la litterature. Un modèle de solubilité du S applicable aux magmas martiens et terrestres a été réalisé.

L'altération de roches volcaniques riches en S, susceptibles d'être présentes sur Mars, entraînent des mélanges de minéraux mafiques avec des sulfates. Une calibration par spectroscopie Raman est réalisée dans des mélanges sulfatés et applicable pour la future mission spatiale.

Pour conclure, ces travaux ré-évaluent le budget en S possible dans l'intérieur martien, mais aussi sur la surface. Des études complémentaires sont nécessaires pour comprendre le comportement d'H_2O et d'autres éléments volatils dans ces magmas atypiques.

Title : H_2O and S behaviors in martian magmatic system: An experimental and spectroscopic approach

Keywords : Mars, volatile species, melts, high-pressure experiments, Mars 2020

Abstract : The understanding of the planet Mars is required to constrain the Solar System's evolution, and notably, the Earth's. The future 2020 Mars mission will include a Raman spectrometer to characterize martian soils and its surficial mineralogy. Through calibrations, volatiles budget can be determined. Quantify volatile species on Mars permits the understanding of the primitive atmosphere formation which have hold liquid water at the surface.

Hence, synthetic martian basalts have been realized at high-pressures with H_2O and S. Hydrated glasses present Free OH groups at low H_2O content, which could lead to a polymerization of the martian melt.

On the opposite, martian glasses can dissolve a high S content, higher than previously estimated in the litterature. A new S solubility model is established and can be applied on both terrestrial and martian melt compositions.

The weathering of possible S-rich igneous rocks at the surface of Mars leads to the formation of mixtures between mafic minerals and sulfates. A new Raman calibration is proposed on sulfate mixtures to quantify S for the future spatial mission.

Consequently, this work re-evaluate the S budget in the martian melts and in the surface. Complentary studies are required to understand the H_2O, and other volatiles, behaviors in martian melts.

Titre : Comportements du S et H$_2$O dans le système magmatique martien : approche expérimentale et spectroscopique.

Mots clés : Mars, espèces volatiles, magmas, expérimentation haute pression, Mars 2020

Résumé : La compréhension de la planète Mars est essentielle pour contraindre l'évolution de notre Système Solaire, notamment celle de la Terre. La future mission spatiale Mars 2020 comportera un spectromètre Raman permettant de caractériser la minéralogie de surface sur Mars. A travers des calibrations préétablies, le budget des éléments volatils présents sur Mars peut être déterminé. Quantifier les volatils sur Mars permet de comprendre la formation de son atmosphère primitive ayant maintenue de l'eau liquide à la surface.

Ainsi, des analogues à des basaltes martiens ont été synthétisés sous pressions en présence d'H$_2$O et S. Les verres hydratés présentent des espèces hydroxyles à très faibles teneurs en H$_2$O, pouvant entraîner une polymérisation du magma martien.

Au contraire, de nouvelles valeurs de teneurs en S sont obtenues et réhaussent celles proposées dans la litterature. Un modèle de solubilité du S applicable aux magmas martiens et terrestres a été réalisé.

L'altération de roches volcaniques riches en S, susceptibles d'être présentes sur Mars, entraînent des mélanges de minéraux mafiques avec des sulfates. Une calibration par spectroscopie Raman est réalisée dans des mélanges sulfatés et applicable pour la future mission spatiale.

Pour conclure, ces travaux ré-évaluent le budget en S possible dans l'intérieur martien, mais aussi sur la surface. Des études complémentaires sont nécessaires pour comprendre le comportement d'H$_2$O et d'autres éléments volatils dans ces magmas atypiques.

Title : H$_2$O and S behaviors in martian magmatic system: An experimental and spectroscopic approach

Keywords : Mars, volatile species, melts, high-pressure experiments, Mars 2020

Abstract : The understanding of the planet Mars is required to constrain the Solar System's evolution, and notably, the Earth's. The future 2020 Mars mission will include a Raman spectrometer to characterize martian soils and its surficial mineralogy. Through calibrations, volatiles budget can be determined. Quantify volatile species on Mars permits the understanding of the primitive atmosphere formation which have hold liquid water at the surface.

Hence, synthetic martian basalts have been realized at high-pressures with H$_2$O and S. Hydrated glasses present Free OH groups at low H$_2$O content, which could lead to a polymerization of the martian melt.

On the opposite, martian glasses can dissolve a high S content, higher than previously estimated in the litterature. A new S solubility model is established and can be applied on both terrestrial and martian melt compositions.

The weathering of possible S-rich igneous rocks at the surface of Mars leads to the formation of mixtures between mafic minerals and sulfates. A new Raman calibration is proposed on sulfate mixtures to quantify S for the future spatial mission.

Consequently, this work re-evaluate the S budget in the martian melts and in the surface. Complentary studies are required to understand the H$_2$O, and other volatiles, behaviors in martian melts.

Titre : Comportements du S et H$_2$O dans le système magmatique martien : approche expérimentale et spectroscopique.

Mots clés : Mars, espèces volatiles, magmas, expérimentation haute pression, Mars 2020

Résumé : La compréhension de la planète Mars est essentielle pour contraindre l'évolution de notre Système Solaire, notamment celle de la Terre. La future mission spatiale Mars 2020 comportera un spectromètre Raman permettant de caractériser la minéralogie de surface sur Mars. A travers des calibrations préétablies, le budget des éléments volatils présents sur Mars peut être déterminé. Quantifier les volatils sur Mars permet de comprendre la formation de son atmosphère primitive ayant maintenue de l'eau liquide à la surface.

Ainsi, des analogues à des basaltes martiens ont été synthétisés sous pressions en présence d'H$_2$O et S. Les verres hydratés présentent des espèces hydroxyles à très faibles teneurs en H$_2$O, pouvant entraîner une polymérisation du magma martien.

Au contraire, de nouvelles valeurs de teneurs en S sont obtenues et réhaussent celles proposées dans la litterature. Un modèle de solubilité du S applicable aux magmas martiens et terrestres a été réalisé.

L'altération de roches volcaniques riches en S, susceptibles d'être présentes sur Mars, entraînent des mélanges de minéraux mafiques avec des sulfates. Une calibration par spectroscopie Raman est réalisée dans des mélanges sulfatés et applicable pour la future mission spatiale.

Pour conclure, ces travaux ré-évaluent le budget en S possible dans l'intérieur martien, mais aussi sur la surface. Des études complémentaires sont nécessaires pour comprendre le comportement d'H$_2$O et d'autres éléments volatils dans ces magmas atypiques.

Title : H$_2$O and S behaviors in martian magmatic system: An experimental and spectroscopic approach

Keywords : Mars, volatile species, melts, high-pressure experiments, Mars 2020

Abstract : The understanding of the planet Mars is required to constrain the Solar System's evolution, and notably, the Earth's. The future 2020 Mars mission will include a Raman spectrometer to characterize martian soils and its surficial mineralogy. Through calibrations, volatiles budget can be determined. Quantify volatile species on Mars permits the understanding of the primitive atmosphere formation which have hold liquid water at the surface.

Hence, synthetic martian basalts have been realized at high-pressures with H$_2$O and S. Hydrated glasses present Free OH groups at low H$_2$O content, which could lead to a polymerization of the martian melt.

On the opposite, martian glasses can dissolve a high S content, higher than previously estimated in the litterature. A new S solubility model is established and can be applied on both terrestrial and martian melt compositions.

The weathering of possible S-rich igneous rocks at the surface of Mars leads to the formation of mixtures between mafic minerals and sulfates. A new Raman calibration is proposed on sulfate mixtures to quantify S for the future spatial mission.

Consequently, this work re-evaluate the S budget in the martian melts and in the surface. Complentary studies are required to understand the H$_2$O, and other volatiles, behaviors in martian melts.

Conclusion

wt %	Dreibus and Wänke (1985)	Sautter et al. (2015)
SiO_2	44.4	62.9
TiO_2	0.1	0.9
Al_2O_3	0.7	16.9
FeO_{tot}	17.9	10.1
MnO	0.5	0
MgO	30.1	1.3
CaO	2.4	3.0
Na_2O	0.5	2.5
K_2O	0	2.4
P_2O_5	0.2	0
Total	97.6	100.7
NBO/T	2.8	0.2
IFS	9.4	11.6

Table C.A1: Chemical composition used for the degassing model (section Conclusion). The NBO/T is calculated according to Brooker et al. (2001) and considering all the Fe content as Fe_{2+}. The IFS calculation is described in the Chapter III (see section III.5.2).